

Dispersive Readout of a Superconducting Qubit Using a SLUG Amplifier

By

David James Hover

A dissertation submitted in partial fulfillment of
the requirements for the degree of

Doctor of Philosophy

(Physics)

at the

UNIVERSITY OF WISCONSIN-MADISON

2013

Date of final oral examination: September 5, 2013

The dissertation is approved by the following members of the Final Oral Committee:

Robert F. McDermott, Associate Professor, Physics

Mark A. Eriksson, Professor, Physics

Mark Saffman, Professor, Physics

Maxim G. Vavilov, Associate Professor, Physics

Irena Knezevic, Professor, Electrical and Computer Engineering

UMI Number: 3596701

All rights reserved

INFORMATION TO ALL USERS

The quality of this reproduction is dependent upon the quality of the copy submitted.

In the unlikely event that the author did not send a complete manuscript and there are missing pages, these will be noted. Also, if material had to be removed, a note will indicate the deletion.



UMI 3596701

Published by ProQuest LLC (2013). Copyright in the Dissertation held by the Author.

Microform Edition © ProQuest LLC.

All rights reserved. This work is protected against unauthorized copying under Title 17, United States Code



ProQuest LLC.
789 East Eisenhower Parkway
P.O. Box 1346
Ann Arbor, MI 48106 - 1346

Abstract

Developing a fast, high-fidelity readout of superconducting quantum bits (qubits) makes significant demands of the cryogenic amplification chain, where the first stage amplifier must have sufficient sensitivity to resolve the state of the qubit and enough gain to overcome the noise of subsequent stages of amplification. Additionally, the architecture of a scalable quantum computer requires an amplifier with a large enough bandwidth and dynamic range to simultaneously measure multiple qubits without sacrificing performance. In this thesis, we describe a novel low-noise phase-insensitive linear amplifier at microwave frequencies based on the Superconducting Low-Inductance Undulatory Galvanometer (SLUG), an amplifier capable of meeting the demands of the superconducting qubit community. We discuss the numerical optimization of the SLUG amplifier and calculate the expected amplifier gain and noise temperature. We walk through the amplifier design and fabrication process before discussing how to fully characterize the fabricated device. We report on amplifiers with measured gain of 10 to 15 dB, bandwidths from 50 to 100 MHz, and added system noise below 2 quanta. Next, we describe the qubit-cavity system and the limits of a dispersive quantum measurement using circuit quantum electrodynamics. Finally, we report on experiments where a SLUG amplifier is used to measure the state of a superconducting qubit, demonstrating improved measurement signal-to-noise ratios of 10 dB and a dynamic range that is an order of magnitude better than any available amplifier currently being developed.

Acknowledgements

There are many people that have made the successful completion of this thesis possible, and I would like to take a few paragraphs to express my thanks.

It is impossible to adequately express the gratitude I have for my Ph.D. advisor, Robert McDermott. Robert always took the time to patiently explain even the smallest detail of my research, and he has been a wellspring of confidence and a daily source of inspiration. He taught me how to build a dilution refrigerator and how to approach a tough electronics problem, but he also gave me the unique opportunity to be a leader and to test out my own ideas. I was very fortunate to have joined the group in its original form, and I benefited both professionally and personally from working side by side with Robert during the group's infancy.

Over the last seven years, I have had the opportunity to see our research group grow from a pair of wide-eyed first years into a small army of determined postdocs and students. Each member of the group has uniquely contributed to my thesis work and has enriched my experience at the University of Wisconsin. I would like to extend special thanks to a few my colleagues that I got to know particularly well over the years. Steve Sendelbach, a friend and cohort who had been in the group since the beginning – he was always there to patiently work through conceptual physics questions and to reflect on the broader themes of life. Dr. Yung-Fu Chen was our first postdoc with whom I spent innumerable hours counting photons and discussing life outside the lab – his generosity and restrained optimism are still an inspiration. Dr. Umesh Patel could always put a smile on my face, and I will miss his daily determination and curiosity. My thesis work would not have converged as quickly or as successfully without the hard work of Dr Shaojiang Zhu and his mastery of the SLUG fabrication process (and his wire bonding skills). I can hardly remember a time in the lab without the dry French wit of one Guilhem Ribeill – he

always kept me honest with his breathless ability to deeply understand everything we were trying to accomplish.

I also owe a great deal to many members of the Martinis group at UCSB – especially, Daniel Sank, Erik Lucero, and Matthew Neeley. I have also benefited from a collaboration with Professor Britton Plourde and Mike DeFeo at Syracuse, and from conversations with Will Oliver at MIT Lincoln Laboratory.

I would never have gotten anything accomplished without the help (and sense of humor) of the university support staff. I extend special thanks to WCAM staff members Rebecca Bauer, Srdjan Milicic, Quinn Leonard, and Dan Christensen. I also want to extend my thanks to many members of the departmental staff: Ann Austin, Aimee Lefkow, the entire machine shop (and especially Doug Dummer), Ian Montgomery, Billy Gates, and Dave Lockman.

I have been fortunate to have a supportive group of friends in Madison and around the country – both from within the physics department and civilians in the “real world.” Their good cheer, compassion, and variety kept me sane and added rich layers to my daily life. I owe them much more than a spot on a couch and a pitcher of beer in Boston, but hopefully they will repeatedly take me up on that offer.

And finally, my family. My sister Kimberly has an infectious laugh that never fails to lift my spirits – she gives me needed perspective, and I continue to be inspired by her enormous sense of generosity and her daily displays of compassion. My parents have been a bedrock of support throughout my life and have always encouraged me to chase after my passions – they have moved mountains for me and I would do the same for them. I love my family deeply and dedicated my thesis to them.

To my family.

Contents

Abstract	i
Acknowledgements	ii
List of Figures	x
1 Introduction	1
1.1 Quantum Bit	3
1.2 Superconducting Qubits	4
1.3 Circuit QED	5
1.4 Qubit Measurement	7
1.5 Jaynes-Cummings Hamiltonian	8
1.6 Multiplexed Readout	11
1.7 Amplification Chain	13
1.7.1 Johnson-Nyquist Noise	14
1.7.2 Added Amplifier Noise	16
1.7.3 Noise Budget	17
1.8 Josephson Based Parametric Amplifiers	19
1.9 Outline of Thesis	20
2 Fundamentals of Superconducting Electronics	21

2.1	Kinetic Inductance	22
2.2	Josephson Effect	24
2.2.1	RCSJ Model	25
2.2.2	Dynamics of the Current Biased Josephson Junction	27
2.3	Flux Quantization	32
2.4	dc SQUID	34
2.4.1	Fluxoid Quantization	34
2.4.2	Transfer Function	35
2.5	SQUID Amplifiers	37
3	SLUG Amplifier Theory	39
3.1	dc SQUID Equations of Motion	40
3.2	SLUG Equations of Motion	43
3.3	DC Characteristics	45
3.4	Scattering Parameters	47
3.5	Noise Properties in the Thermal Regime	53
3.6	Noise Properties in the Quantum Regime	59
3.7	Amplifier Design	61
3.8	Dynamic Range	66
3.9	Effect of Input Circuit Admittance	67
3.10	Reverse Transfer Function	70
3.11	Lumped Element Matching Network	71
3.12	Hot Electron Effects	72
4	SLUG Fabrication	86
4.1	Fabrication Toolbox	86

4.1.1	Superconductor Deposition	86
4.1.2	Niobium Lithography and Etch	88
4.1.3	Silicon Oxide Deposition and Processing	90
4.1.4	Junction Oxidization	91
4.1.5	Resistor Fabrication	92
4.2	Niobium SLUG Recipe	94
4.2.1	Ground Electrode	94
4.2.2	First Dielectric Layer	96
4.2.3	Bottom Electrode	96
4.2.4	Second Dielectric Layer	96
4.2.5	Junction Growth and Top Electrode	97
4.2.6	Resistor	97
4.3	Design Choices	98
5	SLUG Measurements	105
5.1	Experimental Setup	105
5.1.1	Cryogenic Measurement Systems	105
5.1.2	DR SLUG Wiring	107
5.1.3	SLUG Packaging	110
5.2	dc Characteristics	111
5.3	Gain Measurements	115
5.4	Noise Performance	118
5.5	Electron Temperature of Thin Film Resistors	121
5.5.1	Experimental Setup	122
5.5.2	Electron Temperature Measurement	125

5.6	Conclusions and Outlook	130
6	Theory of Superconducting Qubit Readout	133
6.1	Quantization of a Superconducting Circuit	133
6.2	Transmon	137
6.3	Qubit Readout	144
6.3.1	Quarter Wave Resonator	145
6.3.2	Cavity Photon Population	149
6.3.3	Steady State Signal To Noise Ratio	150
6.3.4	SNR With Cavity Ringup	153
6.3.5	Readout Fidelity	156
7	Qubit Measurements	164
7.1	UCSB Xmon	165
7.2	Experimental Setup	166
7.2.1	DR Wiring	166
7.2.2	Qubit Control Electronics	169
7.3	Readout Cavity Spectroscopy	171
7.4	Qubit Spectroscopy	173
7.5	Rabi Oscillations	175
7.6	Qubit Decoherence	176
7.7	Stark Shift Calibration	180
7.8	Cavity Response	182
7.9	Measurement Fidelity Without the SLUG	184
7.10	Improved Fidelity with SLUG Amplifier	190
7.11	Conclusions and Outlook	198

7.11.1	Improving Measurement Fidelity	198
7.11.2	Future Qubit-SLUG Experiments	199
A	Jaynes Cummings Hamiltonian	201
A.1	Full Jaynes Cummings Hamiltonian	201
A.2	Dispersive Approximation for a Two Level System	203
A.2.1	First Order Approximation	203
A.2.2	Higher Order Approximation	205
A.3	Dispersive Limit for Many-Level System	207
B	Numerical Techniques	210
B.1	Numerical Integration	210
B.2	Classical Thermal Noise	212
B.3	Quantum Thermal Noise	213
B.4	SLUG Spectral Noise Components	214
	Bibliography	216

List of Figures

1.1 Bloch Sphere	3
1.2 Cavity QED	6
1.3 Circuit QED	6
1.4 Multiplexed Readout Example	12
1.5 $\lambda/4$ Resonator Read Out	13
1.6 Amplifier Added Noise	16
1.7 Amplifier Chain	18
2.1 S-I-S Junction Cartoon	23
2.2 RCJS Model	25
2.3 Josephson Junction Potential	28
2.4 Single Junction IV Curve	29
2.5 Junction dynamics without noise	30
2.6 Junction Dynamics with Thermal Noise	31
2.7 Flux Quantization	33
2.8 SQUID Transfer Function	36
2.9 Microstrip SQUID Amplifier	37
3.1 dc SQUID	41

3.2	dc SLUG	44
3.3	dc SLUG and SQUID I-V curves	46
3.4	dc SLUG and SQUID V- Φ curves	46
3.5	V_I	48
3.6	Input Impedance Z_{in}	49
3.7	Output Impedance Z_{out}	50
3.8	Equivalent SLUG Circuit	51
3.9	Maximum Gain G_m	52
3.10	Dimensionless SLUG Noises	55
3.11	Classical Optimal Source Impedance	56
3.12	Optimal SLUG Noise Temperature	58
3.13	Quantum Noises	74
3.14	Quantum Optimal Source Impedance	75
3.15	Minimum Number of Added Noise Quanta	75
3.16	Transmission Line Matching Network	76
3.17	Quarter-Wavelength Matching Network	77
3.18	Gain, Noise vs Frequency	78
3.19	Multisection Transformer	79
3.20	Dynamic Range	80
3.21	Circuit Admittance Model	80
3.22	Circuit Admittance I-V, V- Φ	81
3.23	Circuit Admittance Gain and Added Noise	82
3.24	V_I^R	83
3.25	Lumped Element L-C Matching Network	83
3.26	Forward and Reverse Gain for Lumped Element Matching Network	84

3.27	Gain, Added Noise vs. Frequency for Lumped Element Matching Network	85
4.1	Niobium Etch Profile	89
4.2	SiO _x Etch Profile	90
4.3	Junction Exposure	92
4.4	SLUG Layout	95
4.5	SLUG Layout	99
4.6	SLUG Body	100
4.7	Forward and Reverse Gain for Reasonable SLUG	103
5.1	SLUG Wiring Diagram	107
5.2	SLUG Brass Box	110
5.3	SLUGA dc Characteristics	111
5.4	V-Φ Curves for Different Sample Boxes	112
5.5	V-Φ Curves with Low Pass Filter	113
5.6	2D Gain Plot of SLUGA	114
5.7	Gain of SLUGA for Different Bias Points	116
5.8	Gain Comparison	117
5.9	Gain Compression	118
5.10	N_{sys}^S of SLUGA at $I_b = 80 \mu\text{A}$	119
5.11	N_{sys}^S Line Cuts	120
5.12	Electron Temperature Measurement	123
5.13	Correlated Spectrum	127
5.14	Electron Temperature Measurement	128
6.1	Quantized lossless parallel LC resonator	135
6.2	Cooper Pair Box Schematic	138

6.3	Spectra, Eigenfunctions, and Matrix Elements of CPB	141
6.4	Readout Resonator	143
6.5	Quarter Wave Resonator S_{21}	158
6.6	Steady State SNR	159
6.7	Calculated n_{crit} and Dispersive Shift	160
6.8	Output Voltage Profile	161
6.9	Modified SNR	162
6.10	Fidelity Estimate	163
7.1	UCSB-Martinis Xmon	166
7.2	Xmon Wiring Diagram	167
7.3	Xmon Chip Picture	169
7.4	Qubit Control Electronics	170
7.5	Read Out Spectroscopy	172
7.6	Punch Out Spectroscopy	173
7.7	Qubit Spectroscopy	174
7.8	Rabi Oscillations	175
7.9	T_1 Time	176
7.10	Swap Spectroscopy	177
7.11	Fine Qubit Spectroscopy	179
7.12	Ramsey Experiment	180
7.13	Stark Shift	181
7.14	Resonator Photon Occupation	181
7.15	State-Dependent Output Voltage	183
7.16	Heterodyne Signal	184

7.17 Fidelity Histograms	185
7.18 Measurement Fidelity Versus Time and Power	187
7.19 Measurement SNR Versus Time and Power	188
7.20 n_{sys} of Amplifier Chain	190
7.21 SNR Improvement with SLUG	191
7.22 IQ Snapshots at 600 ns	193
7.23 IQ Snapshots at 2 μs	194
7.24 Readout Fidelity with SLUG	195
7.25 Measurement SNR with and without the SLUG	196
7.26 SNR Compression	196
7.27 n_{sys} of SLUG	198
B.1 Computed Spectral Density	215

Chapter 1

Introduction

The accomplishments of the computing and information processing fields not only drive the modern day economy but significantly impact the way we carry out our lives. Beginning with Bardeen and Brattain's seminal work at Bell Labs in 1947, the semiconductor industry has transformed the transistor from a table-top experiment to a logical-bit that works in concert with millions of identical transistors, all contained in a processor the size of a quarter. The impressive trajectory of the transistor provides important context when considering the progress of quantum computers. It has become technologically feasible to isolate and address individual quantum systems over the last few decades, resulting in a wide variety of experiments that have confirmed the theoretical underpinnings of quantum mechanics and have opened the door for the field of quantum information. While a quantum processor capable of solving classically intractable problems is hardly just over the horizon, there has been significant progress that has inspired cross-disciplinary innovation along with the drums of popular science. There are many different quantum computing architectures being developed, but in this thesis we focus on an architecture built with superconducting quantum bits (qubits).

The rapid development of superconducting quantum electronics has motivated a search for near quantum-limited microwave amplifiers for the low-noise readout of qubits and linear cavity resonators [1, 2]. It has long been recognized that devices relying on the dc-superconducting quantum interference device (dc-SQUID) can achieve noise performance approaching the fundamental quantum limit imposed on phase-insensitive amplifiers: namely, the amplifier must add at least half a quantum of noise to the signal it amplifies [3]. For comparison, state of the art semiconductor amplifiers based on High Electron Mobility Transistors (HEMTs) have achieved impressive noise temperatures on the order of 2.5 K, or roughly 20 times the quantum limit, with an instantaneous bandwidth spanning 1 to 10 GHz. Such HEMTs are broadly employed in the cryogenic amplification chain of many experiments within the superconducting electronics community. However, their noise performance is limited by the heating of electrons in the FET channel and recombination noise, making significant improvements in noise performance difficult.

Discovered in 1964 by Jaklevic *et al.* [4] at Ford Motor, the dc-SQUID has been employed as a low-noise amplifier for many different applications, such as in dark matter searches [5], low-field MRI [6], qubit readout [7], magnetic characterization of thin films [8, 9], and for sensitive biomagnetic measurements [10, 11]. Theoretically, amplifiers relying on the dc-SQUID should be capable of amplifying signals from dc to tens of GHz, offering an attractive alternative to semiconductor based architectures. However, it has proven difficult to efficiently couple the input signal to the dc-SQUID when the operating frequency exceeds 1 GHz.

We will discuss the limitations of the dc-SQUID in great detail within Section 2.5, but for the remainder of this introductory chapter we will focus on how quantum computing in particular benefits from a quantum limited microwave amplifier.

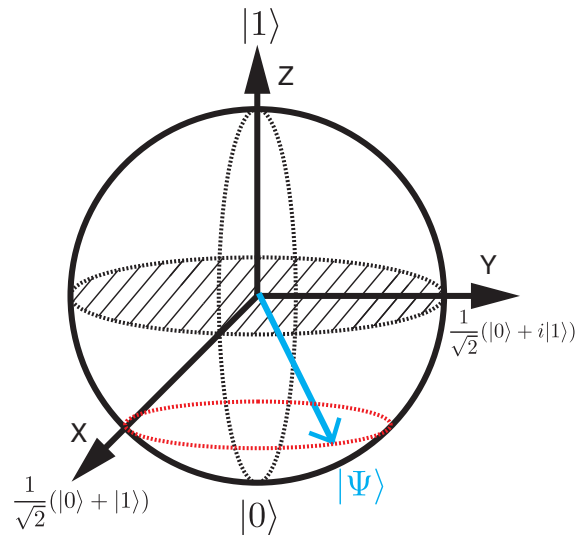


Figure 1.1: Bloch sphere demonstrating the computational space of a qubit, with the $|0\rangle$ and $|1\rangle$ state at the poles and the state vector $|\Psi\rangle$ lying on the surface of the sphere.

1.1 Quantum Bit

A quantum computer is comprised of logic gates that operate on an ensemble of quantum bits. A bit is the most basic unit of classical logic and can occupy one of two discrete states, 0 or 1. A quantum bit, or ‘qubit,’ on the other hand, can be an arbitrary superposition of the eigenstates $|0\rangle$ and $|1\rangle$, or $|\Psi\rangle = a_0|0\rangle + a_1|1\rangle$, where $|a_0|^2$ and $|a_1|^2$ are the occupation probabilities of the $|0\rangle$ and $|1\rangle$ state, respectively. The Bloch sphere in Figure 1.1 illustrates the computational space of a single qubit, where the state vector $|\Psi\rangle$ can lie anywhere on the surface of the sphere, and single qubit gates are realized with arbitrary rotations about the three axes.

Where n classical bits can only exist in one of the 2^n possible states, a quantum processor with n qubits can be placed in a complex superposition state of all 2^n permutations, containing exponentially more information than a conventional processor. Unfortunately, expanding this computational space does not lead to a universal computational speedup;

however, there are certain classically intractable problems that benefit from known quantum algorithms. For example, Shor’s algorithm can factor large numbers exponentially faster than its classical counterpart [12], providing a tool for cracking the RSA encryption protocol [13]. A quantum computer could also be used for large scale quantum simulations of many body systems with over a million degrees of freedom [14]. Fully exploring the field of quantum information is beyond the scope of this thesis, but we encourage the intrepid reader to pick up Nielsen and Chuang [15], or for a more experimentally driven approach we recommend the theses by Jerry Chow [16], Daniel Slichter [17], and Jürgen Lisenfeld [18].

A qubit is simply a pair of addressable quantum levels. The canonical example is an electron in a magnetic field, with the discrete energy levels given by the Zeeman splitting. There are many qubit architectures being actively studied: ensembles of nuclear spins [19], trapped ions [20], and quantum dots [21, 22], to name a few. For this thesis we are interested in qubits that exploit the macroscopic quantum behavior of superconducting circuits.

1.2 Superconducting Qubits

Superconducting qubits [23, 24] are electrical circuits engineered to have discrete, anharmonic spectra – an “artificial atom” fabricated using standard lithographic techniques. The superconducting qubit is an integrated circuit constructed from inductors, capacitors, and transmission lines, along with the Josephson junction [see Section 2.2], which behaves as a non-linear, dissipationless inductor. A quantum computer capable of breaking RSA encryption requires thousands, if not millions of qubits [25], making scalability a central concern. The superconducting architecture has the benefit of flexi-

bility and exploits mature fabrication techniques already developed by the semiconductor industry.

However, these advantages come at the price of a tighter coupling to environmental noise sources, resulting in low coherence times compared to more established architectures. Years of materials research (e.g. developing low-loss dielectrics [26], cleaning up the superconductor-substrate interface [27, 28]), along with aggressive filtering in combination with clever circuit engineering have helped minimize the effect environmental noise sources have on the qubit's degrees of freedom. Because of these efforts, over the last 15 years coherence times have dramatically increased, from the original Cooper pair box qubit [29], where the group at NEC in Japan observed coherent oscillations on the order of 1 ns [30], to the most results with the transmon [31] where coherence times of order 50 μs were measured [32, 28].

1.3 Circuit QED

We use the toolbox provided by circuit quantum electrodynamics (circuit QED) to address and measure our superconducting qubit. Circuit QED, first developed by the Yale group [33, 34, 1], is a direct analogue of cavity QED used in atomic physics. Where atomic physicists use atoms coupled to the electromagnetic field inside a Fabry-Perot cavity [Figure 1.2(a)], we use superconducting qubits coupled to the electric field in a planar transmission line resonator [Figure 1.3(b)]. As illustrated in Figure 1.2(a), cavity QED uses a Fabry-Perot cavity bounded by two semitransparent mirrors, where the length of the cavity and the transparency of the mirrors determine the resonant frequency and linewidth of the transmitted photons. An atom in the cavity interacts

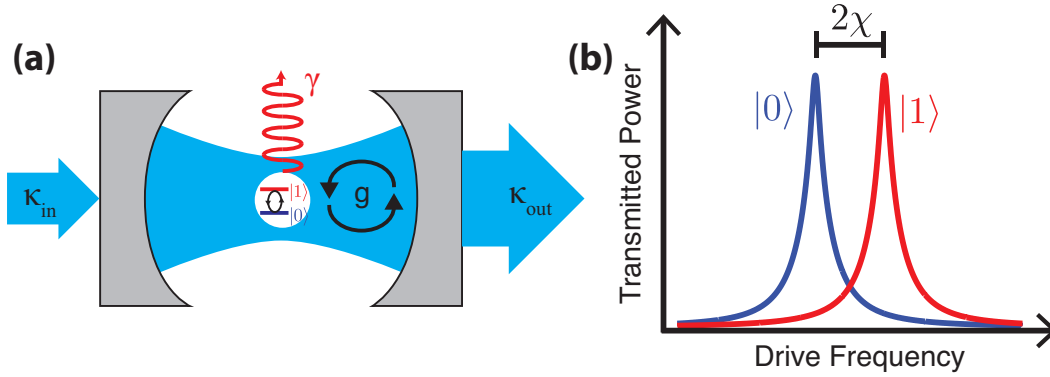


Figure 1.2: **(a)** The electric field in a Fabry-Perot cavity interacting with a qubit, where κ_{in} (κ_{out}) is the coupling strength at the input (output) of the cavity; g is the coupling strength between the qubit and the cavity; and γ is the rate at which the qubit loses information to the environment. **(b)** The frequency response of the photons transmitted through the cavity for the qubit in the $|0\rangle$ and $|1\rangle$ state, where 2χ is the difference in frequency between the dressed states of the cavity.

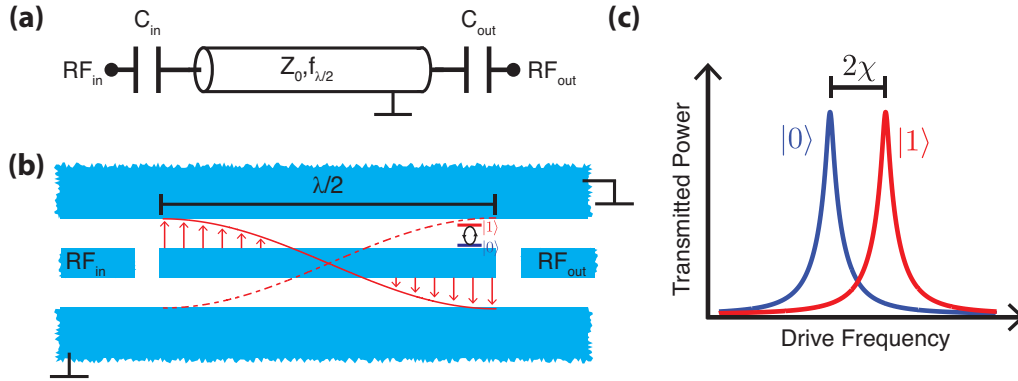


Figure 1.3: **(a)** Circuit schematic of a $\lambda/2$ transmission line resonator with characteristic impedance Z_0 coupled to the outside world via two capacitors: C_{in} and C_{out} . **(b)** Cartoon layout of the schematic in **(a)**, where the resonator is in the coplanar geometry, and the qubit sits at one of the voltage anti-nodes (not to scale). **(c)** Power transmission through the cavity for the qubit in the $|0\rangle$ and $|1\rangle$ state.

with the trapped photons, and a measurement of the photons leaking out of the cavity allows one to probe the state of the atom.

As illustrated in Figures 1.3(a) and (b), in circuit QED the cavity is replaced by a $\lambda/2$ transmission line resonator that interacts with the outside world via two capacitors,

C_{in} and C_{out} . A superconducting qubit sits at a voltage anti-node in the resonator, where the capacitance between the qubit and the resonator sets the interaction strength g . We measure a maximum number of photons leaking out of the resonator (RF_{out}) when the impinging signal (RF_{in}) is on resonance with the cavity-qubit system.

1.4 Qubit Measurement

The qubit isn't very interesting in a vacuum – one must be able to measure its state. A measurement probabilistically maps a superposition of possible states onto a single outcome. The qubit state $|\Psi\rangle = a_0|0\rangle + a_1|1\rangle$ lies on the surface of the Bloch sphere, but the classical meter can only access one eigenstate of the system. For one qubit, this means we measure the z-axis component of $|\Psi\rangle$, returning either the $|0\rangle$ or the $|1\rangle$ state. By making repeated measurements we gain access to $|a_0|^2$ and $|a_1|^2$.

A projective quantum non-demolition (QND) measurement leaves the qubit in its measured eigenstate – e.g. if one measures $|1\rangle$ the state will remain in $|1\rangle$ upon repeated measurements. We introduce this concept with a general Hamiltonian that describes the qubit, the measurement, and the interaction between the two:

$$\hat{H} = \hat{H}_q + \hat{H}_m + \hat{H}_{int}. \quad (1.1)$$

Mathematically, a QND measurement \hat{M} commutes with the full Hamiltonian, meaning:

$$[\hat{H}_q, \hat{M}] = 0, \quad (1.2)$$

$$[\hat{H}_m, \hat{M}] = 0, \quad (1.3)$$

$$[\hat{H}_{int}, \hat{M}] = 0. \quad (1.4)$$

A quantum system can exist simultaneously in multiple eigenstates. A strong QND measurement “instantaneously” forces the system into one of its eigenstates, giving the observer direct access to the commuting eigenstates of the system, while information about the eigenstates of the non-commuting measurements ($\hat{\sigma}_X, \hat{\sigma}_Y$) are lost. Looking back at the Bloch sphere [1.1], a projective measurement of $\hat{\sigma}_Z$ probabilistically collapses the state vector $|\Psi\rangle$ on to the z-axis; the initial x and y-axis components of $|\Psi\rangle$ are lost as a direct consequence of the measurement. Repeatedly measuring $\hat{\sigma}_Z$ returns the same result, while interleaving non-commuting measurements (e.g. $\hat{\sigma}_Y \rightarrow \hat{\sigma}_Z \rightarrow \hat{\sigma}_Y$) will return uncorrelated results.

1.5 Jaynes-Cummings Hamiltonian

The Jaynes-Cummings Hamiltonian [35] describes the qubit-cavity system of Section 1.3: a generalized two level system, or qubit, with an energy splitting ($\hbar\omega_{10}$) interacting with photons in a resonator with resonance frequency ω_r . After making the rotating wave approximation [see A.1], the general measurement Hamiltonian [Equation 1.1] takes the following form:

$$\hat{H}_{JC} = \frac{1}{2}\hbar\omega_{10}\hat{\sigma}_Z + \hbar\omega_r \left(\hat{a}^\dagger \hat{a} + \frac{1}{2} \right) + \hbar g(\hat{a}\hat{\sigma}^+ + \hat{a}^\dagger\hat{\sigma}^-), \quad (1.5)$$

where the first term $\frac{1}{2}\hbar\omega_{10}\hat{\sigma}_Z$ describes the qubit as a two-level system, the second term $\hbar\omega_r(\hat{a}^\dagger\hat{a} + 1/2)$ describes the cavity (or resonator), and $\hbar g(\hat{a}\hat{\sigma}^+ + \hat{a}^\dagger\hat{\sigma}^-)$ is the interaction term. Here, \hat{a}^\dagger and \hat{a} are the harmonic oscillator creation and annihilation operators, while $\hat{\sigma}^+$ and $\hat{\sigma}^-$ are the qubit raising and lower operators given by $\frac{1}{2}(\hat{\sigma}_X \pm i\hat{\sigma}_Y)$.

The special case where the qubit is far detuned from the cavity, such that $\Delta \equiv \omega_{10} - \omega_r \gg g$, is known as the dispersive regime. In this limit, the qubit and cavity do not exchange energy, meaning the eigenstates of the system can be well approximated by the product states of the qubit and cavity. After performing an expansion to first order in g/Δ [see A.2.1], \hat{H}_{JC} becomes:

$$\hat{H}_{disp} = \frac{1}{2}\hbar \left(\omega_{10} + \frac{g^2}{\Delta} + \frac{g^2}{\Delta} \hat{a}^\dagger \hat{a} \right) \hat{\sigma}_Z + \hbar\omega_r \left(\hat{a}^\dagger \hat{a} + \frac{1}{2} \right), \quad (1.6)$$

where the qubit's frequency is now shifted by g^2/Δ - the zero-point energy of the cavity field, known as the Lamb shift - plus the photon dependent Stark shift $g^2\hat{a}^\dagger\hat{a}/\Delta$, with $\hat{a}^\dagger\hat{a}$ being the number of photons in the cavity. To understand how the qubit influences the cavity resonance, we recast \hat{H}_{disp} into the following form:

$$\hat{H}_{disp} = \frac{1}{2}\hbar\omega_{10}\hat{\sigma}_Z + \hbar \left(\omega_r + \frac{g^2}{\Delta} \hat{\sigma}_Z \right) \left(\hat{a}^\dagger \hat{a} + \frac{1}{2} \right), \quad (1.7)$$

where the cavity frequency is shifted by the state dependent $\pm\chi = \pm g^2/\Delta$, known as the dispersive shift. In consequence, probing the resonance of the cavity measures the projected state of the qubit. As illustrated in Figures 1.2(b) and 1.3(c), one can easily distinguish the $|0\rangle$ from the $|1\rangle$ state as long as the dispersive shift is larger than the line width of the cavity ($2\chi > \kappa$). Also note that each term in the dispersive form commutes with a projective measurement onto the z-axis, such that $[\hat{H}_{dips}, \hat{\sigma}_Z] = 0$. This satisfies the conditions of Equation 1.4, meaning an observation of $\hat{\sigma}_Z$ is a projective-QND measurement. Experimentally, one would probe the cavity at a fixed frequency that maximizes distinguishability of the qubit states. The signal leaving the resonator must then be amplified and appropriately filtered for data processing with room temperature electronics.

QND measurements of superconducting qubits have been successfully demonstrated [36, 37, 38, 39], but performing a QND measurement with high single-shot fidelity is not trivial. Single-shot fidelity is a metric of our ability to faithfully resolve the state of the qubit in a single measurement. If one interrogates the cavity with a small signal, the noise of the measurement's amplification chain will drown out the signal, resulting in low fidelity. Driving the resonator strongly induces qubit state mixing, also resulting in a reduced fidelity. As discussed in Section A.2.2, the dispersive approximation breaks down as the number of photons interacting with the qubit in the cavity approaches n_{crit} , defined as:

$$n_{crit} = \frac{\Delta^2}{4g^2}. \quad (1.8)$$

The classical signal measured by the amplification chain will be on the order of -120 dBm¹. A power of this magnitude can easily be measured if we are able to average away the noise for an arbitrary amount of time. Unfortunately, we are limited to time scales on the order of the qubit relaxation rate T_1 ² – the qubit $|1\rangle$ state will relax to $|0\rangle$, reducing the fidelity of the measurement. This limitation puts a large demand on the amplification chain noise budget – the lower the noise, the quicker we are able to resolve the state of the qubit, giving us a greater readout fidelity. In Section 6.3, we discuss in great detail how the probe signal is modified by the qubit, along with the expected distinguishability and measurement fidelity for a given measurement setup.

1.6 Multiplexed Readout

A scalable architecture must incorporate some flavor of multiplexed readout; a separate amplification chain for each qubit is impractical when the processor grows to hundreds of qubits. A simple example capacitively couples a series of resonators with different lengths to a common feed line, as illustrated in Figure 1.4. Each resonator is coupled to a separate qubit, giving us the ability to probe the state of each qubit individually using one amplification chain. This could be done using standard modulation techniques, where the applied microwave tone RF_{in} has spectral components at each resonance. The amplified tone is then captured and demodulated, giving us access to the complex spectral components of each resonator.

A multiplexed readout puts additional demands on the amplification chain. For a simultaneous readout, the amplification chain must have a large enough instantaneous

¹Power in dBm is a logarithmic power in watts referred to 1 mW, $P_{\text{dBm}} = 10 \log_{10}(P/1 \text{ mW})$. A measurement of -120 dBm is the the same as measuring 1 fW.

² T_1 is the rate at which the excited qubit exchanges energy with the environment.

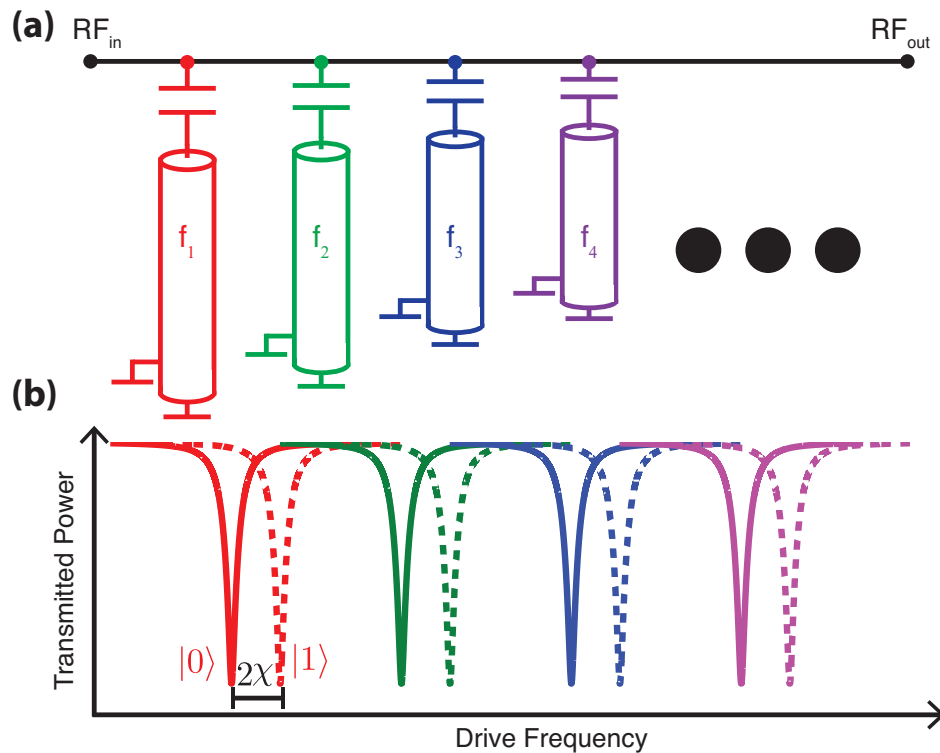


Figure 1.4: **(a)** Cartoon of a possible multiplexed readout, where a series of $\lambda/4$ transmission line resonators of different lengths are capacitively coupled to a common feedline. With each resonator coupled to a different qubit, one can probe the state of each qubit using a single amplification chain, where **(b)** shows the transmitted power through the feedline for the different possible qubit states.

bandwidth to be sensitive to each resonator attached to the feedline. Additionally, more resonators mean the signal to be amplified will carry more power, which must be handled without saturating³ the amplification chain.

The example in Figure 1.4 couples a qubit to a $\lambda/4$ resonator instead of the $\lambda/2$ devices described in the previous sections. A shorter resonator allows for more microwave components on a single chip; additionally, we use this geometry for measuring a qubit Chapter 7 below. As illustrated in Figure 1.5, the $\lambda/4$ resonator has a standing wave

³Saturation is when the amplified signal does not grow linearly with the input signal. A compressed signal with result in a lower signal-to-noise ratio, resulting in a lower measurement fidelity.

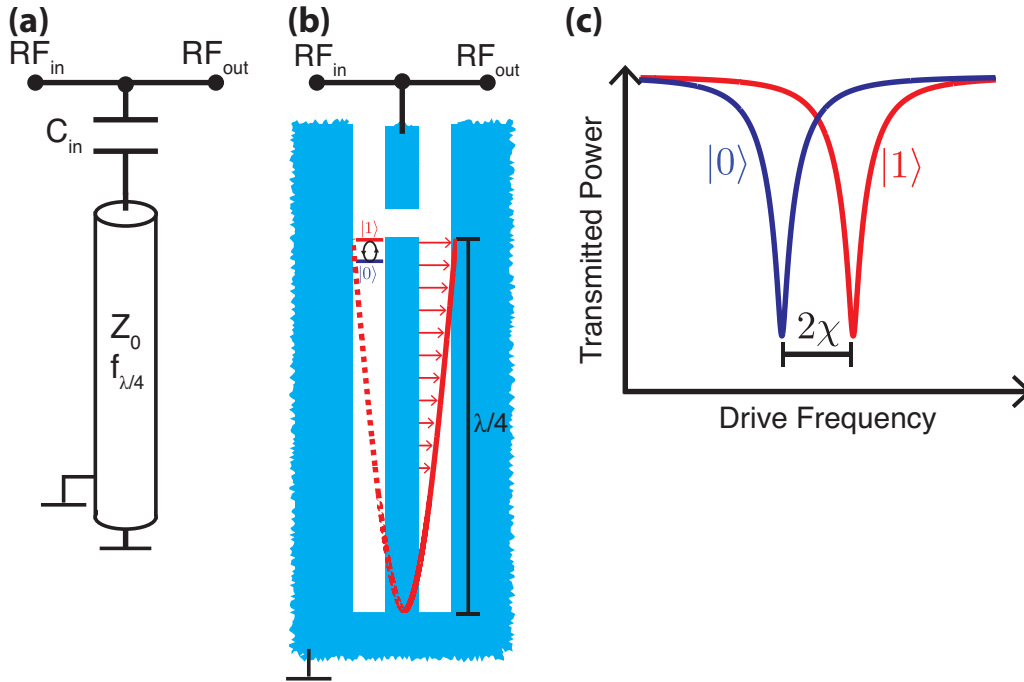


Figure 1.5: **(a)** Schematic of a $\lambda/4$ transmission line resonator capacitively coupled to a common feedline. **(b)** A cartoon of the resonator in the coplanar waveguide geometry, where the resonator is short-circuited on the end without the capacitor. A voltage anti-node occurs on the capacitor end. The qubit sits at the voltage anti-node for maximum coupling to the electric field in the cavity. **(c)** In this geometry the transmitted power goes to zero when the applied microwaves are on resonance with the qubit-cavity system.

with a voltage maximum at the capacitor and a voltage minimum on the short-circuited side of the resonator. On resonance, the cavity maximally absorbs microwaves on the feedline, leading to a dip in transmitted power as a function of frequency.

1.7 Amplification Chain

It should now be clear that a high-fidelity QND readout requires an ultra-low noise, broadband amplification chain, capable of a simultaneous readout of multiple qubits without saturating the signal. To turn the small number of photons leaking out of the

cavity-qubit system into a signal that can be processed by room temperature electronics, a multistage amplification chain is needed, with a total gain on the order of 100 dB. Each amplifier in the chain will add noise to the total signal.

1.7.1 Johnson-Nyquist Noise

The classical noise generated by the thermal fluctuations of electrons in a resistor, known as Johnson-Nyquist noise [40, 41], has a white voltage spectral density:

$$S_V^N(\omega) = 4k_B T R, \quad (1.9)$$

where k_B is the Boltzmann constant, and S_V^N has units of V^2/Hz . When attached to a matched, noiseless load, the current spectral density in the circuit is just $S_I^N = S_V^N/(2R)^2 = k_B T/R$. Multiplying the current spectral density by the resistance R gives us an expression for the power spectral density (watts per unit-bandwidth) dissipated in a matched load:

$$S(\omega) = k_B T. \quad (1.10)$$

A classical treatment of the noise returns a spectral density symmetric in frequency, where $S(\omega) = S(-\omega)$, which physically means that a classical resistor is a perfect black-body, emitting (positive frequency) and absorbing (negative frequency) noise power at the same rate. However, in the limit where $k_B T \ll \hbar\omega$, one must take quantum mechanics into account when describing the statistics of the fluctuators. By applying the

quantum fluctuation-dissipation theorem, we get the following complete expression for the symmetric⁴ voltage spectral density [43]:

$$S_V^N = 2\hbar\omega R \coth\left(\frac{\hbar\omega}{2k_B T}\right). \quad (1.11)$$

We recover the classical form of Equation 1.9 in the limit that $k_B T \gg \hbar\omega$. As $T \rightarrow 0$, Equation 1.11 becomes $2\hbar\omega R$ – the noise due to the zero-point energy of the electric-field, which is similar in origin to the energy stored in a harmonic oscillator in the absence of excitations. For experiments in this thesis ($T \approx 40$ mK, $f \approx 6$ GHz), we will be well into the quantum regime. Following the same analysis as above, one can write down the full form of the power spectral density dissipated in a matched load:

$$S(\omega) = \frac{\hbar\omega}{2} \coth\left(\frac{\hbar\omega}{2k_B T}\right), \quad (1.12)$$

which reduces to $\hbar\omega/2$ for $T = 0$, meaning that in the best case scenario of operating the experiment at absolute zero, our amplification chain will still be sensitive to a half quantum of noise per unit bandwidth. Conventionally, the noise contributions of an amplification chain refer to an effective temperature T_{eff} of the noise source, where:

$$T_{eff} = S(\omega)/k_B. \quad (1.13)$$

⁴The symmetric voltage spectral density is $S(\omega < 0) + S(\omega > 0) = 2\hbar\omega R(n_{BE}(|\omega|) + 2\hbar\omega R(n_{BE}(|\omega|) + 1))$, where $n_{BE}(\omega) = 1/(\exp(\hbar\omega/k_B T) - 1)$ is the Bose-Einstein occupation probability. For an excellent review on quantum noise, see Clerk *et al.* [42].

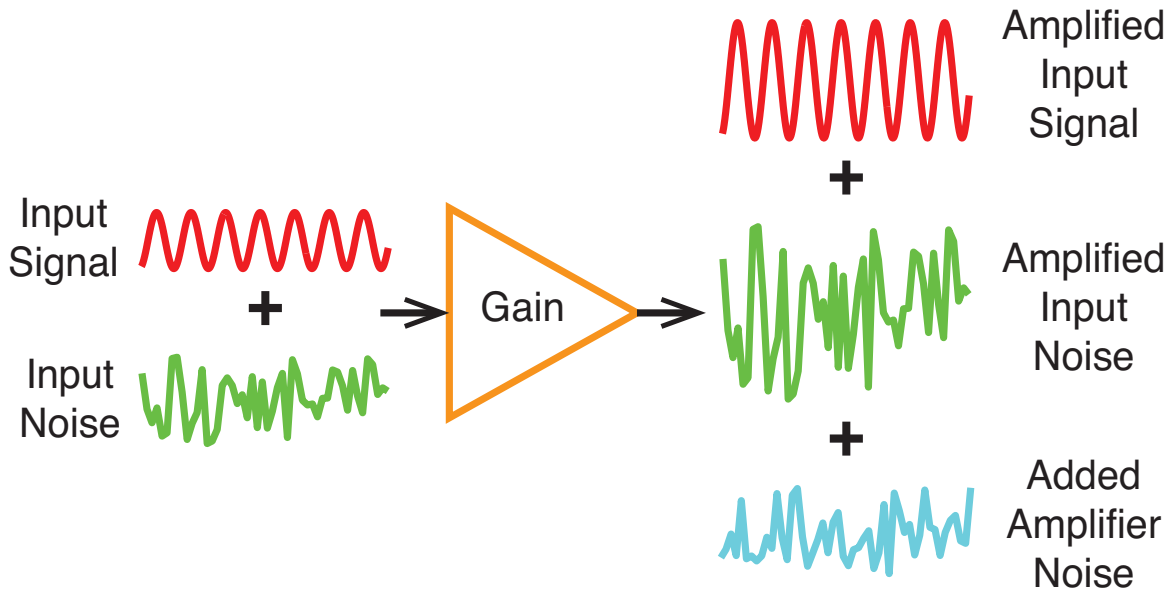


Figure 1.6: The input of the amplifier is sensitive to both the noise and the signal we're interested in analyzing. The amplifier with gain G will output the original voltage traces multiplied by \sqrt{G} , along with noise generated internally by the amplifier.

Likewise, we recast the spectral density into an effective number of noise quanta:

$$n_{eff} = \frac{S(\omega)}{\hbar\omega}. \quad (1.14)$$

1.7.2 Added Amplifier Noise

An amplifier with power gain G takes a voltage trace $V_{in}(t)$ at its input, and outputs an amplified signal $V_{out}(t) = \sqrt{G}V_{in}(t)$. Since an amplifier will uniformly amplify both the input noise and the signal, the signal-to-noise ratio (SNR) will not improve. In fact, the SNR will always get worse, as the amplifier also adds noise $S_{amp}(\omega)$, where $S_{amp}(\omega)$ is typically referred to the input of the amplifier, with an effective noise temperature T_N , or added number of noise quanta n_N :

$$S_{amp}(\omega) = k_B T_N = \hbar \omega n_N. \quad (1.15)$$

For a bandwidth B , the noise power P_N measured at the output of the amplifier in Figure 1.6 is:

$$P_N = k_B (T_{eff} + T_N) GB = \hbar \omega (n_{eff} + n_N) GB. \quad (1.16)$$

This added noise can come from many different sources (*e.g.* electron-hole recombination in semiconductors, thermal fluctuations of charge carriers in resistors), but even the best amplifier falls victim to the consequences of the Heisenberg uncertainty principle, which puts a fundamental limit of an added half quantum of noise for a phase-insensitive amplifier [44]. A quantum limited amplifier is an amplifier with added noise $S_{amp}^Q(\omega)$:

$$S_{amp}^Q = \frac{1}{2} \hbar \omega. \quad (1.17)$$

1.7.3 Noise Budget

It is important to calculate the noise budget of an amplification chain in order to identify the bottlenecks of a measurement setup. Take the three amplifier example shown in Figure 1.7. The total noise power generated by the chain is:

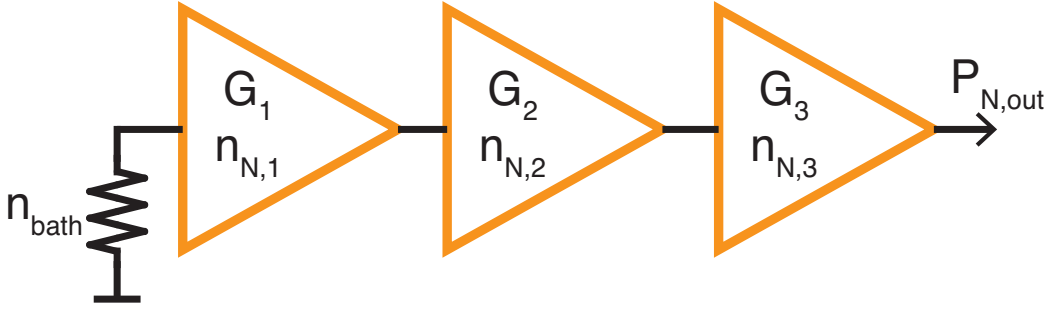


Figure 1.7: A chain of three amplifiers, each with its own gain G_k and added noise $n_{N,k}$ where k is k^{th} amplifier stage.

$$\begin{aligned}
 P_{N,\text{out}} &= \hbar\omega([(n_{\text{bath}} + n_{N,1})G_1 + n_{N,2}]G_2 + n_{N,3})G_3B \\
 &= \hbar\omega[(n_{\text{bath}} + n_{N,1}) + \frac{n_{N,2}}{G_1} + \frac{n_{N,3}}{G_1G_2}]G_1G_2G_3B \\
 &= \hbar\omega(n_{\text{bath}} + n_{\text{sys}})G_{\text{sys}}B,
 \end{aligned} \tag{1.18}$$

where the effective gain G_{sys} and added noise n_{sys} are:

$$G_{\text{sys}} = G_1G_2G_3, \tag{1.19}$$

$$n_{\text{sys}} = n_{N,1} + \frac{n_{N,2}}{G_1} + \frac{n_{N,3}}{G_1G_2}, \tag{1.20}$$

with a SNR of:

$$\begin{aligned}
 \text{SNR} &= \frac{P_{\text{in}}G_{\text{sys}}}{\hbar\omega(n_{\text{bath}} + n_{\text{sys}})G_{\text{sys}}B} \\
 &= \frac{P_{\text{in}}}{\hbar\omega(n_{\text{bath}} + n_{\text{sys}})B}.
 \end{aligned} \tag{1.21}$$

Note that a properly engineered amplification chain relies on the first stage amplifier to maximize SNR, where the noise of the amplification chain is set by $n_{N,1}$ so long as $G_1 n_{N,1} \gg n_{N,2}$ and $G_1 G_2 n_{N,1} \gg n_{N,3}$. Say the second stage amplifier is a state-of-the-art HEMT amplifier, with gain of 30 dB and an added noise of 15 quanta at 6 GHz. A first stage amplifier with gain of 20 dB will reduce the HEMT's contribution to n_{sys} from 15 quanta down to 0.15 quanta of added noise.

1.8 Josephson Based Parametric Amplifiers

There has been significant recent progress in the development of low-noise Josephson parametric amplifiers (JPAs) [45, 46, 47, 48, 49] including such milestones as demonstrating quantum feedback control for the stabilization of Rabi-oscillations [50], and the observation of quantum jumps of the projected qubit state [39]. Because these amplifiers squeeze the input state, they can achieve added noise numbers for one field quadrature below the standard quantum limit of half a quantum. Moreover, these devices operate with negligible dissipation, circumventing the practical problems associated with hot-electron effects that are intrinsic to devices that operate in the finite-voltage regime.

For a complete review of JPAs, please consult R. Vijay's thesis [49]. Gain in a parametric amplifier is achieved by driving a parameter of the amplifier system strongly with a pump tone. Due to the non-linearity of the system, some of this pump energy gets transferred into another frequency mode, chosen to be the signal frequency. The JPA is simply an anharmonic oscillator, with a non-linearity introduced by the presence of a Josephson junction. A JPA is a one port network, where the amplified signal is reflected off the JPA. Since the amplifier operates in reflection mode with a microwave bias, the measurement chain must include a handful of bulky microwave components (isolators,

circulators, directional couplers, etc.) that introduce loss between the measured qubit and the amplifier. JPAs also exhibit low gain-bandwidth products (50 MHz bandwidth with about 20 dB gain) and a limited dynamic range (saturating with approximately -120 dBm input signals). While the noise performance of the JPA is well suited for the readout of one qubit, its limitations make the JPA unsuitable for the large scale multiplexed readout of an ensemble of qubits. Another flavor of parametric amplifier is the traveling wave parametric amplifier (TWPA), which relies on many Josephson junctions embedded in a transmission line [51]. The TWPA is a non-reciprocal two-port device which has demonstrated broadband amplification. In principle, the TWPA should be a quantum limited amplifier with a bandwidth that exceeds two GHz. It isn't clear yet if the dynamic range of TWPA is better than a JPA.

1.9 Outline of Thesis

The rest of this thesis is organized as follows: in Chapter 2 we'll discuss some fundamentals of superconducting electronics, with a focus on the dynamics of the resistively and capacitively shunted Josephson junction and the dc SQUID. In Chapter 3, we'll introduce the superconducting low-inductance undulatory galvanometer (SLUG) and discuss its optimized gain and noise performance as an amplifier. In Chapter 4, we'll give an overview of steps involved in fabricating the SLUG amplifier, including a discussion of our circuit design choices. Measurements of the SLUG amplifier gain and noise performance are discussed in Chapter 5. In Chapter 6 we briefly discuss the theory behind the transmon qubit, and finally in Chapter 7 we go over the measurements of the qubit, comparing the single shot readout fidelity with and without the SLUG amplifier.

Chapter 2

Fundamentals of Superconducting Electronics

As described in 1957 by Bardeen, Cooper, and Schrieffer in their Nobel Prize winning work [52], the electrons of some metals undergo a phase transition at a critical temperature T_C , forming the superconducting state. Below T_C , electrons of opposite spins and momenta form Cooper pairs due to an attraction mediated by lattice phonons. The paired electrons form spin-zero bosons, and it follows that the charge carriers of the conductor condense into a state that can be described by a single quantum mechanical wave function:

$$\Psi(\vec{r}, t) = n(\vec{r}, t)^{1/2} e^{i\theta(\vec{r}, t)}, \quad (2.1)$$

where $\theta(\vec{r}, t)$ is the phase of the wave function and $n(\vec{r}, t)$ is the Cooper pair density.

As H. Kamerlingh Onnes first observed in 1911 [53], the first hallmark feature of superconductivity is the absence of electrical resistivity below T_C . Perfect conductivity has been further demonstrated by experiments that measure persistent currents in superconducting rings, placing a lower bound on the characteristic decay time of 10^5 years.

Type I superconductors also exhibit perfect diamagnetism, known as the Meissner effect [54], where the superconductor expels magnetic field as it is cooled through T_C , which implies the existence of a critical magnetic field H_C that destroys superconductivity. This behavior forces the supercurrent to the edges of superconductor, where the magnetic field is exponentially screened from the interior of the bulk superconductor with a decay constant known as the temperature dependent London penetration depth λ_L [55].

2.1 Kinetic Inductance

While a superconductor has zero resistance for direct current (dc) signals, it presents a nonzero impedance for an applied alternating current (ac) signal. In addition to a geometric inductance, a superconductor has a non-negligible kinetic inductance. An electric field applied near the surface of a superconducting wire with cross section A and length ℓ will cause the Cooper pairs to accelerate, storing a kinetic energy equal to [56]:

$$KE = \frac{1}{2}(2mv^2)(n_s \ell A) = \frac{1}{2}L_K I^2, \quad (2.2)$$

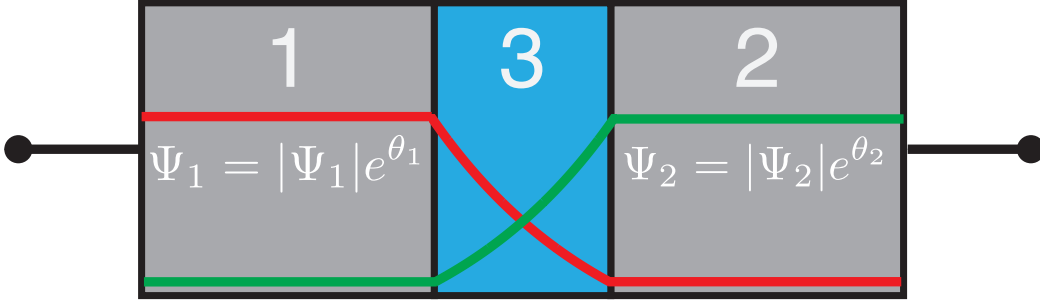


Figure 2.1: Cartoon of an S-I-S Josephson junction. Junction is made of two superconducting electrodes (regions 1 and 2) separated by a thin insulating barrier (region 3). The Cooper pairs in each electrode can be described by a wave function Ψ_k , which has an order parameter θ_k , known as the phase of the condensate. The red and green traces represent the amplitude of the wave functions in the first and second electrodes, respectively.

where the current $I = 2evn_s$, m and e is the mass and charge, respectively, of an electron, and n_s is the uniform Cooper-pair density, giving the following form to the kinetic inductance L_K :

$$L_K = \frac{m\ell}{2n_s e^2 A}. \quad (2.3)$$

Qualitatively, the inertia of the Cooper-pairs resist a quickly changing electric field, creating a phase lag in the charge carriers due to the finite time it takes for the Cooper-pairs to change directions. The total series inductance of the wire is just $L_T = L_G + L_K$, where L_G is the geometric inductance of the wire. Taking L_K into account will be important when designing our integrated circuits.

2.2 Josephson Effect

The workhorse of the superconducting electronics community is the Josephson junction: two superconductors allowed to interact through a weak link, where the “weak link” can be a thin insulating barrier, a normal metal, or a narrow superconducting constriction—respectively referred to as an S-I-S, S-N-S, or S-C-S junction. In 1962, Brian Josephson predicted that a supercurrent I_S will tunnel through this weak link [57], as described by the “dc Josephson Effect”:

$$I_S = I_0 \sin(\delta). \quad (2.4)$$

Illustrated in Figure 2.1, $\delta = \theta_1 - \theta_2$ is the phase difference of the two wave functions that describe the electrode¹, where I_0 is the maximum supercurrent that the junction can support. I_0 , also referred to as the junction “critical current,” depends on the superconducting gap of the electrodes, the applied magnetic field, and the geometry of the junction.

Additionally, the “ac Josephson Effect” describes a voltage that develops across the junction proportional to phase difference’s rate of change:

$$V_J = \frac{\Phi_0}{2\pi} \frac{d\delta}{dt}, \quad (2.5)$$

where $\Phi_0 = h/2e = 2.0678 \times 10^{-15} \text{ Tm}^2$ is the magnetic flux quantum, h is the Planck constant, and e is the absolute charge of a single electron. If you apply a dc voltage

¹I’ve ignored the effect of the magnetic field seen by the junction. This is an appropriate assumption, given the small footprint of the junctions made in this thesis. For more details, refer to 6.2.3 in [56].

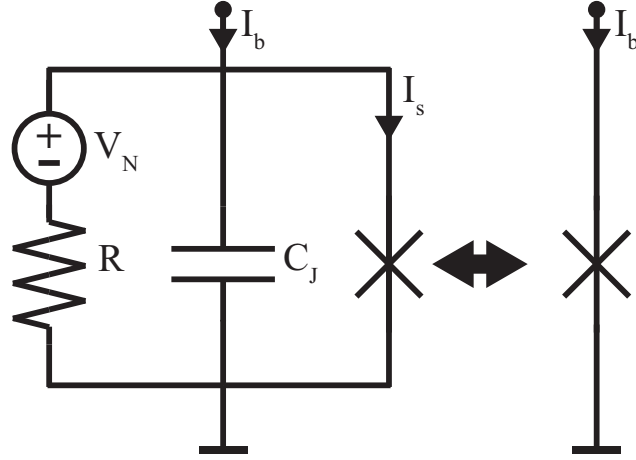


Figure 2.2: Resistively and capacitively shunted junction (RCSJ) model of the Josephson junction. C_J is the self capacitance of the junction, R is the shunt resistance across the junction, and V_N represents the voltage noise generated by the resistor. The cross represents the junction behavior captured by Equation 2.4. The cross will schematically represent the RCJS junction for the remainder of the thesis.

V_0 across the junction, it follows that the junction behaves like an ac current source with frequency $f_J = V_0/\Phi_0$, approximately 484 MHz per μV . Additionally, the junction behaves as a nonlinear inductance, described by:

$$L_J(\delta) = \frac{V_J}{\dot{I}_S} = \frac{\Phi_0/2\pi\dot{\delta}}{I_0\cos(\delta)\dot{\delta}} = \frac{L_J(0)}{\cos(\delta)}, \quad (2.6)$$

where $\dot{x} = dx/dt$, and $L_J(0) = \Phi_0/(2\pi I_0)$.

2.2.1 RCSJ Model

One can intuitively approach the dynamics of the Josephson junction using the Resistively and Capacitively Shunted Junction (RCSJ) model [58, 59, 60, 61], schematically shown in Figure 2.2. The RCJS model captures the behavior of the physical junction in

both the voltage and supercurrent state. C_J is the self capacitance of the junction coming from the overlapping electrodes, $50 \text{ fF}/\mu\text{m}^2$ for our process, R is the resistance shunting the junction, giving quasiparticles a dissipation channel in the junction's voltage state². For voltages greater than $V_g = 2\Delta/e$, where Δ is the superconducting gap, the applied voltage breaks Cooper pairs, giving a tunneling resistance [62]:

$$R_N = \frac{\pi V_g}{4I_0} \tanh(\Delta/2k_b T), \quad (2.7)$$

where k_b is Boltzmann's constant. For most instances in this thesis, a shunt resistor is explicitly formed by a normal metal thin film during device fabrication. Finally, V_N is the voltage noise generated by both quantum and thermal fluctuations present in the shunt resistor.

The current I_b flowing through the RCJS junction is:

$$I_b = I_0 \sin(\delta) + \frac{1}{R} \left(\frac{\Phi_0}{2\pi} \dot{\delta} - V_N \right) + C \frac{\Phi_0}{2\pi} \ddot{\delta}, \quad (2.8)$$

which can be arranged to form the equation of motion for δ :

$$\ddot{\delta} = -\frac{1}{M} \frac{dU(\delta)}{dt} - \delta\eta_0 + \eta_0 \tilde{V}_N, \quad (2.9)$$

where Equation 2.8 recast as a fictitious particle with momentum $p = M\dot{\delta}$ and mass $M = C(\frac{\Phi_0}{2\pi})^2$ moving in potential energy landscape:

²For the purpose of this thesis, we'll assume a linear shunt resistance. In reality, the quasiparticle conductance is strongly voltage-dependent.

$$U(\delta) = -\frac{\Phi_0 I_0}{2\pi} (\cos(\delta) + \frac{I_b}{I_0} \delta), \quad (2.10)$$

with a drag force coefficient $\eta_0 = \frac{1}{RC}$. $\tilde{V}_N = V_N(2\pi/\Phi_0)$ represents the noise due to the normal current flowing through R in the voltage state of the junction.

It is qualitatively helpful to illustrate the junction potential for different current biases, as shown in Figure 2.3. $U(\delta)$ looks like a corrugated wash board, where the tilt of the potential depends linearly on the bias current of the junction $i_b = I_b/I_0$. One can imagine a fictitious phase particle with mass M transversing the potential landscape. At $i_b = 0$, the state of the junction is confined to a local minima of the potential, periodically spaced by 2π . As the applied current approaches I_0 , the barrier confining the fictitious particle becomes shallow until it vanishes at $i_b = 1$. For $i_b > 0$, the phase particle freely rolls down the slope, acquiring a velocity $\dot{\delta}$, which appears as a voltage across the junction, per Equation 2.5.

In the absence of damping η_0 , the kinetic energy of the phase particle will keep the junction in the voltage state until the $i_b = 0$, resulting in hysteretic behavior, as plotted in Figure 2.4(a). Hysteresis can be avoided by introducing damping, which forces the moving phase particle to dissipate its kinetic energy, such that the state retraps for an $i_b > 0$. The overdamped junction will retrap at $i_b = 1$.

2.2.2 Dynamics of the Current Biased Josephson Junction

To further understand the behavior of Josephson junction, it is helpful to numerically examine the dynamics of the overdamped junction. First, we'll use the following definitions to recast the equations of motion into their dimensionless forms:

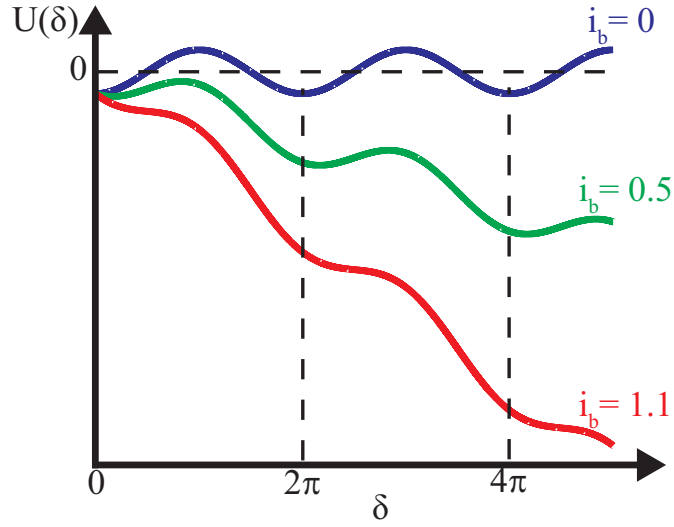


Figure 2.3: RCJS potential energy Equation 2.10 for three different current biases $i_b = I_b/I_0$.

$$\begin{aligned}
 \theta &\equiv (2\pi I_0 R / \Phi_0) t, \\
 \tilde{v} &\equiv \frac{V}{I_0 R}, \\
 i &\equiv I / I_0, \\
 \phi &\equiv \Phi / \Phi_0, \\
 \beta_C &\equiv 2\pi I_0 C R^2 / \Phi_0, \\
 \beta_L &\equiv 2I_0 L / \Phi_0, \\
 \Gamma &\equiv \frac{2\pi k T}{I_0 \Phi_0}, \\
 \frac{dA}{d\theta} &\equiv A',
 \end{aligned} \tag{2.11}$$

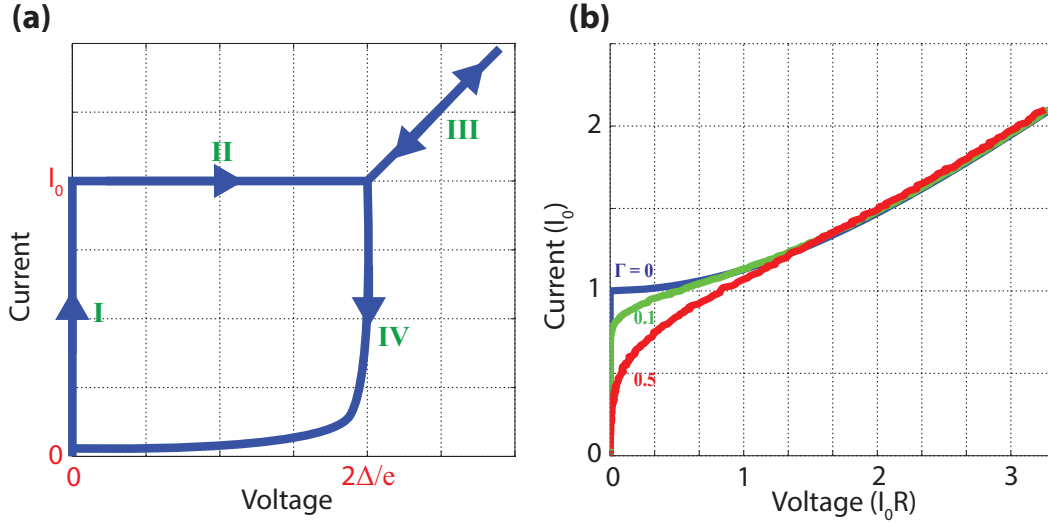


Figure 2.4: **(a)** The hysteretic current-voltage characteristic of an underdamped Josephson junction. On branch **I** the junction is in the superconducting state until the applied current exceeds I_0 , at which a voltage $2\Delta/e$ develops (branch **II**). As the current continues to increase (branch **III**) the excess current flows through the parallel resistor R . As the current is reduced below I_0 (branch **IV**) a voltage remains across the junction. **(b)** Current-voltage characteristic of an overdamped junction for three different normalized temperatures Γ .

where θ , \tilde{v} , i , ϕ , β_C , β_L and Γ are the dimensionless time, voltage, current, flux, capacitance, inductance, temperature, and time derivative respectively. In the dimensionless form, Equation 2.8 becomes:

$$i_b = \sin(\delta) + \delta' - \tilde{v}_N + \beta_C \delta'', \quad (2.12)$$

which is a second order differential equation that can easily be solved using the numerical techniques described in Appendix B.1.

Figure 2.5 shows the time evolution of δ and junction voltage ($\tilde{v} = \delta'$) for two different current biases greater than I_0 . Notice how δ jumps by 2π with a Josephson frequency

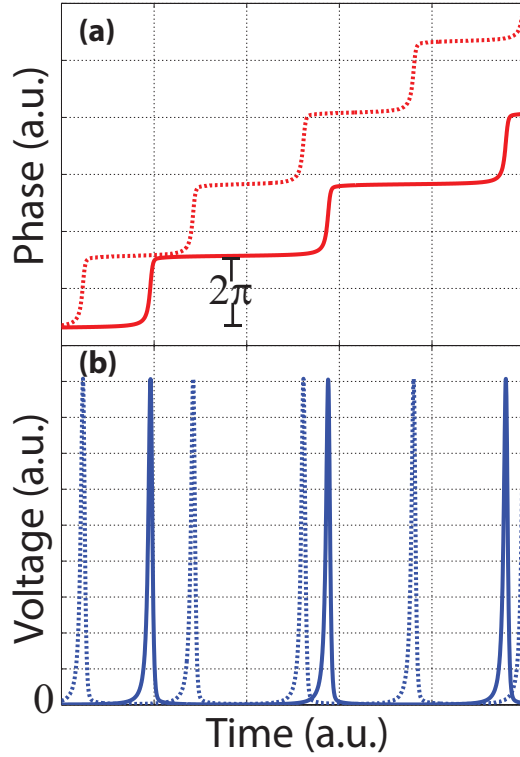


Figure 2.5: Noiseless junction dynamics with $\beta_C = 0.5$. Junction is biased just above I_0 . The solid and dashed lines represent two different bias currents, with the bias current of the dashed line is greater than that of the solid line. The phase difference δ (a) and the voltage across the junction (b) are plotted as a function of time.

f_J that increases with i_b , resulting in voltage spikes that occur as the fictitious phase particle traverses the step regions of $U(\delta)$ pictured in Figure 2.3. As the tilt in $U(\delta)$ becomes steeper, the voltage spikes increase in frequency, resulting in a larger average voltage $\langle \tilde{v} \rangle$:

$$\langle \tilde{v} \rangle = 2\pi \tilde{f}_J, \quad (2.13)$$

where \tilde{f}_J is the dimensionless Josephson frequency. We are interested in the average voltage when calculating the IV characteristics of a device, as the bandwidth of our

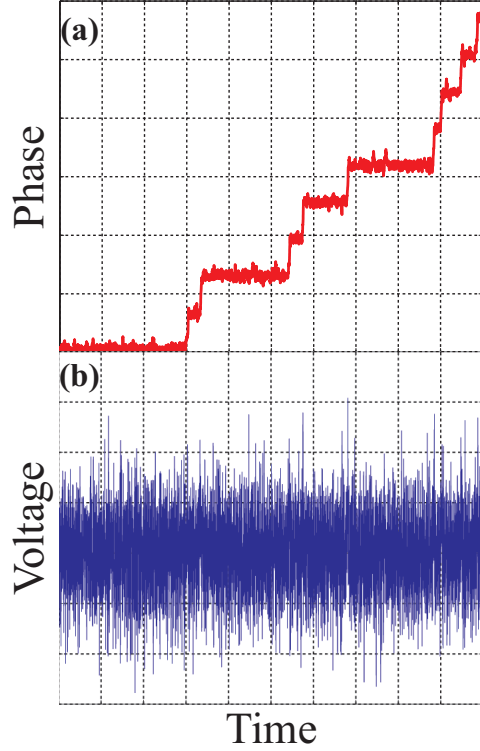


Figure 2.6: Junction dynamics with $\beta_C = 0.5$, $\Gamma = 0.1$, and I_b slightly below I_0 . The phase difference δ (a) and the voltage across the junction (b) are plotted as a function of time.

experimental setup is much lower than the typical f_J , which is on the order of tens of GHz.

In the presence of classical thermal noise, defined by the dimensionless voltage spectral density \tilde{S}_V^N :

$$\tilde{S}_V^N = 4\Gamma, \quad (2.14)$$

a voltage can develop across the junction for $I_b < I_0$. In the context of the washboard potential, the fictitious phase particle is thermally activated over the potential barrier

into the adjacent minima. Classical noise is included in junction numerics according to Appendix B.2. The dynamics of a junction in the presence of noise is plotted in Figure 2.6, where I_b is slightly less than I_0 , allowing the thermal noise to randomly advance δ by 2π . This random walk down the tilted washboard potential averages out to a nonzero voltage across the junction, as shown by the IV curves of Figure 2.4(b).

2.3 Flux Quantization

Flux quantization in a superconducting loop is a direct consequence of the single valued nature of the phase of the condensate $\theta(\vec{r})$ [56], resulting in:

$$\oint \nabla\theta(\vec{r}) \cdot d\vec{l} = 2\pi s \text{ for } s \in \mathbb{N}. \quad (2.15)$$

The current density \vec{j} in a superconductor is:

$$\vec{j} = q\Psi^*(\vec{r}, t)\vec{v}\Psi(\vec{r}, t) = nq \left(\hbar\nabla\theta(\vec{r}) - q\vec{A} \right) / m, \quad (2.16)$$

where $\vec{v} = \left(-i\hbar\nabla - q\vec{A} \right) / m$ is the velocity of a particle with charge q in the magnetic vector potential \vec{A} , and $\Psi(\vec{r}) = \sqrt{n} \exp(i\theta(\vec{r}))$. From the Meissner effect, there exists a contour within the superconductor [Figure 2.7(a)], such that $\vec{j} = 0$. Taken with Equation 2.15 and Stoke's theorem, a path integral of Equation 2.16 gives:

$$\oint \vec{j} \cdot d\vec{l} = \frac{nq}{m} (\hbar 2\pi s - q\Phi_T) = 0, \quad (2.17)$$

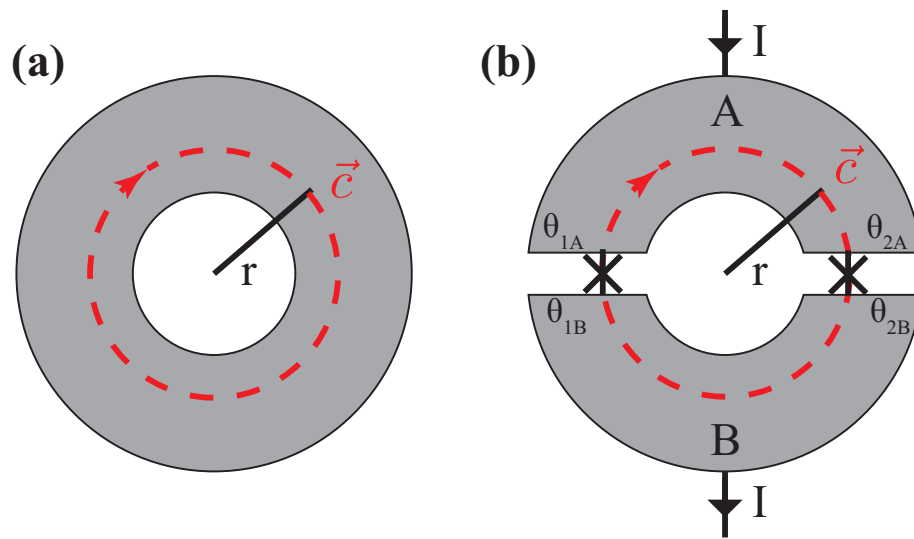


Figure 2.7: (a) Superconducting loop with the path of integration \vec{c} . (b) Superconducting loop interrupted by two Josephson junctions.

resulting in the flux quantization condition, with Φ_T being the total magnetic flux penetrating the loop:

$$\Phi_T = s\Phi_0, s \in \mathbb{N}. \quad (2.18)$$

An externally applied flux Φ_x will induce a current in the loop to create an equal and opposite flux, maintaining flux quantization. Once $\Phi_x > \Phi_0/2$, it becomes energetically favorable for one Φ_0 to slip into the loop, reversing the direction of the induced current.

2.4 dc SQUID

2.4.1 Fluxoid Quantization

The dc SQUID [Figure 2.7(b)] is a superconducting loop interrupted by two Josephson junctions. The presence of the junctions modifies Equation 2.15:

$$\oint \nabla\theta(\vec{r}) \cdot d\vec{l} = (\theta_{2A} - \theta_{1A}) + (\theta_{1B} - \theta_{2B}) = \delta_1 - \delta_2, \quad (2.19)$$

where $\delta_i = \theta_{iB} - \theta_{iA}$. It follows that the total magnetic flux through a dc SQUID is:

$$\Phi_T = \frac{\Phi_0}{2\pi}(\delta_1 - \delta_2). \quad (2.20)$$

Assuming that both junctions have a critical current I_0 , we can write the total current I flowing through the SQUID as:

$$\begin{aligned} I &= I_0 [\sin(\delta_1) + \sin(\delta_2)] \\ &= I_0 \left[\sin \left(\delta_2 + \frac{2\pi\Phi_T}{\Phi_0} \right) + \sin(\delta_2) \right] \\ &= 2I_0 \cos \left(\frac{\pi\Phi_T}{\Phi_0} \right) \sin \left(\delta_2 + \frac{\pi\Phi_T}{\Phi_0} \right), \end{aligned} \quad (2.21)$$

where we've used Equations 2.4 and 2.20. It follows that the dc SQUID behaves like a single junction with a flux modulated critical current I_M :

$$I_M(\Phi_T) = \left| 2I_0 \cos\left(\frac{\pi\Phi_T}{\Phi_0}\right) \right|. \quad (2.22)$$

In general, the total magnetic flux in the SQUID loop has contributions from an externally applied flux Φ_x and the circulating current J coupled through the self-inductance of the SQUID loop L :

$$\Phi_T = \Phi_x + JL = \frac{\Phi_0}{2\pi}(\delta_1 - \delta_2). \quad (2.23)$$

2.4.2 Transfer Function

If we ignore the self inductance³, the dynamics of a dc SQUID behave like a single Josephson junction with a critical current given by 2.22, where $\Phi_T = \Phi_x$. In the overdamped case, where $\beta_C \rightarrow 0$, the equation of motion of the SQUID (described by 2.12) becomes:

$$2\delta' = i_b - i_M(\phi_x) \sin(\delta). \quad (2.24)$$

δ' is rescaled by two since the total shunt resistance is now $R/2$ due to the parallel junctions. We integrate δ from 0 to 2π to find the period $T = 1/\tilde{f}_J$ which gives us the average voltage across the junction according to Equation 2.13.

³We ignore L for an exact solution of the phase dynamics. The SQUID self inductance modifies Φ_T according to 2.23, preventing I_M from modulating to 0. We fully account for L in the next chapter.

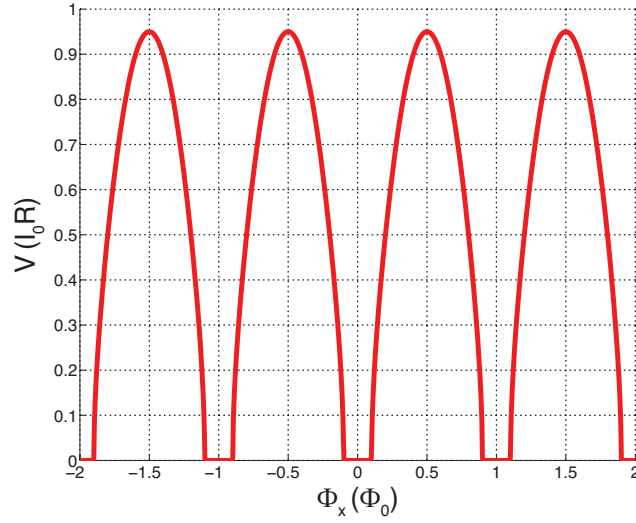


Figure 2.8: Voltage across the dc SQUID as a function of flux, for $I_b = 1.9 I_0$.

$$\int_0^{2\pi} 2d\delta(i_b - i_M(\phi_x)\sin(\delta))^{-1} = 4\pi/\sqrt{i_b^2 - i_M(\phi_x)^2} = T = 1/\tilde{f}_J = 2\pi/\langle\tilde{v}\rangle. \quad (2.25)$$

It finally follows that the average voltage across the SQUID is:

$$\begin{aligned} \langle\tilde{v}\rangle &= \frac{1}{2}\sqrt{i_b^2 - i_M(\phi_x)^2} \\ &= \frac{1}{2}\sqrt{i_b^2 - |2\cos(\pi\phi_x)|^2}. \end{aligned} \quad (2.26)$$

The voltage across the dc SQUID is plotted as a function of quasistatic flux for $I_b = 1.9 I_0$ in Figure 2.8.

All amplifiers have a transfer function that map the input signal to its output. For a transistor-based amplifier, a small change in the voltage across the gate maps to a large change in the source-drain current. In the case of a dc SQUID, an externally applied

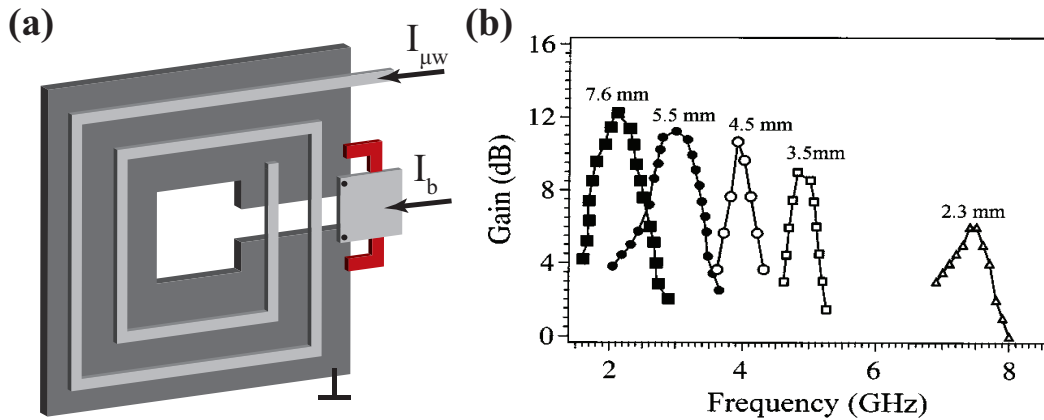


Figure 2.9: (a) Ketchen-Jaycox SQUID washer coupled to a planar multi-turn spiral inductor. In the microstrip configuration, one side of the input coil is left open. (b) The plot taken from [63] shows that as the operating frequency of a microstrip amplifier increases the gain decreases.

magnetic flux maps to a voltage across the SQUID. By statically biasing the SQUID at a steep point in the transfer function ($\Phi_x = 0.25\Phi_0$ for 2.8), a small change in Φ_x results in a large change in output voltage. For small signals, the slope of the transfer function appears linear.

2.5 SQUID Amplifiers

An amplifier based on the dc SQUID⁴ must transform the signal to be amplified into a magnetic flux that threads the superconducting loop. The Ketchen-Jaycox [65] geometry, illustrated in Figure 2.9(a), uses a superconducting square washer with a slit as the inductive loop, where two resistively shunted via style Josephson junctions sit at the mouth of the slit. The input coil is a planar multi-turn spiral inductor separated from the SQUID washer by a thin dielectric layer. The input voltage signal is transformed into

⁴See John Clarke's review article [64].

a current by the impedance of the input coil, and then into a flux through the washer from the inductive coupling. Conventionally, one side of the input coil is grounded.

For low-frequency operation (less than 1 MHz), the amplifier is operated in a flux locked loop, where the feedback flux pins the bias point of the SQUID to the maximum of the $V\Phi$ curve. The feedback flux counters the flux generated by the signal, maintaining the total flux threading the SQUID loop. The feedback flux is then converted to a voltage, which is the recorded output signal. Ignoring low-frequency $1/f$ noise, amplifiers operated in this manner typically have noise on the order of $1 \mu\Phi_0/\sqrt{\text{Hz}}$. For intermediate frequencies (up to 200 MHz), the SQUID is operated open-loop with a tuned input-circuit to minimize the noise-temperature of the device [66].

At higher operating frequencies, the parasitic capacitance between the input coil and the SQUID washer cause a roll-off in gain. Mück *et al.* [67] avoided this rolloff by keeping one side of the input coil open, thus operating the input as a $\lambda/2$ microstrip resonator, where the SQUID washer acts as the groundplane for the coil. The noise temperature of a microstrip SQUID amplifier has been measured to be 47 ± 10 mK and 48 ± 5 mK at frequencies of 519 MHz and 612 MHz, respectively, more than an order of magnitude lower than the best semiconductor amplifiers available and within a factor of 2 of the quantum limit [68, 69]. However, efforts to extend the operating frequencies of these amplifiers into the gigahertz range are hampered by the fact that a reduction of the length of the input resonator results in a reduced mutual inductance between the input coil and the SQUID [63], as shown in Figure 2.9(b). It is possible to compensate for the reduced coupling by increasing the slope of the transfer function, but this strategy has diminishing returns [70, 71]. Alternative approaches have included the integration of a high-gain SQUID gradiometer into a coplanar waveguide resonator at a current antinode [72, 73, 74].

Chapter 3

SLUG Amplifier Theory

The numerical study in this chapter was motivated by the development of a new device configuration that enables the efficient coupling of a GHz-frequency signal to a low-inductance, high gain SQUID that should achieve noise performance approaching the standard quantum limit. The gain element is more properly termed a superconducting low-inductance undulatory galvanometer (SLUG), as the signal is not coupled to the device inductively, but rather injected directly into the device loop as a current [75]. The low-inductance design is straightforward to model at microwave frequencies, and the SLUG is readily integrated with an on chip matching network in such a way that the modes of the SLUG element and the matching network remain clearly resolved, greatly simplifying analysis of the circuit. In this chapter we present a comprehensive theoretical study of the gain and noise performance of the SLUG microwave amplifier. Our goals are to clearly spell out the design tradeoffs, to outline a clear path to device optimization, and to identify the fundamental limits to performance.

As we shall see, the scattering parameters of the SLUG are very similar to those of the more familiar dc SQUID, apart from a trivial shift in flux bias that arises from the

asymmetric division of bias current between the two arms of the SLUG. However, while it is straightforward to fabricate a low-inductance (~ 10 pH) SLUG and to embed the device in a 50Ω environment, it is challenging to engineer a clean, purely inductive coupling to a conventional dc SQUID at microwave frequencies [see discussion in Section 2.5]. It is for this reason we focus our discussion of microwave amplifiers on the SLUG geometry.

This chapter is organized as follows. In Sections 3.1 and 3.2, we introduce the circuit models of the symmetrically coupled dc SQUID and the symmetric SLUG, respectively. In Section 3.3, we calculate the dc characteristics of the devices. In Section 3.4, we evaluate the SLUG scattering parameters and examine the maximum achievable gain over the range of device parameters. Sections 3.5 and 3.6 present an analysis of the noise properties in the thermal and quantum regimes, respectively. In Section 3.7, we describe the design and performance of practical SLUG amplifiers for GHz frequency operation, and in Section 3.8 we discuss amplifier dynamic range. In Section 3.9, we describe the effect of the finite admittance of the input circuit on device characteristics, gain, and noise. In Section 3.10, we briefly examine the reverse transfer function of the bare SLUG amplifier, and in Section 3.11 we consider the performance of the SLUG with a lumped element LC input matching network. Finally, in Section 3.12 we discuss hot-electron effects. Most of the work in this chapter was described by *G. Ribeill et al.* [76].

3.1 dc SQUID Equations of Motion

To draw parallels with earlier numerical studies [77, 78, 79, 80, 81, 82], we consider the familiar symmetrically coupled dc SQUID, schematically shown in Figure 3.1. The dc SQUID consists of two overdamped Josephson junctions embedded in a superconducting loop with inductance L . The junctions (with phase differences $\delta_{1,2}$) have identical critical

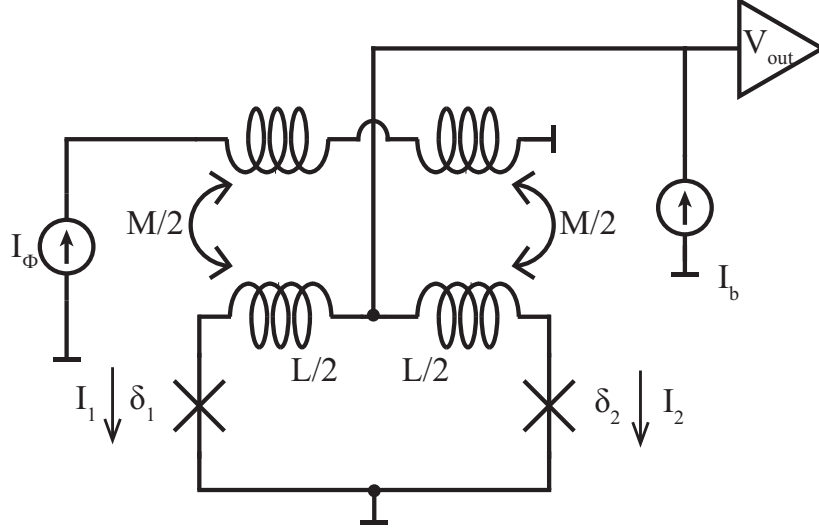


Figure 3.1: Symmetrically coupled dc SQUID with total loop inductance L and two identical resistively and capacitively shunted junctions, biased by I_b . The input signal I_Φ is symmetrically coupled to the SQUID loop with mutual inductance M .

currents I_0 , shunt resistances R and self-capacitances C . The superconducting loop is formed from two equal branches, each with inductance $L/2$; for the conventional loop geometry we can neglect the mutual inductance between the branches. A dc current bias I_b and bias flux Φ_b establish a quasistatic operating point. The input signal $I_\Phi = I_{\Phi,dc} + I_{\Phi,rf}$ is symmetrically coupled to the SQUID loop with total mutual inductance M , where $\Phi_b = MI_{\Phi,dc}$ and $I_{\Phi,rf}$ is the rf-signal to be amplified. Using Equation 2.8, the currents through the junctions are given by:

$$\begin{aligned} I_1 &= I_0 \sin(\delta_1) + \frac{1}{R} \left(\frac{\Phi_0}{2\pi} \dot{\delta}_1 - V_{N,1} \right) + C \frac{\Phi_0}{2\pi} \ddot{\delta}_1, \\ I_2 &= I_0 \sin(\delta_2) + \frac{1}{R} \left(\frac{\Phi_0}{2\pi} \dot{\delta}_2 - V_{N,2} \right) + C \frac{\Phi_0}{2\pi} \ddot{\delta}_2. \end{aligned} \quad (3.1)$$

The output voltage V_{out} is given by:

$$\begin{aligned}
V_{out} &= \frac{\Phi_0}{2\pi} \dot{\delta}_1 + \frac{L}{2} \dot{I}_1 \\
&= \frac{\Phi_0}{2\pi} \dot{\delta}_2 + \frac{L}{2} \dot{I}_2.
\end{aligned} \tag{3.2}$$

Employing Equation 2.20, the total flux through the SQUID loop Φ_T is given by:

$$\begin{aligned}
\Phi_T &= I_1 \frac{L}{2} + I_\Phi M - I_2 \frac{L}{2} \\
&= LJ + I_\Phi M = \frac{\Phi_0}{2\pi} (\delta_2 - \delta_1),
\end{aligned} \tag{3.3}$$

where the J is the circulating current in the SQUID loop¹:

$$J = \frac{I_1 - I_2}{2}. \tag{3.4}$$

Using the dimensionless variables introduced by Equations 2.11 and the node relationship $I_b = I_1 + I_2$, the equations of motion become:

$$\begin{aligned}
\beta_C \delta_1'' &= \frac{i_b}{2} - i_{\phi,\text{rf}} + \frac{\delta_2 - \delta_1 - 2\pi\phi_b}{\pi\beta_L} - \sin(\delta_1) - \delta_1' + \tilde{v}_{N,1}, \\
\beta_C \delta_2'' &= \frac{i_b}{2} + i_{\phi,\text{rf}} - \frac{\delta_2 - \delta_1 - 2\pi\phi_b}{\pi\beta_L} - \sin(\delta_2) - \delta_2' + \tilde{v}_{N,2}.
\end{aligned} \tag{3.5}$$

The quasistatic output voltage and the circulating current are given by:

¹We define $J > 0$ in the counterclockwise direction, hence the sign difference compared with Equation 2.20.

$$\tilde{v}_{out} = \frac{1}{2} (\delta'_2 + \delta'_1), \quad (3.6)$$

$$j = \frac{1}{\pi\beta_L} (\delta_2 - \delta_1 - 2\pi\phi_b). \quad (3.7)$$

3.2 SLUG Equations of Motion

In the SLUG geometry of Figure 3.2, the device loop is formed from two superconducting traces separated by a thin dielectric layer, and the input signal is injected directly into one of the traces. In the case where the SLUG is integrated into a microstrip transmission line, the device is realized in three metallization steps (corresponding to the circuit groundplane and the two inductive arms of the SLUG), with two dielectric thin films of thickness t separating the metal layers. The SLUG loop inductance L is determined from the self and mutual inductances of the base electrode (BE) and top electrode (TE) traces: $L \approx L_{TE} + L_{BE} - 2L_M$, where L_{TE} (L_{BE}) is the inductance of the trace formed in the TE (BE) layer and L_M is the mutual inductance between the two traces. For a SLUG element of length ℓ , trace width w , and with the BE (TE) trace separated from the groundplane by distance t ($2t$), we find the geometric inductance $L_{BE} \approx \mu_0 t \ell / w$, with $L_{TE} \approx 2L_{BE}$ and $L_M \approx L_{BE}$. Therefore, we have $L \approx L_{BE}$, and the mutual coupling M of the signal current I_Φ to the device loop is also L . I_b biases the device in the finite-voltage state and $I_{\Phi,dc}$ establishes a quasistatic flux bias $\Phi_b = LI_{\Phi,dc}$. We refer to this configuration as the symmetric SLUG, where similar device geometries were studied in [75, 83].

The total flux through the SLUG loop is:

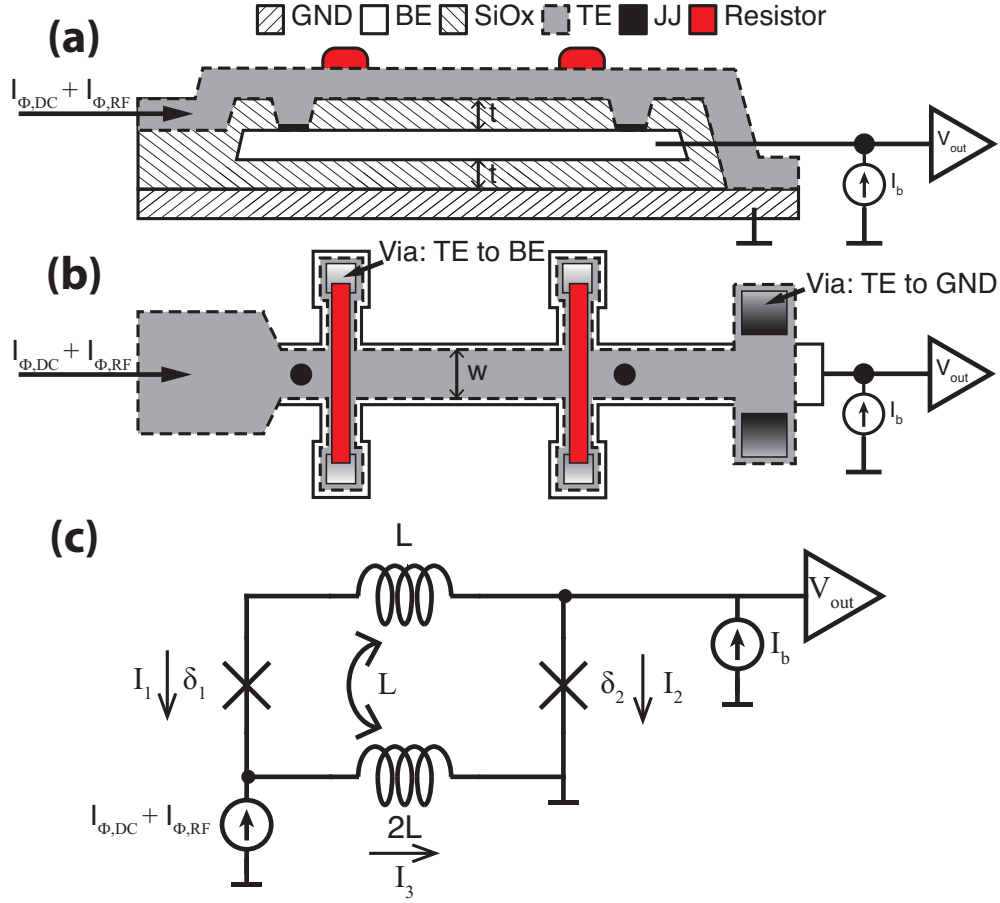


Figure 3.2: Symmetric dc SLUG with total loop inductance L and two identical resistively and capacitively shunted junctions, biased by I_b and $I_{\phi,dc}$. The input signal I_{Φ} is coupled to the SLUG loop with mutual inductance M . (a) SLUG layer stackup. GND is the groundplane, BE is the bottom electrode, TE is the top electrode, and JJ are the Josephson junctions. (b) Layout of the SLUG element as seen from above (not to scale). (c) Circuit schematic of the SLUG.

$$\begin{aligned}
 \Phi_T &= (I_1 L - I_3 L) + (I_3 2L - I_1 L) \\
 &= (I_1 + I_{\Phi}) L = \frac{\Phi_0}{2\pi} (\delta_2 - \delta_1),
 \end{aligned} \tag{3.8}$$

where $I_3 = I_1 + I_{\Phi}$. The dimensionless equations of motion for the junction phases are:

$$\begin{aligned}
\beta_C \delta_1'' &= \frac{\delta_2 - \delta_1 - 2\pi\phi_b}{\pi\beta_L} - i_{\phi,\text{rf}} - \sin(\delta_1) - \delta_1' + \tilde{v}_{N,1}, \\
\beta_C \delta_2'' &= -\frac{\delta_2 - \delta_1 - 2\pi\phi_b}{\pi\beta_L} + i_b + i_{\phi,\text{rf}} - \sin(\delta_2) - \delta_2' + \tilde{v}_{N,2}.
\end{aligned} \tag{3.9}$$

The output voltage and circulating current are given by:

$$\tilde{v}_{out} = \delta_2', \tag{3.10}$$

$$j = \frac{\delta_2 - \delta_1 - 2\pi\phi_b}{\pi\beta_L} - \frac{i_{\phi,\text{rf}}}{2}. \tag{3.11}$$

To operate the SQUID or the SLUG as an amplifier, one chooses I_b and Φ_b to establish a quasistatic operating point where the transfer function $V_\Phi \equiv \partial V / \partial \Phi$ is large. In both cases, the device acts as a transimpedance element: the input signal is coupled to the device as a current and the output signal is coupled from the device as a voltage.

3.3 DC Characteristics

Equations 3.5 and 3.9 were numerically integrated according to Appendix B.1, where noise terms are ignored for now. In Figures 3.3(a) and 3.3(b), we show the current-voltage (I-V) characteristics of the symmetrically coupled dc SQUID and the symmetric SLUG with $\beta_L = 1$ and $\beta_C = 0.8$; Figures 3.4(a) and 3.4(b) show the voltage-flux (V- Φ) characteristics of the same devices.

We observe that the dc characteristics of the symmetric SLUG closely match those of the symmetrically coupled SQUID, apart from a shift in flux bias point that arises

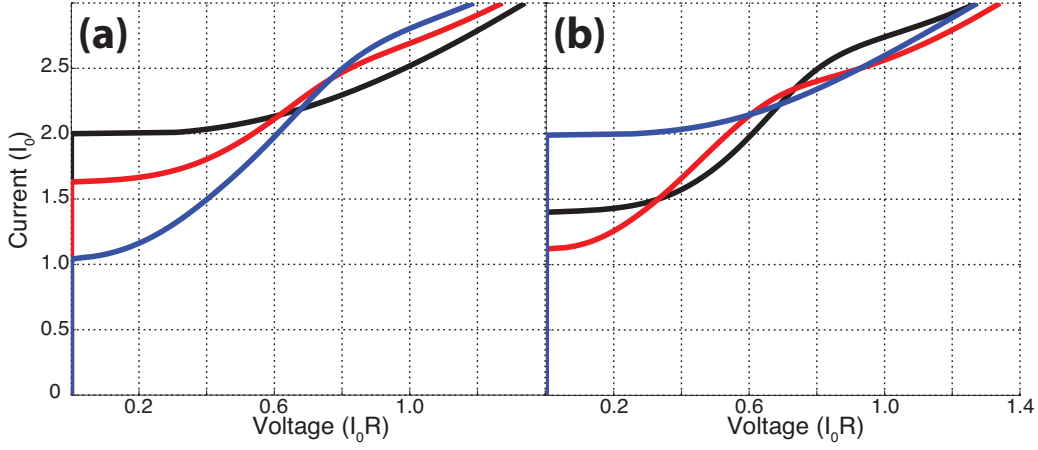


Figure 3.3: I-V characteristics of the (a) symmetrically coupled dc SQUID and (b) symmetric SLUG for different flux biases: $\Phi_b = 0.0$ (black), 0.25 (red), 0.5 (blue).

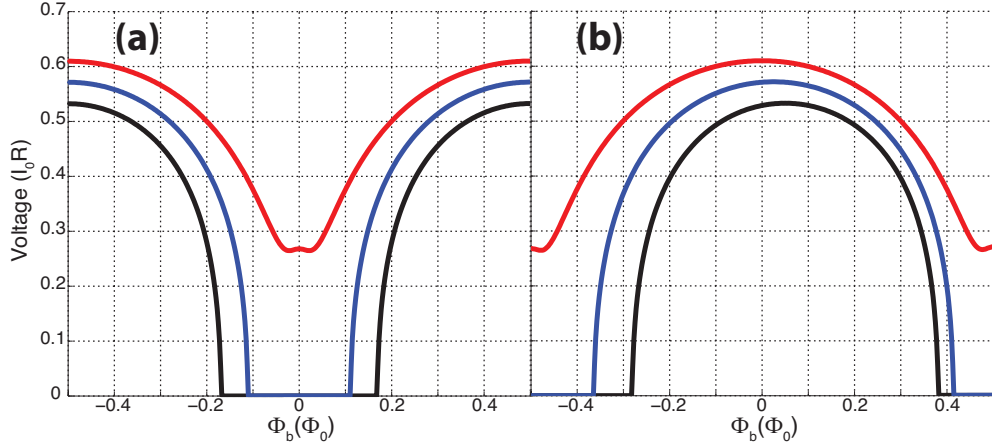


Figure 3.4: $V-\Phi$ characteristics of the (a) symmetrically coupled dc SQUID and (b) symmetric SLUG for different current biases: $1.8 I_0$ (black), $1.9 I_0$ (blue), $2.0 I_0$ (red).

from the asymmetric division of the SLUG bias current. Similarly, we have found that most scattering parameters and noise properties of the SLUG and the SQUID are closely matched, with the exceptions noted in the applicable sections below.

For the sake of simplicity, we focus on the following set of SLUG parameters for the remainder of this chapter: $\beta_L = 1$, $\beta_C = 1$, $L = 10$ pH, and junction self capacitance $C = 50$ fF, corresponding to a $1 \mu\text{m}^2$ junction with $I_0 = 100 \mu\text{A}$, and a shunt resistance

of $R = 7.26 \Omega$. These parameters were used for the dc characteristics already plotted. Several considerations lead us to this choice. First, inductances of order 10 pH are realized in a reliable, controlled way in the SLUG geometry, and the compact nature of the resulting device should be immune to parasitic reactances and is straightforward to model at microwave frequencies. This requires a critical current density of $J_0 = 10 \text{ kA/cm}^2$, within the reach of standard Nb-AlO_x-Nb technology [84, 85]. For $\beta_L = 1$, the transfer function is proportional to the product of the shunt resistance and junction critical current [81]. For a fixed β_C , the transfer function goes as:

$$V_\Phi \propto RI_0 = \sqrt{\frac{\Phi_0 \beta_C I_0}{2\pi C}} = \sqrt{\frac{\Phi_0 \beta_C J_0}{2\pi \tilde{C}}}, \quad (3.12)$$

where $\tilde{C} = 50 \text{ fF}/\mu\text{m}^2$ is the junction capacitance per unit area. The amplifier gain increases with V_Φ , so it follows that to maximize gain one must maximize J_0 .

A $\beta_L = 1$ was chosen based on the numerical studies in [81], which found the optimal noise performance² of a dc SQUID to occur at $\beta_L = 1$.

3.4 Scattering Parameters

In order to optimize the SLUG amplifier design, it is necessary to understand the forward transfer function and the complex input and output impedances of the gain element. With the help of the scattering parameters, we can design a matching network to optimize the amplifier's gain and noise performance. To extract these from our model, we apply an oscillating current at either the input ($I_{\phi,\text{rf}}$) or the output ($I_{b,\text{rf}}$), and measure the voltage response across both the input and the output. We make sure that the amplitude

²Tesche *et al.* [81] minimized the energy resolution of a dc SQUID for a fixed temperature.

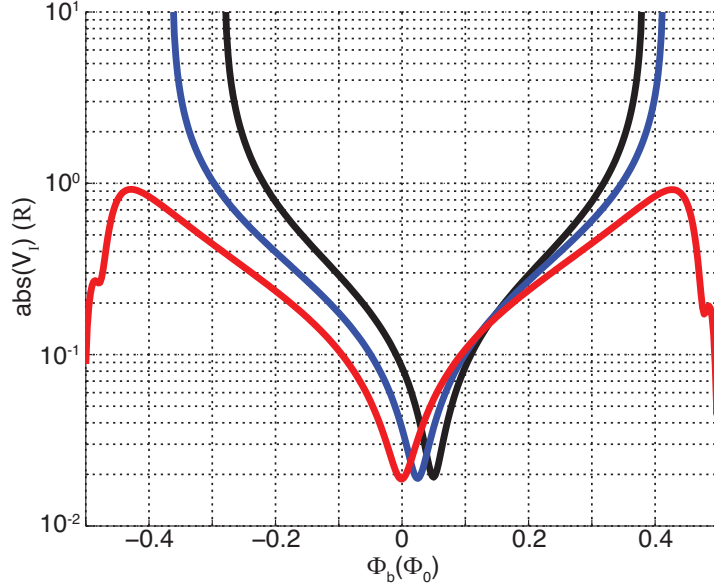


Figure 3.5: Forward transimpedance V_I for the SLUG at different current biases: $1.8 I_0$ (black), $1.9 I_0$ (blue), $2.0 I_0$ (red).

of the excitation is small enough to not affect the measured scattering parameter. The probe frequency f_p for the figures in this section is 6 GHz, and we consider bias points where the Josephson frequency $f_J \gg f_p$. The dimensionless form of the input voltage is as follows:

$$\tilde{v}_{in} = \pi\beta_L i'_{\phi,rf} + (\delta'_2 - \delta'_1). \quad (3.13)$$

We first consider the forward transimpedance ($V_I \equiv \partial V_{out} / \partial I_{\phi,rf}$), plotted versus flux in Figure 3.5. Once again, we consider a SLUG with $\beta_L = 1$, $\beta_C = 1$, $L = 10$ pH, and junction self capacitance $C = 50$ fF, corresponding to a $1 \mu\text{m}^2$ junction with $I_0 = 100 \mu\text{A}$, and a shunt resistance of $R = 7.26 \Omega$. As expected, flux biases near the supercurrent branch see a larger transimpedance.

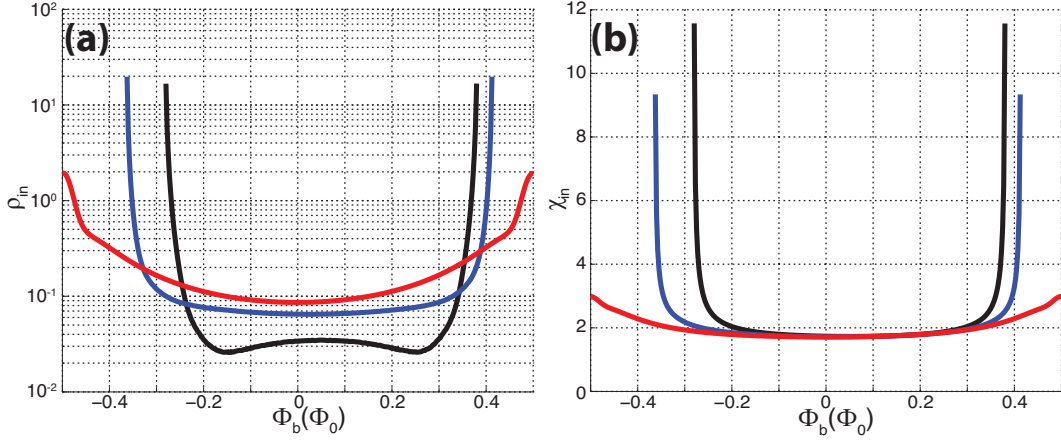


Figure 3.6: Dimensionless Z_{in} , where (a) is the dimensionless real component ρ_{in} and (b) is the dimensionless imaginary part χ_{in} for the SLUG at different current biases: 1.8 I_0 (black), 1.9 I_0 (blue), 2.0 I_0 (red).

Next, we consider the input return loss. The SLUG input is an inductive short to ground at low frequencies, and the complex input impedance $Z_{in} \equiv \partial V_{in}/\partial I_{\phi,rf}$ is frequency dependent, taking on the following form:

$$\begin{aligned} Z_{in} &= R_{in} + iX_{in} \\ &= \rho_{in} \frac{(\omega L)^2}{R} + i\chi_{in}\omega L, \end{aligned} \quad (3.14)$$

where ρ_{in} and χ_{in} are frequency independent and plotted versus flux in Figures 3.6(a) and (b), respectively.

Note that both ρ_{in} and χ_{in} get larger as the SLUG is biased closer to the supercurrent branch. Figures 3.7(a) and (b) plot the components of the SLUG's real ρ_{out} and imaginary χ_{out} output impedance, where

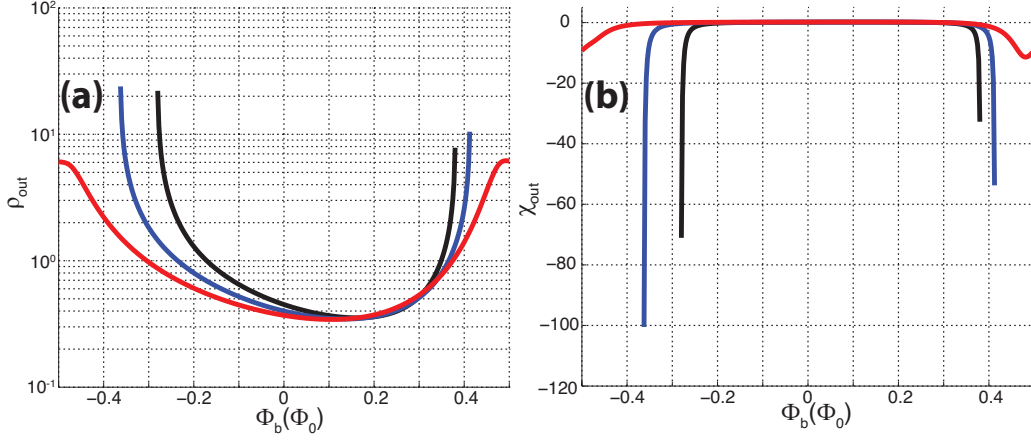


Figure 3.7: Dimensionless Z_{out} , where (a) is the dimensionless real component ρ_{out} and (b) is the dimensionless imaginary part χ_{out} for the SLUG at different current biases: $1.8 I_0$ (black), $1.9 I_0$ (blue), $2.0 I_0$ (red).

$$\begin{aligned}
 Z_{out} &= R_{out} + iX_{out} \\
 &= \rho_{out}R + i\chi_{out}\omega L.
 \end{aligned} \tag{3.15}$$

Note that ρ_{out} and χ_{out} are asymmetric, arising from the asymmetric division of the SLUG bias current. This asymmetry is not present in the SQUID.

As we will see in later sections, amplifier gain, bandwidth, operating frequency and noise performance depend sensitively on Z_{in} , V_I and Z_{out} . The numerically determined scattering parameters allow one to extract the gain of the SLUG element embedded in an arbitrary two port network [86], shown found in Figure 3.8, where for the time being we ignore the embedded noise sources. The maximum available power gain G_m occurs for a conjugately matched input impedance $Z_s = Z_{in}^*$ and $Z_o = Z_{out}^*$. Gain is defined as the ratio of power dissipated in Z_o with and without the SLUG in the circuit:

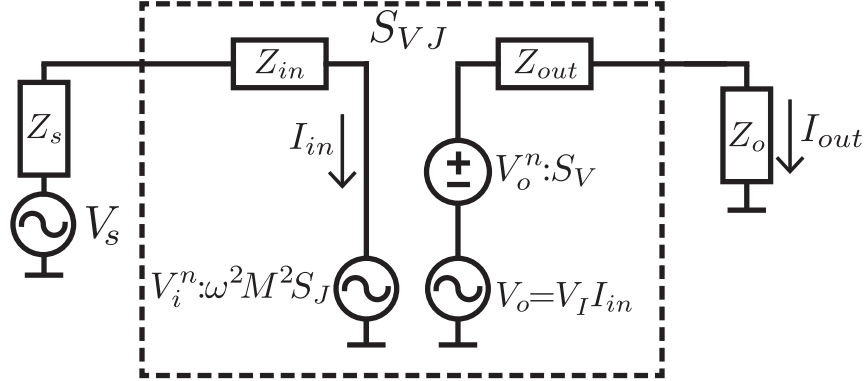


Figure 3.8: The dashed box contains the numerically determined complex input Z_{in} and output Z_{out} impedances, while Z_s and Z_o are external source and output impedances, and V_s is the input voltage source. I_{in} and I_{out} are the input and output currents, respectively. V_o is a voltage source that depends on the I_{in} and the forward transimpedance V_I . V_i^n and V_o^n are noise sources.

$$P_{SLUG} = \frac{V_s^2 |V_I|^2 \rho_{out} R}{(4\rho_{in}\rho_{out}\omega^2 L^2)^2}, \quad (3.16)$$

$$P_{ref} = \frac{V_s^2 R}{4\rho_{in}\omega^2 L^2}, \quad (3.17)$$

giving G_m the form:

$$G_m = \frac{P_{SLUG}}{P_{ref}} = \frac{|V_I|^2}{4\rho_{in}\rho_{out}\omega^2 L^2}. \quad (3.18)$$

In Figure 3.9(a), we plot G_m versus Φ_b for different current biases, evaluated at 6 GHz. Over a broad range of bias parameters, gain in excess of 20 dB is readily achievable. While G_m does degrade when the SLUG is operated at higher frequencies, as Figure 3.9(b) illustrates, the gain element is still useful even at 10 GHz. It is important to note, however, that a conjugate match to a 50 Ω source does not yield best amplifier noise

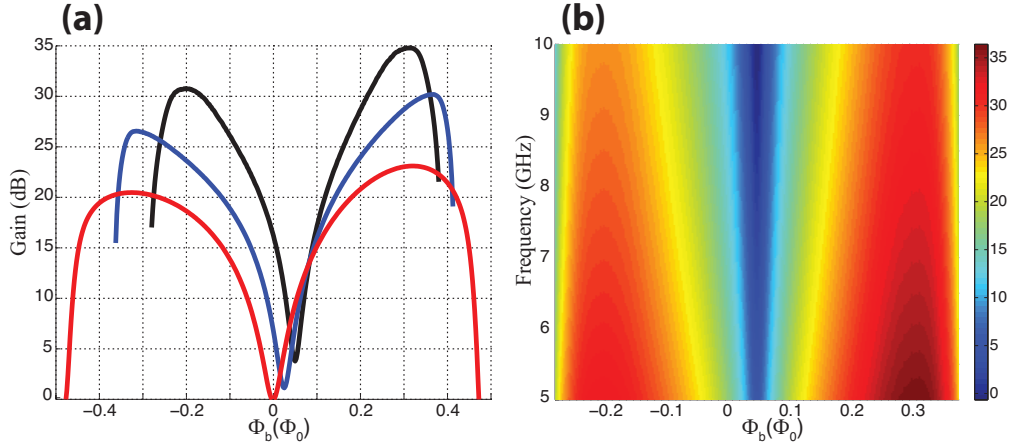


Figure 3.9: Maximum gain evaluated (a) at 6 GHz for different current biases: $1.8 I_0$ (black), $1.9 I_0$ (blue), $2.0 I_0$ (red), and (b) for $I_b = 1.8 I_0$ as a function of frequency and Φ_b , where the false color is gain in dB.

performance, due to the mismatch between the real part of the SLUG input impedance R_{in} and the optimal noise-matched source impedance, which can be significantly larger than R_{in} . Amplifier optimization, therefore, involves a tradeoff between gain and noise performance, as discussed in detail below.

The bandwidth of the SLUG amplifier will be determined by the coupling to the low-impedance input port, as the device output port is reasonably well-matched to typical transmission line impedances. To get a rough idea of amplifier bandwidth, we consider a 50Ω source impedance and assume that conjugate matching at the device input is accomplished via a simple quarter-wave transmission line section with characteristic impedance $Z_0 = \sqrt{50 \Omega \times R_{in}}$; for simplicity, we neglect the imaginary part of the SLUG input impedance. Assuming reflected power goes to zero, we get the following approximation for the quality factor Q of the matching network [87]:

$$\begin{aligned}
Q &\approx \frac{\pi}{8} \sqrt{\frac{50 \Omega}{R_{in}}} \\
&= \frac{\pi}{8\omega L} \sqrt{\frac{50 \Omega \times R}{\rho_{in}}}.
\end{aligned} \tag{3.19}$$

The bandwidth of an amplifier designed at an operating frequency $\omega/2\pi$ is then $\omega/2\pi Q$. For an operating frequency of 6 GHz, we find that R_{in} is of the order 0.1 Ω . Therefore we expect Q of the order 10, meaning amplifier bandwidths on the order of hundreds of MHz. For a current bias $I_b < 2 I_0$ and for a narrow range of fluxes corresponding to bias points near the supercurrent branch, we find that it is possible to achieve extremely high power gain [Figure 3.9]. However, the high gains achieved at these bias points are due largely to vanishing R_{in} ; an amplifier designed to operate in this regime would have a rather small bandwidth. It is important to note that Equation 3.19 presents only a rough guideline for the bandwidth rather than a fundamental limit. In particular, it is possible to obtain a larger bandwidth with no degradation in gain by employing either a tapered transmission line matching section or a multi-section input transformer with stepped transmission line impedances [87].

3.5 Noise Properties in the Thermal Regime

In the previous section we ignored the Johnson noise of the shunt resistors, which gives rise to a voltage noise at the device output and to a circulating current noise in the device loop; moreover, these noises are partially correlated, since the circulating current noise couples a flux noise to the loop, which in turn yields a voltage noise across the device. The above calculated scattering parameters are unaffected by the noise magnitudes relevant to

this thesis, especially when limiting our analysis to biases where the Josephson frequency $f_J > 5$ GHz. The noise is numerically introduced according to the method described in Section B.2, while the noise spectra were calculated according to Section B.4. Following Tesche and Clarke [79] and Hilbert and Clarke [66], we introduce the dimensionless noise parameters γ_V , γ_J and γ_{VJ} , such that the voltage S_V , circulating current S_J and the correlated S_{VJ} noise spectral densities are given by:

$$S_V = 2\gamma_V k_B T R, \quad (3.20)$$

$$S_J = 2\gamma_J k_B T / R, \quad (3.21)$$

$$S_{VJ} = 2\gamma_{VJ} k_B T, \quad (3.22)$$

where T is the electron temperature of the shunt resistors. The noises γ do depend on on the noise parameter Γ , due to the possibility of saturation and smearing of the device characteristics at elevated temperature. In Figure 3.10, we plot the dimensionless noises over a range of bias parameters for the same realization of the SLUG as the previous section and $\Gamma = 4 \times 10^{-5}$, which corresponds to an electron temperature of 100 mK when considering a SLUG with $\beta_L = 1$, $\beta_C = 1$, $L = 10$ pH, and junction self capacitance $C = 50$ fF, corresponding to a $1 \mu\text{m}^2$ junction with $I_0 = 100 \mu\text{A}$, and a shunt resistance of $R = 7.26 \Omega$. We note that at high bias current, $I_b \gg I_0$, $\gamma_{V,J}$ approach the expected Johnson noise limit of 1 for the two shunt resistors in parallel.

The device noise temperature T_n is evaluated from the circuit shown in Figure 3.8, where we calculate the total open circuit spectral density ($Z_o \rightarrow \infty$). It follows from Equation 3.13 that the spectral density of V_i^n is just $S_J \omega^2 L^2$ ³. We assume a noiseless

³The input voltage can be rewritten as $\tilde{v}_{in} = \pi\beta_L j' + 3\pi\beta_L i_{\phi,\text{rf}}/2$, where j is the circulating current in the SLUG loop. $i_{\phi,\text{rf}}$ is a noiseless current source, meaning the input voltage has a spectral density that

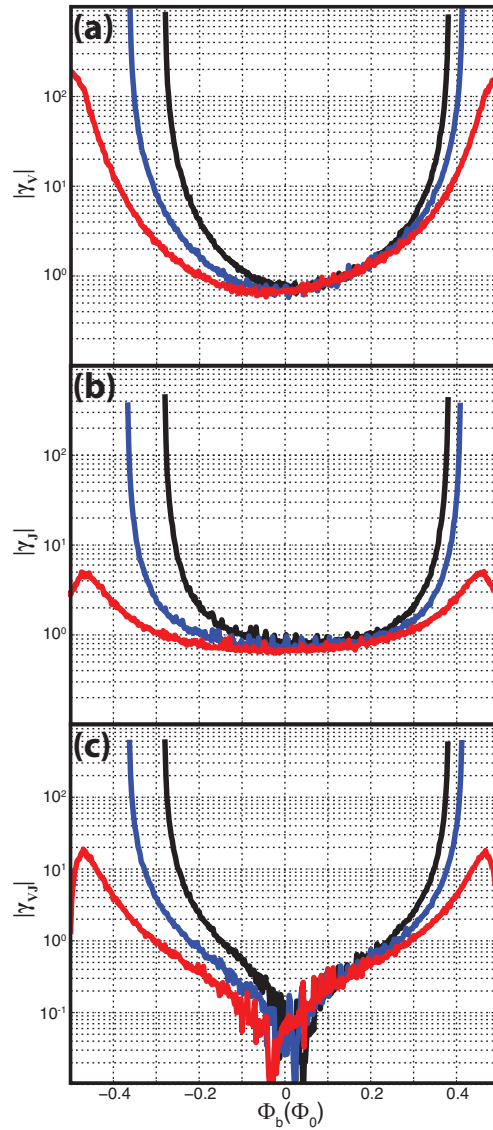


Figure 3.10: Dimensionless SLUG noises (a) γ_V , (b) γ_J , and (c) γ_{VJ} versus flux for $\Gamma = 4 \times 10^{-5}$ and various current biases: $1.8 I_0$ (black), $1.9 I_0$ (blue), $2.0 I_0$ (red).

source impedance $Z_S = R_S + jX_S$ and equate the total noise of the amplifier to the noise contribution from a source resistance R_S with a single side power spectral density

depends only on the time derivative of the circulating current noise, S_J . Since the Fourier transform of a time derivative goes as $\mathcal{F}_t[\dot{f}(t)](\omega) = i\omega\mathcal{F}_t[f(t)](\omega)$, it follows that V_i^n has a spectral density equal to $S_J\omega^2L^2$.

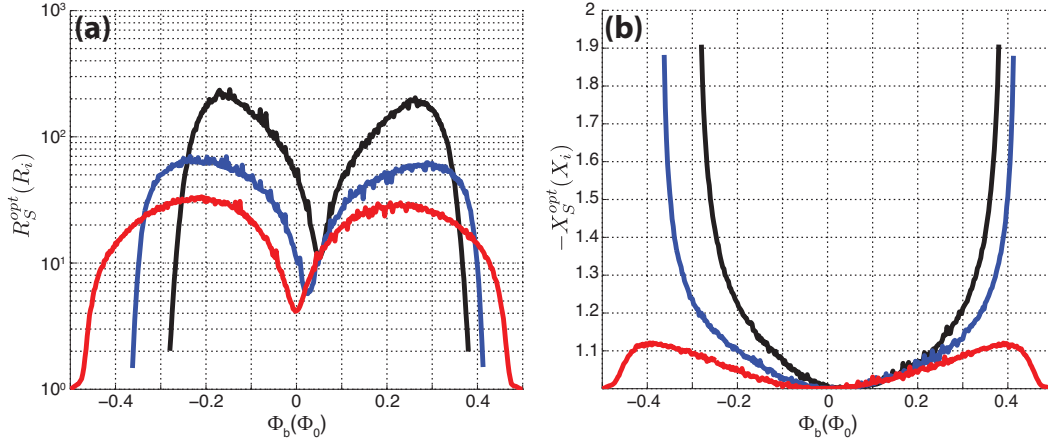


Figure 3.11: (a) Optimal real R_S^{opt} and (b) imaginary X_S^{opt} source impedance for the minimum noise temperature at $T = 100$ mK. Plotted for different current biases: $1.8 I_0$ (black), $1.9 I_0$ (blue), $2.0 I_0$ (red).

of $4k_B T_n R_S$, where T_n is the effective temperature of the source resistor. We refer all noises to the device output. We find:

$$\begin{aligned}
 4k_B T_n R_S \frac{|V_I|^2}{R_t^2 + X_t^2} &= S_V + S_J \frac{\omega^2 |V_I|^2 L^2}{R_t^2 + X_t^2} + 2S_{VJ} \frac{\omega |V_I| L X_t}{R_t^2 + X_t^2} \\
 &= 2\gamma_V k_B T R + \frac{2\gamma_J k_B T \omega^2 |V_I|^2 L^2}{R} + 4\gamma_{VJ} k_B T \frac{\omega |V_I| L X_t}{R_t^2 + X_t^2}. \quad (3.23)
 \end{aligned}$$

Here, $R_t = R_S + R_{in}$ ($X_t = X_S + X_{in}$) is the sum of the real (imaginary) parts of the source impedance and the device input impedance. The noise temperature is thus given by:

$$T_n = \left[\frac{\gamma_V (R_t^2 + X_t^2) R}{2 |V_I|^2 R_S} + \frac{\gamma_J \omega^2 L^2}{2 R R_S} + \gamma_{VJ} \frac{\omega L X_t}{|V_I| R_S} \right] T. \quad (3.24)$$

We use the condition $\partial T_n / \partial X_S = 0$ to solve for the imaginary part of the optimal source impedance. We find:

$$X_S^{opt} = -\frac{\gamma_V J \omega |V_I| L}{\gamma_V R} - X_{in}. \quad (3.25)$$

Similarly, the condition $\partial T_n / \partial R_S = 0$ yields the real part of the optimal source impedance. We have:

$$R_S^{opt} = \left[1 + \frac{1}{\gamma_V^2 \rho_{in}^2} \left(\frac{|V_I|}{L\omega} \right)^2 (\gamma_V \gamma_J - \gamma_{VJ}^2) \right]^{1/2} R_{in}. \quad (3.26)$$

For the bias points where V_I is highest, we have the following approximate expression for R_S^{opt} :

$$\begin{aligned} R_S^{opt} &\approx \frac{1}{\gamma_V \rho_{in}} \frac{|V_I|}{L\omega} (\gamma_V \gamma_J - \gamma_{VJ}^2)^{1/2} R_{in} \\ &= \frac{\omega |V_I| L}{\gamma_V R} (\gamma_V \gamma_J - \gamma_{VJ}^2)^{1/2}. \end{aligned} \quad (3.27)$$

In Figures 3.11(a) and (b), we plot R_S^{opt}/R_{in} and X_S^{opt}/X_{in} versus flux for various current biases. For typical device parameters, we have $R_S^{opt} \gg R_{in}$. For this reason, it is not possible to achieve a simultaneous power match and noise match. It is worthwhile to note, however, that the ratio R_S^{opt}/R_{in} scales with frequency as ω^{-1} , facilitating simultaneous attainment of high gain and good noise performance at higher operating frequencies.

When the signal is coupled to the device via a source with optimal impedance $Z_S^{opt} = R_S^{opt} + jX_S^{opt}$, the amplifier noise temperature becomes:

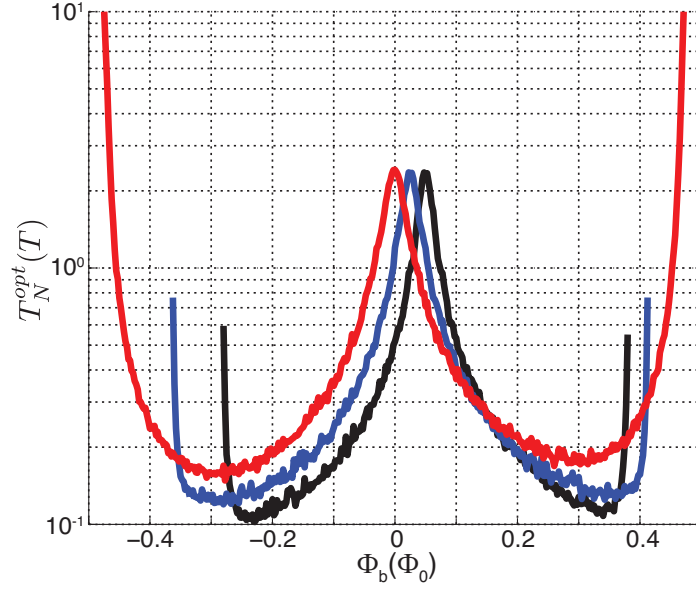


Figure 3.12: Optimal SLUG noise temperature versus flux, operated at a temperature $T = 100$ mK. Plotted for different current biases: $1.8 I_0$ (**black**), $1.9 I_0$ (**blue**), $2.0 I_0$ (**red**).

$$T_n^{opt} = \frac{\omega L}{|V_I|} (\gamma_V \gamma_J - \gamma_{VJ}^2)^{1/2} T. \quad (3.28)$$

In Figure 3.12, we show the optimal noise temperature T_n^{opt} for a SLUG amplifier over a range of bias points at an operating frequency $\omega/2\pi = 6$ GHz. Note that every point in these plots corresponds to a different realization of the input matching network; in Section 3.9, we will examine the bias and frequency-dependent noise temperature of SLUG amplifiers operated with a fixed input network.

3.6 Noise Properties in the Quantum Regime

At sufficiently low temperature, the zero-point fluctuations of the resistive shunts are expected to make the dominant noise contribution. The full expression for the spectral density of voltage noise produced by the resistors is written as $2hfR \coth(hf/2k_B T)$. We have calculated the added noise of the symmetric SLUG in the zero-temperature limit, where the voltage spectral density of the shunt resistors becomes $2hfR$. We generate a single-sided quantum spectral density as described by Section B.3. Using the quantum noise as a driving term in the SLUG equations of motion 3.9, we evaluate the voltage power spectral density $S_V(f)$ at the device output, the circulating current spectral density $S_J(f)$, and the cross spectral density $S_{VJ}(f)$; in Figure 3.13, we plot these noises versus flux for various bias currents. Once again, the device noise temperature T_n can be evaluated from the circuit of Figure 3.8. We assume a zero-temperature source impedance $Z_S = R_S + jX_S$ and equate the total noise of the amplifier to the noise contribution from a source resistance R_S at a finite effective temperature T_n . The amplifier noise temperature is obtained from the relation:

$$2hfR_S \coth\left(\frac{hf}{2k_B T_n}\right) \frac{|V_I|^2}{R_t^2 + X_t^2} = S_V + S_J \frac{\omega^2 |V_I|^2 L^2}{R_t^2 + X_t^2} + 2S_{VJ} \frac{\omega |V_I| L X_t}{R_t^2 + X_t^2} + 2hfR_S \frac{|V_I|^2}{R_t^2 + X_t^2}. \quad (3.29)$$

Alternatively, we can express the noise contribution of the device in terms of an added number of noise photons n , where n and T_n are related as follows:

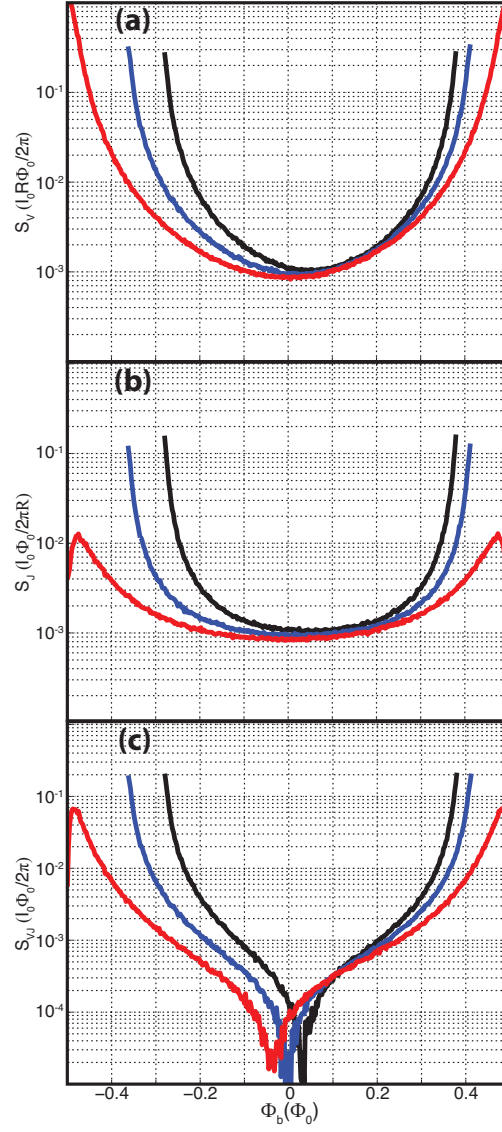


Figure 3.13: Quantum noises (a) S_V , (b) S_J , and (c) S_{VJ} versus flux for various current biases: $1.8 I_0$ (black), $1.9 I_0$ (blue), $2.0 I_0$ (red).

$$\coth\left(\frac{hf}{2k_B T_n}\right) = 2n + 1, \quad (3.30)$$

so that:

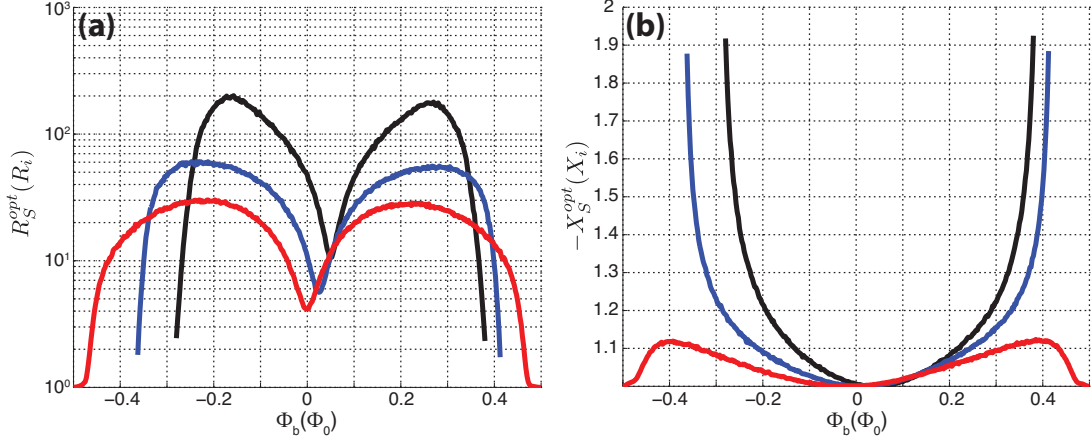


Figure 3.14: (a) Optimal real R_S^{opt} and (b) imaginary X_S^{opt} source impedance for the minimum number of added noise quanta. Plotted for different current biases: 1.8 I_0 (black), 1.9 I_0 (blue), 2.0 I_0 (red).

$$n = \frac{1}{2hfR_S} \left[\frac{S_v R_t^2 + X_t^2}{2 |V_I|^2} + \frac{S_J}{2} \omega^2 L^2 + S_{VJ} \frac{\omega L}{|V_I|} X_t \right]. \quad (3.31)$$

The optimal source impedance $Z_s^{opt} = R_S^{opt} + jX_S^{opt}$ is obtained from the relations $\partial n / \partial X_S = 0$ and $\partial n / \partial R_S = 0$. The imaginary part of the optimal source impedance is given as follows:

$$X_S^{opt} = -\frac{S_{VJ}}{S_V} \omega |V_I| L - X_i. \quad (3.32)$$

Similarly, the real part of the optimal source impedance is written:

$$R_S^{opt} = \left[1 + \left(\frac{|V_I| R}{\rho_{in} \omega L S_V} \right)^2 (S_V S_J - S_{VJ}^2) \right]^{1/2} R_{in}. \quad (3.33)$$

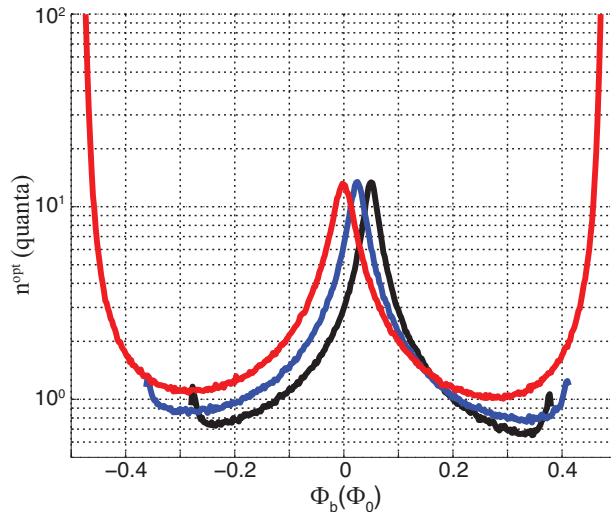


Figure 3.15: Minimum number of added noise quanta in the quantum regime n_{opt} versus flux operated at 6 GHz for different current biases: $1.8 I_0$ (**black**), $1.9 I_0$ (**blue**), $2.0 I_0$ (**red**).

In the limit $V_I \gg \omega$, we find:

$$R_S^{opt} \approx \frac{\omega |V_I| L}{S_V} (S_V S_J - S_{VJ}^2)^{1/2}. \quad (3.34)$$

In Figures 3.14(a) and (b), we plot R_S^{opt}/R_{in} and X_S^{opt}/X_{in} in the quantum regime versus flux for a range of current biases. For the optimally matched source, the added number of noise quanta is given by:

$$n_{opt} = \frac{L}{2\hbar |V_I|} (S_V S_J - S_{VJ}^2)^{1/2}. \quad (3.35)$$

In Figure 3.15, we plot n_{opt} versus flux, for various current biases. We see that for an appropriately noise-matched source, the SLUG approaches a noise level that is close to

the standard quantum limit $n_{SQL} = 1/2$, the minimum achievable added noise for a phase-insensitive amplifier [44].

3.7 Amplifier Design

The above analysis demonstrates that the SLUG is an attractive gain element for the realization of a low-noise microwave amplifier. We now consider concrete external networks used to embed the device in a 50Ω environment. The tasks are to maximize power transfer to and from the device and to match the 50Ω source to the optimal noise impedance at the desired operating frequency. For example, to maximize gain, we design a conjugate matching network to transform the 50Ω source to $R_{in} - jX_{in}$. On the other hand, optimal noise performance is achieved for an input matching network that transforms the 50Ω generator to the complex optimal source impedance $Z_S^{opt} = R_S^{opt} + jX_S^{opt}$. Since $R_S^{opt} \gg R_{in}$ for typical parameters, it is generally not possible to achieve a simultaneous power match and noise match. However, it is possible to find a compromise where there is reasonable gain and good noise performance over a relatively broad bias range. Figure 3.16(a) shows a schematic diagram of a SLUG-based microwave amplifier with transmission line matching sections at the input and output. To calculate amplifier gain and noise performance, we treat the SLUG as a “black box” with scattering parameters derived from the calculations above [Figure 3.16(b)].

As an example, we show in Figure 3.17 the frequency dependent gain, operating frequency, instantaneous bandwidth, and added noise quanta n for SLUG amplifiers operated with different single-section transmission line input couplers with characteristic impedance in the range from $1 - 3 \Omega$. Here, we have used the full expression of Equation 3.31 to evaluate the frequency dependent added noise quanta of the amplifier. The

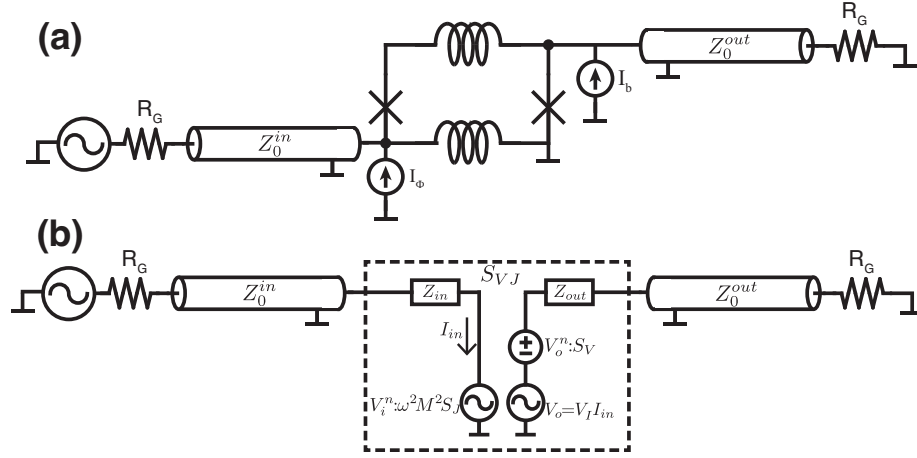


Figure 3.16: (a) Schematic of SLUG microwave amplifier. (b) Black box circuit for amplifier analysis

length of the input coupler provides a bare quarter-wave resonance at 9 GHz; inductive loading of the SLUG pulls the operating frequency to lower frequencies. To evaluate the source impedance $Z_S = R_S + jX_S$ in Equation 3.31, we need to evaluate the impedance of the input coupler loaded by the generator resistance $R_G = 50 \Omega$. The general form for the input impedance of a lossless transmission line with arbitrary load Z_L and characteristic impedance Z_0 is given by [87]:

$$Z_{tran} = Z_0 \left(\frac{Z_L + jZ_0 \tan(\beta\ell)}{Z_0 + jZ_L \tan(\beta\ell)} \right), \quad (3.36)$$

where $\beta = 2\pi/\lambda = 2\pi f/v_{ph}$ is the wave number, v_{ph} is the phase velocity, and ℓ is the physical length of the transmission line. For a quarter-wave resonance $f_{\lambda/4}$, the length of the matching section is $\ell = v_{ph}/4f_{\lambda/4}$, and the source impedance becomes:

$$Z_S = Z_0 \left(\frac{R_G + jZ_0 \tan\left(\frac{\pi f}{2f\lambda/4}\right)}{Z_0 + jR_G \tan\left(\frac{\pi f}{2f\lambda/4}\right)} \right). \quad (3.37)$$

To evaluate the frequency dependent gain, we must calculate the current I_{in} flowing through Z_{in} , giving us the following expression for the dissipated power at the output:

$$P_{out}^{SLUG} = \left| \frac{I_{in} V_I}{Z_{out} + R_G} \right|^2 R_G. \quad (3.38)$$

For the purposes of this simple example, we have ignored the quarter-wave output coupler in Figure 3.16, directly connecting Z_{out} to R_G . To calculate the gain, we must refer P_{out}^{SLUG} to the output power with no SLUG in the circuit P_{out}^{ref} :

$$P_{out}^{ref} = \frac{V_G^2}{4R_G}. \quad (3.39)$$

The gain is then defined as $G = P_{out}^{SLUG}/P_{out}^{ref}$. To evaluate I_{in} , we make use of the Telegrapher's equations to arrive at following expression for the voltage along a lossless transmission line [87]:

$$V_{tr}(z) = V_o^+ [\exp(-j\beta z) + \Gamma_L \exp(j\beta z)]. \quad (3.40)$$

By convention, the load sits at $z = 0$, and the transmission line input is at $z = -\ell$. V_o^+ is the voltage wave incident on the load, and Γ_L is the reflection coefficient at the load:

$$\Gamma_L = \frac{Z_L - Z_0}{Z_L + Z_0}, \quad (3.41)$$

where the voltage reflected off the load is $V_o^- = \Gamma_L V_o^+$. For our circuit, the voltage at the input of the transmission line V_{in} is:

$$V_{in} = \frac{V_G Z_{tran}}{R_G + Z_{tran}} = V_o^+ [\exp(j\beta\ell) + \Gamma_L \exp(-j\beta\ell)], \quad (3.42)$$

where we've made use of Equation 3.40 evaluated at $z = -\ell$. Z_{tran} and Γ_L are evaluated using Equations 3.36 and 3.41, where the load impedance Z_L is just equal to the calculated input impedance of the SLUG Z_{in} , and $\beta\ell = \frac{\pi f}{2f_{\lambda/4}}$. Finally, Equation 3.42 allows us to calculate the voltage incident V_o^+ on the load as a function of frequency and, in turn, the current flowing through Z_{in} :

$$\begin{aligned} I_{in} &= \frac{V_o^+}{Z_{in}} (1 + \Gamma_{in}) \\ &= \frac{V_{in}}{Z_{in}} \left(\frac{1 + \Gamma_{in}}{\exp(j\beta\ell) + \Gamma_{in} \exp(-j\beta\ell)} \right) \\ &= \frac{V_G Z_{tran}}{R_G + Z_{tran}} \left(\frac{1}{Z_{in}} \right) \left(\frac{1 + \Gamma_{in}}{\exp\left(j\frac{\pi f}{2f_{\lambda/4}}\right) + \Gamma_{in} \exp\left(j\frac{\pi f}{2f_{\lambda/4}}\right)} \right), \end{aligned} \quad (3.43)$$

where Γ_{in} and Z_{tran} are:

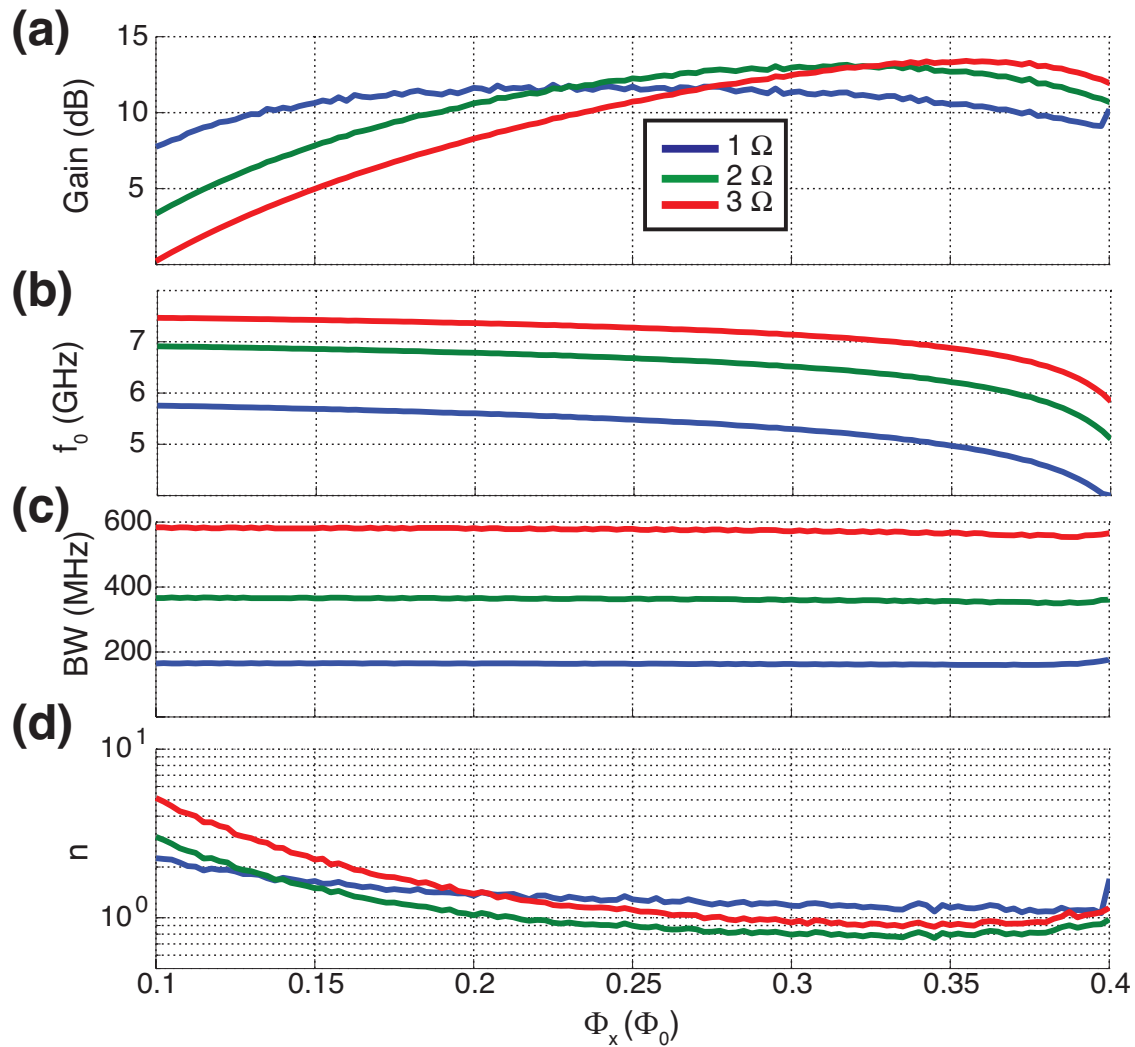


Figure 3.17: (a) Gain, (b) operating frequency, (c) instantaneous bandwidth, and (d) added noise quanta for a SLUG amplifier using a single transmission line section matching network with a $\lambda/4$ resonance of 9 GHz, and a characteristic impedance indicated in the figure. Gain and the added noise quanta are evaluated at the operating frequency – the frequency where the quantum noise contribution of the SLUG is minimum. The plots were evaluated for a range of Z_0 's as indicated in the figure.

$$\Gamma_{in} = \frac{Z_{in} - Z_0}{Z_{in} + Z_0}, \quad (3.44)$$

$$Z_{tran} = Z_0 \left(\frac{Z_{in} + jZ_0 \tan\left(\frac{\pi f}{2f_{\lambda/4}}\right)}{Z_0 + jZ_{in} \tan\left(\frac{\pi f}{2f_{\lambda/4}}\right)} \right). \quad (3.45)$$

We evaluate gain as a function of frequency with Equations 3.43, 3.38, 3.39. For the data plotted in Figure 3.17, we've assumed a perfect match at the output, modifying Equation 3.38:

$$P_{out}^{SLUG} = \left| \frac{I_{in} V_I}{Z_{out} + Z_{out}^*} \right|^2 R_{out}. \quad (3.46)$$

We remark that the transmission line impedances considered here are readily achieved with thin-film microstrip technology: for example, a trace width of 10 μm and a dielectric with relative permittivity $\epsilon_r = 4$ and thickness 100 nm corresponds to a characteristic impedance of 2 Ω .

In Figure 3.18, we consider the frequency-dependent gain and noise performance of SLUG amplifiers operated at different flux biases for a fixed a quarter-wave transformer with a characteristic impedance $Z_0 = 2 \Omega$ and a $\lambda/4$ resonance of 9 GHz. Due to the non vanishing cross spectral density S_{VJ} , the minimum added noise occurs at a frequency that is somewhat lower than the frequency of maximum gain. For the simulated SLUG parameters, we achieve noise within 50% of the standard quantum limit at a frequency where amplifier gain is 15 dB and noise within a factor of two of the standard quantum limit at a frequency where the gain is 18 dB.

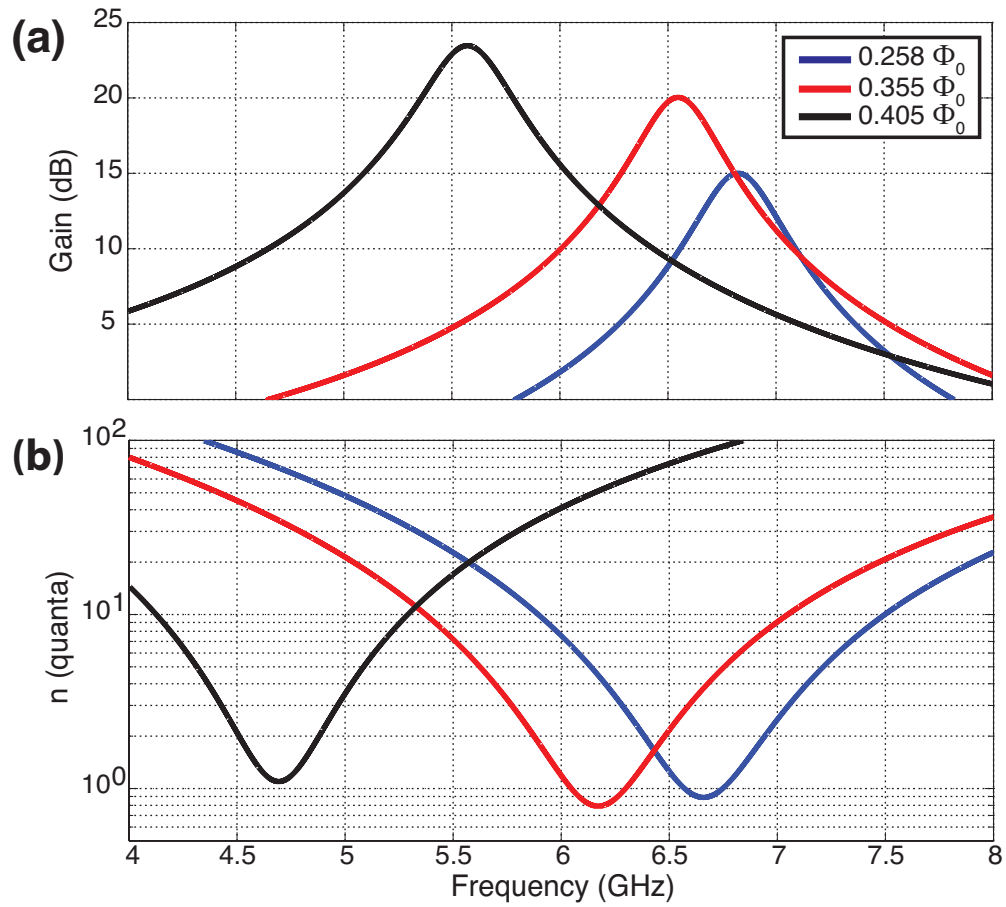


Figure 3.18: (a) Gain, and (b) added noise quanta versus frequency for a SLUG amplifier using a single transmission line section matching network with a $\lambda/4$ resonance of 9 GHz, and a characteristic impedance of $Z_0 = 2 \Omega$. Gain and noise are evaluated for three different quasistatic flux biases, as indicated in the figure.

Finally, we note that it is possible to increase the amplifier bandwidth significantly by coupling the input signal to the device via a multisection transformer with stepped characteristic impedances. As an example, we show in Figure 3.19 the frequency-dependent gain and added noise for amplifiers operated with different three-section matching networks. Here, the length of each transmission line section was chosen to provide a bare quarter-wave resonance at 5 GHz and the characteristic impedances were determined by numerical minimization of the added noise contribution of the SLUG in the frequency range from 4.5 to 5.5 GHz. The source impedance Z_S and current flowing through the input of the SLUG I_{in} were calculated in a similar method as the single section transformer described above.

3.8 Dynamic Range

The strong nonlinearity of the SLUG leads to gain compression and harmonic generation when the device is driven with a large-amplitude signal. It is important to verify that the SLUG dynamic range will be sufficient for the desired application. In Figure 3.20(a), we plot the normalized SLUG gain⁴ versus signal power coupled to the device input over a range of different bias parameters. These plots were generated by solving the SLUG equations of motion [Equation 3.9] with a sinusoidal driving term of varying amplitude⁵. Depending on the bias point, the 1 dB compression point occurs somewhere in the range from -110 dBm to -90 dBm, corresponding to input powers from 10 fW to 1 pW. These 1 dB compression points are comparable to those seen in other SQUID-based microwave amplifiers[73] and 1-2 orders of magnitude higher than those

⁴The gain was normalized to the simulated gain at a -130 dBm input power.

⁵Specifically, the gain was calculated assume conjugate matching at the output and input of the SLUG.

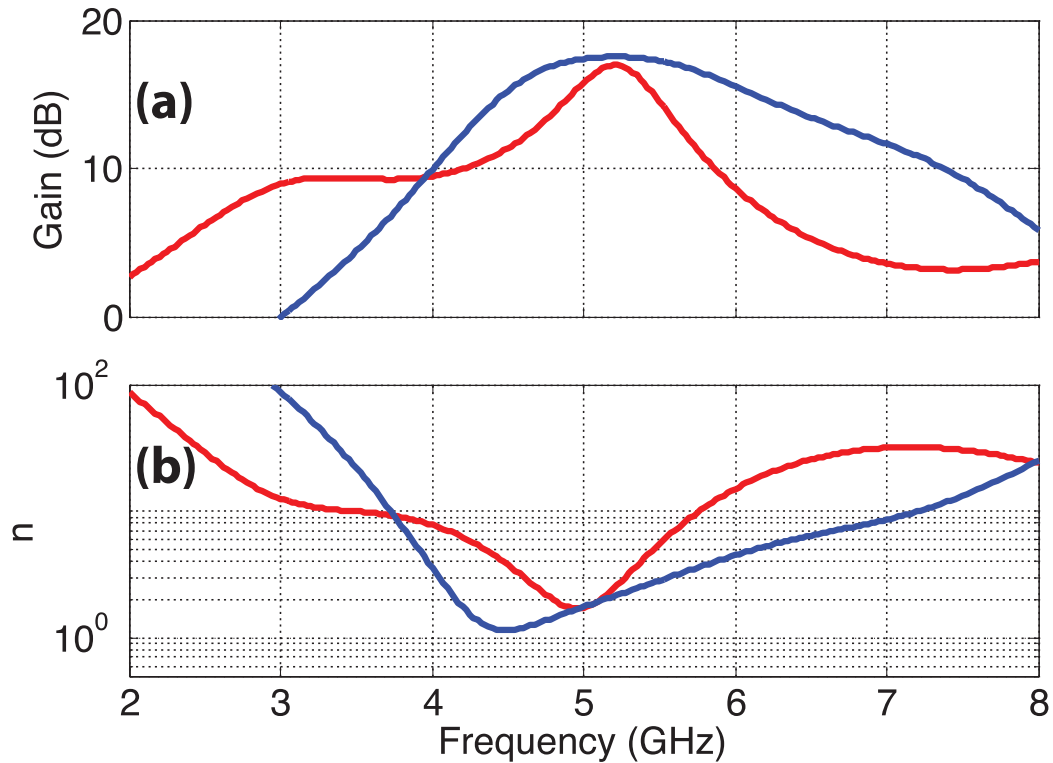


Figure 3.19: **(a)** Gain, and **(b)** added noise quanta versus frequency for a SLUG amplifier with $I_b = 1.8 I_0$, and $\Phi_B = 0.35 \Phi_0$. The red traces correspond to a three-section input matching network with quarter-wave resonances at 5 GHz and with characteristic impedances of 24.4Ω , 17.4Ω , and 3.0Ω , derived from numerical minimization of the SLUG quantum noise over the band from 4.5 to 5.5 GHz. The blue traces correspond to a matching network consisting of three sections with characteristic impedances of 29.8Ω , 7.1Ω , and 1.1Ω followed by a series capacitance of 38 pF to tune out the imaginary part of the SLUG input impedance at a frequency of 5 GHz.

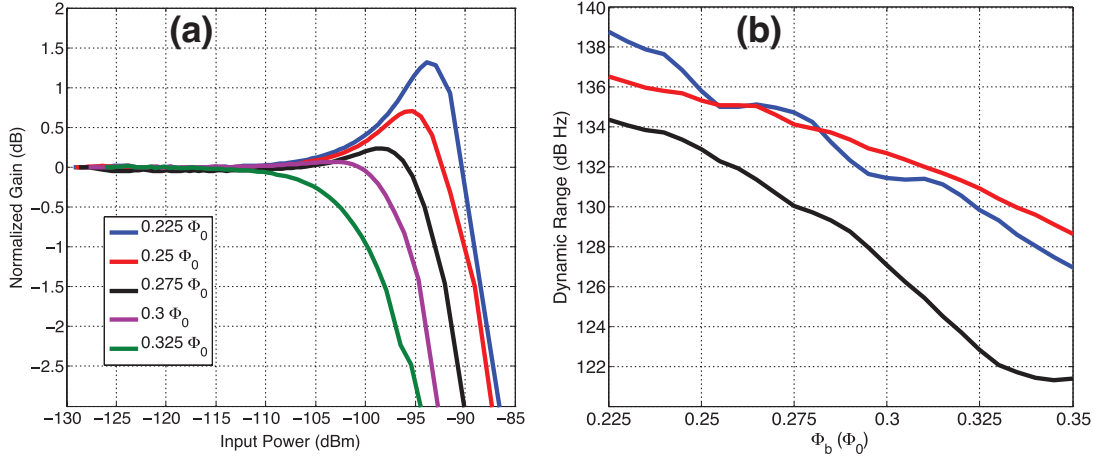


Figure 3.20: **(a)** Normalized gain versus input power for a SLUG element conjugately matched to the input and output for $I_b = 1.8 I_0$ and various flux bias points. **(b)** SLUG dynamic range versus flux for various current bias points; we assume a zero-temperature quantum spectral density for the SLUG shunt resistors.

achieved with typical Josephson parametric amplifiers[47]. Amplifier dynamic range is a ratio of the 1 dB compression point to the noise power contributed by the SLUG over a given bandwidth. In Figure 3.20(b), we plot SLUG dynamic range; here, we have used the zero-temperature quantum spectral density for the shunt resistors of the SLUG. We find a typical value of 130 dB Hz, corresponding to a dynamic range of 40 dB in an amplifier bandwidth of 1 GHz. For applications related to the dispersive readout of qubits in a circuit QED architecture, where the focus is on the measurement of signals at the level of single microwave quanta in bandwidths of order 100 MHz to 1 GHz, the dynamic range of the SLUG is more than adequate.

3.9 Effect of Input Circuit Admittance

In the above analysis, we have solved for the behavior of the isolated SLUG element and then treated the device as a “black box” with known scattering parameters for

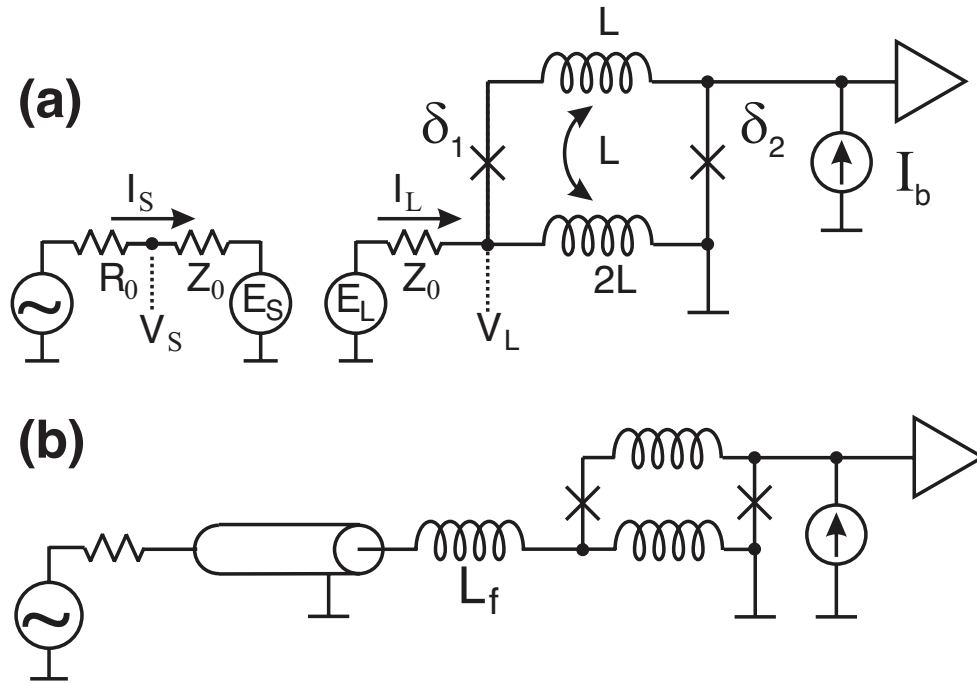


Figure 3.21: (a) Model for circuit analysis with finite input admittance. (b) Amplifier circuit with filter inductor L_f to decouple SLUG from modes of the input circuit.

the purpose of designing appropriate matching networks. In reality, the nonvanishing admittance at the device input and output will modify the device characteristics, and a complete treatment must take loading by the external circuit into account. The scattering parameters will now depend on the particular realization of the matching network and a full exploration of the space of design parameters become tedious. However, we find that the performance of the SLUG amplifier is not greatly affected by the nonvanishing input circuit admittance, particularly once modest steps are taken to decouple the SLUG element from the higher-order modes of the resonant input matching network.

To take into account the admittance of the resonant input matching network, we modify the junction equations of motion 3.9 to include an additional term representing the current drawn by the input circuit. The circuit model is shown in Figure 3.21(a). The input transmission line of impedance Z_0 can be exactly modeled as a pair of coupled,

time dependent voltage sources E_L and E_S . These are related to the voltages $V_{L,S}$ and currents $I_{L,S}$ at the two ends of the transmission line as follows:

$$\begin{aligned} E_L(t) &= V_S(t - t_D) + Z_0 I_S(t - t_D), \\ E_S(t) &= V_L(t - t_D) - Z_0 I_L(t - t_D), \end{aligned} \quad (3.47)$$

where $t_D = \frac{1}{4f_{\lambda/4}}$ is the propagation delay along the transmission line. The input current is then determined by the additional differential equation:

$$\dot{I}_L = \frac{1}{L} \left[\frac{\Phi_0}{2\pi} (\dot{\delta}_2 - \dot{\delta}_1) - E_L + I_L Z_0 \right]. \quad (3.48)$$

Using the modified equations of motion for the junction phases, we calculate the dc characteristics of the SLUG. The I-V and V- Φ curves of the same 10 pH, $\beta_L = 1$ SLUG with a 10 GHz quarter-wave input transformer are shown in Figures 3.22(a) and 3.22(b). We observe sharp Shapiro step-like structure at voltages corresponding to Josephson frequencies that are integer multiples of the half-wave resonance of the input circuit. While quantum fluctuations of the SLUG shunts smooth out this structure somewhat, it is clearly desirable to decouple the SLUG from the higher-order standing wave modes of the input circuit, as these mode will limit amplifier dynamic range and lead to excess noise.

To suppress the resonances of the input circuit, we insert a filter inductor L_f of order tens of pH between the input coupler and the SLUG element, as shown in Figure 3.21(b).

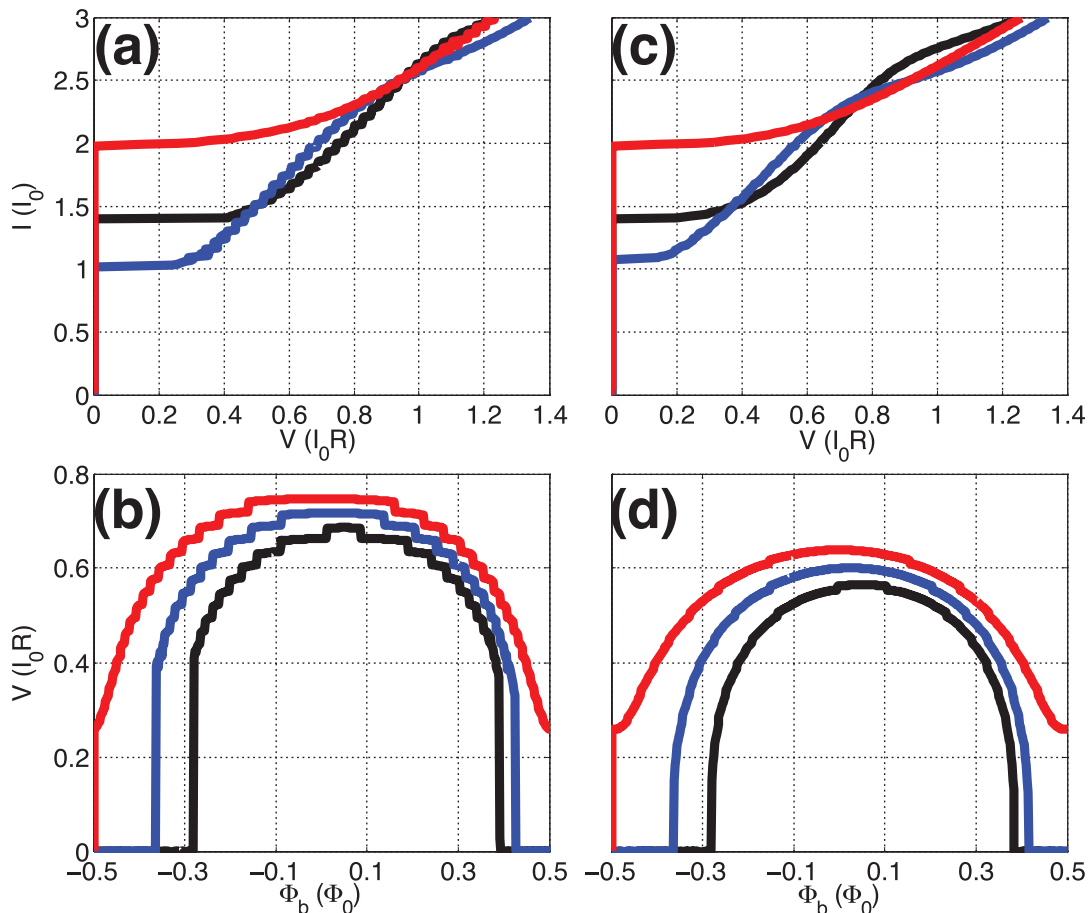


Figure 3.22: (a) I-V curves of a SLUG operated with a transmission line input circuit with characteristics impedance $Z_0 = 2 \Omega$ and bare quarter-wave resonance at 10 GHz for various flux bias points. (b) V- Φ curves of the same SLUG for various current bias points. (c) - (d) As in (a) - (b), respectively, for a circuit incorporating a 60 pH filter inductor L_f to decouple the modes of the SLUG from the modes of the input circuit.

In Figures 3.22(c) and 3.22(d), we plot the SLUG characteristics with a 60 pH filter inductor in place. We see that the resonant structure is greatly suppressed.

We can now calculate the gain and noise properties of a the complete circuit of Figure 3.21(b) by performing a full integration of the amplifier equations of motion. Power gain and bandwidth are determined by driving the amplifier with a sinusoidal input tone and monitoring the SLUG output at the excitation frequency. In Figure 3.23(a), we

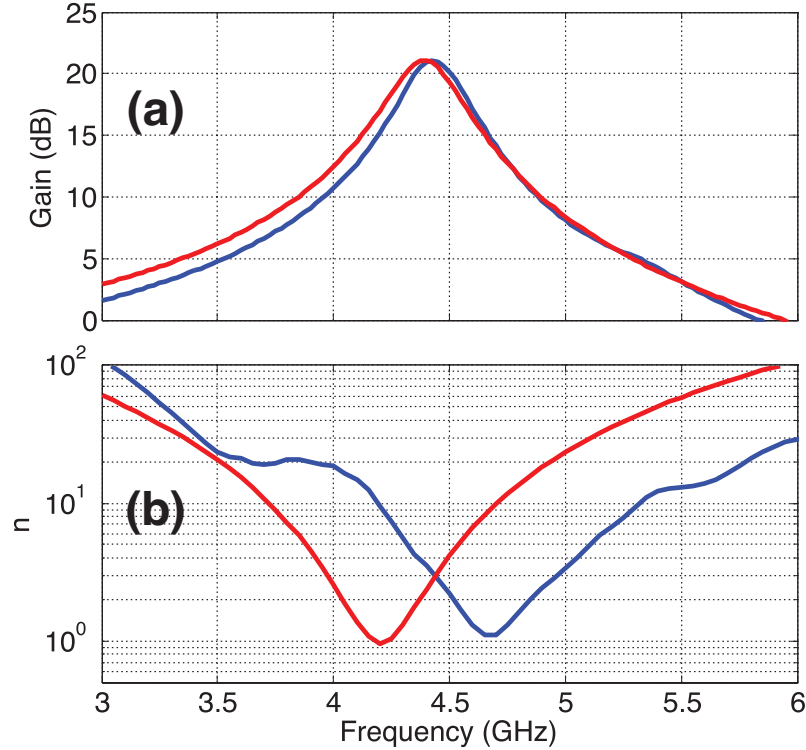


Figure 3.23: (a) Gain and (b) added noise quanta for SLUG amplifiers calculated using the “black box” scattering parameters of the isolated SLUG or by solving the full circuit model of Figure 3.22. The SLUG was biased at $I_b = 1.8 I_0$ and $\Phi_b = 0.35 \Phi_0$. The input matching network consists of a 2Ω transmission line section with bare quarter-wave resonance at 10 GHz followed by a filter inductor $L_f = 60$ pH. The blue trace is the solution to the full circuit simulation, while the red trace shows the “black box” solution.

plot frequency-dependent gain for the SLUG circuit. The blue trace is the result of the full circuit simulation, where we have taken a transmission line input with characteristic impedance $Z_0 = 2 \Omega$ and a length corresponding to a bare quarter-wave resonance at 10 GHz, significantly higher than the amplifier operating frequency of 4.5 GHz in order to compensate for the additional reactive loading by the filter inductor. The red trace was obtained by treating the SLUG as a “black box” with scattering parameters calculated as described above in Section 3.4. The agreement with the full circuit simulation is good,

confirming that the filter inductance has effectively isolated the modes of the SLUG and the input circuit.

To calculate the frequency-dependent added noise, we simulate a “hot load/cold load” experiment where we compare the power spectra $S_{V,cold}$ and $S_{V,hot}$ at the device output for source resistances at temperatures $T = 0$ and T_b respectively. In the quantum regime, we find:

$$\frac{\coth(\hbar f/2k_B(T_b + T_n))}{\coth(\hbar f/2k_B T_n)} = \frac{S_{V,hot}}{S_{V,cold}}. \quad (3.49)$$

The added noise number is then obtained from Equation 3.30. In Figure 3.23(b), we plot the added noise of a 5 GHz SLUG amplifier calculated with the full circuit model and with the “back box” scattering parameters of the isolated SLUG. The noise magnitude is similar in the two cases, although the full circuit solution predicts a higher frequency for the minimum in the amplifier noise contribution. We understand the shift in the frequency-dependent noise characteristics to be due to a modification of the circulating current spectral density S_J by the nonvanishing admittance of the input circuit.

3.10 Reverse Transfer Function

So far we have only considered the forward transfer function $[V_I$ from Section 3.4] in our analysis of the SLUG amplifier. The reverse transfer impedance $V_I^R = \partial V_{in}/\partial I_{out}$ is the voltage that develops across the input circuit due to a current excitation at the output of the SLUG. Earlier numerical studies [86] of SQUID amplifiers have also treated the SQUID as a fully non-reciprocal gain element with a negligible reverse transfer function

[88]. This may be an appropriate assumption for SQUID based amplifiers at low-frequencies, but the reverse transimpedance is not negligible at higher frequencies:

$$V_I^R = \rho_T^R \frac{(\omega L)^2}{R} + j\chi_T^R \omega L, \quad (3.50)$$

where ρ_T^R and χ_T^R are the dimensionless real and imaginary reverse transfer function coefficients, respectively. We've calculated both ρ_T^R and χ_T^R for a SLUG with $\beta_L = 1$, $\beta_C = 0.8$, a junction self capacitance $C = 50$ fF, and SLUG inductance $L = 10$ pH at three different current biases, shown in Figure 3.24. For the frequencies and SLUG parameters of this chapter, the imaginary part of V_I^R dominates the reverse transimpedance. The most striking feature of the calculated χ_T^R in Figure 3.24(b) is the four-orders of magnitude asymmetry close to the supercurrent branch of the transfer function. This asymmetry suggests that the reverse gain of a SLUG based amplifier will be significantly lower when biased on one side of the V- Φ curve. An amplifier that isolates the measured system from the amplifier chain is highly desirable for cryogenic qubit measurements, reducing the need for bulky, magnetic isolators at the cold stage of the measurement.

3.11 Lumped Element Matching Network

In this section, we separately consider the SLUG amplifier with a lumped element input matching network. We match the 50Ω generator to the SLUG through an inductor-capacitor impedance transformer illustrated in Figure 3.25(a), with resonance $\omega_0 = 1/\sqrt{L_R C_R}$ and characteristic impedance $Z_0 = \sqrt{L_R/C_R}$. This simple lumped element circuit is more compact than a quarter-wave transformer; moreover, the LC

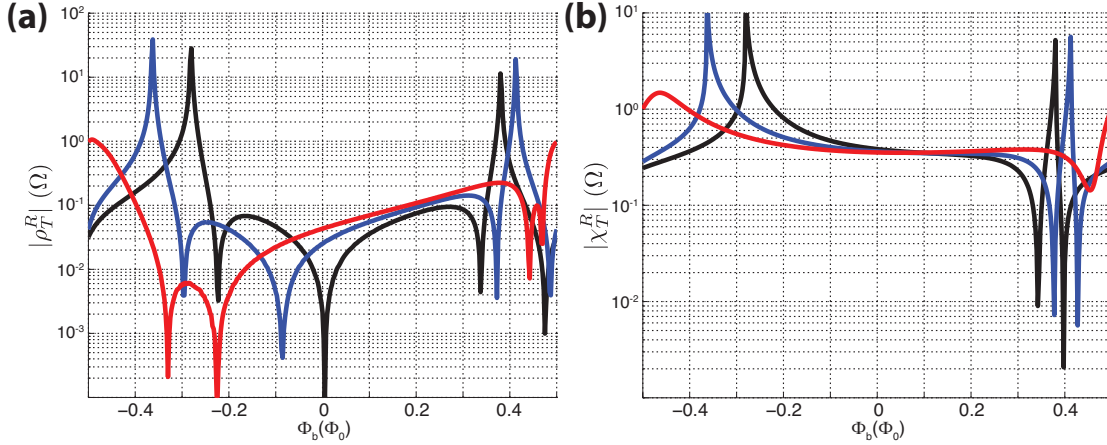


Figure 3.24: The real **(a)** and imaginary **(b)** coefficients of the reverse transimpedance V_I^R for the SLUG at different current biases: $1.8 I_0$ (**black**), $1.9 I_0$ (**blue**), $2.0 I_0$ (**red**).

matching network has a single resonant mode at ω_0 , resulting in a clean transfer function without having to take extra precautions, like the choke inductor of Section 3.9.

In Figure 3.26, we compare the transfer function, forward-gain, and reverse-gain of the SLUG amplifier when solving the equations of motion for the full-circuit [Figure 3.25(a)] and in the “black box” approximation [Figure 3.25(b)]. Notice that the “black box” approximation in Figure 3.25(b) now includes a voltage source $V_i = V_I^R I_{in}$ for calculating the reverse gain. The solutions were solved for a SLUG with $\beta_L = 1$, $\beta_C = 0.8$, a junction self capacitance $C = 50$ fF, and SLUG inductance $L = 10$ pH, for a current bias $I_b = 1.9 I_0$. The LC matching network was designed with $\omega_0 = 8$ GHz and $Z_0 = 2 \Omega$, for a $L_R = 40$ pH and $C_R = 10$ fF. Comparing the full circuit simulations of Figures 3.26(a-c) to the “black box” solutions of Figures 3.26(d-f) reveals little noticeable difference between the two numerical approaches.

As predicted in Section 3.10, the reverse gain of the amplifier is asymmetric with an optimal flux bias point close to $\Phi_b = 0.37 \Phi_0$, where the reverse-gain peaks at about -60 dB. In Figure 3.27, we plot the forward-gain (a), reverse-gain (b), and added noise quanta

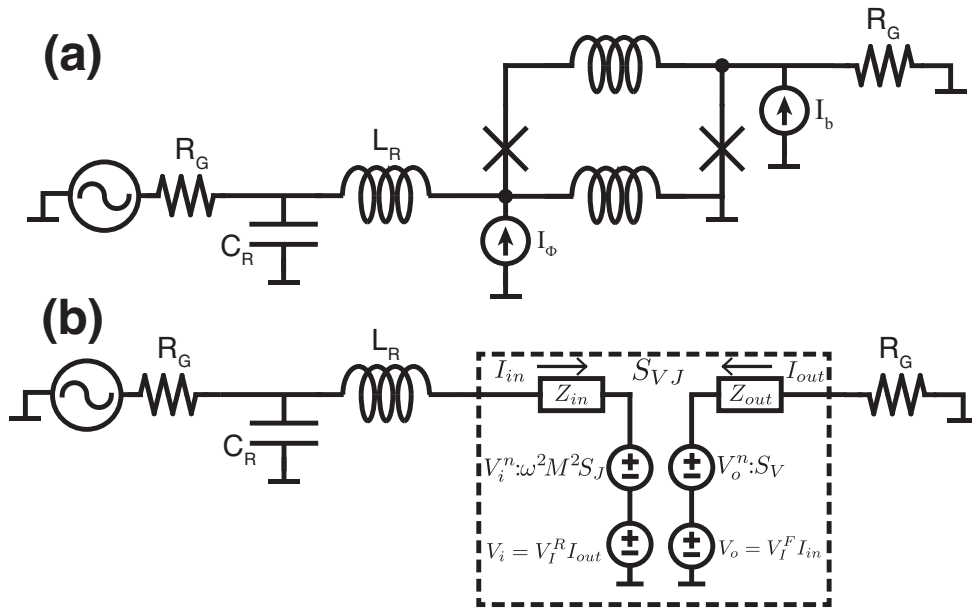


Figure 3.25: The full-circuit (a) and “black box” model (b) of the SLUG gain element with input matched to R_G through a lumped element matching network with inductance L_R and capacitance C_R .

(c) as a function of frequency for different flux biases, solved using the “black box” model. Similar to the performance of the quarter-wave transformer of Section 3.9, the amplifier can operate with forward-gain close to 15 dB and a bandwidth of approximately 300 MHz, while adding approximately one quantum of noise.

3.12 Hot Electron Effects

At milikelvin temperatures, electrons decouple from the phonons and the electron temperature of the SLUG shunts can be significantly higher than the bath temperature. Wellstood *et al.* [89] showed that the electron temperature T_E in a metal thin film resistor is given by:

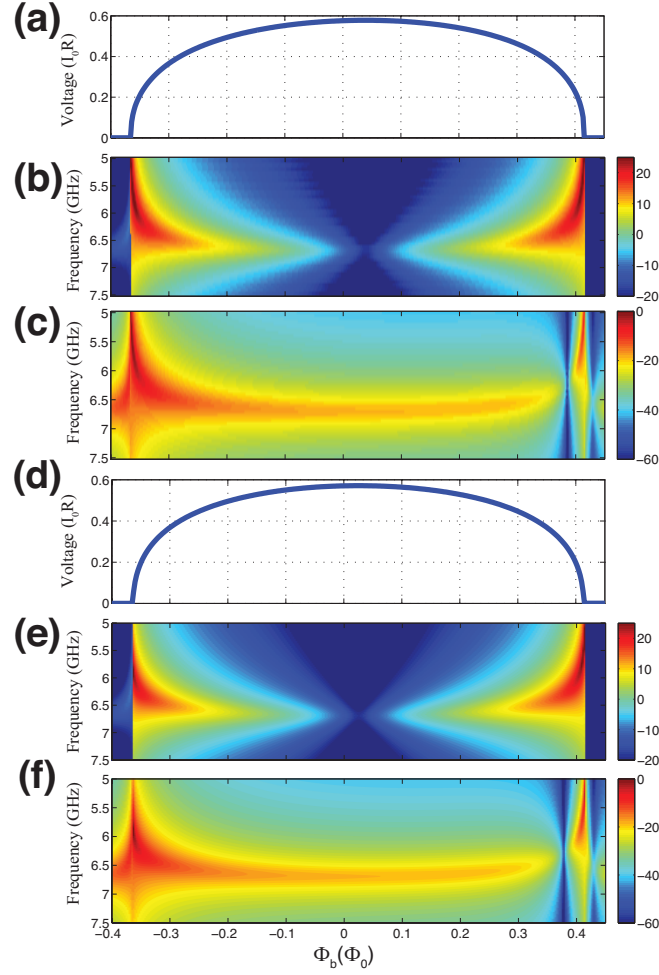


Figure 3.26: The V - Φ curve (a), forward-gain (b), and reverse-gain (c) for the full-circuit model of Figure 3.25(a). The V - Φ curve (d), forward-gain (e), and reverse-gain (f) for the “black box” model of Figure 3.25(b). The solutions were solved for $I_b = 1.9 I_0$, $L_R = 40$ pH and $C_R = 10$ pF. The gain plots are solved as a function of flux bias and signal frequency, where the gain is in units of dB.

$$T_E = \left(\frac{P}{\Sigma\Omega} + T_{Ph}^5 \right)^{1/5}, \quad (3.51)$$

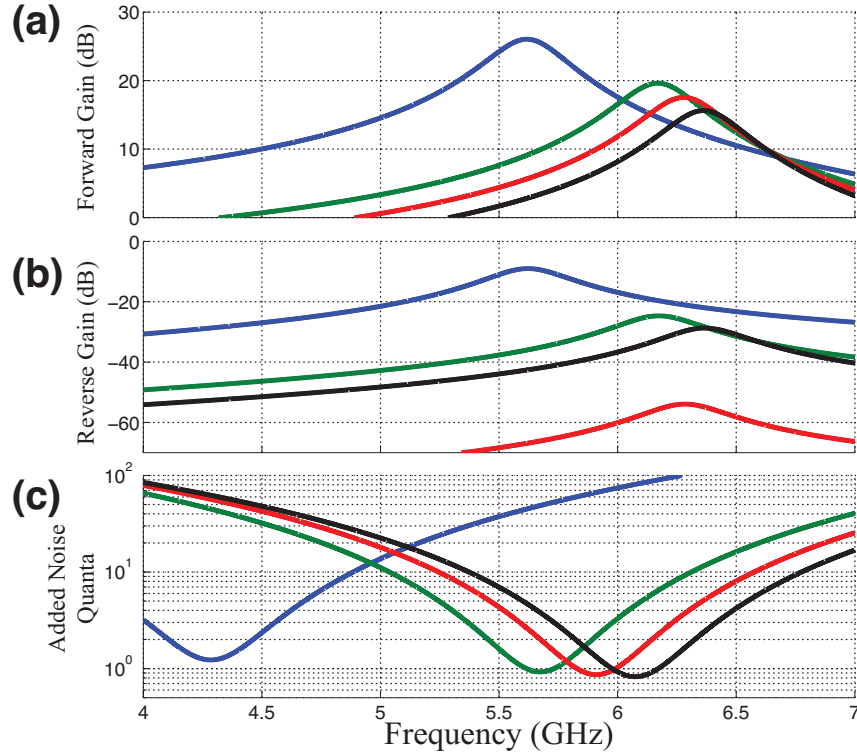


Figure 3.27: Forward-gain (a), reverse-gain (b), and added noise quanta (c) vs. frequency for the the SLUG amplifier with $I_b = 1.9 I_0$, $L_R = 40$ pH and $C_R = 10$ fF. The solutions were obtained with the “black box” model of Figure 3.25(b), at flux biases of $0.41 \Phi_0$ (blue), $0.39 \Phi_0$ (green), $0.3775 \Phi_0$ (red), and $0.3625 \Phi_0$ (black).

where P is the power deposited in the resistor, Σ is a material constant typically on the order of 10^9 W/(m³K⁵), Ω is the normal metal’s volume, and T_{Ph} is the phonon temperature. The elevated temperature of the shunt resistors translates directly to elevated noise temperature of the amplifier. For a device with fixed β_C , the power dissipation in the shunts scale as $1/R^3$. Hot electron effects will be particularly relevant for the microwave amplifiers discussed here, as optimal performance is achieved for a small SLUG inductance, corresponding to large critical currents and small shunt resistances.

A proven strategy to promote thermalization of the SLUG shunts at millikelvin temperatures is to fabricate large-volume normal metal cooling fins in metallic contact with

the resistor element. At low temperatures, the inelastic diffusion length is of order several mm [89]; the cooling fins thus allow hot electrons generated in a localized region of the shunt resistor to diffuse over a large volume and thermalize with cold electrons and phonons. Wellstood *et al.* [90] demonstrated a significant reduction in the electron temperature of dc SQUIDs incorporating $400 \times 400 \mu\text{m}^2$ CuAu cooling fins with thickness around $1 \mu\text{m}$, with measured electron temperatures under 40 mK. A similar approach has been used to suppress hot-electron effects and reduce the noise temperature of microstrip SQUID amplifiers operated in the radiofrequency regime [69]. It would be straightforward to integrate normal metal cooling fins with area of order 1 mm^2 in a standard microwave SLUG amplifier geometry without compromising the microwave integrity of the circuit. We anticipate that the addition of such cooling fins will make it possible to attain electron temperatures under 100 mK for the device parameters considered here, corresponding to operation far in the quantum regime for frequencies in the range from 5-10 GHz. We experimentally examine the electron temperature of the resistors of our SLUGs in Section 5.5.

Chapter 4

SLUG Fabrication

In this chapter, we discuss the niobium SLUG fabrication process. The SLUG based amplifier has gone through many design iterations since its conception. For the purpose of this thesis, we'll describe the state-of-the-art SLUG amplifier and justify our design choices throughout this chapter and the next by drawing on the lessons learned from earlier SLUG generations. In Section 4.1, we first populate our fabrication tool box with descriptions of the common thin-film deposition and processing tools used by our lab. We then build up the six layers of the SLUG body in Section 4.2. And in Section 4.3, we map the integrated-circuit layout to the lumped-element components of the ideal SLUG described in the circuit-schematic of Figure 3.2.

4.1 Fabrication Toolbox

4.1.1 Superconductor Deposition

The main superconductor deposition system in our lab is the Kurt-Lesker sputter deposition chamber, which houses both an aluminum and niobium target, along with

an ion mill gun for *in situ* surface cleaning. The wafer is first placed on an aluminum platen and clamped in place at the circumference of the wafer, where an indium O-ring is used to thermally sink the wafer. The sample is cleaned with dry nitrogen before being pumped down to the vacuum chamber base pressure (on the order of 10^{-8} Torr).

We first clean the sample surface using the ion mill. The ion mill removes material from the surface of the sample using a physical etch process. Argon ions are generated by a plasma and accelerated towards the sample, removing material on impact. Typically, we operate the mill with an argon pressure of 10^{-4} Torr, a bias voltage of 800 V, and a beam current of 20 mA, resulting in an etch rate of approximately 1 nm/s. We mill for 30 seconds to ensure that the surface is clean of unwanted oxide and other contaminants before depositing the niobium film. It should be noted that we mill before every metal deposition. For the ground layer milling is less critical, but when making metal-to-metal contact and Josephson junctions it is important to have an oxide-free surface. To guarantee that the unwanted oxide has been removed, we etch for longer than needed, which causes damage (etches and roughens the surface) to the underlying layer. This must be considered when designing the fabrication workflow.

After cleaning the surface, we are ready to deposit our metal layer. Sputter deposition relies on bombarding a target with highly energetic ions. The target is composed of the material (aluminum or niobium) to be deposited on the sample. The energetic ions (argon plasma magnetically confined about the target) physically eject the atoms of the target upon impact, which then coat the entire surface of the chamber, including the sample. For niobium deposition, the argon plasma (at pressure 3.9 mTorr) is created with a constant power regulated dc source. Niobium deposition occurs in two steps: with a shutter protecting the sample, the target is cleaned for two minutes with power

400 W. The power is then increased to 500 W and the shutter is opened for deposition, which occurs at a rate of 50 nm/min.

Special precautions must be made to reduce the stress of niobium films. Film stress depends on many factors: deposition power, argon pressure, sample distance to target, and the age of the target. The stress is calculated by measuring the curvature of a substrate with and without the niobium film. We periodically check the stress of our niobium films and make adjustments in argon pressure when needed.

4.1.2 Niobium Lithography and Etch

The niobium film is first cleaned with Acetone and IPA, and then spun dry on a wafer spinner. Next, a uniform film of Shipley Microposit SPR955 positive photoresist is spun onto the wafer at 3000 rpm for 30 s, followed by a 95° C pre-bake for 60 s. The film is exposed by the Nikon wafer stepper for approximately 240 ms. The sample is then post-baked at 110° C for 60 s and then agitated in the developer (MF-24A) for 60 s. For a positive photoresist, the developer removes the exposed photoresist, opening up a window for selective etching of the metal. While MF-24A does slowly etch aluminum, it does not affect niobium (or SiO_x). After developing the resist, the wafer is rinsed for 60 s and dried with nitrogen.

The exposed niobium is then etched in a reactive ion etch (RIE) chamber, where the material is removed by exposing it to a chemically reactive plasma. For niobium, this is done in an atmosphere of SF₆. An RIE etches anisotropically, which can lead to an etch profile that is difficult to cover with the subsequent thin film (resulting in poor “step coverage”). The gas flow, pressure, and power were optimized so that the photoresist etches at the same rate as the niobium, allowing us to transfer the resist profile to the niobium. After developing the resist, the wafer is placed on a 120° C

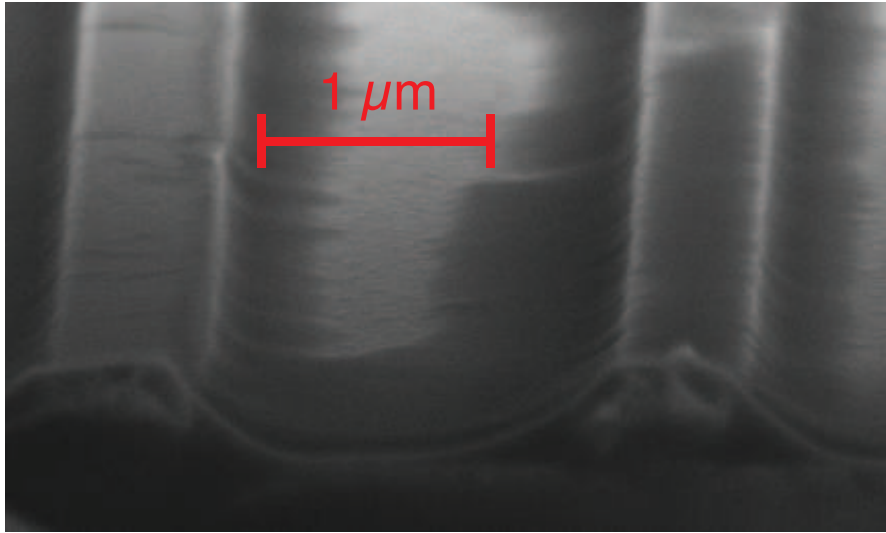


Figure 4.1: SEM image of niobium etch profile in RIE system with $SF_6=15$ sccm, $O_2=20$ sccm, pressure = 200 mT, power = 150 W, resulting in a 110 nm/min etch rate for both the Nb and resist.

hotplate for 3 minutes, which relaxes the resist and results in a sloped profile near the edge of the pattern. A scanning electron microscope (SEM) image of a Nb film etched with the optimized RIE recipe is shown in Figure 4.1, where we've used the following etch parameters: $SF_6=15$ sccm, $O_2=20$ sccm, pressure = 200mT, power = 150 W, giving a 110 nm/min etch rate for both Nb and resist. We typically over-etch the Nb by 50%, or 90 s for a 100 nm film. This SF_6 recipe will also etch Si and SiOx, albeit at a slower rate – the selectivity should be considered when designing the processing workflow.

The remaining resist must be stripped from the sample after the etch, which can be difficult to remove. The sample gets hot during the etch which causes the resist to strongly adhere to the surface. A 30 minute soak in Acetone and/or a hot bath of Microposit 1165 will strip the resist – repeat as needed. We can reliably produce 1 μm features with this process.

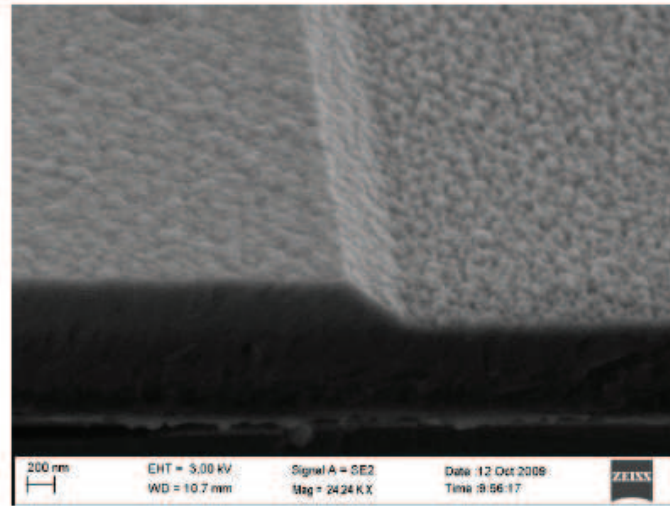


Figure 4.2: SEM image of SiOx etch profile in RIE system with $CHF_3=50$ sccm, $O_2=20$ sccm, pressure = 100 mT, power = 150 W, for a 30 nm/min etch rate for both SiOx and resist.

4.1.3 Silicon Oxide Deposition and Processing

We grow a plasma enhanced chemical vapor deposition (PECVD) silicon oxide (SiOx) film as the wiring dielectric for the SLUG amplifier. A PECVD tool works by bringing together an atmosphere of different gases that react, with the resultant product precipitating as a solid onto the sample. An rf plasma is generated to catalyze the reaction. Additionally, the sample is heated to promote surface mobility that reduces surface roughness and pinholes. We've measured a deposition rate of 36 nm/min for the following recipe in the Plasmatherm PT70: 900 sccm flow of N_2O ; 400 sccm flow of SiH_4 ; 900 mTorr chamber pressure; 25 W plasma power; substrate temperature of 250° C. It should be noted that the deposition rate and uniformity change with chamber cleanliness.

We process SiOx using the same lithography steps as discussed above in Section 4.1.2, except we treat the surface with HDMS between cleaning and spinning the resist to promote adhesion of the resist to the SiOx. We use the same RIE tool for etching SiOx

and niobium, but with CHF_3 as the active reactant. A recipe was also optimized for the SiOx etch to give a 45° profile to the edge, as shown in the SEM image of Figure 4.2, where we've used the following parameters for an etch rate of 30 nm/min: $\text{CHF}_3=50$ sccm; $\text{O}_2=20$ sccm; pressure = 100 mT; power = 150 W. Including over-etch, we typically etch a 200 nm film of SiOx for 9 min.

4.1.4 Junction Oxidization

We use a Nb/Al-AlOx-Al/Nb stack to realize our junctions [84, 85]. Junction oxidation takes place in the sputter deposition system so that the junction stack can be grown immediately after the native oxide is removed from the bottom electrode of the stack. A clean junction interface is critical for realizing a robust and repeatable high-critical current junction. For this reason, we first mill the sample for 45 seconds to ensure that the surface is clean of native oxide inside the junction via. Next, a thin layer of aluminum is grown (about 8 nm) at low power. A thin aluminum layer won't uniformly cover the niobium, while a thick aluminum layer runs the risk of shorting out the junction by covering the via-step. Next, oxygen is introduced into the chamber to form the tunnel barrier. Initially, the chamber is seeded with a 1 mTorr oxygen flow for two minutes. The gate valve is then closed, allowing the oxygen pressure to rise to the target value. The sample is held in the oxygen atmosphere for 10 minutes, after which the oxygen is pumped out. A 4 nm cap of aluminum is deposited, directly followed by 100 nm of niobium.

The junction oxidation is the most variable part of the SLUG fabrication process. The critical current of the junctions is set by the oxidation exposure, which is just the product of the oxygen partial pressure and the time. The critical current density (J_C , critical current per junction area) scales inversely with the square root of exposure [91], as experimentally verified in Figure 4.3. We use this data to determine our exposure, where

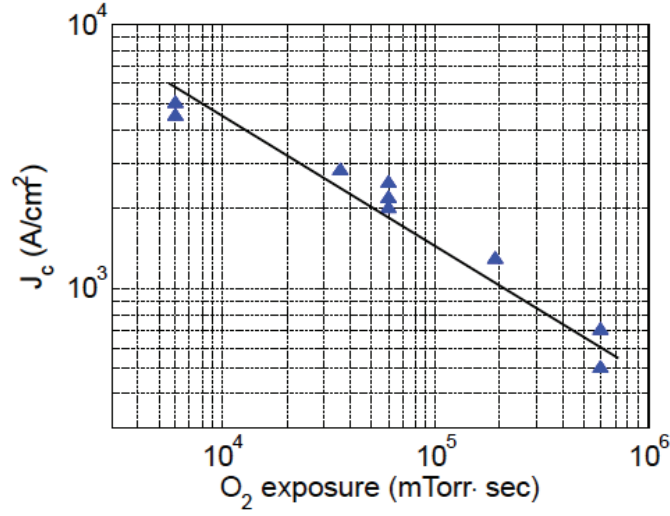


Figure 4.3: Experimentally determined critical current density for a Nb/Al-AlO_x-Al/Nb junction stack versus junction exposure.

we typically target between 1.5-3 kA/cm² for the SLUG process. We can also estimate the junction critical current by probing their room temperature resistance, using the following expression [62]:

$$I_0 = \frac{\pi\Delta}{2R_N}, \quad (4.1)$$

where R_N is the probed normal state resistance, and Δ is the superconducting gap energy, which for niobium $\Delta \approx 1.5$ meV.

4.1.5 Resistor Fabrication

The junction shunt resistors are formed from palladium Pd backed by a thin layer of titanium Ti used for adhesion. The metals are deposited with an electron beam physical vapor deposition system in which the target metal is bombarded by a beam of electrons

in a high vacuum (10^{-9} Torr for our system). The electron beam transfers its kinetic energy into thermal energy upon hitting the target metal, causing the metal to melt and evaporate into the vacuum. The evaporated metal coats everything within the line of sight of the molten metal. The deposition rate is controlled by adjusting the electron beam current and monitored using a quartz crystal. The resonance of the quartz crystal is modified by the amount of metal on the surface of the monitor. Tracking the change in crystal resonance provides realtime feedback for the deposition rate.

Our evaporation system has an *in situ* ion mill, allowing us to clean the native oxide off the surface of the sample before deposition. A mill time of 17 s has been calibrated for our resistor process. After milling, 3 nm of Ti is deposited as an adhesion layer, followed by a layer of Pd with a thickness determined by the desired resistance. The room temperature resistance of our thin film Pd scales inversely with thickness, where a 20 nm thick Pd film has a room temperature resistance of $12.5 \Omega/\square$ ¹. The RRR value of a metal is the room temperature resistance divided by the films resistance at 4 K². The RRR is about 2.5 for a 20 nm film, giving a Pd film with $5 \Omega/\square$ at low temperature.

Resistors are formed using a liftoff process. Before evaporating the metal, a negative image of the resistor is formed in the photoresist. The sample is then uniformly coated by the metal in the evaporation chamber. Next, the resist is removed and any metal on top of the resist lifts off with the resist. For lithography, we clean the wafer and prep the surface with HDMS. We then spin on AZ-5214 negative resist at 4000 rpm. The pre-bake is once again 60 s at 95° C, and then the wafer is exposed at a lower dose of 75 ms. Following exposure, the sample is post-baked for 60 s at 110° C. Next, the wafer

¹ Ω/\square is a standard expression for sheet resistance, where you count the number of squares in the film footprint between your measurement leads.

²The resistance of Pd films do not change much below 4 K. We use 4 K because these resistance measurements are quickly done in liquid helium.

is uniformly exposed with UV light on the contact aligner for 60 s. Finally, the wafer is developed for 45 s, rinsed, and dried. Unlike positive resist, AZ-5214 undercuts the step edge of the resist profile to promote liftoff. After lithography and metal deposition, the wafer is soaked in Acetone for around one hour, or until most of the undesired metal has lifted off. A light ultrasonic treatment is sometimes necessary to complete the liftoff process.

4.2 Niobium SLUG Recipe

The SLUG amplifier is realized through the deposition and processing of six thin film layers, all fabricated at the University of Wisconsin-Madison using standard photolithography techniques. Each layer of the isolated SLUG element is illustrated by the 6 panels of Figure 4.4.

4.2.1 Ground Electrode

The microwave integrity of the chip must be considered when laying out the SLUG amplifier. The ground electrode is wire bonded to a sample box held at the ground potential. At high frequencies, the return path of the current flowing from on chip components to ground will have a non-negligible inductance. The currents in a superconducting film flow at the edges of the lithographically defined features. To minimize ground-loops and parasitic chip resonances it is important to maintain the integrity of the ground electrode.

The ground electrode is a sputtered 100 nm thick layer of niobium grown directly on a commercially provided 3" oxidized silicon wafer, where the 150 nm thick thermal oxide electrically isolates the on chip components. The layer is lithographically defined and etched for 90 s. When designing the SLUG, we go to great lengths to minimize

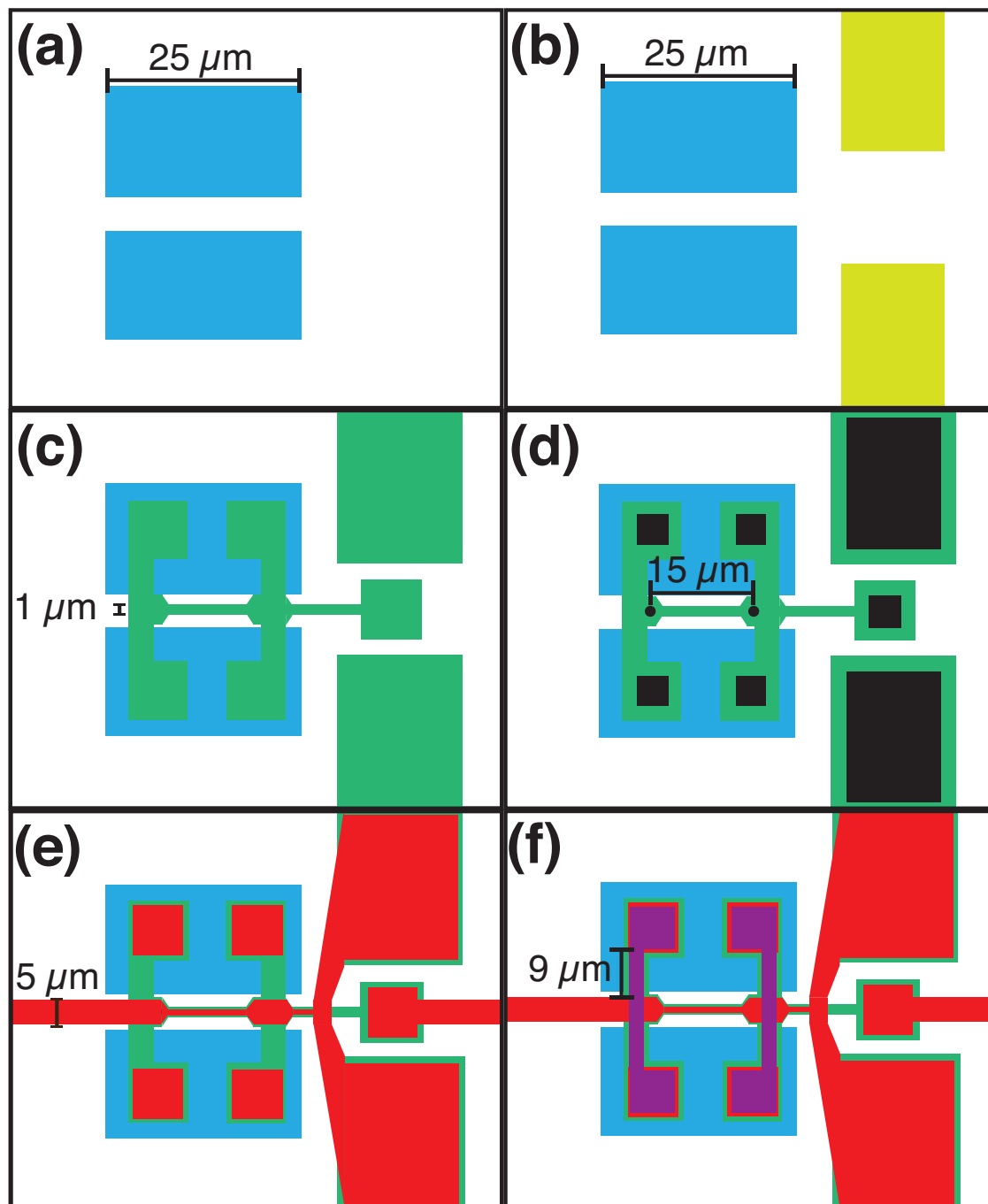


Figure 4.4: The ground layer (blue, negative) (a), bottom-to-ground via (yellow, negative) (b), bottom electrode (green, positive) (c), top-to-bottom via and junctions (black, negative) (d), top electrode (red, positive), and resistors (purple, positive) (e). Negative (positive) means the image is the absence (presence) of the thin film.

parasitics that aren't included in the ideal lumped element SLUG model. For example, the cavities in the ground electrode [Figure 4.4(a)] reduce the capacitance between ground and the higher-level metalizations. The strip of ground between the two cavities screen the inductive branches of the SLUG loop, which is necessary for efficient coupling between the input signal and the SLUG loop.

4.2.2 First Dielectric Layer

Next, a 200 nm of PECVD SiOx is deposited. The dielectric thickness will be reduced to approximately 170 nm during the subsequent ion mill step before depositing the bottom electrode. Large vias [Figure 4.4(b)] that connect the bottom electrode to ground are lithographically defined and etched for 9 mins.

4.2.3 Bottom Electrode

The bottom electrode [Figure 4.4(c)] is a 100 nm thick layer of sputtered niobium that makes up the L inductive branch of the SLUG loop. Notice that the SLUG bias current I_b and voltage out lead are defined in the the bottom electrode, extending to the right of the SLUG body.

4.2.4 Second Dielectric Layer

A second 200 nm layer of PECVD SiOx is deposited and etched with the via pattern seen in Figure 4.4(d). The vias define both the explicit $2 \mu\text{m}^2$ junctions (circular vias separated by $15 \mu\text{m}$ in the Figure) and the wiring vias connecting the top to the bottom electrode. Each via defined in the second dielectric layer etch is a Josephson junction. A parasitic junction will behave like a via so long as the junction critical current isn't

exceeded during normal amplifier operation ³. Parasitic junctions have a larger area than the explicit junctions to ensure that the “vias” don’t switch to their voltage state. This comes at the price of a larger SLUG footprint and, in consequence, more parasitic capacitance. These parasitics could be avoided with additional processing steps.

4.2.5 Junction Growth and Top Electrode

The sample is then milled for 45 s to ensure that a clean interface exists before growing the junctions. We follow the junction growth procedure found in Section 4.1.4. The 100 nm niobium top electrode defines the $2L$ inductive branch of the SLUG, which is a $1\ \mu\text{m}$ wide trace in Figure 4.4. Notice that the SLUG body gets wider to accommodate the junctions, where we like to leave $1\ \mu\text{m}$ clearance of metal surrounding vias to accommodate possible lithography imperfections (misalignment, over etch, over exposure, etc.). The input signal comes in from the $5\ \mu\text{m}$ trace to the left of the SLUG body and is grounded through the SLUG body at the right of the SLUG. The output voltage (and input current bias) is extracted from the top electrode through a via to the bottom electrode. The top electrode is etched for 90 s in the RIE chamber. An additional mill step and wet etch in Transene removes the thin layer of aluminum grown to cap the junction.

4.2.6 Resistor

Two parallel resistors shunt each junction, where each resistor is comprised of three $3\ \mu\text{m} \times 3\ \mu\text{m}$ squares in series. We use two resistors per junction to maximize the volume-per-watt of dissipated power in the shunt resistors, reducing the electron temperature and, in consequence, the added noise. One must also consider the parasitic inductance and

³This isn’t totally correct. In the superconducting state the junction still behaves like a nonlinear inductor which could in principle affect the behavior of the SLUG. According to Equation 2.6, $L_J(0)$ scales inversely with I_0 of the junction.

capacitance of the resistor traces: removing the middle-electrode underneath the resistor will reduce the parasitic capacitance, but at the price of a larger series inductance due to the absence of screening. Inductively shunted Josephson junctions are well known to exhibit chaotic dynamics [92, 93, 94], leading to rich structure in the I-V curves and complicated noise behavior. We chose to minimize the inductance by keeping the middle electrode below the resistor. The capacitance between the two traces is approximately 5 fF, which is significantly less than the self-capacitance of the junctions.

4.3 Design Choices

The SLUG amplifier described in Chapter 3 has a $\beta_L = 1$, and a $\beta_C = 0.8$, with SLUG loop inductance $L = 10$ pH and junction capacitance $C = 50$ fF. This corresponds to a junction critical current of $I_0 = 100$ μA – a critical current density of 10 kA/cm² for a 1 μm^2 junction area with a reasonable 50 fF/ μm^2 . A SLUG with these parameters are within reach of our cleanroom facilities, but for this thesis we took a conservative approach when designing the SLUG amplifier.

The junction area of the fabricated SLUG shown in Figure 4.5 has a designed 2 μm^2 area, but, with overetch, the junction area is closer to 2.2 μm^2 for a self capacitance of $C = 120$ fF. While we’re currently exploring 1 μm^2 junction technology, it can be difficult to get a consistent exposure across the 3” wafer for 1 μm^2 vias. Recipes for high quality Josephson junctions with a large critical current density have been developed by the superconducting community, but junctions with current densities approaching 10 kA/cm² rely on a Nb-AlOx-Nb trilayer process [95, 96, 97, 98] that we are still developing⁴.

⁴For a trilayer junction we need a low-temperature dielectric process for depositing an insulator after the junction has been defined—our standard 250° C SiOx PECVD process would damage the junction. An rf-sputtered SiOx would be a possible alternative. Additionally, we need to make contact to the top of the junction after depositing the dielectric. This would involve either an anodization and etch (see

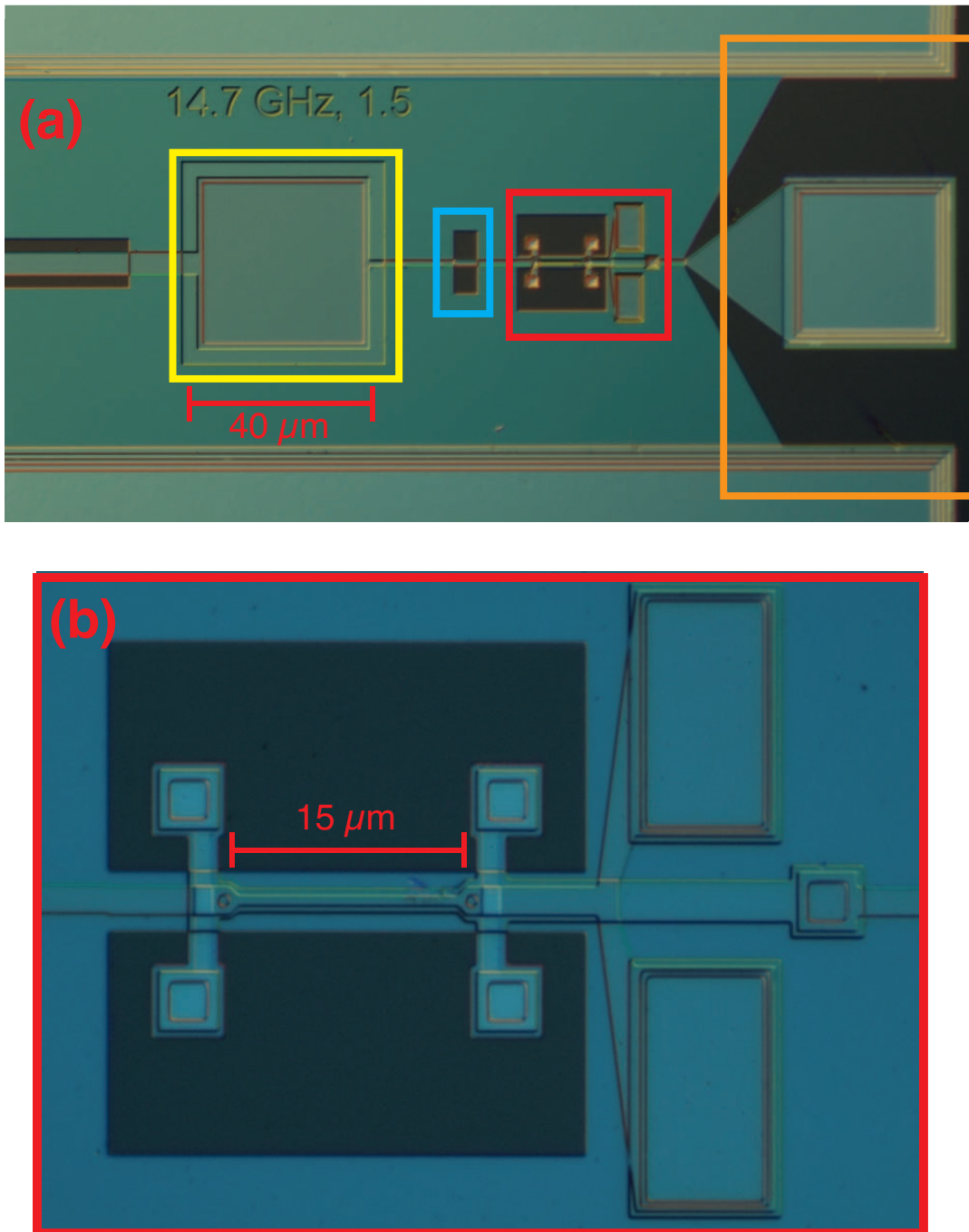


Figure 4.5: (a) Layout of the SLUG amplifier, with the lumped element input matching network comprised of a parallel plate capacitor to ground (yellow box), and the in-series coplanar inductor (blue box). The orange box highlights the output bonding pad. The SLUG (red box) is blown up in (b).

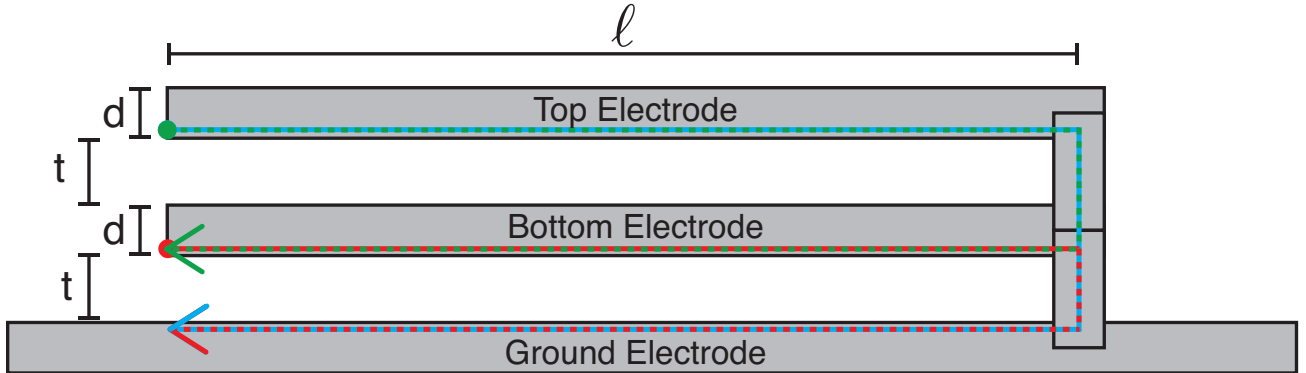


Figure 4.6: Simplified SLUG stack-up to illustrate the inductor paths of the SLUG loop. The input inductance is formed by the top electrode with the inductive path highlighted in blue. The second branch inductance is formed by the bottom electrode with the inductive path highlighted in red. The SLUG loop is highlighted in green.

As described in Section 4.1.4, we can reliably make $1.5\text{-}3\text{ kA/cm}^2$ junctions, or junctions with critical currents of $30 - 60\ \mu\text{A}$ for our $2\ \mu\text{m}^2$ via process.

A simple cartoon stack-up of the SLUG body is shown in Figure 4.6 to illustrate the inductive elements comprising the SLUG body. The SLUG input inductor arm L_{TE} is the loop defined by the top electrode, where the return currents flow through the ground, while the other arm of the SLUG inductive loop L_{BE} is formed by the bottom electrode and the ground plane. In general, the total inductance L_T has a geometric L_G and a kinetic contribution L_K , where the geometric inductance of a microstrip is approximated by:

$$L_G = \mu_0 t \ell / w, \quad (4.2)$$

HYPRES design guide) or planarization using a chemical mechanical polishing (CMP) tool (see MIT Lincoln Lab design guide).

where $\mu_0 = 4\pi \times 10^{-7}$ H/m is the vacuum permeability constant, w is the width of the microstrip, ℓ is the length of the inductor, and t is the distance between the microstrip and the return currents in the ground plane. For Equation 4.2, the distance between the trace and ground is the space where a magnetic flux can exist, unimpeded. Following Mazin *et al.* [99], we can include the kinetic inductance with the following expression:

$$L_T = L_G \left[1 + \frac{2\lambda}{t} \coth(d/\lambda) \right], \quad (4.3)$$

where λ is the thin-film London penetration depth, which we assume to be 100 nm for our niobium films. The three metal traces are equally spaced by dielectric distance $t = 160$ nm, as in Figure 4.6, with film thickness of $d = 100$ nm. We compare branch inductances calculated with Equation 4.3 to the inductances calculated using the FastHenry simulation package[100] in Table 4.1.

Table 4.1: SLUG Inductance

w	ℓ	L_{top}^{est}	L_{bottom}^{est}	L_{top}^{FH}	L_{bottom}^{FH}	$M_{t,b}^{FH}$	L^{FH}	M^{FH}
1 μm	20 μm	17.2 pH	10.6 pH	19.2 pH	7.3 pH	3.7 pH	9.1 pH	5.2 pH
2 μm	40 μm	17.2 pH	10.6 pH	18.3 pH	8.3 pH	5.0 pH	9.5 pH	6.1 pH

The lumped element input matching network (Figure 4.5) is just a parallel plate capacitor to ground and an in-series coplanar inductor. We design the inductor to be much shorter than the relevant wavelengths, and with low capacitance. For a transmission line, the inductance per unit length L_ℓ and capacitance per unit length C_ℓ are related to the phase velocity v_{ph} and impedance Z_0 by:

$$L_\ell = Z_0/v_{ph}, \quad (4.4)$$

$$C_\ell = 1/Z_0v_{ph}, \quad (4.5)$$

where v_{ph} and Z_0 are set by the materials and geometry of the transmission line [101]. By picking a large Z_0 , we reduce the parasitic capacitance of the lumped element capacitor, which in turn pushes the resonance of the inductor to higher frequencies. This simple analysis does not take kinetic inductance or the extra inductance coming from the edges of the finite-length inductor into account.

The parameters of the non-ideal SLUG are then plugged into the numerical toolbox assembled in Chapter 3 to calculate the scattering parameters of the amplifier. Figure 4.7 plots the transfer function [(a),(d)], the forward-gain [(b),(e)], and reverse-gain [(c),(f)] for a SLUG with $\beta_L = 0.3$, $\beta_C = 0.5$, $L = M = 10$ pH, $C = 120$ fF, and a matching network with $Z_0 = 2 \Omega$ and $f_0 = 8$ GHz. The lower β_C was chosen to ensure that the SLUG is non-hysteretic in the presence of possible parasitic capacitance channels. To capture the effect of the input circuit on the SLUG dynamics, the equations of motion for the full circuit were solved [Figure 3.25(a)]. From the simulations, the fabricated SLUG amplifier will have forward-gain of about 15 dB with a bandwidth approaching 200 MHz. The reduced critical current and β_C results in an amplifier with lower gain, where the transfer function is proportional to I_0R [Equation 3.12].

Shapiro step-like structure from the LC resonance of the input circuit is present at bias points close to the supercurrent branch of the $V-\Phi$ curve in Figure 4.7(d). Two resonant plateaus occur at voltages corresponding to Josephson frequencies of about 6.5 GHz and 13 GHz. The step at 6.5 GHz lines up with the input-circuit resonance (8

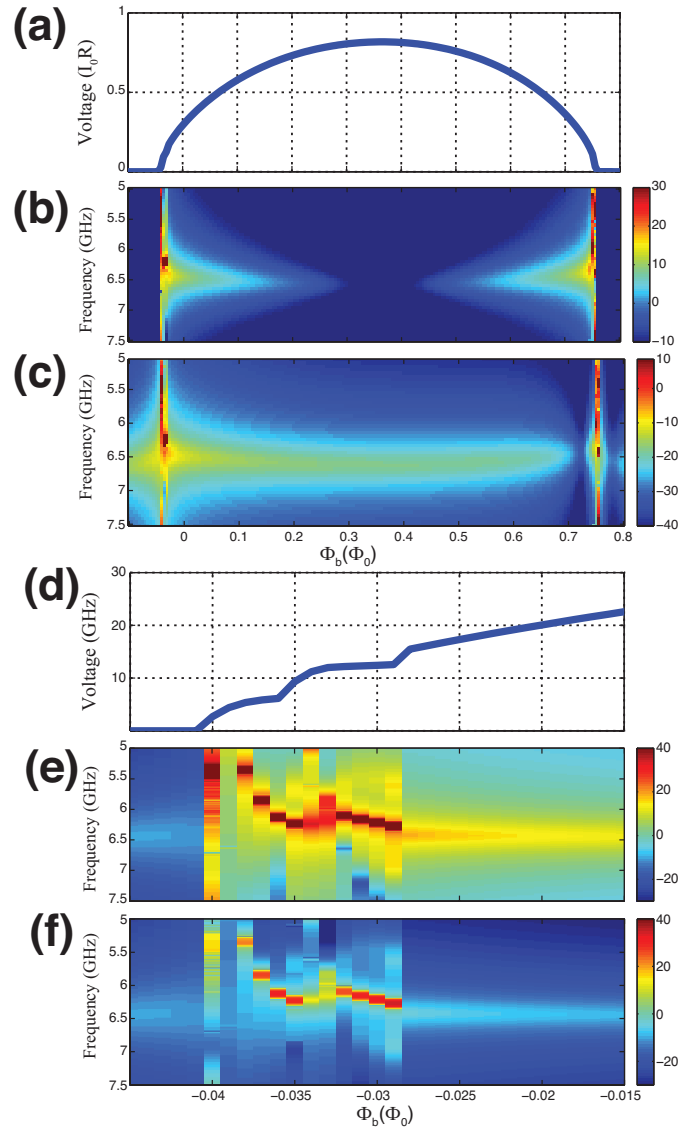


Figure 4.7: The V - Φ curve (a), forward-gain (b), and reverse-gain (c) for the full-circuit model of Figure 3.25(a). The V - Φ curve (d), forward-gain (e), and reverse-gain (f) examined close to the supercurrent branch. The solutions were solved for $I_b = 1.9 I_0$, $L_R = 40$ pH and $C_R = 10$ pF. The gain plots are solved as a function of flux bias and signal frequency, where the gain is in units of dB.

GHz) reduced by the input inductance of the SLUG (20 pH). The origins of the 13 GHz step is a feature still under investigation. Notice that the amplifier has high forward and reverse-gain with a very low bandwidth at bias points close to the resonant steps; the dynamic range and noise performance will also suffer from this non-linear behavior of the SLUG.

Chapter 5

SLUG Measurements

In this chapter we discuss measurements of the SLUG amplifier. We've fabricated and measured SLUG amplifiers on over 40 wafers in the last three years. Instead of fleshing out the evolution of the every third antenna and second tail, we concentrate on a few choice amplifiers that illustrate the steps taken to measure the dc characteristics [Section 5.2], gain [Section 5.3], noise performance [Section 5.4] of a state-of-the-art SLUG amplifier. We conclude with a discussion about the electron temperature of the shunt resistors [Section 5.5].

5.1 Experimental Setup

5.1.1 Cryogenic Measurement Systems

Most SLUGs measured in this thesis are cooled down well below the transition temperature of the niobium thin films comprising the SLUG ($T_c = 9.3$ K). The dc characteristics (I-V and V- Φ curves) can be quickly measured at 4.2 K using a dip probe in a liquid helium dewar. Dip probe measurements are used to screen devices before cooling

them down for careful characterization. Dewar measurements are more susceptible to environmental noise (magnetic and rf), and the relatively hot measurement suppresses the junction critical current and washes out interesting resonant structure that may be present at low temperatures.

The adiabatic demagnetization refrigerator (ADR) is a single shot cooling system that can keep the measured sample below 100 mK for a few hours. The ADR is cooled down to 4 K using a pulse tube cooler, while adiabatic demagnetization of a salt pill is required to get the system down to the base temperature. The 24 hour turn around time of the ADR makes this system attractive for quick measurements of the SLUG performance; however, the small cold stage makes it difficult to do an *in situ* calibration of the gain, and the limited hold time at the base temperature makes full characterization of the noise and scattering parameters cumbersome.

The cryogenic workhorse of this thesis is the dilution refrigerator (DR), which has a base temperature of 40 mK¹ and can stay cold indefinitely. The refrigerator consists of a nested set of shields that get progressively colder, all contained by a vacuum jacket. The outer two shields are thermally anchored to a tank of liquid nitrogen and liquid helium, which boil off at 77 K and 4 K, respectively. A thin capillary slowly feeds liquid He into a small volume called the “1K pot.” This small volume is pumped by a vacuum pump, lowering the boiling point of the liquid He to 1.5 K. A mixture of He-3 and He-4 are circulated to reach the base temperature, where the cooling power is a result of the entropy increase when mixing He-3 into He-4. The dilution unit consists of a still that selectively removes He-3 from the mixture by evaporation, and a mixing chamber where the He-3 is allowed to return into the mixture at the base temperature of the DR.

¹The same DR historically cools to 25 mK, but with a lighter wiring heat load than the experiments described in this thesis.

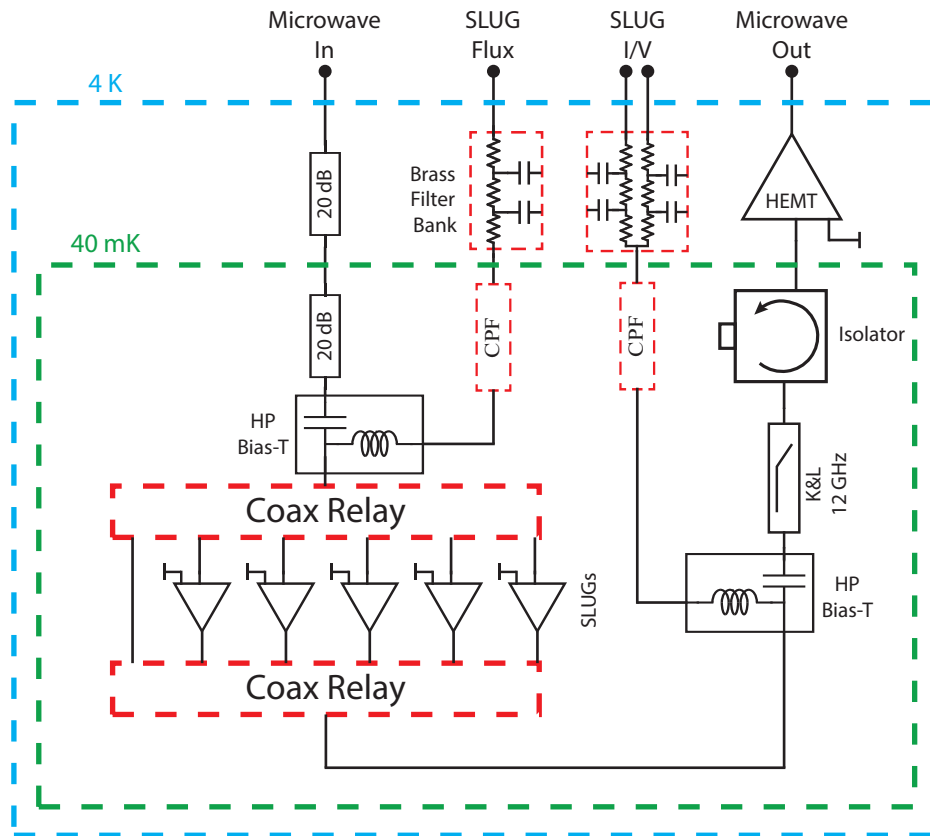


Figure 5.1: Wiring diagram of DR when measuring the SLUG amplifier.

The mixture must take thermal energy from the environment in order to conserve the entropy of the system. A coil of heat exchangers efficiently cool the He-3 as it returns to the mixing chamber using the evaporated He-3 headed to the still. Our DR has a large sample stage (7" radius) which allows us to run the DR with multiple experiments on the cold stage. A set of cryogenic coax-relays promote modularity and functionality.

5.1.2 DR SLUG Wiring

While we present data taken in both the ADR and the DR, we will only discuss the details of a typical rf measurement in the DR. The wiring diagram for SLUG amplifier measurements in the DR is shown in Figure 5.1. The microwave lines between the room

temperature electrical feed-through and the 4K plate are semirigid CuNi coax lines with a silver clad inner conductor to reduce electrical loss. Microwave lines below the 4K stage are plain CuNi, as the silver plating places too large of a heat load on the colder stages. There are 20 dB attenuators on the input microwave lines, heat sunk at both 4K and at base temperature. The attenuation is necessary to prevent the thermal noise generated up stream of the mixing plate from reaching the measured sample.

The SLUG amplifier requires a quasistatic flux and current bias. Lossy shielded brass cables connect the room temperature port to a bank of brass RC low pass filters heat sunk at 4 K. The brass filters are formed from a channel drilled into a brass block, with the channel just large enough to accommodate the body of an axial resistor. Three axial resistors are soldered mouth-to-tail, acting as a distributed resistance that is capacitively coupled to the grounded brass block. The DR is setup for a standard 3-wire measurement of the SLUG dc characteristics. Two channels are tied together downstream from the resistors inside the brass filter bank. The two wires allow us to simultaneously current bias the SLUG while reading out the heavily filtered average voltage at the output. This arrangement is sensitive to both the desired SLUG dynamic resistance and the unknown inline loss between 4K and the output of the SLUG. The explicit resistance in the filter channel (1-10 k Ω) is much larger than the dynamic resistance of the SLUG, allowing us to treat our voltage bias as a current source. A superconducting niobium coax line electrically connects the 4K filter bank to the mixing plate. We use a superconductor to minimize the power being dissipated on the cold stages, while also minimizing the thermal link between plates. The dc signal is filtered again by a bank of copper powder filters (CPF) that attenuate high frequency fields from eddy current losses in an inductively coupled powder and does not require a series resistance.

The dc flux bias and input microwave lines are tied together with a commercial HP-11612A bias-T, which combines a low-frequency and high-frequency signal with little insertion loss. The combined input signal goes into the common port of a modified Radiall 6-port switch. The switching is done by six solenoids that move pistons with a magnetic field to close or open the connection. By choosing the polarity of the applied current, we can either open or close any switch. The relay has been modified to operate at the base temperature of the DR, where a switching sequence only raises the temperature of the mix plate by approximately 5 mK. A superconducting NbTi wiring harness goes from 4 K to base temperature, with a manganin harness making the rest of the journey to room temperature. A custom pulsed voltage supply controls the switch. A series of two switches allow us to characterize five SLUGs on one cool down, with a calibration line on the sixth channel. The calibration line is a low loss flexible copper coax line. On the common side of the output coax relay is another bias-T which ties the I/V line into the amplified output signal. We want to minimize loss between the SLUG amplifier and the HEMT at 4 K in order to minimize the system noise temperature of our measurement chain [Section 1.7.3], but we also need to reject thermal noise generated at the warmer stages along with any backaction from the HEMT. An isolator is a non-reciprocal device that allows signal to flow in one direction with little insertion loss, while attenuating any signal from the output. Isolators rely on a strong magnet for their reciprocity. The isolators at the mixing plate are double shielded with high permeability Cryoperm, but we still make an effort to keep the isolators as far as possible from the superconducting samples. A magnetic field will suppress junction critical currents and trap vortices in the thin film superconductors of our samples. A niobium coax line connects the microwave signal at the output to the input of a broadband JPL HEMT amplifier with noise temperature on the order of 3K and gain approaching 30 dB.

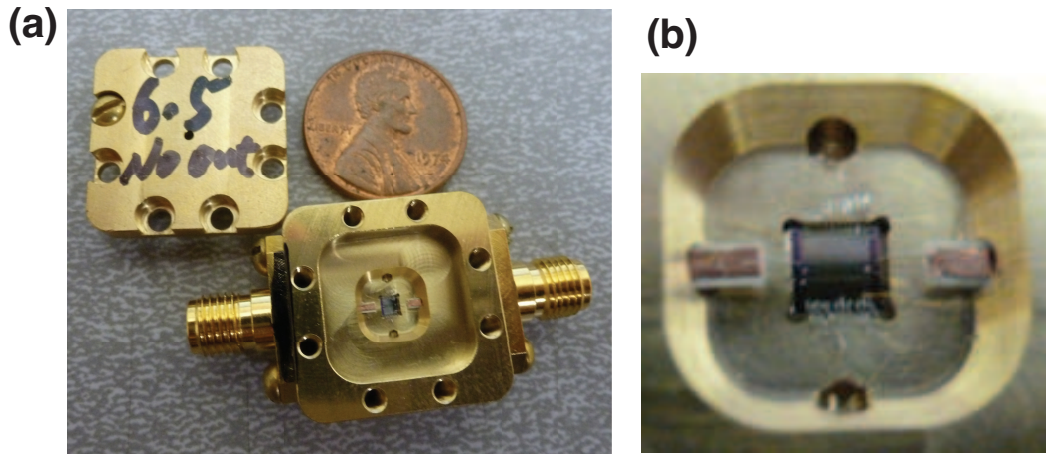


Figure 5.2: (a) Brass box used to house the 2 mm SLUG amplifier. (b) 2 mm SLUG chip bonded to PCB diving boards and box.

5.1.3 SLUG Packaging

The SLUG amplifier die is housed in the monolithic brass box pictured in Figure 5.2(a), with a closeup of the mounted die shown in Figure 5.2(b). The box cavity will resonant in the 10s of GHz, and this box mode will couple to the high frequency Josephson oscillations generated by the SLUG operated in its voltage state. For this reason, we choose a normal metal brass box to dampen out the resonant modes of the cavity. The ground plane of the chip is densely bonded to the box with both aluminum and gold wire bonds, where the gold bonds heat-sink the die to the box. Densely packed short wire bonds robustly ground the chip by minimizing the roughly 1 nH/mm inductance of the bond. We did not pay close attention to the bond spacing, which can introduce crosstalk between the output and input ports of the chip as discussed by Wenner *et al.* [102]. The microwave feed lines are formed with a narrow strip of PCB material soldered to an SMA connector on the outside of the box. The feed lines were designed to be nicely matched to 50 Ω . The PCB “diving board” extends to the chip, with wire bonds making the final electrical connection.

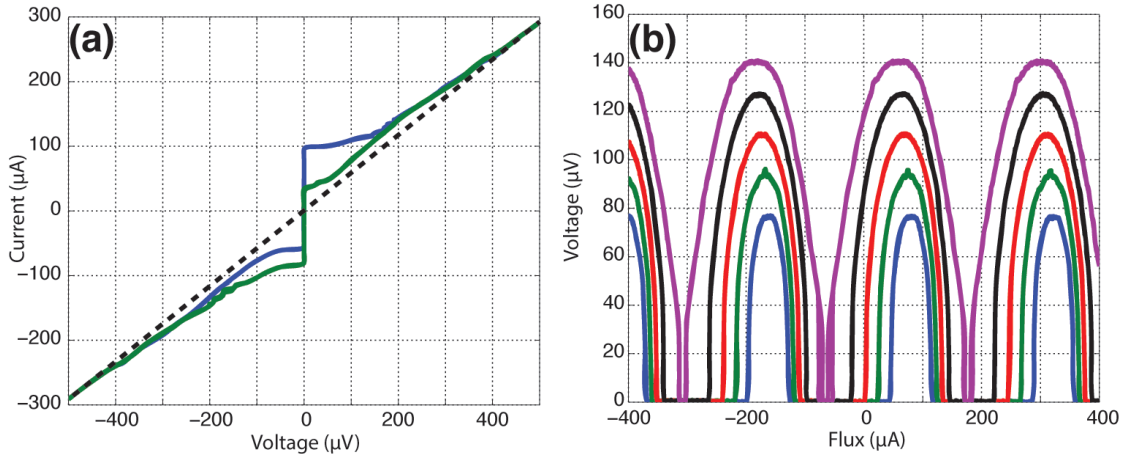


Figure 5.3: I-V (a) and V- Φ (b) characteristics of SLUGA measured at 40 mK in a DR. The I-V curves are taken at flux biases that minimize and maximize the positive supercurrent. The V- Φ curves are taken at a handful of current biases: 60 μA (blue), 70 μA (green), 80 μA (red), 90 μA (black), and 100 μA (purple).

5.2 dc Characteristics

A SLUG amplifier (designated SLUGA) was cooled down in the DR to 40 mK for characterization. SLUGA is a $3 \times 3 \text{ mm}^2$ chip that houses a $2 \mu\text{m}$ wide and $40 \mu\text{m}$ long SLUG body; the amplifier has an input LC matching network with a designed characteristic impedance $Z_0 = 2 \Omega$ and bare resonance $f_0 = 11.5 \text{ GHz}$. The measured I-V and V- Φ characteristics of the SLUG are shown in Figure 5.3. The two I-V traces in Figure 5.3(a) represent the maximum and minimum supercurrent when modulated by the dc flux bias. The current source is a Wavetek function generator, and the measured voltage is amplified and filtered at room temperature by the $\times 1000$ PreAmp card. The voltage was averaged on the order of 50 times over one period of the Wavetek. The maximized supercurrent is $2I_0$, for a measured $I_0 = 50 \mu\text{A}$; the slope of the voltage state that linearly extrapolates to the origin (dashed line) is the total resistance that shunts the SLUG ($2R$), giving a single junction shunt resistance of $R = 3.3 \Omega$. The V- Φ curves

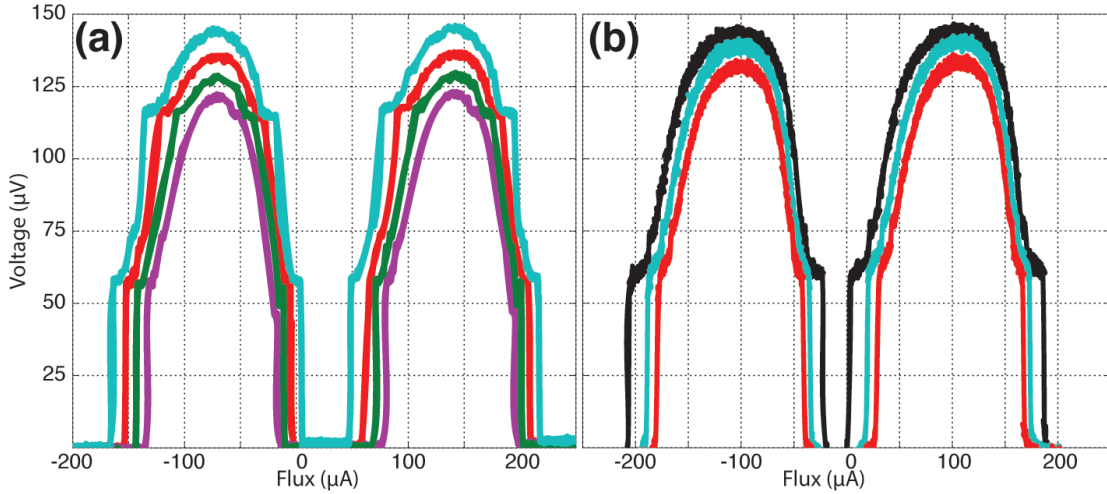


Figure 5.4: V - Φ curves of a $6 \times 6 \text{ mm}^2$ die SLUG amplifier when placed in an aluminum (a) and a brass (b) sample box for different current biases. This measurement occurred at 200 mK in the ADR.

of Figure 5.3(b) are each taken at different static current biases, where the supercurrent branch vanishes at $I_b = 2I_0$. We extract the mutual inductance M between the SLUG input and the SLUG loop from the Φ_0 periodicity of the V - Φ curve, giving $M = 8.5 \text{ pH}$. By assuming that $L = M$ and that the junction self capacitance is 120 fF, we calculate a $\beta_L = 0.4$ and $\beta_C = 0.2$.

The SLUG amplifier couples to resonant modes on the chip and in the sample box. These modes are defined by the LC matching network [Figure 4.7], the box cavity, and the geometry that defines the integrated circuit. We take two approaches to reduce their impact on device performance: we push the parasitic modes above the relevant Josephson frequencies, and we make an effort to decouple and dampen the modes that we can't remove. As plotted in Figure 5.4, mounting the SLUG in a brass box dampens the cavity mode of the sample box; note that the sharp feature at $120 \mu\text{V}$ [Figure 5.4(a)] vanishes when the die is placed in a brass box [Figure 5.4(b)]. A brass box will not shield the SLUG from ambient magnetic fields present in the cryostat; however, reduced

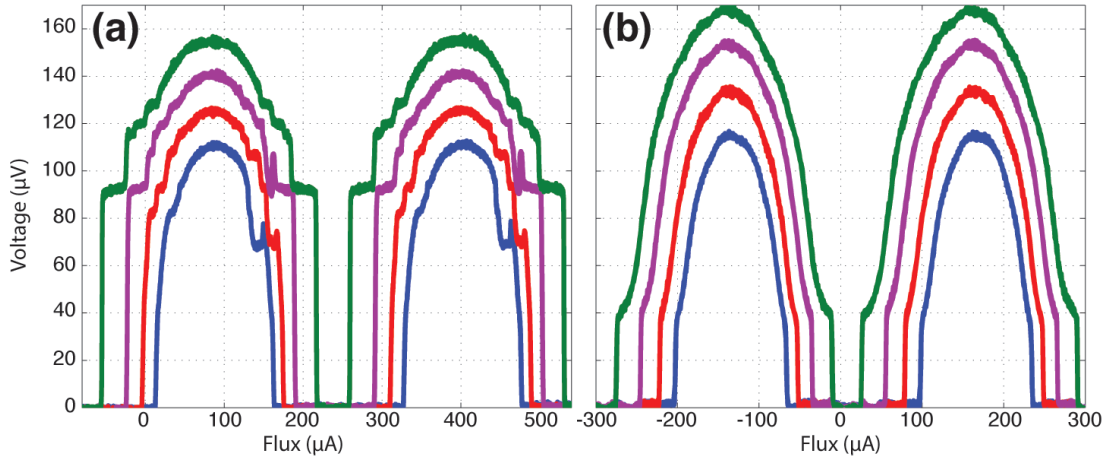


Figure 5.5: V - Φ curves of two similar SLUG amplifiers without **(a)** and with **(b)** an LC low pass filter at the output. The output filter has a nominal $Z_0 = 10 \Omega$ and $f_0 = 8$ GHz. The curves are plotted for different current biases. For **(a)**, I_b is $30 \mu\text{A}$ (blue), $34 \mu\text{A}$ (red), $38 \mu\text{A}$ (purple), and $42 \mu\text{A}$ (green). For **(b)**, I_b is $30 \mu\text{A}$ (blue), $35 \mu\text{A}$ (red), $40 \mu\text{A}$ (purple), and $44 \mu\text{A}$ (green). This measurement occurred at 200 mK in the ADR.

shielding should not affect the performance of the amplifier because of the small SLUG junction area and superconducting loop. Additionally, we've shrunk the die size from the original $6 \times 6 \text{ mm}^2$ design to a compact $3 \times 3 \text{ mm}^2$ and $2 \times 2 \text{ mm}^2$ chip size, which pushes the chip modes to larger frequencies. There is also some evidence in simulations that the coplanar launchers [see orange box in Figure 4.6(a)] resonate, so we've reduced their footprint to an area that accommodates two wire bonds. While these efforts have improved the performance of the SLUG, the amplifier can't reach its full potential until the resonant structure is cleaned up further.

Placing a low pass filter at the output of the SLUG element attenuates the Josephson oscillations radiating from the SLUG into the chip. The V - Φ curves of two SLUGs from the same wafer are plotted in Figure 5.5, each with a measured critical current $I_0 = 45 \mu\text{A}$, shunt resistance $R = 7.5 \Omega$, and mutual inductance $M = 6.8 \text{ pH}$. The SLUG of Figure 5.5(b) has an integrated LC filter at its output with a designed $Z_0 = 10 \Omega$ and

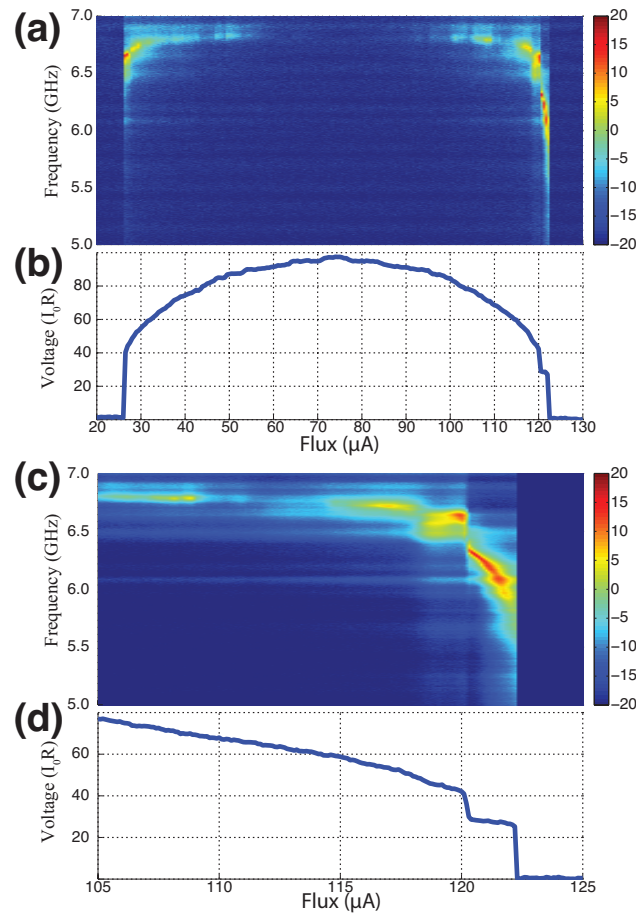


Figure 5.6: Frequency dependent gain (in dB) [(a) & (c)], and voltage [(b) & (d)] as a function of flux bias for SLUGA with a current bias $I_b = 70 \mu\text{A}$. Plots (c) and (d) focused on one region of the flux bias parameter space.

$f_0 = 8 \text{ GHz}$. It is clear from Figures 5.5(a) and (b) that a filter at the output of the SLUG dramatically cleans up the resonant structure present in the V - Φ curves. While we have not successfully operated a dual matching network device as an amplifier, we are confident that an experimental exploration of matching network parameters will yield an amplifier that performs as well as the devices simulated in Chapter 3.

5.3 Gain Measurements

The scattering parameters of the cryogenic amplifier chain found in Figure 5.1 are measured with a vector network analyzer (VNA). VNAs are commonly used to characterize the reflection and transmission coefficients of a multiple port network. In the context of this thesis, the VNA simply excites the input port and measures the transmitted power at its output port, commonly known as a measurement of $|S_{21}|^2$. We bias the SLUG using two channels of the battery powered FastBias card, which is a low-noise dc voltage source that we communicate with via a fiber-optic link.

We first calibrate the insertion loss of the amplification chain without the SLUG using the calibration line between the two relays. We then perform an automated scan over flux bias and frequency for different current biases. The output power of the VNA is chosen so that the SLUG is not saturated². We average the measured $|S_{21}|^2$ approximately 20 times. The dc voltage at the SLUG output is also monitored. The data shown Figure 5.6 was taken for SLUGA [described in Section 5.2], which has a designed input matching network of $Z_0 = 2 \Omega$ and $f_0 = 11.5$ GHz. The two-dimensional scan plotted in Figure 5.6 illustrates that the gain [(a) & (c)] tracks with the shape of the transfer function [(b) & (d)]. In Figures 5.6(c) and (d), we focus on the performance of the SLUG biased close to a resonant mode. Notice that the gain is large with a narrow bandwidth at the voltage plateau, qualitatively similar to the simulations shown in Figure 4.7. At SLUG voltages greater than $40 \mu\text{V}$, the transfer function smooths out, but this comes at the price of reduced gain.

Also, note that the gain and measured voltage is asymmetric in flux bias, shown in Figures 5.6(a) and (b). The asymmetry is due to hysteretic steps near the supercurrent

²The high gain ($G \approx 30$ dB) bias points at the plateau have a comparatively small saturation power. We choose the VNA power to avoid saturating the amplifier at bias points away from the plateau.

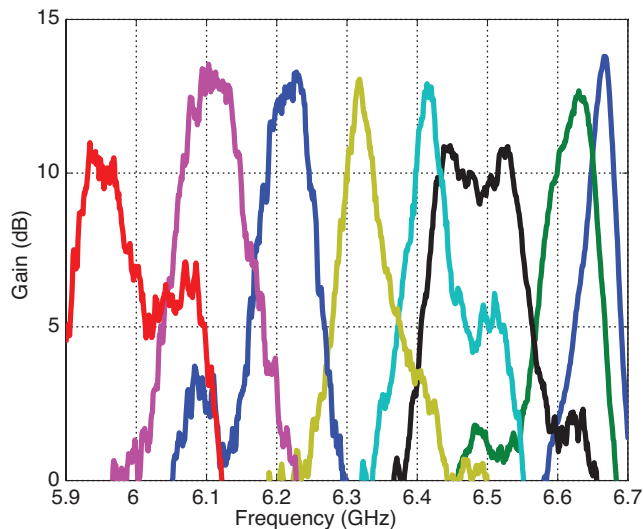


Figure 5.7: Frequency dependent gain for SLUGA at an assortment of current and flux biases.

branch, where the gain and voltage appear asymmetric because we only sweep the flux bias in the positive direction. Numerical studies [103] show that a resonator tightly coupled to a SQUID loop is responsible for hysteretic steps in the $V-\Phi$ curve. The $V-\Phi$ curve with $I_b = 100 \mu\text{A}$ plotted in Figure 5.3(b) appears hysteretic near the step edge of the transfer function; however, the quick characterization of the transfer function with the relatively noisy Wavetek function generator washes out the hysteresis present in the $V-\Phi$ curves captured at a lower current bias. This hysteresis is observed at low I_b when biasing the SLUG with the low-noise FastBias card.

We typically measure the flux dependence of the gain for a handful of current biases. In Figure 5.7, we've selected a few gain curves taken at different current and flux bias points to illustrate the bandwidth of SLUGA. We can dynamically tune SLUGA between 5.9 GHz and 6.7 GHz, with gain close to 13 dB and instantaneous bandwidths between 50 and 100 MHz. Our numerical simulations suggest that an SLUGA should have broader bandwidth and more gain. We suspect that the presence of parasitic resonances coupled

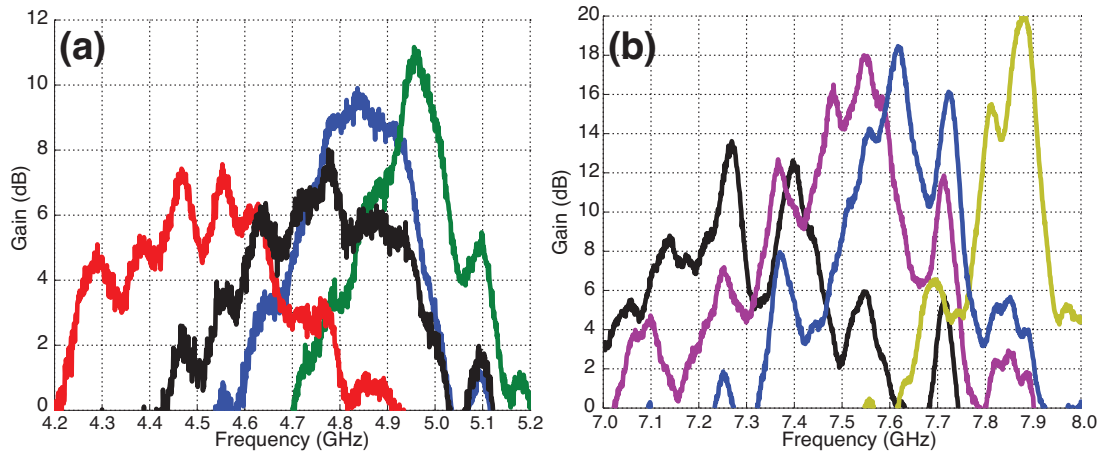


Figure 5.8: Line cuts of two different SLUG amplifiers operating at 5 GHz (a) and 8 GHz(b).

to the SLUG play a large role in undermining the gain-bandwidth product of the amplifier. In Figure 5.8, we plot gain line cuts at choice bias points for two different SLUG amplifiers that operate at 5 and 8 GHz. We believe the standing-wave like structure in the plotted gain line cuts come from an impedance mismatch at the output of the SLUG.

We rarely measure the 1 dB compression power of the SLUG amplifier. Informally, the SLUGs described in this section do not show signal compression when operated at bias points with 15 dB gain and input powers of approximately -115 dBm; unfortunately, the attenuation of the input microwave chain must be measured to calibrate the power at the input of the SLUG. This is not a trivial task, as the microwave chain will have different behavior when cold. One strategy is to set up two identical input paths and measure the roundtrip insertion loss. This calibration is flawed, as the insertion loss of a microwave chain depends greatly on the variability of solder joints and commercial products that were never intended to be cooled down to 40 mK. An example of gain compression calibrated in this way is plotted in Figure 5.9 for an earlier generation SLUG that operated at 2.85 GHz, showing a 1 dB compression input power of -95 dBm.

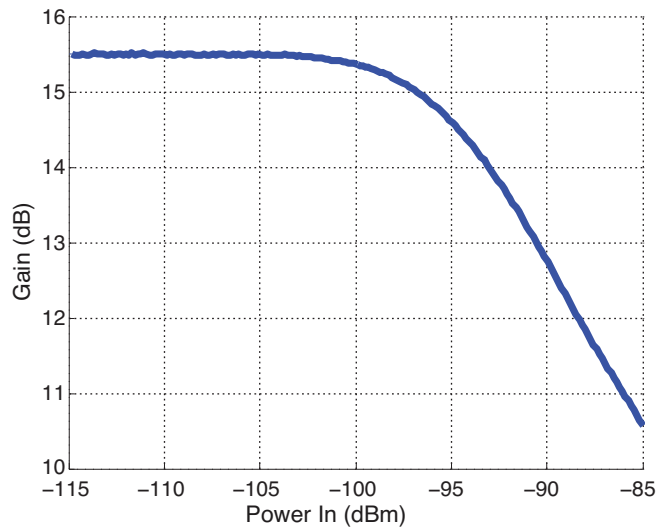


Figure 5.9: Gain compression for a SLUG amplifier operated at 2.85 GHz.

While we don't expect the gain compression is any worse for an amplifier like SLUGA, we haven't experimentally confirmed this. Additionally, the linearity of the SLUG is modified by the parasitic resonance. We discuss signal compression further when we use a SLUG to readout a qubit in Section 7.10.

5.4 Noise Performance

We characterize the noise performance of the SLUG amplifier by measuring the noise power of the amplification chain with (P_N^R) and without (P_N^S) the SLUG. Following the analysis of Equation 1.18, the measured noise powers have the following form:

$$P_N^R = \hbar\omega B(1/2 + N_{sys})G_R, \quad (5.1)$$

$$P_N^S = \hbar\omega B(1/2 + N_{sys}^S)G_S G_R, \quad (5.2)$$

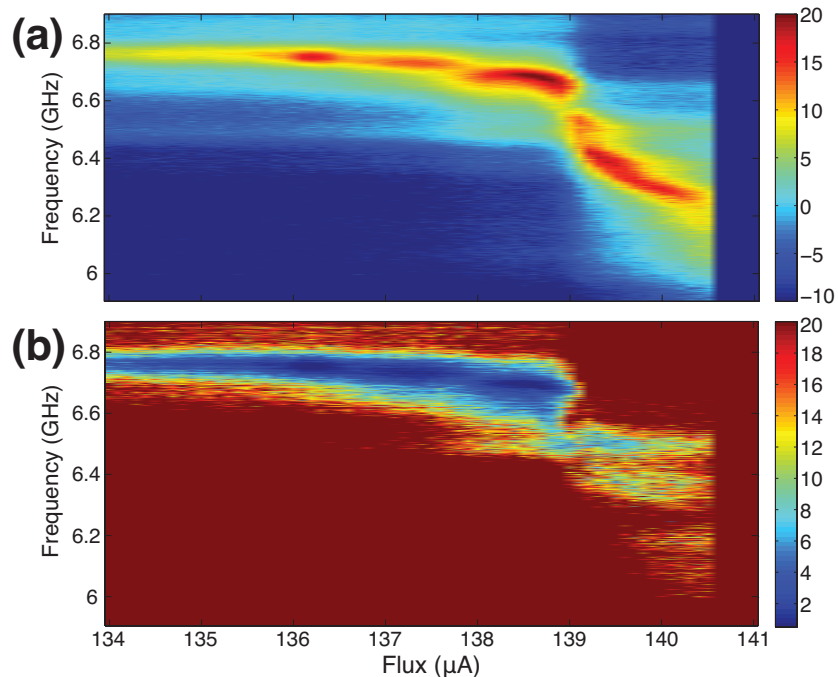


Figure 5.10: Gain **(a)** and N_{sys}^S **(b)** for SLUGA as a function of frequency and flux bias for $I_b = 80 \mu\text{A}$. We've assumed a $N_{sys} = 20$ when calculating N_{sys}^S .

where B is the bandwidth of the measurement, N_{sys} is the added system noise quanta without the SLUG, G_R is the unknown reference gain of the amplification chain without the SLUG, G_S is the measured SLUG gain, and N_{sys}^S is the added system noise quanta with the SLUG in the circuit. Taking their ratio and solving for N_{sys}^S gives:

$$N_{sys}^S = (1/2 + N_{sys}) \frac{P_N^S}{P_N^R} \frac{1}{G_S} - 1/2. \quad (5.3)$$

We measure P_N^R and P_N^S with a spectrum analyzer (SA), which captures the absolute power of the input signal versus frequency for a chosen resolution bandwidth. Once the noise powers are measured, we record the gain for the same set of SLUG bias parameters.

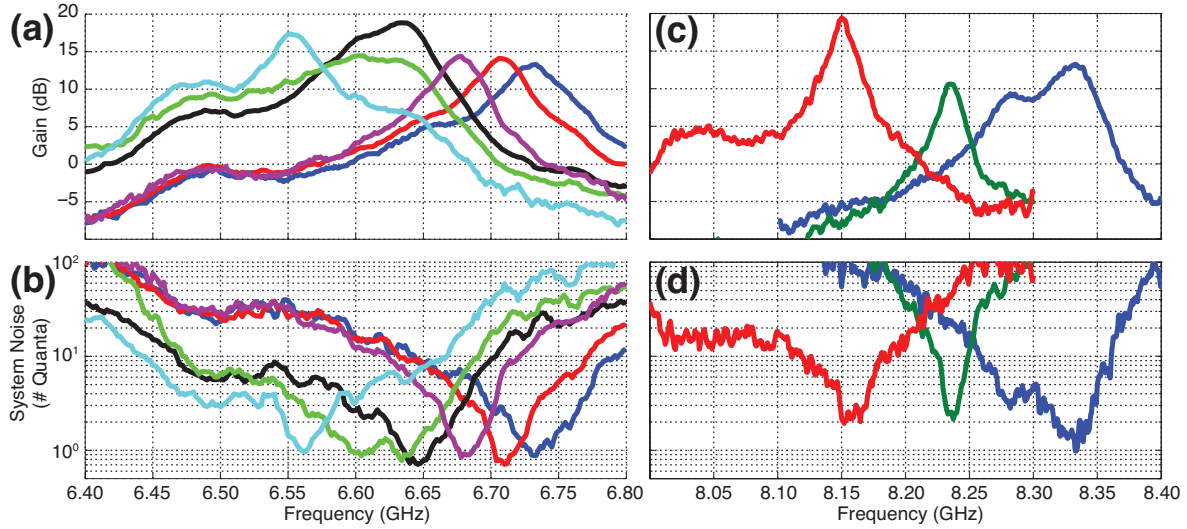


Figure 5.11: Gain (a) and N_{sys}^S (b) for SLUGA as a function of frequency for different current and flux biases. Gain (c) and N_{sys}^S (d) for a SLUG with measured $I_0 = 72 \mu\text{A}$, $R = 4.6 \Omega$, and $M = 7.8 \text{ pH}$, and a designed matching network with $Z_0 = 2 \Omega$ and $f_0 = 14.7 \text{ GHz}$. We've assumed a $N_{sys} = 20$ when calculating N_{sys}^S for both devices.

N_{sys}^S also depends on N_{sys} ³, which we have not explicitly measured for our setup. For the N_{sys}^S data plotted in this chapter, we've assumed a conservative $N_{sys} = 20$ quanta – this is equivalent to the HEMT having a noise temperature of 3.5K at 6.5 GHz with 2 dB of attenuation between the SLUG and the HEMT⁴. This attenuation could be coming from the insertion loss of the cryogenic components between the SLUG and the HEMT.

Gain and N_{sys}^S for SLUGA are plotted in Figure 5.10 as a function of frequency and flux bias for $I_b = 80 \mu\text{A}$. At this current bias, there is a resonant step edge at $\Phi_b = 139 \mu\text{A}$. There are flux bias points above the resonant step edge ($\Phi_b < 139 \mu\text{A}$) with gain greater than 15 dB and N_{sys}^S just less than one. On the other side of the

³ N_{sys} can be measured using the hot/cold load method, which presents the input of our amplification chain with two known noise powers, generated from a resistor with variable temperature on the cold stage.

⁴The noise temperature of an attenuator sitting at temperature T with gain $G < 1$ is $T(1/G - 1)$. In the quantum limit, where the attenuator is held at a $T \ll \hbar\omega/kb$, the equivalent added quanta of noise for the attenuator is $0.5(1/G - 1)$.

resonant step ($\Phi_b > 139 \mu\text{A}$), the gain is close to 15 dB but the noise performance is significantly worse. It is unclear if the poor noise performance below the step edge is due to bad noise matching due to a modified SLUG input impedance, or if there is something more fundamental about the chaotic dynamics of the junctions interacting with the parasitic resonance. This divergent behavior of the noise has been observed for SLUG amplifiers with different matching networks and different device parameters (β_C , β_L). In Figures 5.11 (a) and (b), we plot the gain and N_{sys}^S for SLUGA as a function of frequency for select current and flux biases. Bias points are chosen for $N_{sys}^S < 2$ between 6.55 GHz and 6.75 GHz. The instantaneous bandwidth of the plotted gain is less than the bandwidth reported in Figure 5.7, as we are selecting for bias points with low N_{sys}^S instead of high bandwidth. In Figures 5.11(c) and (d), we plot the gain and N_{sys}^S for a SLUG amplifier with different parameters, reported in the Figure’s caption, where we’ve also assumed a $N_{sys} = 20$ when calculating N_{sys}^S . N_{sys}^S appears larger for the SLUG operating at a larger frequency, but direct comparisons are misleading since N_{sys} will change with frequency and between cool downs. An absolute measurement of the noise temperature will be necessary to fully explore the dependence of N_{sys}^S on SLUG fabrication parameters.

5.5 Electron Temperature of Thin Film Resistors

As discussed in Section 3.12, Joule heating of the thin film resistors that shunt the SLUG junctions increases the electron temperature T_E , which has a direct impact on the noise performance of the amplifier. Multiple theoretical studies [90, 104, 105] relate the power dissipated in the resistor P to T_E with the following equation:

$$P = \Sigma \Omega (T_E^5 - T_{Ph}^5), \quad (5.4)$$

where Σ is the volume of the resistor, T_{Ph} is the phonon temperature of the resistor, and Σ is a material constant⁵. Each junction in SLUGA is shunted by two 6.6Ω resistors in parallel, each with volume $\Omega = 3 \mu\text{m} \times 9 \mu\text{m} \times 30 \text{ nm}$, optimally operated at a bias point with approximately $50 \mu\text{V}$ across each resistor, for a dissipated power of $P = 380 \text{ pW}$. Falferi et al. [107] measured $\Sigma \approx 2 \times 10^9 \text{ W}/(\text{m}^3\text{K}^5)$ for rf sputtered palladium thin films, which for a phonon temperature equal to the base temperature of the DR ($T_{Ph} = 40 \text{ mK}$) results in an electron temperature of $T_E = 748 \text{ mK}$. For context, using Equation 1.14, the effective number of 6.5 GHz noise quanta dissipated into a matched load at $T = 748 \text{ mK}$ is 2.4 quanta – almost five times the quantum limit. As was shown in Section 3.5, the optimal noise temperature of the SLUG amplifier is not limited to the physical temperature of the shunt resistors; however, future generations of the SLUG will dissipate more power in pursuit of a large gain-bandwidth product. In this section we experimentally examine the noise temperature of our palladium films.

5.5.1 Experimental Setup

Measuring the electron temperature of a resistor is equivalent to measuring the current spectral density of the noise generated by the resistor, $S_I = 4k_b T_E / R$. We measure T_E as a function of dissipated power by biasing a pair of identical resistors in parallel and measuring the current spectral density of one branch with a pair of correlated SQUID amplifiers, illustrated by the schematic in Figure 5.12(a). The two resistors are

⁵Pleikies *et al.* [106] summarizes the different theoretical treatments and experimental results of Joule heating.

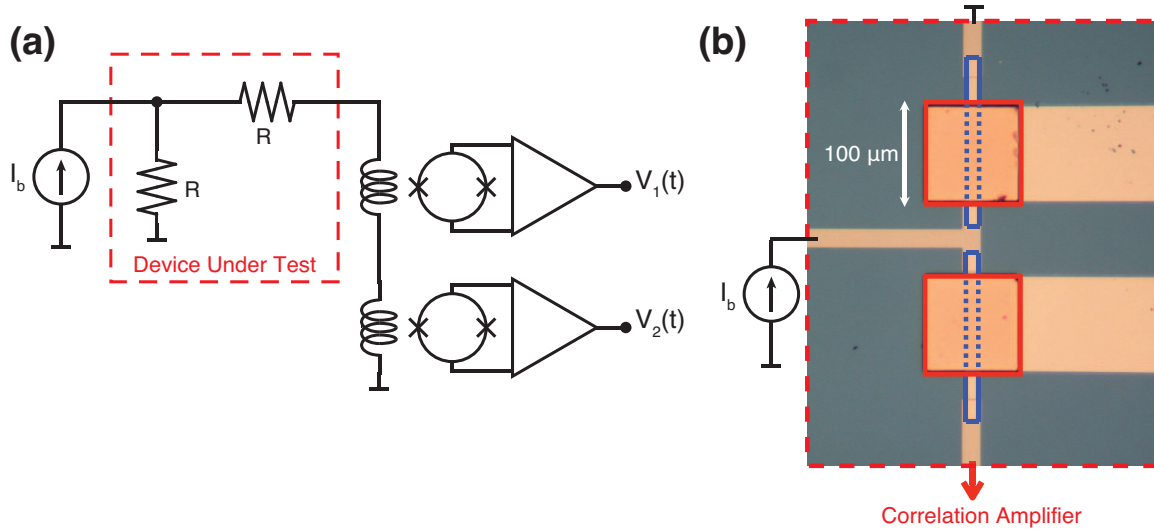


Figure 5.12: (a) The circuit schematic of the correlation amplifier measurement of a resistor's electron temperature as a function of dissipated power. (b) Picture of the electroplated copper cooling fin (red outline) anchored to a thin film Pd resistor (blue outline). The two electroplating leads extending right are severed before the measurement.

evaporated Ti backed Pd thin films with a sputter deposited superconducting aluminum film comprising the test leads. We measured T_E as a function of dissipated power for two different samples: a bare Pd resistor and a Pd resistor attached to an electroplated copper cooling fin. The bare resistor sample mimics the measured SLUG amplifier, with a $3 \mu\text{m} \times 9 \mu\text{m} \times 30 \text{ nm}$ volume, and a resistance of $R = 5.55 \Omega$, measured at 100 mK in the ADR with a sensitive 4-wire setup⁶.

Increasing the volume Σ of the resistor is the most obvious approach for reducing T_E at a fixed P . Unfortunately, increasing the footprint and thickness of the resistor is not a practical solution for most superconducting electronics. The performance of the SLUG amplifier relies on keeping the parasitic inductance and capacitance of the

⁶Actually, the two resistors were slightly different from each other, where the resistance to ground was 5.22Ω , and the resistor in the measured current branch was 5.88Ω . $R = 5.55 \Omega$ is the average resistance. We ignore this small discrepancy in the analysis.

resistor vanishingly small. Several groups have studied the impact of connecting a large, electrically neutral, two-dimensional volume to the dissipating resistor, which allows the electrons to diffuse into a larger volume to efficiently interact with the cold lattice phonons of the metal [89, 106, 108, 107]. These two-dimensional cooling fins become less effective at high powers. The diffusion length of the hot electrons depend inversely on temperature, meaning the hot electrons have less volume to thermalize. At high enough powers, the electrons do not noticeably diffuse into the electrically neutral volume, behaving as if the cooling fins do not exist. In fact, recent studies have shown almost no difference in electron temperature at 1 nW of dissipated power when comparing resistors with and without cooling fins. The ideal SLUG considered in Chapter 3 dissipates over 10 nW of power into 14Ω resistors, resulting in a resistor with T_E above 1 K. Two-dimensional cooling fins would do nothing to alleviate this problem. This is why we decided to add a third dimension for the electron-phonon interaction. By electroplating a thick layer of copper in the middle of the dissipating element, we provide a larger volume within the diffusion volume of the hot electrons.

Each resistor of the electroplated sample, pictured in Figure 5.12(b), consists an evaporated Ti backed Pd resistor with a volume of $35 \mu\text{m} \times 10 \mu\text{m} \times 35 \text{nm}$ attached to a $7 \mu\text{m}$ thick electroplated copper cooling fin with a $100 \mu\text{m} \times 100 \mu\text{m}$ footprint. The copper fin sits in the middle of the Pd resistor to minimize the distance hot electrons have to travel before interacting with the cold phonon lattice of the large volume copper block. The electroplated copper is backed by Pd that is electrically connected to Pd at the edge of the wafer – this connection is severed before measuring the sample. After the Pd film is defined, a $7 \mu\text{m}$ layer of photoresist is patterned, opening up holes to the Pd patterns to be electroplated. Our colleagues in Syracuse electroplated the samples at Cornell using a standard acid copper bath, where the wafer was electrically connected

at the edge after wiping away the photoresist. The plated resistors each had measured resistance of 4.35Ω at 100 mK.

The resistor sample was placed in a Nb box with the readout SQUIDS, where the sample was stuck onto a piece of the thin copper foil with Apiezon vacuum grease, which was thermally sunk to the cold stage through the copper ground shield of a coax line. The sample was also thermally sunk to the copper foil with many gold wire bonds. We were paranoid about heat sinking the sample to ensure that the phonon bath was quickly thermalized in the presence of large on chip power dissipation. The sample box was mounted to the cold stage of the ADR, which was fully enclosed in an aluminum box for additional shielding. The SQUID control lines and resistor bias were heavily filtered at 3 K with a low pass brass filter bank, and at the cold stage with a copper powder filter. The power dissipated by each resistor on the chip is:

$$P = (I_b/2)^2 R. \quad (5.5)$$

5.5.2 Electron Temperature Measurement

Steve Sendelbach describes the SQUID correlation amplifier in great detail within Section 3.2 of his thesis [109], including how to calibrate a flux locked loop measurement, so we'll only touch on the fundamentals of the setup. For two resistors R in parallel held at an electron temperature T_E , the measured current spectral density is:

$$S_I = 2k_b T_E / R + S_I^f, \quad (5.6)$$

where S_I^f represents the sum of all the other noise terms, which include the noise generated by the current bias resistor, the noise from the current supply, and noise from the SQUID readout electronics. For a $T_E = 100$ mK and a resistor with $R = 5.55 \Omega$, the first term of Equation 5.6 is approximately $0.5 \text{ pA}^2/\text{Hz}$. The current is then transformed into a flux threading the readout washer of each readout SQUID, with a measured mutual inductance of approximately 6.5 nH –meaning the minimum flux noise we must be sensitive to is $2.2 \mu\Phi_0/\sqrt{\text{Hz}}$. The measurement SQUIDs in our setup are operated in a flux locked loop, described in Section 2.5, which have a noise floor on the order of $20 \mu\Phi_0/\sqrt{\text{Hz}}$. In consequence, S_I^f will dominate the measured S_I , washing out the contribution from small changes in T_E .

The SQUID correlation amplifier is a twin set of SQUID amplifiers, each receiving a copy of S_I generated by the resistor sample. The noise generated by the hot resistor will be correlated, while the noise added by each SQUID amplifier will, in principle, not be correlated. We Fourier transform each measured voltage trace, $V_1(t)$ and $V_2(t)$:

$$\mathcal{F}_{1,2}(f) = \int_{-\infty}^{\infty} V_{1,2}(t) \exp(-2\pi i f t) dt. \quad (5.7)$$

The correlation function S_{12} can be computed:

$$S_{12} = \langle \mathcal{F}_1^* \mathcal{F}_2 \rangle, \quad (5.8)$$

where the brackets represent averaging over each recorded time series. From the calibration of the SQUID amplifier, we can convert this correlated voltage to a correlated current spectral density running through the input coils of the two SQUID amplifiers. As

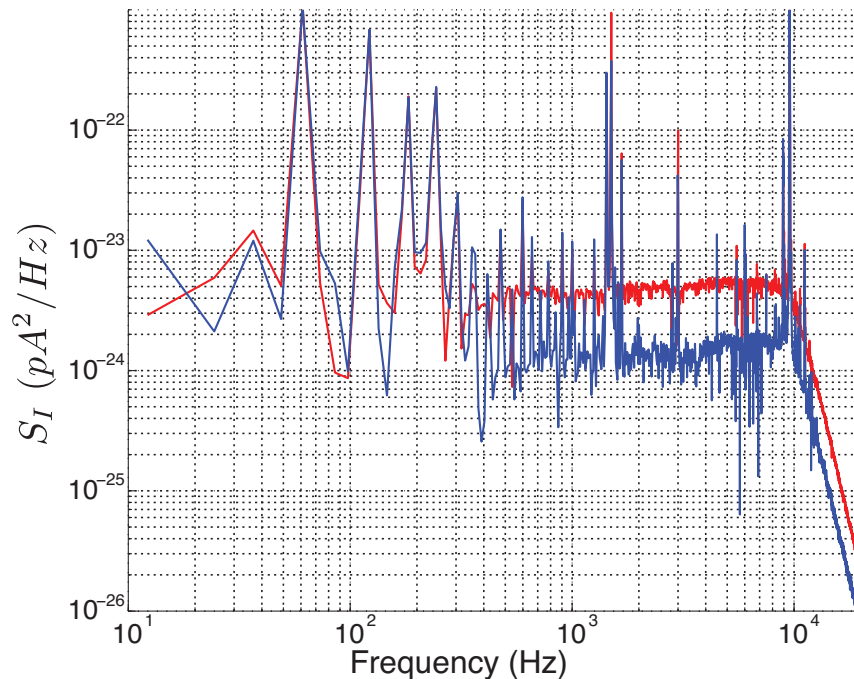


Figure 5.13: Correlated current spectral density S_I for two different dissipated powers in the bare resistor sample.

we average more, the correlated spectrum falls until it ultimately saturates. This saturation indicates that the uncorrelated noise contribution from the SQUID amplifiers has been removed. The variance of the spectrum will continue to decrease with averages. In Figure 5.13, we plot the correlated spectra of the bare resistor for two different dissipated powers after averaging 10,000 measurements of the correlated signal. We heavily filter the current source at room temperature using a low-pass filter with cutoff frequency of several Hz, which explains the elevated noise at lower frequencies in Figure 5.13. The output of the flux locked loop is also filtered above 10 kHz to prevent aliasing. We average the white component of the final spectrum, digitally filtering the correlated 60 Hz noise present in the spectra.

The correlated amplifier removes a large fraction of S_I^f from Equation 5.6, but not all of it – there are still contributions from the current bias chain and cross-talk between the

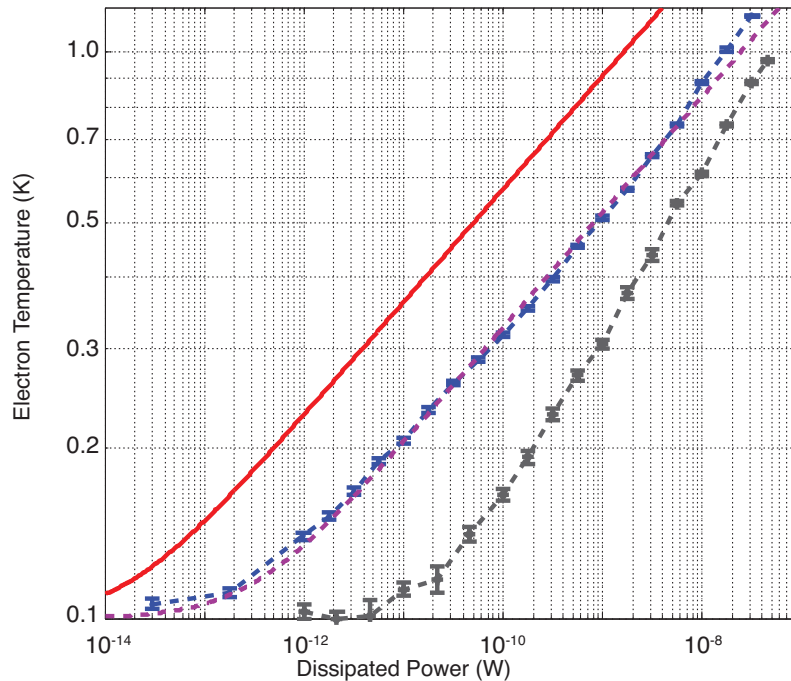


Figure 5.14: Measured T_E as a function of dissipated power for the bare resistor sample (blue) and the copper cooling fin sample (black). We've fit the bare resistor sample data with Equation 5.4 to extract a $\Sigma = 30 \times 10^9 \text{ W/m}^3\text{K}^5$, assuming $\Omega = 3 \mu\text{m} \times 9 \mu\text{m} \times 30 \text{ nm}$ (purple). We've also plotted T_E for $\Sigma = 2 \times 10^9 \text{ W/m}^3\text{K}^5$, assuming $\Omega = 3 \mu\text{m} \times 9 \mu\text{m} \times 30 \text{ nm}$ (red).

two SQUID amplifiers. We first measure the sample at 100 mK when $I_b = 0$, meaning $T_E = 100 \text{ mK}$. With R and T_E known, we can back out S_I^f from Equation 5.6, which is typically on the order of $0.1 \text{ pA}^2/\text{Hz}$. We then measure S_I for different current biases and extract T_E from Equation 5.6, where we've assumed that S_I^f does not change with I_b . The T_E of both the bare resistor and the copper cooling fin sample is plotted as a function of dissipated power in Figure 5.14, where the variance of the average cross spectral density is plotted as an error bar about the average

We extract a $\Sigma = 30 \times 10^9 \text{ W/m}^3\text{K}^5$ by fitting the bare resistor T_E to Equation 5.4, where we've assumed a volume $\Omega = 3 \mu\text{m} \times 9 \mu\text{m} \times 30 \text{ nm}$. The measured material constant Σ is over an order of magnitude larger than previously measured values of

$\Sigma \approx 2 \times 10^9 \text{ W/m}^3\text{K}^5$ for Pd resistors [107]. The only apparent difference between our Pd film and the film in the literature is the deposition method, where our Pd films are evaporated in a clean system with a base pressure of 10^{-9} Torr, compared to the rf sputtered films of Falferi *et al.* [107]. This unexpected result is great news for the noise performance of the SLUG amplifier, as the T_E of the resistor is only 450 mK, or 3 times the quantum limit at 6.5 GHz, for the bias parameters of SLUGA described above.

However, we can do better with the electroplated cooling fin, which has a $T_E \approx 230$ mK for the same dissipated power. Even more encouraging, the electroplated cooling fin provides a 300 mK improvement over the bare resistor at 10 nW of dissipated power, something that has not been observed in the literature with a two-dimensional cooling fin. Notice at high-powers that the electroplated cooling fin has a power dependence with exponent less than 5. This is direct evidence that the hot electrons are still interacting with the cold phonons in the electrically neutral cooling fin. A numerical treatment of the electron-phonon interaction for this three-dimensional geometry, along with an experimental exploration of parameter space is necessary to further optimize the electroplated cooling fins. For example, electroplating literature suggests that we can improve the copper-palladium barrier by seeding the palladium with a thin layer of evaporated copper. Additionally, we may be limited by the Kapitza resistance, where the phonons of the large copper structure are not optimally thermalizing with the substrate at high powers. In any case, this is a promising topic to explore as the SLUG parameters track towards larger power dissipation.

5.6 Conclusions and Outlook

The SLUG is the only microwave linear amplifier being actively researched that can satisfy the demands of a large-scale, superconducting quantum computer that relies on a QND dispersive readout. Parametrically driven Josephson junction amplifiers have reached the limit of their theoretical performance, with the Martinis group maximizing the gain-bandwidth product for a quantum limited JPA with a reported 20 dB gain, 50 MHz bandwidth, and a 1 dB compression point of about -115 dBm. In this chapter, we experimentally examined a SLUG amplifier that improved the signal to noise ratio of the amplifier chain by over 10 dB with an instantaneous bandwidth of 50 MHz. The SLUG in this chapter underperforms the equivalent numerical SLUG (same β_L , β_C , L , C), resulting in a smaller gain-bandwidth product than expected. It is encouraging that these first iterations of the SLUG amplifier match the performance of the best possible JPA. We are confident that a systematic examination of the SLUG integrated circuit and its packaging will result in an amplifier that converges with the expected numerical performance. Once we have understood the origin of the amplifier parasitics, we can focus on optimizing the SLUG parameters, pushing to larger critical currents and smaller junctions. With a focused engineering effort, the SLUG stands to play a large role in future quantum computing architectures.

A systematic exploration of the parasitic modes present on the chip and in the packaging will improve the performance of the SLUG and help guide future design decisions. First, we must standardize the chip packaging and minimize impedance mismatches. The present SLUG box consists of an SMA connector soldered to a PCB diving board that extends towards a recessed 2 mm chip sitting at the center of a brass cavity. Wire bonds make the final connection. Each transition and component between the coax line

and the on-chip coplanar launcher has a complex impedance that differs from $50\ \Omega$, resulting in reflected power and standing waves. Simple modifications, like recessing the copper boards into the box, will improve matching. Additionally, we need to measure the scattering parameters of the lumped element matching networks so that we can reliably match the $50\ \Omega$ generator impedance to the impedances of the SLUG input and output. A calibration can be performed by using a series of on-chip LC resonators capacitively coupled to a common feedline. A measurement of the transmitted power allows us to extract the inductance and capacitance of each resonator. Once we are able to reliably design the matching networks and have standardized the rest of the SLUG fabrication process, we can examine the gain and noise performance of the SLUG as a function of input matching network. This brute force method will deliver the best possible amplifier while also shedding light on the actual scattering parameters of the bare SLUG element. A stable high critical current junction process is also key for a reliable exploration of parameter space. We must develop a trilayer junction process [see discussion in Section 4.3] and accurately control for the film stress and SiO_x roughness in order to standardize the SLUG fabrication process.

There are many experiments that we would like to perform in the short term with the SLUG amplifier. The superconducting qubit community is interested in a non-reciprocal amplifier that does not require an isolator between the qubit and the amplifier. There are plans to measure the forward and reverse scattering parameters of the SLUG amplifier, along with the reflection coefficients. Such a measurement would involve de-embedding the scattering parameters from a cryogenic measurement using a pair of coax relays, directional couplers, and HEMTs [110]. Additionally, we'd like to cascade two SLUG amplifiers, allowing us to improve the gain-bandwidth product and the system noise of the amplification chain. This could initially be done with two chips using four separate

dc bias lines. However, this could eventually be moved onto one chip using a single flux and current bias.

Chapter 6

Theory of Superconducting Qubit Readout

In the previous chapters we focused on the classical dynamics of Josephson junction based integrated circuits, building a numerical framework for optimizing the SLUG amplifier for linear low noise amplification of classical signals. In this chapter we discuss the quantum behavior of superconducting circuits, with a derivation of the LC resonator Hamiltonian in Section 6.1 followed by the transmon qubit in Section 6.2. In Section 6.3, we calculate the expected signal-to-noise ratio of an amplification chain when measuring the state of the qubit.

6.1 Quantization of a Superconducting Circuit

Summarized conceptually by Devoret [111] and rigorously formalized by Bukard *et al* [112], the quantum behavior of a lumped element circuit can be described by deriving

the classical Hamiltonian of the circuit, followed by replacing the classical variables with their corresponding quantum operators.

Because we are interested in circuits containing Josephson junctions, it is helpful to use the macroscopic phase difference $\hat{\delta}$ across a circuit element as the position coordinate within the equations of motion. In accordance with BCS theory, the number of Cooper pairs \hat{N} on an electrode is conjugate to the $\hat{\delta}$, such that [56]:

$$[\hat{\delta}, \hat{N}] = i. \quad (6.1)$$

In circuits without junctions, it is more intuitive to work with magnetic flux $\hat{\Phi}$ and charge \hat{Q} as the conjugate variables. We can replace $\hat{\delta}$ with the $\hat{\Phi}$ generated by the non-linear inductance of a junction by examining the voltage across the junction [Equation 2.5], where $\dot{\Phi} = V_J = \frac{\hbar}{2e}\dot{\delta}$, and it follows that $\hat{\Phi} = \frac{\hbar}{2e}\hat{\delta}$. The total charge on an electrode is just $Q = 2eN$, giving Equation 6.1 the following form:

$$[\hat{\Phi}, \hat{Q}] = i\hbar. \quad (6.2)$$

The lossless parallel LC resonator, shown in Figure 6.1(a), is a trivial illustration of a quantized electrical circuit. We define the classical magnetic flux generated by any circuit element as:

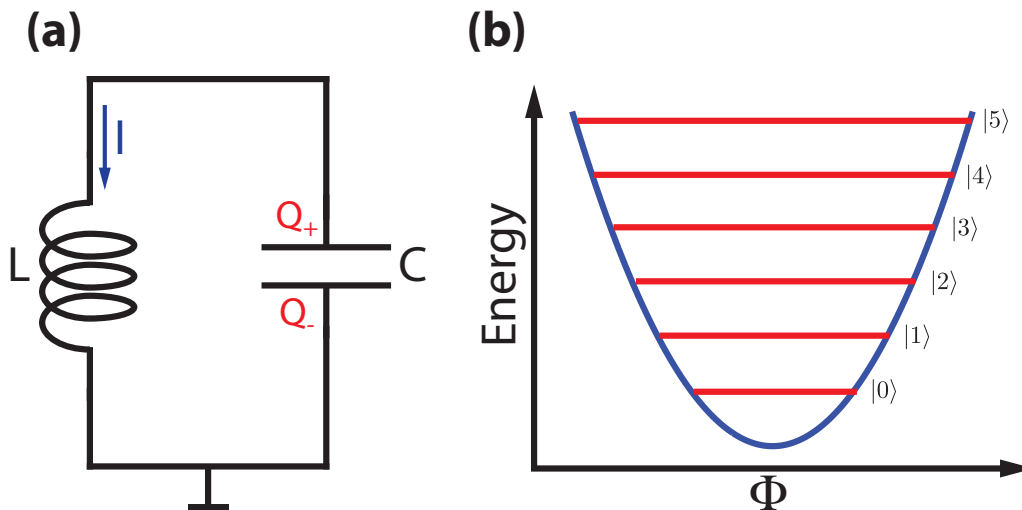


Figure 6.1: (a) Circuit schematic of LC resonator, where L is the inductance and C is the capacitance. Q is the charge on the capacitor, and I is the counterclockwise circulating current. (b) Potential energy of the LC resonator, with magnetic flux Φ as the position coordinate. The quantized energy levels of the harmonic system are equally separated.

$$\Phi(t) = \int_{-\infty}^t V(t') dt', \quad (6.3)$$

$$V(t) = \dot{\Phi}(t), \quad (6.4)$$

where $V(t)$ is assumed to be zero at $t = -\infty$. It follows that the total energy in the capacitor is:

$$U_C = \int_{-\infty}^t V(t') I(t') dt' = \int_0^Q \frac{Q'}{C} dQ' = \frac{Q^2}{2C} = \frac{CV^2}{2} = \frac{C\dot{\Phi}^2}{2}, \quad (6.5)$$

where $V = QC$. The magnetic energy in the inductor is:

$$U_L = \int_{-\infty}^t V(t')I(t')dt' = \int_0^I LI'dI' = \frac{LI^2}{2} = \frac{\Phi^2}{2L}, \quad (6.6)$$

where $V = L\dot{I}$. With the resonator energy depending on Φ , we can write down the circuit Lagrangian \mathcal{L} and conjugate momentum p , where U_C and U_L are the kinetic and potential energy of the circuit, respectively:

$$\mathcal{L} = U_C - U_L = \frac{C\dot{\Phi}^2}{2} - \frac{\Phi^2}{2L}, \quad (6.7)$$

$$p = \frac{\partial \mathcal{L}}{\partial \dot{\Phi}} = C\dot{\Phi} = Q, \quad (6.8)$$

It is now straightforward to write down the Hamiltonian of the resonator:

$$H = \dot{x}p - \mathcal{L} = \frac{Q^2}{2C} + \frac{\Phi^2}{2L} = \frac{p^2}{2m} + \frac{1}{2}m\omega_0^2x^2. \quad (6.9)$$

Equation 6.9 suggestively maps the LC resonator to a Hamiltonian that describes a fictitious particle of mass $m = C$ moving in a harmonic potential with $\Phi \rightarrow x$ and a plasma frequency $\omega_0 = 1/\sqrt{LC}$. Since the conjugate variables Q and Φ satisfy Equation 6.2, the quantized resonator circuit takes the following familiar form:

$$\hat{H} = \hbar\omega_0(\hat{a}^\dagger\hat{a} + \frac{1}{2}), \quad (6.10)$$

with the ladder operators \hat{a} and \hat{a}^\dagger defined as:

$$\hat{a} = \frac{1}{\sqrt{2\hbar Z}}(\hat{\Phi} + iZ\hat{Q}), \quad (6.11a)$$

$$\hat{a}^\dagger = \frac{1}{\sqrt{2\hbar Z}}(\hat{\Phi} - iZ\hat{Q}), \quad (6.11b)$$

where the characteristic impedance $Z = \sqrt{L/C}$. As illustrated in Figure 6.1(b), the quantized LC resonator contains an infinite number of uniformly spaced energy levels, separated by $\hbar\omega_0$.

6.2 Transmon

As discussed in Section 1.1, a qubit is an object whose state can be placed in an arbitrary superposition of two discrete eigenstates, labeled $|0\rangle$ and $|1\rangle$. Quantized superconducting circuits, like atoms, are defined by an infinite-dimensional Hilbert space; however, the computational manifold of a qubit occupies only two dimensions of Hilbert space. The quantized harmonic oscillator discussed above is defined by an infinite number of eigenstates with equally spaced energy levels. It is impossible to independently address two eigenstates of the circuit. For example, if we drive a two-level system at a frequency equal to the energy splitting f_{10} , the qubit will cyclically absorb and emit photons, causing the state to oscillate between the $|0\rangle$ and $|1\rangle$ state. However, the harmonic oscillator will continue to absorb photons as the state climbs the ladder.

Superconducting qubits rely on the non-linear inductance of the Josephson junction [Equation 2.6] to modify the potential of the harmonic oscillator, resulting in a discrete, anharmonic spectra with $f_{10} > f_{21}$. There are many different flavors of superconducting

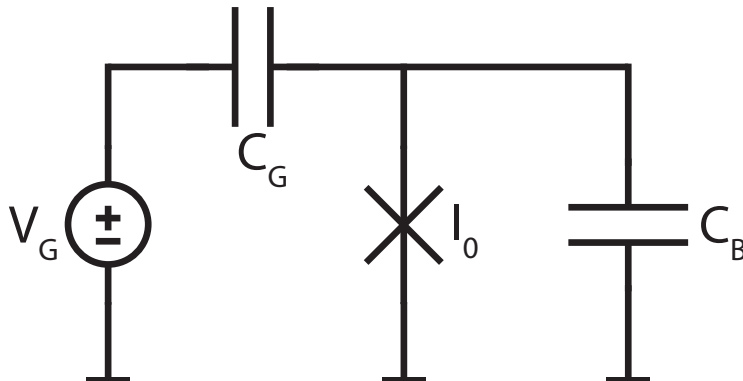


Figure 6.2: Schematic of the Cooper Pair Box, with gate voltage V_G , gate capacitance C_G , a Josephson junction with critical current I_0 and C_B is total capacitance shunting the junction.

qubits, separated by circuit topology and component values¹. In this thesis we measure a transmon qubit, first discussed by the Yale group [31]. The transmon qubit is a Cooper pair box (CPB) capacitively coupled to a resonator. The CPB, schematically shown in Figure 6.2, consists of a Josephson junction with critical current I_0 , and a total shunt capacitance C_B . The junction is connected to a voltage source V_G through a gate capacitor C_G . From the Josephson relations in Equations 2.4 and 2.5, the energy of a junction U_J with critical current I_0 is:

$$U_J = \int_0^t I_J(t') V_J(t') dt' = \frac{I_0 \Phi_0}{2\pi} \int_0^\delta \sin(\delta') d\delta' = E_J [1 - \cos(\delta)], \quad (6.12)$$

where the Josephson energy $E_J = \frac{I_0 \Phi_0}{2\pi}$. The energy stored in the capacitance U_C is:

¹For a taxonomy of the superconducting qubit kingdom, read the review by Devoret *et al.* [23].

$$\begin{aligned}
U_C &= \frac{1}{2}C_G (V_G + V_J)^2 + \frac{1}{2}V_J^2 \\
&= \frac{1}{2}C_G \left(V_G + \frac{\hbar}{2e}\dot{\delta} \right)^2 + \frac{1}{2}C_B \left(\frac{\hbar}{2e} \right)^2 \dot{\delta}^2.
\end{aligned} \tag{6.13}$$

Ignoring the constant terms, it follows that the Lagrangian \mathcal{L} is:

$$\begin{aligned}
\mathcal{L} = U_C - U_L &= \frac{1}{2}C_G \left(V_G + \frac{\hbar}{2e}\dot{\delta} \right)^2 + \frac{1}{2}C_B \left(\frac{\hbar}{2e} \right)^2 \dot{\delta}^2 + E_J \cos(\delta) \\
&= \frac{1}{2} \left[\frac{(2en_G)^2}{C_G} + 2n_G\hbar\dot{\delta} + C_G \left(\frac{\hbar}{2e} \right)^2 \dot{\delta}^2 \right] + \frac{1}{2}C_B \left(\frac{\hbar}{2e} \right)^2 \dot{\delta}^2 + E_J \cos(\delta),
\end{aligned} \tag{6.14}$$

where $V_G = 2en_G/C_G$. The conjugate momentum is:

$$\begin{aligned}
p &= \frac{\partial \mathcal{L}}{\partial \dot{\delta}} = n_G\hbar + C_\Sigma \left(\frac{\hbar}{2e} \right)^2 \dot{\delta} \\
&\equiv n\hbar,
\end{aligned} \tag{6.15}$$

where $C_\Sigma = C_B + C_G$, and where we've defined n as the conjugate momentum, physically interpreted as the number of Cooper pairs on the junction. The Hamiltonian of the system is written as:

$$\begin{aligned}
H = p - \mathcal{L} &= \frac{1}{2} \left(\frac{\hbar}{2e} \right)^2 \dot{\delta}^2 C_\Sigma - E_J \cos(\delta) \\
&= 4E_C (n - n_G)^2 - E_J \cos(\delta),
\end{aligned} \tag{6.16}$$

where $E_C = e^2/2C_\Sigma$ is the energy required to bring one electron onto the junction. Since the phase across the junction δ and the number of Cooper pairs n are conjugate coordinates [Equation 6.1], we can rewrite the Hamiltonian of the CPB with quantum operators $\hat{\delta}$, \hat{n} :

$$\hat{H} = 4E_C (\hat{n} - n_G)^2 - E_J \cos(\hat{\delta}). \tag{6.17}$$

We can numerically solve the CPB Hamiltonian to illustrate the spectra of the qubit for different E_J/E_C ratios. A numerical solution is obtained by rewriting Equation 6.17 in the charge basis, truncating the infinite Hilbert space to a manageable subspace of dimension $2N$:

$$\hat{H} = 4E_C \sum_{j=-N}^N (j - n_G)^2 |j\rangle\langle j| - \frac{E_J}{2} \sum_{j=-N}^{N-1} (|j+1\rangle\langle j| + |j\rangle\langle j+1|), \tag{6.18}$$

where the second term physically represents the tunneling of Cooper pairs across the junction. With the Hamiltonian in this form, it is trivial to numerically solve for the eigenvalues and eigenvectors of the resultant $2N \times 2N$ matrix. The first four energy splittings $E_{i+1,i} = E_{i+1} - E_i$ are plotted in Figure 6.3(a) as a function of gate charge

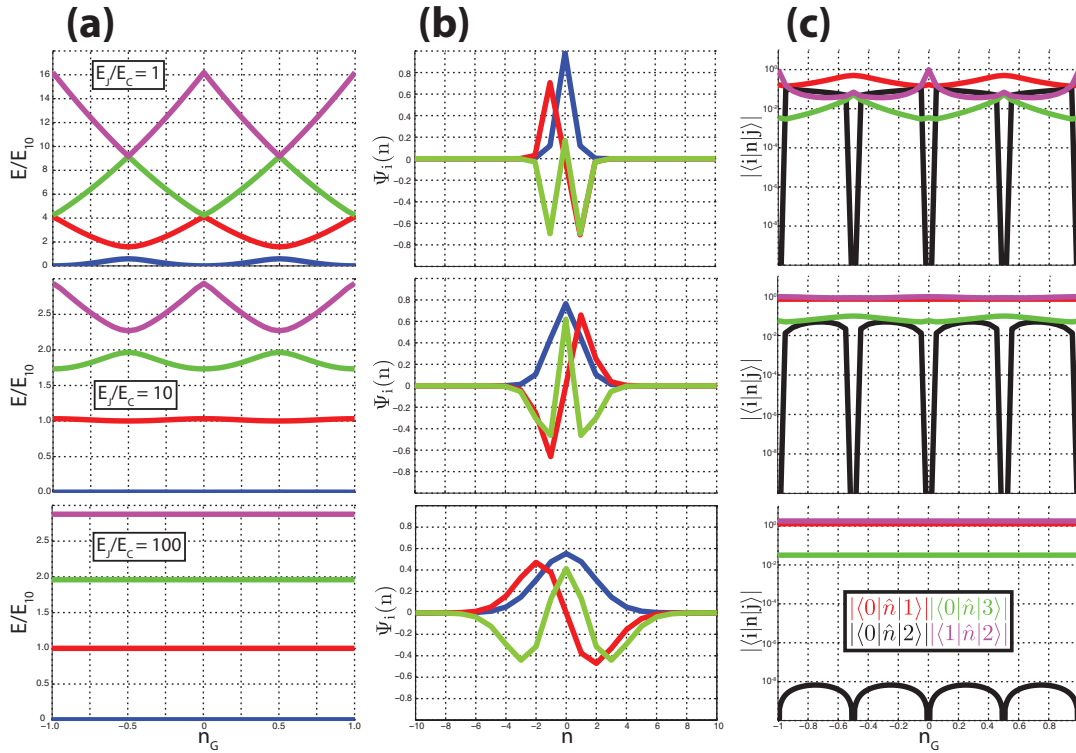


Figure 6.3: Column (a) plots the spectra of the first four energy splitting of the CPB, normalized to E_{10} . The Hamiltonian is solved for three different energy ratios. Column (b) shows the eigenfunctions for the $|0\rangle$ (blue), $|1\rangle$ (red), and $|2\rangle$ (green) at $n_G = 0$. Column (c) has numerical solutions of four matrix elements $|\langle i|\hat{n}|j\rangle|$ as a function of gate charge n_G .

n_G . The energy ratio E_J/E_C determines the anharmonicity and the charge dispersion of the qubit. A large anharmonicity ($E_{21} - E_{10}$) is necessary to remain in the two-state computational manifold during qubit operations. Increasing E_J/E_C reduces the anharmonicity of the qubit. Charge dispersion describes how the energy of the qubit varies with gate-voltage fluctuations. As the energy ratio increases, the effects of charge dispersion vanishes. Koch *et al.* [31] showed that charge dispersion reduces exponentially in E_J/E_C , while anharmonicity decreases algebraically, leaving room for compromise. The transmon is a CPB with $E_J/E_C \gg 1$, eliminating the need for electrostatic gates

for tuning the qubit to a charge insensitive sweet spot. It can be shown that for large E_J/E_C the first two energies of the qubit have the following form [31]:

$$E_{10} = \sqrt{8E_J E_C} - E_C, \quad (6.19)$$

$$E_{21} = \sqrt{8E_J E_C} - 2E_C, \quad (6.20)$$

giving an anharmonicity of $E_{21} - E_{10} = E_C$. The transmon measured in the following Chapter is fabricated with two junctions embedded in a low-inductance superconducting loop. As described by Equation 2.21, the two junctions act as a single junction with a flux adjustable critical current. This arrangement gives us the ability to tune the spectra of the qubit using a simple dc bias.

The transmon is capacitively coupled to the voltage antinode of a transmission line resonator. Koch *et al.* [31] derived an expression for the dipole coupling constant g_{ij} of the Jaynes-Cummings hamiltonian [Equation 1.5]:

$$\hbar g_{ij} = 2e\beta V_{rms}^0 \langle i | \hat{n} | j \rangle, \quad (6.21)$$

where $V_{rms}^0 = \sqrt{\hbar\omega_r/2C_r}$ is the RMS zero-point voltage of the resonator, C_r is the total capacitance of the resonator, and $\beta = C_g/C_\Sigma$ is the ratio of the gate capacitance to the total capacitance. We compute several matrix elements $\langle i | \hat{n} | j \rangle$ in Figure 6.3(c). The neighboring coupling constants are well approximated by:

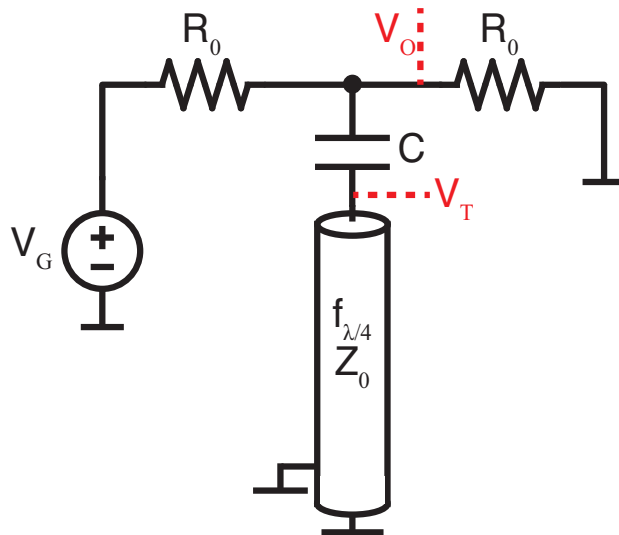


Figure 6.4: Schematic of the readout resonator circuit, configured as a $\lambda/4$ transmission line resonator with bare resonance $f_{\lambda/4}$ and characteristic impedance Z_0 . The resonator is capacitively coupled to a R_0 feedline driven by a generator V_G .

$$\hbar g_{i+1,i} \approx 2e\beta V_{rms}^0 \sqrt{\frac{i+1}{2}} \left(\frac{E_J}{8E_C} \right)^{1/4} = \sqrt{i+1} g_{10} \quad (6.22)$$

Additionally, as $E_J/E_C \rightarrow \infty$ the non-neighboring matrix elements vanish, such that:

$$g_{ij} = 0 \text{ for } |i - j| > 1. \quad (6.23)$$

Calculating the g-factors is important for calculating the dispersive and Stark shift using the analysis of Section [A.3](#).

6.3 Qubit Readout

As discussed in Section 1.5, we probe the state of the qubit by measuring the dressed state of a cavity coupled to the qubit. In the dispersive limit, the resonance of the cavity depends on the state of the qubit [see Equation A.20]. We interrogate the state of the cavity-qubit system with a single microwave tone, at a frequency chosen to maximize the distinguishability of the $|0\rangle$ and $|1\rangle$ state. For the qubit measured in this thesis, the readout resonator is a $\lambda/4$ coplanar transmission line resonator capacitively coupled to a $50\ \Omega$ feedline, as illustrated in the schematic of Figure 6.4. In this section, we investigate the expected signal-to-noise ratio (SNR) of a dispersive measurement of the qubit.

The microwave generator probes the state of the cavity at angular frequency ω and amplitude V_G . The complex impedance of the qubit-cavity system modifies the amplitude and phase of the probe signal, giving the output voltage $V_O(t)$ the following form:

$$\begin{aligned}
 V_O(t) &= A \sin(\omega t + \theta) \\
 &= I \cos(\omega t) - Q \sin(\omega t) \\
 &= \text{Real}[(I + iQ) \exp(i\omega t)],
 \end{aligned} \tag{6.24}$$

where, in the steady state, the quadrature components I and Q are constant in time and are related to the phase and magnitude in the following way:

$$A = \sqrt{I^2 + Q^2}, \tag{6.25}$$

$$\theta = \arctan(I/Q). \tag{6.26}$$

In a standard heterodyne measurement, we have access to both the quadratures of $V_O(t)$, allowing us to back out how the the cavity-qubit system modifies the probe signal.

6.3.1 Quarter Wave Resonator

Following along with Mazin [113], from Equation 3.36, the impedance of a lossless quarter-wave transmission line with a short-circuited load takes the form:

$$\begin{aligned} Z_T &= Z_0 \tanh(i\beta\ell) \\ &= Z_0 \tanh\left(i\frac{\pi\omega}{2\omega_{\lambda/4}}\right), \end{aligned} \quad (6.27)$$

where $\omega_{\lambda/4}$ is the bare angular resonance of the transmission line. For $|\omega - \omega_{\lambda/4}| \ll 1$, Equation 6.27 is well approximated by:

$$Z_T \approx -\frac{i2Z_0}{\pi\delta x}, \quad (6.28)$$

where $\delta x = (\omega - \omega_{\lambda/4})/\omega_{\lambda/4}$. The impedance of the coupling capacitor C in series with Z_T is:

$$\begin{aligned} Z &= \frac{1}{i\omega C} - \frac{i2Z_0}{\pi\delta x} \\ &\approx iR_0Q_c\delta x', \end{aligned} \quad (6.29)$$

where we've assumed that the capacitor does not significantly modify the bare resonance $[(\omega_0 - \omega_{\lambda/4})/\omega_{\lambda/4} \ll 1]$, giving the following forms to Q_c , the modified resonance ω_0 , and $\delta x'$:

$$Q_c = \frac{\pi}{2Z_0 R_0 \omega_0^2 C^2}, \quad (6.30)$$

$$\omega_0 \approx \omega_{\lambda/4} \left(1 - \sqrt{\frac{2Z_0}{\pi R_0 Q_c}} \right), \quad (6.31)$$

$$\delta x' = \frac{\omega - \omega_0}{\omega_0}. \quad (6.32)$$

The quality factor is a measure of how quickly the resonator loses energy, which is defined by $Q = \omega_0 \tau_{1/e}$, where ω_0 is the resonance of the system and $\tau_{1/e}$ is the exponential time constant of the energy stored in the resonator. A fraction of the stored energy is lost to the substrate and the oxide at the metal substrate interface (described by the intrinsic quality factor Q_i). By design, the energy will also escape through the capacitor, defined by the coupling quality factor Q_c . The loss channels add in parallel, for a loaded Q_L of:

$$1/Q_L = 1/Q_c + 1/Q_i. \quad (6.33)$$

We can treat the resonator as lossless in the limit of $Q_i \gg Q_c$. The coupling quality factor Q_c is calculated with the following argument. The $\lambda/4$ transmission line has a voltage profile that oscillates in time with the following dependence:

$$V_\ell(t, x) = V_A \sin(\omega t) \cos(2\pi x/\lambda_0), \quad (6.34)$$

where $x = 0$ is the capacitor side of the resonator, $0 \leq x \leq \lambda_0/4$, and $\lambda_0 = v_{ph}/f_{\lambda/4}$. The energy stored in the capacitance of the resonator averaged over one clock cycle and the length of the line is:

$$\begin{aligned} E_C &= \frac{1}{2} C_\ell \frac{4}{\lambda_0} \int_0^{\lambda_0/4} dx \frac{1}{T} \int_0^T dt |V_A|^2 \sin^2(2\pi t/T) \cos^2(2\pi x/\lambda_0) \\ &= \frac{1}{8} C_\ell |V_A|^2, \end{aligned} \quad (6.35)$$

where the total capacitance C_ℓ of the line is [87]:

$$C_\ell = \frac{\pi}{2\omega_{\lambda/4} Z_0}. \quad (6.36)$$

Half of the energy in the resonator is stored in the electric field of the capacitor, with the other half stored in the magnetic field of the inductance, for a total average energy:

$$E = 2E_C = \frac{1}{4} C_\ell |V_A|^2 = \frac{\pi}{8\omega_{\lambda/4} Z_0} |V_A|^2. \quad (6.37)$$

The average power leaking out of the resonator is:

$$\begin{aligned}
P &= |I|^2 R_0/4 \\
&= \left| \frac{V_A}{\frac{1}{i\omega_{\lambda/4}C} + R_0/2} \right|^2 R_0/4 \\
&\approx |V_A|^2 (\omega_{\lambda/4}C)^2 R_0/4.
\end{aligned} \tag{6.38}$$

The decay time $\tau_{1/e}$ is just:

$$\tau_{1/e} = E/P = \frac{\pi}{2\omega_{\lambda/4}Z_0R_0(\omega_{\lambda/4}C)^2}. \tag{6.39}$$

Finally, we write down Q_c :

$$\begin{aligned}
Q_c &= \omega_{\lambda/4}\tau_{1/e} = \frac{\pi}{2Z_0R_0\omega_{\lambda/4}^2C^2} \\
&\approx \frac{\pi}{2Z_0R_0\omega_0^2C^2}.
\end{aligned} \tag{6.40}$$

From Equation 6.29, the forward voltage transfer function of the resonator S_{21} is:

$$S_{21} = 2V_O/V_G = \frac{2}{2 + R_0/Z} = \frac{i2Q_c\delta x'}{i2Q_c\delta x' + 1}. \tag{6.41}$$

Figures 6.5(a) and (b) show the transmitted power and phase for a resonator with $Q_c = 5000$. On resonance, the transmitted power is at a minimum, while the phase inflects about 0. The quadrature components of the complex signal trajectory are plotted in

Figure 6.5(c) for different frequencies. For a heterodyne measurement, we capture the quadrature components of the output voltage V_O :

$$V_O = S_{21}V_G/2. \quad (6.42)$$

6.3.2 Cavity Photon Population

The expected voltage difference between the two resonator states depends on how hard the cavity-qubit system is driven. The dispersive form of the Jaynes-Cummings hamiltonian breaks down as the number of photons in the cavity approaches n_{crit} [Equation A.16]. We want a functional form of V_O for a known average cavity photon population. Using Equation 6.37, the total average energy E in the resonator is related to the average photon number \bar{n} as follows:

$$\bar{n} = \frac{E}{\hbar\omega} = \frac{\pi}{8\omega_0 Z_0 \hbar\omega} |V_A|^2. \quad (6.43)$$

From Equations 6.42, 6.29, and 6.28, the voltage across the transmission line V_A depends on V_G as:

$$\begin{aligned} V_A &= V_O \frac{Z_T}{Z} = \frac{S_{21}V_G Z_T}{2Z} \\ &= \frac{-iV_G 2Z_0}{\pi R_0 (\delta x' - \sqrt{\frac{2Z_0}{\pi R_0 Q_c}})(1 + i2Q_c \delta x')}. \end{aligned} \quad (6.44)$$

We are interested in frequencies about the linewidth of the resonator $\kappa = \omega_0/Q_c$, such that $\delta x' \ll \sqrt{2Z_0/(\pi R_0 Q_c)}$, giving:

$$V_A \approx iV_G \sqrt{\frac{2Z_0 Q_c}{\pi R_0}} \left(\frac{1}{1 + i2Q_c \delta x'} \right). \quad (6.45)$$

Equation 6.43 becomes:

$$\bar{n} = \frac{V_G^2 Q_c}{4R_0 \omega_0 \omega \hbar} \left(\frac{1}{1 + (2Q_c \delta x')^2} \right). \quad (6.46)$$

6.3.3 Steady State Signal To Noise Ratio

We define the signal-to-noise ratio (SNR) as the voltage difference between the two states $|V_{sig}|$ divided by the sum of the standard deviations that define the voltage distribution of each state $\sigma_{|0\rangle} + \sigma_{|1\rangle}$:

$$SNR = \frac{|V_{sig}|}{\sigma_{|0\rangle} + \sigma_{|1\rangle}}. \quad (6.47)$$

As illustrated in Figure 6.6(a), the two dressed cavity states occupy a different point on the complex plane of the measured output voltage V_O , which is given the following form using Equation 6.42:

$$\begin{aligned}
V_O &= \frac{V_G(\Delta\omega/\kappa)(2\Delta\omega/\kappa + i)}{1 + (2\Delta\omega/\kappa)^2} \\
&= |V_O|(\cos\theta + i\sin\theta),
\end{aligned} \tag{6.48}$$

where we've replaced $Q_c = \omega_0/\kappa$. The magnitude $|V_O|$ and phase θ are given by:

$$|V_O| = |V_G| \left| \frac{\Delta\omega}{\kappa} \right| (1 + (2\Delta\omega/\kappa)^2)^{-1/2}, \tag{6.49}$$

$$\tan\theta = \frac{\kappa}{2\Delta\omega}, \tag{6.50}$$

where $\Delta\omega = \omega - \omega_0$. The dressed cavity state modifies ω_0 . For the $|0\rangle$ state, $\Delta\omega$ becomes:

$$\Delta\omega \rightarrow \Delta\omega^{|0\rangle} = \omega - \omega_0^{|0\rangle}, \tag{6.51}$$

and for the $|1\rangle$ state:

$$\begin{aligned}
\Delta\omega \rightarrow \Delta\omega^{|1\rangle} &= \omega - \omega_0^{|1\rangle} \\
&= \omega - (\omega_0^{|0\rangle} + 2\chi) \\
&= \Delta\omega^{|0\rangle} - 2\chi,
\end{aligned} \tag{6.52}$$

where 2χ is the dispersive shift defined by Equation [A.22](#). The measured voltage difference between the two states is $|V_{sig}|$:

$$\begin{aligned}
|V_{sig}| &= \sqrt{(|V_O^{(0)}| \sin \theta^{(0)} - |V_O^{(1)}| \sin \theta^{(1)})^2 + (|V_O^{(0)}| \cos \theta^{(0)} - |V_O^{(1)}| \cos \theta^{(1)})^2} \\
&= \sqrt{|V_O^{(0)}|^2 + |V_O^{(1)}|^2 - 2|V_O^{(1)}||V_O^{(0)}| \cos(\theta^{(0)} - \theta^{(1)})},
\end{aligned} \tag{6.53}$$

where the $|0\rangle$ ($|1\rangle$) superscript means we've plugged Equation 6.51 (6.52) into Equation 6.50 for calculating $|V_{sig}|$ and θ . We've also defined $|V_G|$ by the number of photons in the resonator when the qubit is in the $|0\rangle$ state, from Equation 6.46:

$$|V_G|^2 = 4\hbar\omega\kappa R_0\bar{n}[1 + (2\Delta\omega^{(0)}/\kappa)^2]. \tag{6.54}$$

Using Equation 1.21, the standard deviation of the measured voltage distribution σ is equal to the RMS voltage of the system noise of the amplification chain:

$$\sigma = V_{RMS} = \sqrt{R_0\hbar\omega(1/2 + n_{sys})B}, \tag{6.55}$$

where the noise quanta added by the system n_{sys} is defined by Equation 1.20, and B is the equivalent noise bandwidth (ENB) of our measurement chain, which we assume to be $B = 1/\tau_m$ for a simple rectangular window function of duration τ_m . The SNR of a qubit measurement as a function of detuning $\Delta\omega^{(0)}$ and cavity-qubit detuning $\Delta_0 = \omega_{10} - \omega^{(0)}$ is plotted in Figure 6.6(b). For this illustration, we have chosen $\bar{n} = n_{crit} = g_{10}^2/(4\Delta_0^2)$, $\omega^{(0)}/2\pi = 6.6$ GHz, $Q_c = 5000$, $n_{sys} = 1$, $R_0 = 50 \Omega$, $g_{10}/2\pi = 33$ MHz, and $\tau_m = 600$ ns. The dispersive shift of the cavity 2χ as a function of Δ_0 is calculated with the analysis in

Section A.3 and plotted in Figure 6.7(b), where we've assumed the following reasonable anharmonicities: $\alpha_1 = \omega_{21} - \omega_{10} = -230$ MHz and $\alpha_2 = \omega_{23} - \omega_{21} = -250$ MHz.

Notice that the calculated SNR is largest when probing at a frequency halfway between the cavity states ($\Delta\omega^{(0)} = \chi$). Qualitatively, the cavity must be driven harder (a larger $|V_G|$) in order to maintain a fixed number of photons in a cavity when driven off resonance. Also, note that for a fixed κ , there exists a Δ_0 where the SNR is at a maximum. As the qubit is detuned further from the cavity, the dispersive shift 2χ gets smaller, which results in a lower SNR for a fixed number of photons in the cavity. However, n_{crit} also increases with larger detuning, which means the cavity can be driven harder. A weakly anharmonic system modifies χ , and, in consequence, the SNR starts to decrease below a critical Δ_0 .

6.3.4 SNR With Cavity Ringup

The above analysis solves the output voltage in the steady state. In practice, one must consider the dynamics of the cavity and the amount of time it takes to load the cavity with photons. In the above example, the cavity has a characteristic time of $\tau_c = 2\pi/\kappa = 2\pi Q_c/\omega^{(0)} = 758$ ns. By solving for V_O as a function of time, we can calculate a more accurate measurement SNR. For $(\omega - \omega_0)/\omega_0 \ll 1$, we rewrite the impedance of the series capacitor- $\lambda/4$ resonator of Equation 6.29 as an inductor L_r in series with a capacitor C_r :

$$L_r = \frac{R_0 Q_c}{2\omega_0}, \quad (6.56)$$

$$C_r = \frac{2}{\omega_0 R_0 Q_c}, \quad (6.57)$$

$$\omega_0 = \frac{1}{\sqrt{L_r C_r}}, \quad (6.58)$$

where ω_0 is the modified resonance defined by Equation 6.32. It is straightforward to derive an equation of motion for the current flowing through the series LC resonator I_{LC} :

$$\ddot{I}_{LC} + \frac{\omega_0}{Q_c} \dot{I}_{LC} + \omega_0^2 I_{LC} = \frac{V_G \omega \omega_0}{R_0 Q_c} \cos(\omega t), \quad (6.59)$$

where we've assumed the generator has the functional form $V_G \sin(\omega t)$. We take a Laplace transform of Equation 6.59 and solve for $\mathcal{L}\{I_{LC}(t)\}(s)$:

$$\mathcal{L}\{I_{LC}(t)\}(s) = \frac{V_G \omega}{R_0 Q_c \omega_0} \left[\frac{s}{s^2 + \omega^2} \right] \left[\left(\frac{s}{\omega_0} \right)^2 + \left(\frac{s}{\omega_0 Q_c} \right) + 1 \right]^{-1}, \quad (6.60)$$

where s is a complex number, and we've assumed $\dot{I}_{LC}(t=0) = I_{LC}(t=0) = 0$. We numerically perform an inverse Laplace transformation of Equation 6.60 to solve for $I_{LC}(t)$. The output voltage is given by:

$$V_O(t) = \frac{|V_G|}{2} [\sin(\omega t) - R_0 I_{LC}(t)], \quad (6.61)$$

where $|V_G|$ sets the number of photons in the cavity when the qubit is in the $|0\rangle$ state, as defined by Equation 6.54. For direct comparison, we consider the same cavity-qubit system as the previous section, with $\omega^{10} = 6.6$ GHz, $Q_c = 5000$, $n_{sys} = 1$, $R_0 = 50 \Omega$, $g_{10}/2\pi = 33$ MHz, and the same dispersive shift plotted in Figure 6.7(b). Note that the dispersive shift does change with the number of photons in the resonator, a fact ignored in this analysis. In Figure 6.8, we plot the envelope of $V_O(t)$ when the qubit is in the $|0\rangle$ and $|1\rangle$ state, for $\Delta_0 = -600$ MHz and $\Delta\omega^{10} = 0$. At $\tau_m = 0$ the output voltage $V_O(t) = V_G/2$, as expected. After roughly $\tau_m = 1.5 \mu s$, the amplitudes of each state dependent $V_O(t)$ reach their steady state solution.

The amplitude $|V_O|$ and phase θ are calculated with a Fourier transform of $V_O(t)$ over an integration time τ_m . The SNR is calculated from Equations 6.53 and 6.55. In Figure 6.9(a), we plot the SNR of the cavity-qubit readout for $\tau_m = 600$ ns. Compared to the steady state solution of Figure 6.6(b), the SNR is noticeably reduced, and the maximum SNR occurs when the qubit is tuned several hundred MHz closer to the resonance of the cavity. A comparison between the steady state and modified SNR is plotted in Figure 6.9(b) as a function of τ_m . For long times both solutions converge with a $\sqrt{\tau_m}$ dependence. However, the SNR and in consequence the measurement fidelity is limited by the ring-up time of the cavity. A larger κ is necessary for a fast measurement, but to maximize SNR the dispersive shift 2χ must also increase with κ^2 . Unfortunately, an increase in χ and κ cause the qubit to relax via the Purcell effect, with the Purcell relaxation rate γ_{purc} [31, 33]:

²Gambetta et al.[114] argue that the maximum SNR occurs at $\kappa = 2\chi$, but their analysis does not take the weak anharmonicity of the qubit and the ring-up of the cavity into account. As shown in the last two sections of this thesis, designing for a maximum SNR depends on the a web of qubit-cavity parameters. However, keeping κ close to 2χ is a good rule of thumb.

$$\gamma_{\text{purc}} = \kappa g^2 / \Delta^2 \approx \kappa \chi^2 / \Delta. \quad (6.62)$$

The eigenstates of the Jaynes-Cummings Hamiltonian have a small photonic component leaking out of the cavity, resulting in qubit relaxation. However, there are design strategies that provide Purcell protection of the qubit [115].

6.3.5 Readout Fidelity

At the end of the day, we are interested in maximizing the readout fidelity of the qubit. The fidelity is determined by preparing and measuring the qubit in both the $|0\rangle$ and $|1\rangle$ state. We take a large number of measurements, allowing us to estimate the conditional probability of measuring the qubit in the $|0\rangle$ state when prepared in the $|1\rangle$ state $P(|0\rangle||1\rangle)$, and the initialization error where the qubit was left in its $|0\rangle$ state but measured as a $|1\rangle$ state $P(|1\rangle||0\rangle)$, giving the following definition for readout fidelity:

$$F = 1 - P(|1\rangle||0\rangle) - P(|0\rangle||1\rangle). \quad (6.63)$$

F depends on how well the qubit is initialized, the fidelity of the qubit gates, the relaxation rate between the $|1\rangle$ and the $|0\rangle$ state, and the SNR of the amplification chain. Gambetta *et al.* [116] studied how the readout fidelity depends on SNR, taking into account qubit relaxation and different demodulation schemes³. For the simple rectangular window considered above, one can approximate the fidelity with the following expression [116]:

³To draw parallels with [116], their $r_{sn} = T_1 B(SNR)^2$.

$$F \approx \exp\left(-\frac{\tau_m}{2T_1}\right) \operatorname{erf}(SNR/\sqrt{2}), \quad (6.64)$$

where [116] assumes perfect qubit initialization, a QND measurement, and no gate errors. The calculated SNR of Figure 6.9 with a $T_1 = 10 \mu\text{s}$ is plugged into Equation 6.64, giving the estimated fidelity as a function of $\Delta\omega^{(0)}$ and cavity-qubit detuning Δ_0 . As plotted in Figure 6.10, an amplification chain that adds $n_{sys} = 1$ can achieve a readout fidelity of 0.98 with a measurement time of 600 ns. The fidelity can easily exceed 0.99 for the same n_{sys} and at shorter measurement times by increasing T_1 and with the design changes discussed at the end of the previous section.

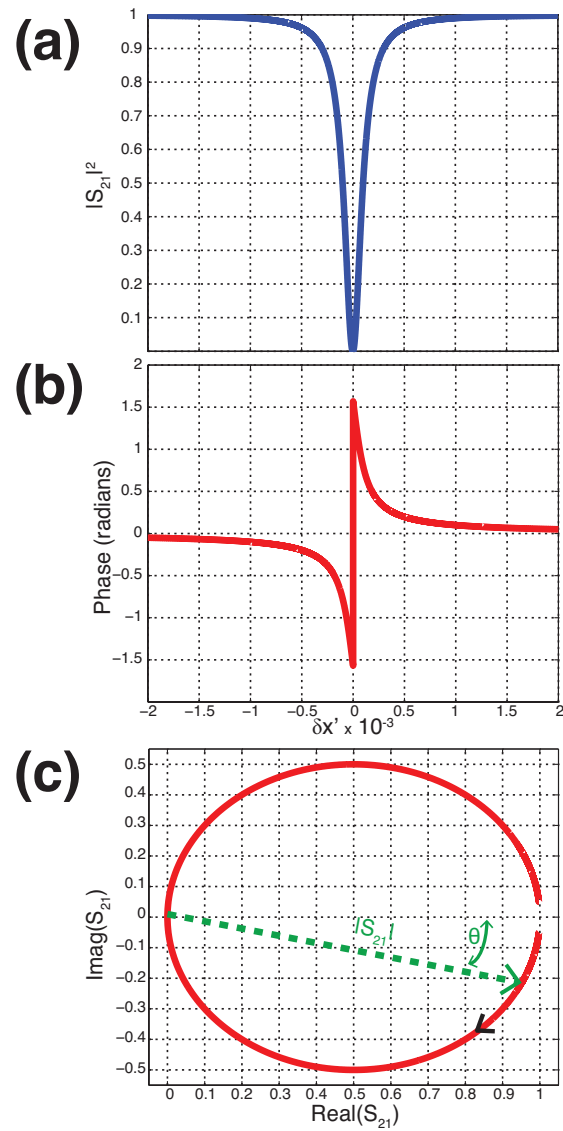


Figure 6.5: Magnitude-squared (a) and phase (b) of the quarter-wave resonator S_{21} as a function of $\delta x'$. The quadrature components (c) are plotted for different frequencies, where the black arrow points in the direction of increasing frequency. A $Q_c = 5000$ is used for this figure.

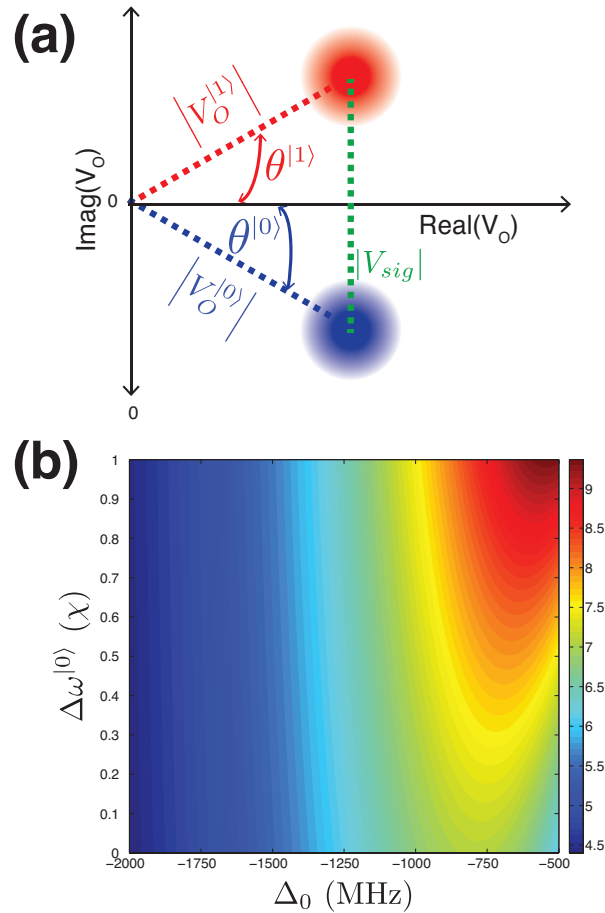


Figure 6.6: **(a)** The complex output voltage V_O for the two dressed cavity states. $|V_{sig}|$ is the magnitude of the voltage difference between the two states. The measured voltage has a gaussian distribution with standard deviation σ that is equal to the RMS voltage that defines the noise on the signal. **(b)** The steady state SNR as a function of detuning from the $|0\rangle$ cavity resonance $\Delta\omega^{(0)}$ and cavity-qubit detuning Δ_0 . The SNR was calculated for $\bar{n} = n_{crit}$, $\omega^{(0)}/2\pi = 6.6$ GHz, $Q_c = 5000$, $n_{sys} = 1$, and a measurement time of 600 ns. The calculated dispersive shift χ is plotted in Figure 6.7(b).

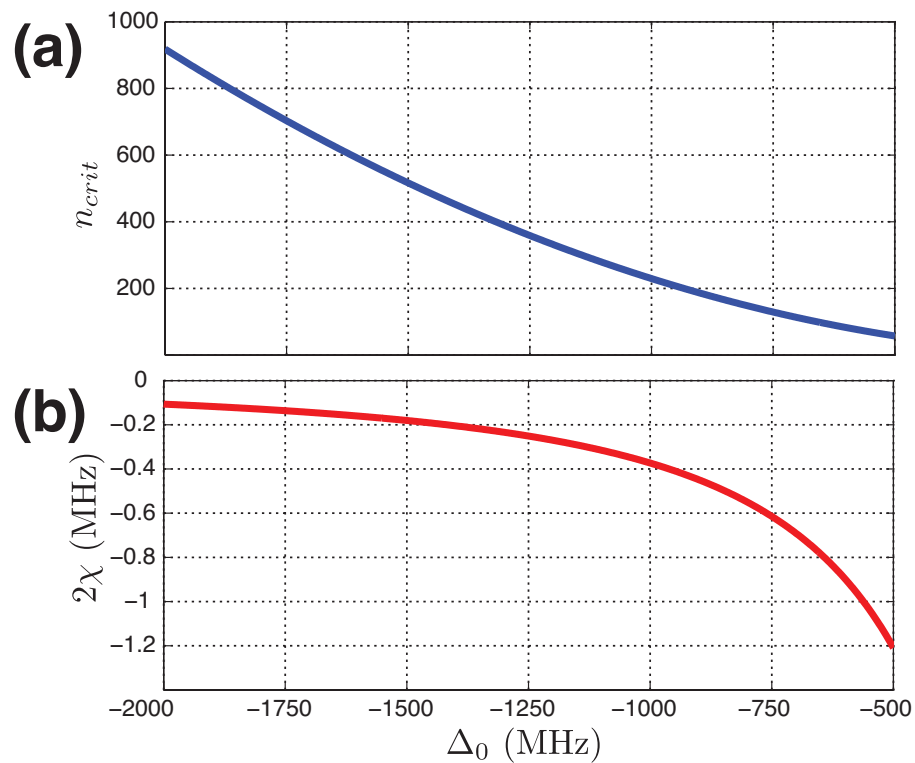


Figure 6.7: The calculated critical photon number n_{crit} (a) and the dispersive shift 2χ (b) are plotted as a function of qubit-cavity detuning Δ_0 . For the calculations of this figure we assume a $\omega^{(0)}/2\pi = 6.6$ GHz and the following reasonable anharmonicities: $\alpha_1 = \omega_{21} - \omega_{10} = -230$ MHz and $\alpha_2 = \omega_{23} - \omega_{21} = -250$ MHz.

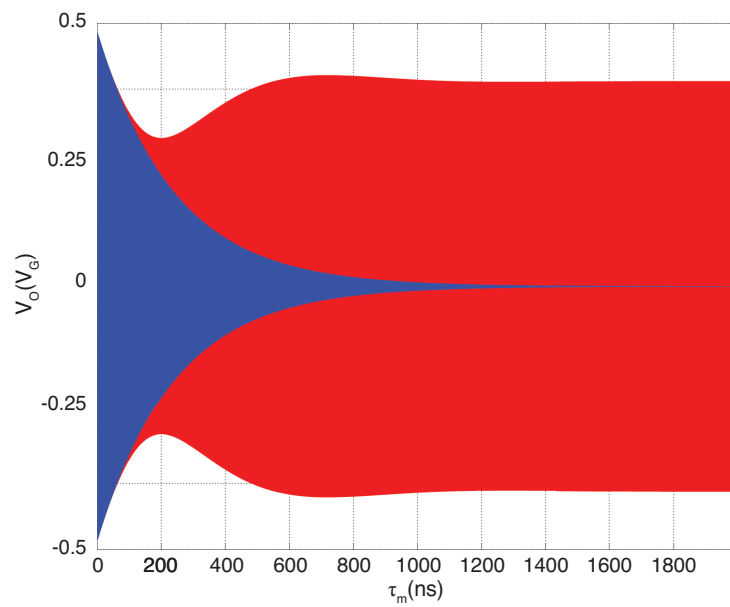


Figure 6.8: $V_O(t)$ for driven resonator when the qubit is in the $|0\rangle$ state (blue) and the $|1\rangle$ state (red).

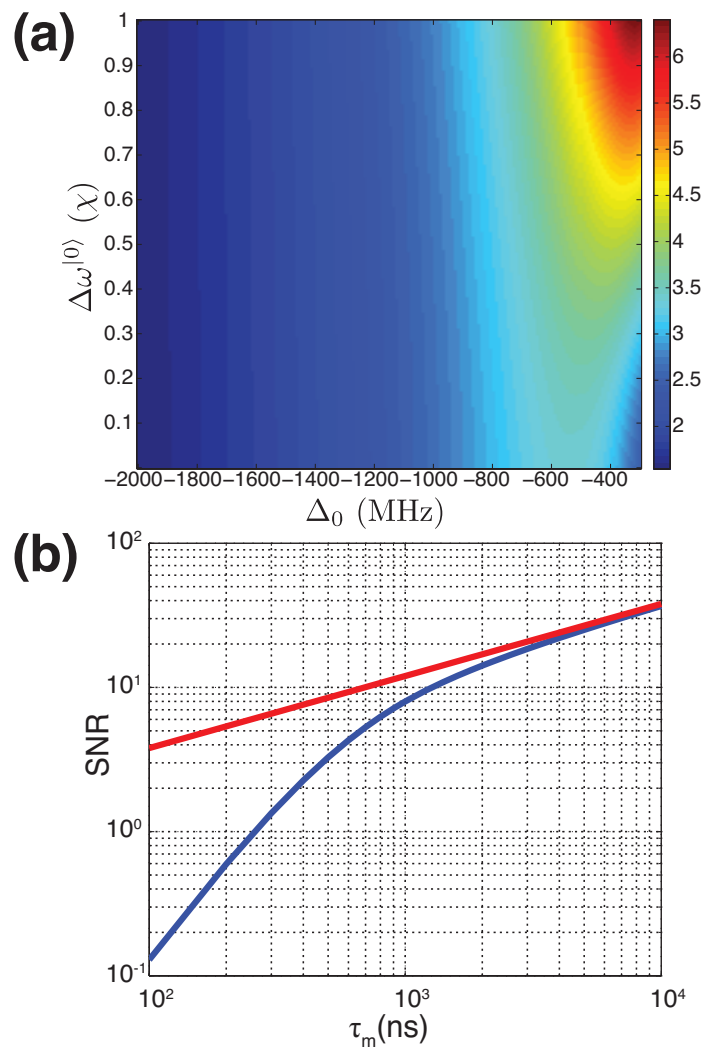


Figure 6.9: **(a)** The modified SNR as a function of detuning from the $|0\rangle$ cavity resonance $\Delta\omega^{(0)}$ and cavity-qubit detuning Δ_0 . The SNR was calculated for $\bar{n} = n_{crit}$, $\omega^{(0)}/2\pi = 6.6$ GHz, $Q_c = 5000$, $n_{sys} = 1$, and an integration time of 600 ns. The calculated dispersive shift χ is plotted in Figure 6.7(b). **(b)** A comparison of the steady state SNR (red) to the modified SNR (blue) as a function of τ_m , calculated at $\Delta_0/2\pi = -600$ MHz and $\Delta\omega^{(0)} = \chi$.

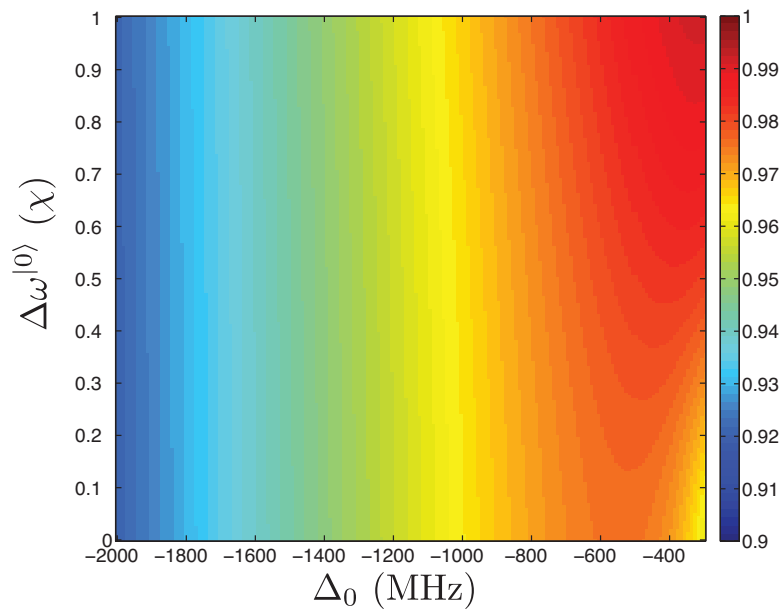


Figure 6.10: The estimated fidelity for a measurement time of 600 ns and a relaxation rate of $T_1 = 10 \mu\text{s}$, calculated with the SNR of Figure 6.9(a) and Equation 6.64.

Chapter 7

Qubit Measurements

In this chapter, we discuss our efforts to read out a qubit with a SLUG amplifier. This chapter also serves as a guide for how to characterize an Xmon qubit for the first time. In Section 7.1, we give an overview of the measured Xmon qubit. In Section 7.2, we go over the experimental setup for qubit readout, highlighting the role of the room temperature electronics. We probe the state of the resonator and the qubit in Sections 7.3 and 7.4, respectively. In Sections 7.5 and 7.6, we calibrate a simple qubit gate and explore the coherence of the qubit. The number of photons in the cavity as a function of cavity drive power is measured with the Stark shift in Section 7.7. In Section 7.8, we discuss the heterodyne measurement, and in Sections 7.9 and 7.10 we determine the measurement fidelity of the qubit when read out without and with the SLUG, respectively. In Section 7.11, we take a step back and discuss some simple adjustments that can be made to improve the measurement fidelity, and we outline some future experiments that we would like to carry out..

7.1 UCSB Xmon

The Martinis group at UCSB was kind enough to lend us an ‘Xmon’ qubit’ [32] – a design based on the planar transmon that minimizes radiative loss and reduces coupling to material-related defects on the chip. The design of the Xmon, pictured in Figure 7.1, was motivated by recent advances with high quality-factor coplanar resonators [27]. Similar to the transmon, the heart of the Xmon is a frequency tunable aluminum qubit comprised of two submicron Josephson junctions in a low-inductance loop; this SQUID loop is inductively coupled to an external bias line with a designed mutual inductance $M = 2.2$ pH. The energy scales of the qubit were chosen to minimize charge dispersion without sacrificing nonlinearity, with an $E_J/E_C \approx 95$ and an anharmonicity of 230 MHz.

The qubit is embedded in an uninterrupted groundplane, with four branches arranged in an X-pattern (hence the name); the coplanar capacitors suppress parasitic slotline modes at the perimeter of the resonators and control lines. One branch of the ‘X’ inductively couples to the qubit bias, while the remaining three ports capacitively couple to the qubit drive line, the readout resonator, and a quantum-bus used to mediate interactions with other qubits. The $50\ \Omega$ readout resonator is a short-circuited $\lambda/4$ coplanar waveguide with the voltage anti-node of the standing wave located at the same end as the qubit. The resonator is capacitively coupled to a $50\ \Omega$ feedline. The Martinis group have demonstrated energy relaxation times up to $T_1 = 44\ \mu\text{s}$ with devices from the same wafer as the device measured in this chapter. For a complete description of the Xmon qubit, please read Barends *et al.* [32].

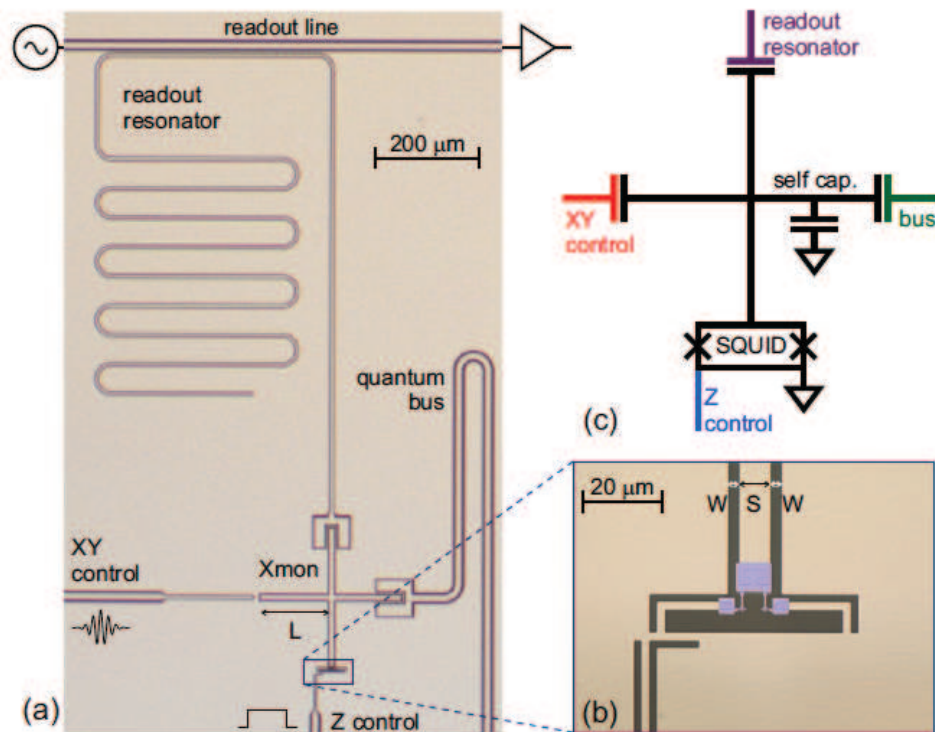


Figure 7.1: Picture of the UCSB-Martini's Xmon, stolen directly from Barends *et al.* [32]. Picture of the full Xmon circuit (a) the SQUID loop (b) with Z-control line. (c) The equivalent electrical schematic of the qubit island and its four-port coupler.

7.2 Experimental Setup

7.2.1 DR Wiring

We measure the Xmon in the DR at 40 mK using a similar cryogenic setup as the one used to measure the SLUG, described in Section 5.1.2. Illustrated in Figure 7.2, the cold stage of the DR is wired with a third coax relay; this gives us the ability to switch the Xmon in and out of the amplification chain. As discussed in the previous section, the Xmon chip has three input ports: a microwave line that probes the read-out resonator (ROin), a microwave line that performs qubit rotations (QDrive), and a flux bias line (Bias). A custom bias-T ties together a heavily filtered dc bias line (Xmon Bias)

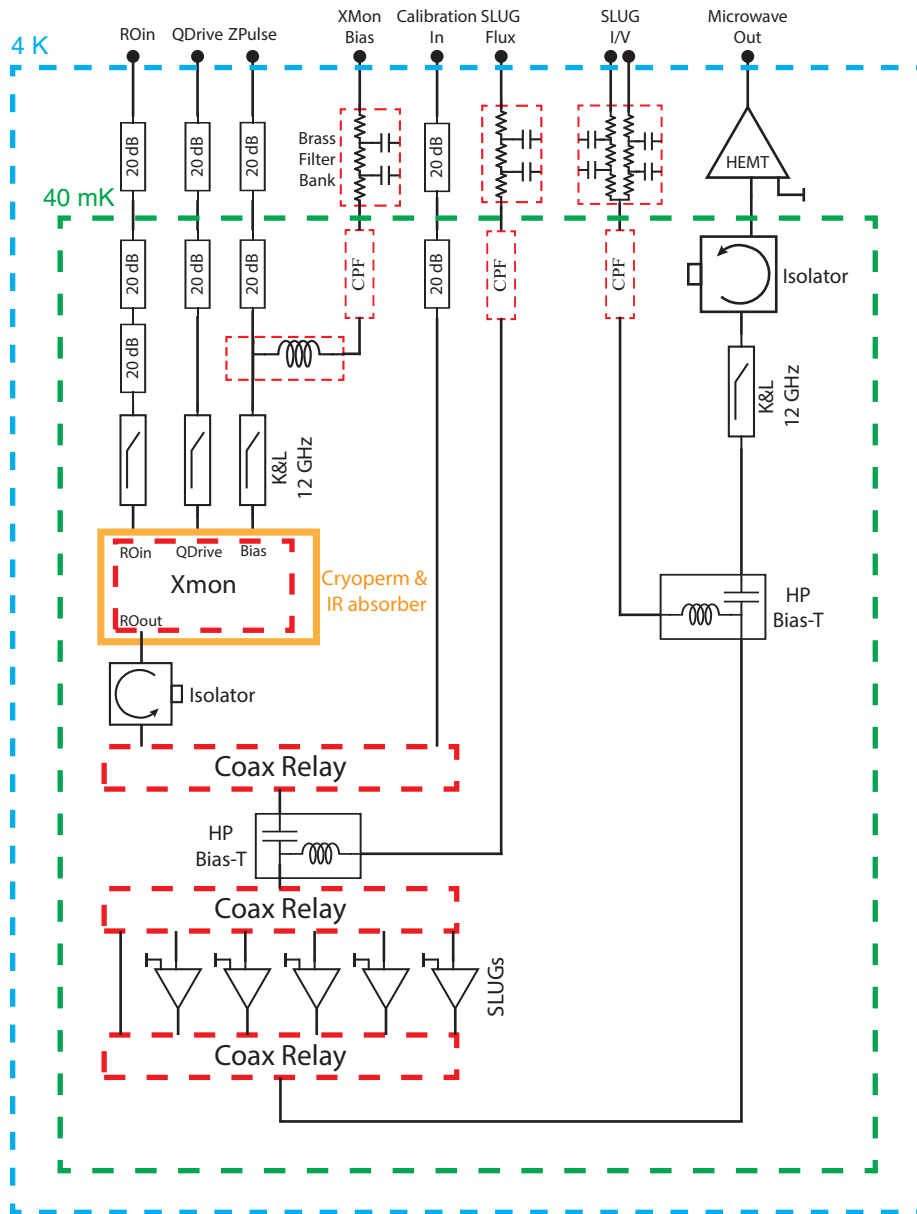


Figure 7.2: Wiring diagram of DR for measuring the Xmon with and without the SLUG amplifier.

for static control of the Xmon’s operating point, and a microwave line that allows us to perform precise Z-rotations by momentarily changing the bias point of the qubit. Each channel is appropriately attenuated and filtered at 40 mK before entering the qubit box.

Quasiparticle generation from stray infrared light [117] and ambient magnetic fields on the order of milligauss [27] are major sources of decoherence in superconducting qubits. We minimize the magnetic field at the surface of the qubit by placing the sample box in a high magnetic permeability Cryoperm shield. Additionally, all the screws and coax connectors within the shield were made with non-magnetic brass. The sample is enclosed in a light-tight box to prevent infrared radiation from reaching the qubit. This is accomplished by enclosing the sample stage in a large 40 mK copper can painted with a “black coating” that absorbs stray light. The “black coating” consists of a mixture of silica powder, fine carbon powder, and 1 mm SiC grains in stycast epoxy, having an absorptivity of 90% over a wide angle in the 0.3-2.5 THz range [118]. The same coating is applied to the inside of the Cryoperm shield for an additional stage of absorption. An additional isolator sits between the readout port of the Xmon and the coax relay, preventing any noise at the input of the SLUG amplifier from reaching the qubit. The rest of the wiring is identical to the SLUG setup already described.

The qubit is mounted in an aluminum box that embraces the same design philosophy as the SLUG box, pictured in Figure 5.2(a). The superconducting aluminum provides additional shielding, and a thin coat of black stycast epoxy is painted on the inside of the lid for additional protection against stray infrared radiation. The qubit chip, pictured in Figure 7.3, contains three qubits (Q0, Q1, Q2) coupled to three readout resonators ($R0 \approx 6.4$ GHz, $R1 \approx 6.5$ GHz, $R2 \approx 6.6$ GHz). There are two additional check resonators (R3, R4) that are not coupled to a qubit. Unlike the Xmon described in the previous section, no quantum bus exists on this chip.

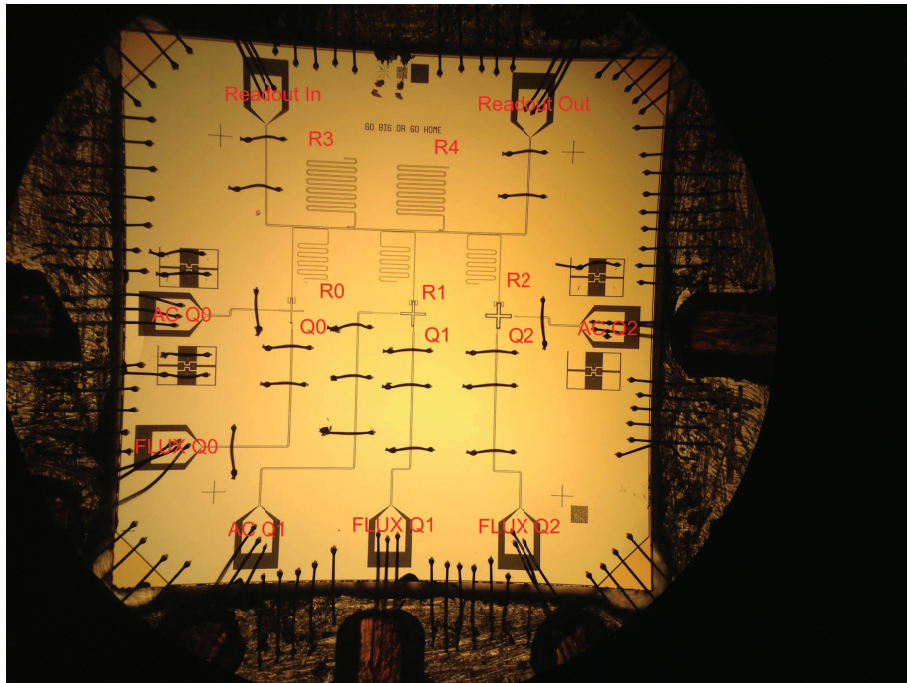


Figure 7.3: Picture of the Xmon chip we are measuring (photo taken by Julian Kelley, UCSB). We measure Q2 in this chapter.

7.2.2 Qubit Control Electronics

As diagramed in Figure 7.4, the microwave control and readout pulses are generated and shaped using off-the-shelf microwave components along with custom FPGA-based signal generators¹. Each FPGA board controls two 14-bit digital-to-analog converters (DACs) with nanosecond resolution, allowing us to synthesize waveforms of frequencies up to 500 MHz with amplitudes up to 1 V. The differential outputs of each DAC are filtered and then fed into a differential amplifier. The DAC filters are chosen to give the pulse shapes a Gaussian step edge, which prevents the generation of high frequency spectral components that can reduce qubit gate fidelity.

¹Read Marcus Ansmann's thesis for a detailed overview of the custom electronics and the control software [119].

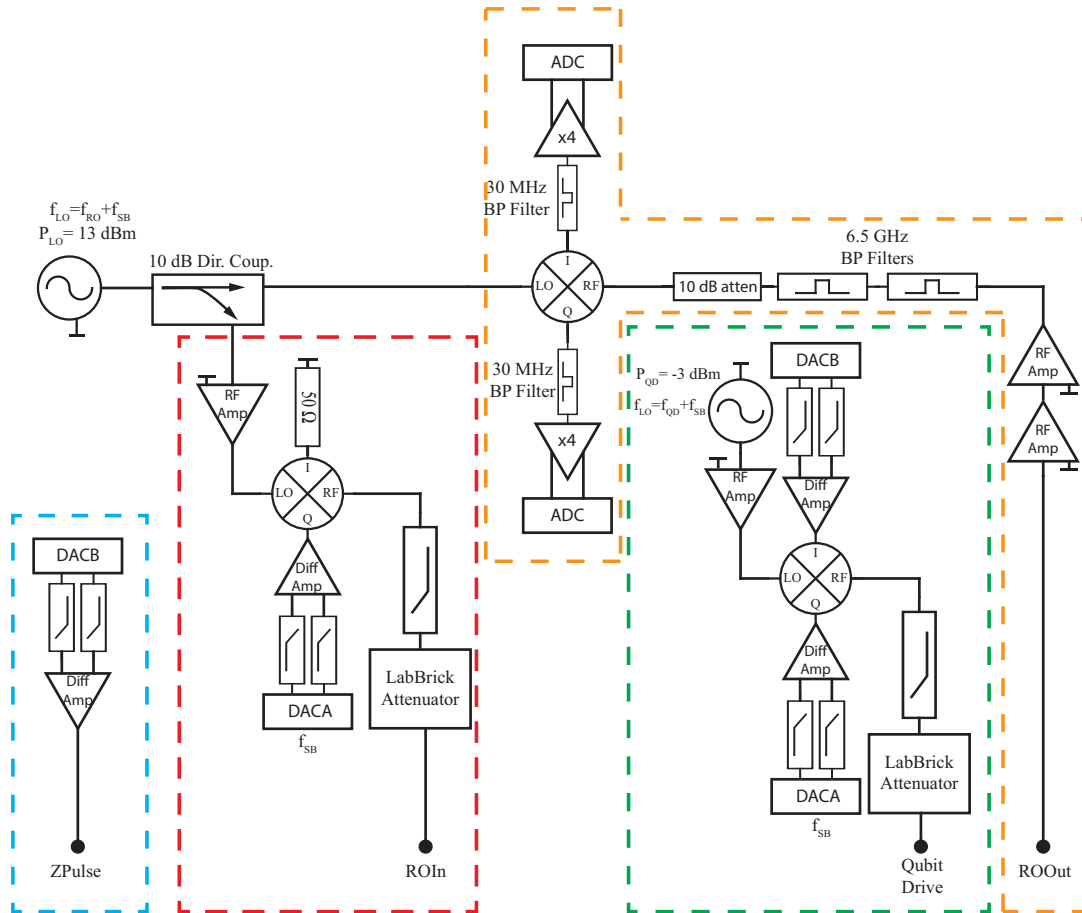


Figure 7.4: Room temperature qubit control electronics.

The I/Q mixer serves two purposes in our measurement setup. We generate microwave control pulses with nanosecond precision by mixing a control pulse generated by the DACs (I and Q port of the mixer) with a high frequency local oscillator (LO port), giving us full control over the phase and amplitude of the signal going into the fridge (RF port on the mixer), where $V_{RF} = I(t) \sin(\omega_{LO} t) + Q(t) \cos(\omega_{LO} t)$. We typically excite the qubit and apply the readout signal by modulating the LO-signal with a low frequency sine wave generated by the DACs. For example, the DACs generate a signal with frequency f_{SB} on one quadrature of the mixer, then the output signal will have a spectral component at both $f_{LO} - f_{SB}$ and $f_{LO} + f_{SB}$ (with some leak through at f_{LO}). If needed, we can

remove one of the sidebands by either filtering or by generating the appropriate tone on the other quadrature.

We also use the mixer to extract the quadrature components [see discussion in 6.3] of an RF signal, a useful technique for digitizing the amplitude and phase of a high frequency signal. Heterodyne detection down-converts the high-frequency signal at the rf-port to an intermediate-frequency for easy signal processing. We use a custom FPGA-based analog-to-digital converter ADC card to capture the two quadratures of the down-converted signal. The FPGA on the card picks out the spectral components of the downconverter signal that contains information about the qubit. We use additional lowpass and bandpass filters in the readout chain to minimize the voltage noise recorded by the ADCs. The LabBrick attenuators are digital attenuators controlled via USB.

7.3 Readout Cavity Spectroscopy

In the next few sections, we discuss the procedure for characterizing the Xmon once it has been cooled down to the base temperature of the DR. We first spectroscopically probe the readout cavity using the vector network analyzer (VNA). In the dispersive limit, where the average number of photons in the cavity is $\bar{n} < n_{crit}$, the $|0\rangle$ state qubit modifies the resonance ω_r of the bare cavity by χ_0 ²:

$$\omega_r - \omega^{|0\rangle} \approx \chi_0 = \frac{g_{10}^2}{\Delta_0} \quad (7.1)$$

where $\Delta_0 = \omega_{10} - \omega_r$, $\omega^{|0\rangle}$ is the resonance of the cavity when the qubit is in the $|0\rangle$ state, and g_{10} is the dipole coupling constant between the cavity and the ω_{10} mode of the qubit.

²The resonator is actually modified by S_0 of Equation A.18, but in the dispersive limit $S_0 \approx \chi_0$.

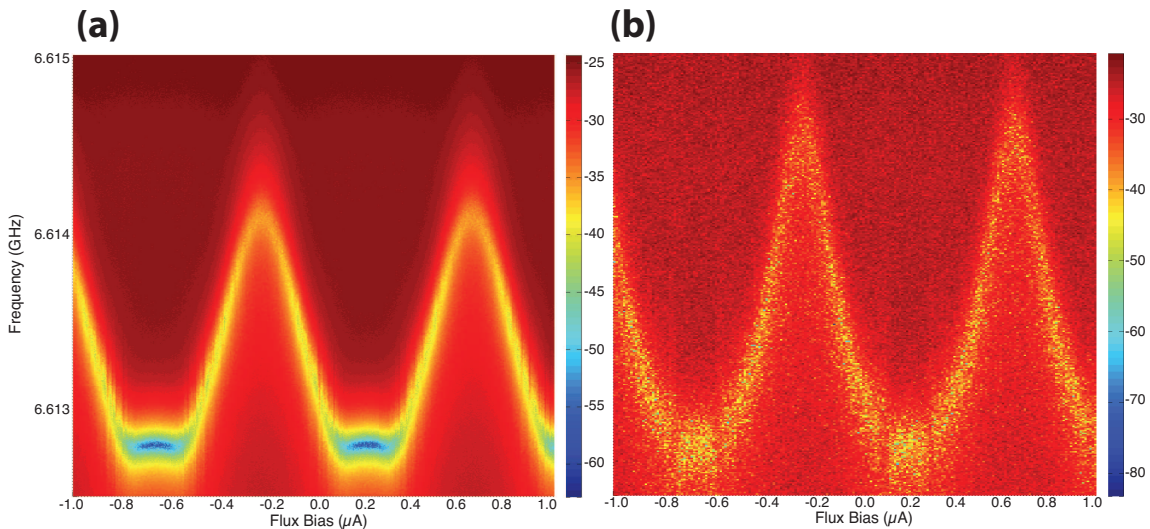


Figure 7.5: Transmitted power through the readout channel as a function of probe frequency and flux bias for a VNA power of -30 dBm **(a)** and -70 dBm **(b)**. The transmitted power is in units of dB.

In Figures 7.5(a) and (b), we plot the power transmitted through the readout channel as a function of probe frequency and qubit flux bias. The flux bias tunes the Josephson energy E_J , which consequently modifies the frequency of the qubit.

If the cavity-qubit system is driven at a high power, the cavity response becomes strongly nonlinear, causing $\omega^{(0)}$ to approach ω_r [120, 121, 122]. A large number of photons in the cavity ($\bar{n} \gg n_{crit}$) causes the cavity to behave classically – the cavity is no longer influenced by the presence of the qubit. A “punch out” calibration returns χ_0 ; a separate measurement of f_{10} allows us to extract g_{10} from the measured χ_0 . In Figure 7.6 (a), we plot transmitted power through the readout channel as a function of probe frequency for different VNA powers. In Figure 7.6(b), we plot the cavity response at low and high driving power, with a measured $\chi_0/2\pi = 1.49$ MHz. We fit the transmitted power to extract the intrinsic and coupling quality factors of the cavity, Q_i and Q_c respectively

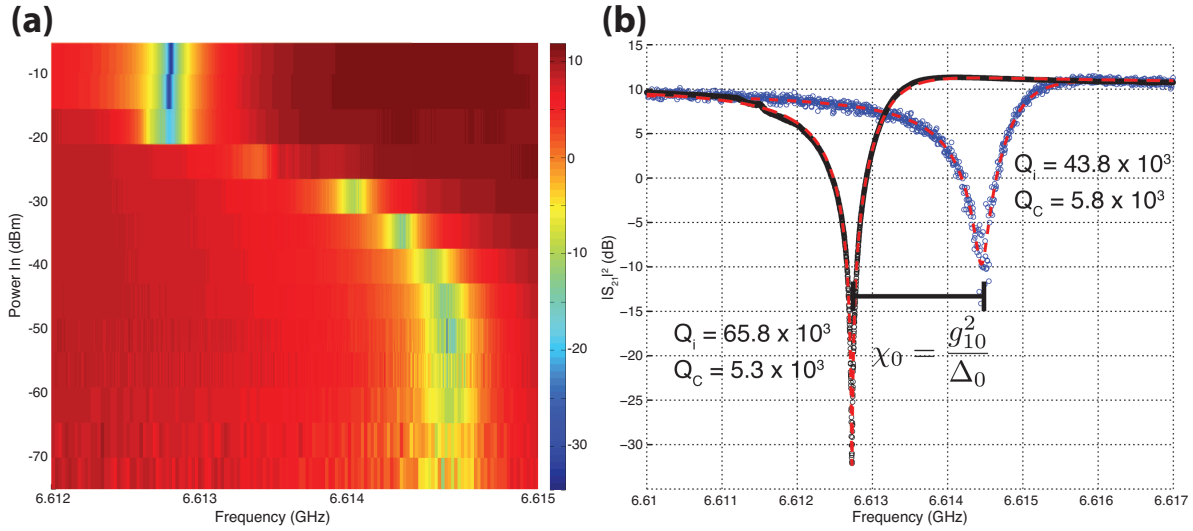


Figure 7.6: This figure illustrates the “punch out” calibration of the readout cavity. (a) Line cuts of the transmitted power through the readout channel for different VNA powers. (b) The cavity response when weakly driven (blue) and strongly driven (black). The transmitted power is fitted to extract the quality factors of the cavity Q_i and Q_c .

[113]. At low powers, with $\bar{n} \ll n_{crit}$, the cavity has a measured $Q_i = 43.8 \times 10^3$ and $Q_c = 5.8 \times 10^3$.

7.4 Qubit Spectroscopy

We set the readout probe tone to $\omega_p = \omega^{|0\rangle}$, and the readout power is chosen such that $\omega^{|0\rangle} \approx \omega_r - \chi_0$. Probing on resonance gives maximum distinguishability between the $|0\rangle$ and $|1\rangle$ state when monitoring the amplitude of the output voltage. The qubit frequency ω_{10} is determined by spectroscopically probing the qubit, where the response of the readout resonator is monitored as a function of qubit drive frequency. We precisely control the qubit and readout microwave drive, as shown in the pulse sequence illustration in Figure 7.7(a), where $\tau_{\mu w} = 10 \mu s$ is the duration of the qubit microwave drive tone, and $\tau_m = 1 \mu s$ is the duration of the microwave measurement tone. The same pulse sequence

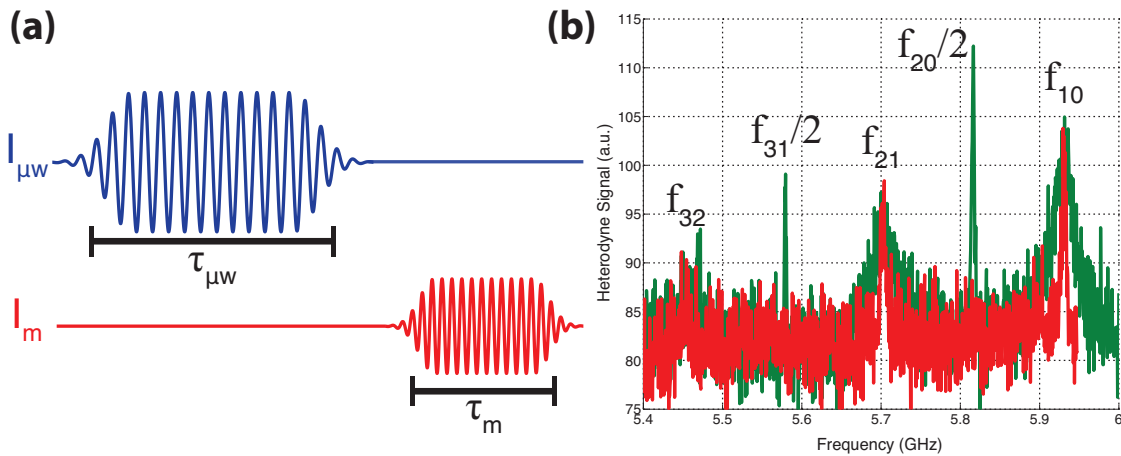


Figure 7.7: The pulse sequence **(a)** and averaged heterodyne signal **(b)** for qubit spectroscopy. The green data was taken at a high qubit drive power. $I_{\mu w}$ is the qubit drive pulse, and I_m is the measurement pulse.

is repeated on the order of 1000 times and the average magnitude of the heterodyne voltage is recorded. We choose $\tau_{\mu w}$ to be on the order of T_1 , ensuring a measurable percentage of the ensemble are $|1\rangle$ states. The measurement time τ_m is chosen to be long enough for decent SNR but much shorter than T_1 to minimize $|1\rangle$ state relaxation.

In Figure 7.7(b), we plot the averaged heterodyne voltage as a function of qubit drive frequency for two different qubit drive powers. If we increase the power of the qubit microwave drive, we can excite two photon transitions between the $|0\rangle$ and $|2\rangle$ state in addition to higher-order transitions; when the qubit drive power is reduced higher-order transitions vanish and the f_{10} line width reduces. The measured qubit transition is Lamb shifted by $\omega_{10} + \chi_0$; however, in the dispersive limit the Lamb shift will not change our calculations of the Stark shift and g_{10} by a significant margin.

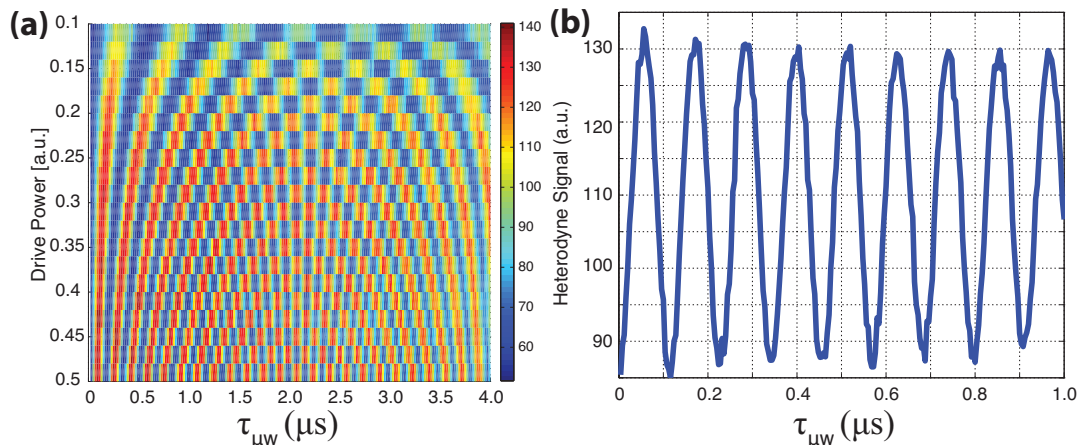


Figure 7.8: Rabi oscillations with the (a) averaged heterodyne voltage as a function of drive power and qubit microwave drive time $\tau_{\mu w}$. (b) Rabi oscillations at one power with a π -pulse time of $\tau_{\pi} = 60$ ns.

7.5 Rabi Oscillations

Rabi oscillations, shown in Figures 7.8(a) and (b), give us a calibration of the qubit drive pulse amplitude and duration needed to flip the $|0\rangle$ state of the qubit to the $|1\rangle$ state – a gate called a π -pulse since the state of the qubit rotates 180° about either the x or y-axis. The pulse sequence is the same as shown in Figure 7.7(a), but we sweep over both the qubit drive power and $\tau_{\mu w}$. As illustrated by the data in Figure 7.8(a), at larger qubit drive powers the frequency of the Rabi oscillations gets larger. The speed of π -pulse is fundamentally limited by the anharmonicity of the qubit, which is on the order of $\alpha/2\pi = f_{21} - f_{10} \approx 250$ MHz, for a minimum pulse duration of approximately $2\pi/\alpha = 4$ ns. In practice, we aim to keep τ_{π} much shorter than T_1 but longer than the anharmonic limit. The qubit drive amplitude of the data in Figure 7.8(b) gives a $\tau_{\pi} = 60$ ns.

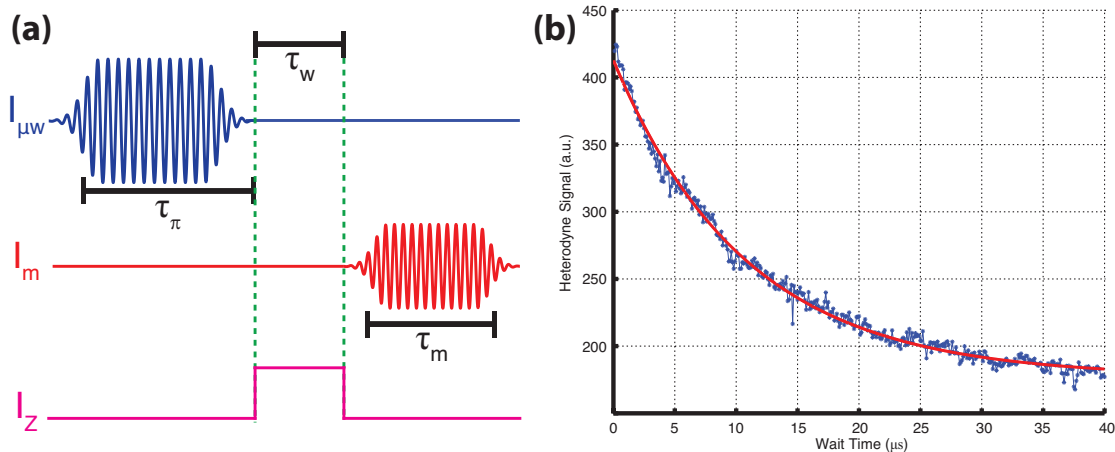


Figure 7.9: **(a)** The pulse sequence used to measure the energy relaxation time constant T_1 . The qubit is prepared in the $|1\rangle$ with a π -pulse of duration τ_π . The qubit is then measured after wait time τ_w . The optional z-pulse changes the bias of the qubit during the wait time interval, useful for swap spectroscopy. **(b)** The measured heterodyne voltage as a function of τ_π , with a $T_1 = 10.8 \mu s$.

7.6 Qubit Decoherence

Decoherence refers to the assorted processes by which coupling to the environment cause the state of the qubit to degrade, consisting of two parts: dephasing and relaxation. Computationally, decoherence results in random-rotations about the three axes of the Bloch-sphere, scrambling the prepared state of the qubit. Dephasing describes rotations about the z-axis caused by noise in the control parameters that define the Hamiltonian of the qubit. For example, flux noise of the two-junction SQUID loop results in E_J fluctuations and consequently fluctuations in ω_{10} [123]; fluctuations in ω_{10} cause the state vector to randomly rotate about the z-axis. Relaxation describes the process by which the $|1\rangle$ state of the qubit loses energy to the environment and decays to the $|0\rangle$ state. In the language of NMR, decoherence is benchmarked by the exponential decay times T_1 and T_2 : T_1 describes the lifetime of a qubit prepared in the $|1\rangle$ state, while T_2 describes the lifetime of qubit prepared at the equator of the Bloch sphere. The state

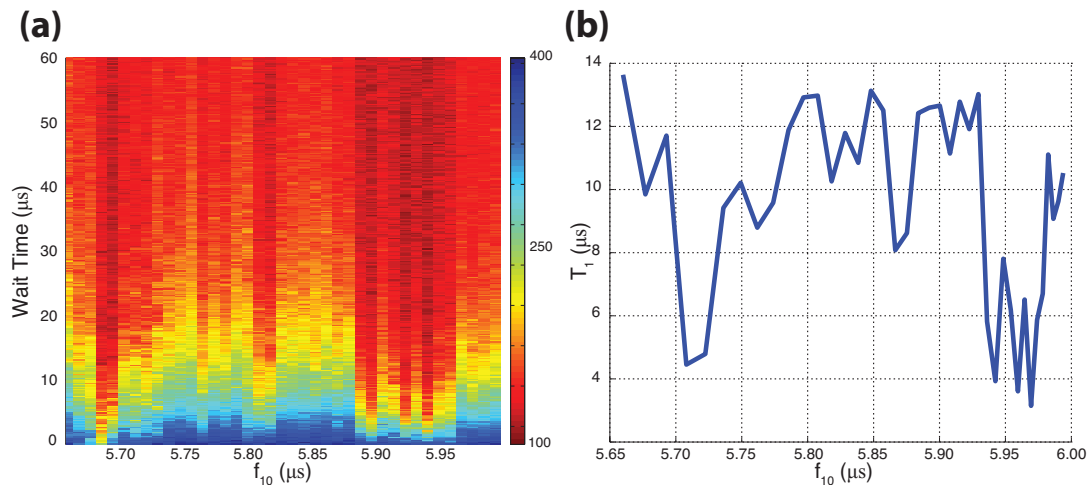


Figure 7.10: Swap spectroscopy experiment. In (a), we plot the heterodyne signal as a function of wait time τ_w and qubit frequency f_{10} . We fit each trace to extract T_1 as a function of f_{10} , shown in (b).

prepared in the x-y plane of the Bloch sphere is sensitive to both energy relaxation and dephasing with T_2 given as:

$$\frac{1}{T_2} = \frac{1}{2T_1} + \frac{1}{T_\phi}, \quad (7.2)$$

where T_ϕ is the dephasing time constant. In the absence of dephasing, the measured T_2 is set by the relaxation rate.

We measure T_1 with the pulse sequence illustrated by Figure 7.9(a), where the $|1\rangle$ state is prepared with a calibrated π -pulse of duration τ_π , and we wait a time τ_w before measuring the state of the qubit. An ensemble average of the qubit state is recorded as a function of τ_w by repeating the pulse sequence on the order of five-thousand times. As plotted in Figure 7.9(b), the heterodyne voltage is fit to an exponential decay function, giving us access to T_1 .

The energy relaxation rate depends on the qubit frequency ω_{10} , where we observe dramatic changes in T_1 over a small range of qubit biases. We perform a swap-spectroscopy scan in qubit bias using the pulse sequence of Figure 7.9(a), where the bias of the qubit is adjusted with a z-pulse of variable amplitude between state preparation and qubit readout. The heterodyne readout signal as a function of wait time τ_w and qubit frequency f_{10} is plotted in Figure 7.10 (a). We fit the data at each bias point to extract T_1 as a function of f_{10} [Figure 7.10(b)]; the qubit exhibits a fine structure of variable relaxation rates. In order to investigate the bias dependence in T_1 , we perform fine qubit spectroscopy using the same pulse sequence of Figure 7.7(a), except we change the bias using the z-pulse control line when driving the qubit. As plotted in Figure 7.11, f_{10} shows the expected dependence on qubit bias, varying smoothly without any noticeable energy splittings at the qubit frequencies with reduced T_1 times. The absence of avoided level crossings indicate the absence of strongly coupled defects [26]. As Barends *et al.* [32] explain, the fine structure of the relaxation rate is consistent with the qubit incoherently interacting with a sparse bath of surface defects present near the metal edges of the capacitor. Additionally, the UCSB group has consistently observed maximum relaxation rates of over 40 μs for the Transmon, suggesting that an element of our experimental setup is contributing to qubit relaxation. The major difference between our setup and the UCSB setup is our lack of infrared filters on the microwave lines of the qubit. They developed a 50 Ω infrared filter with little insertion loss that are place on all the microwave channels of the qubit. We are presently developing the same components and hope their addition will dramatically improve the lifetime of the qubit.

The Ramsey pulse sequence, illustrated in Figure 7.12(a), measures T_2^* of the qubit. The $|0\rangle$ state of the qubit is brought to the equator of the Bloch sphere with a calibrated $\pi/2$ -pulse of duration $\tau_{\pi/2} = \tau_\pi/2$. The state is allowed to dephase for a time τ_H until a

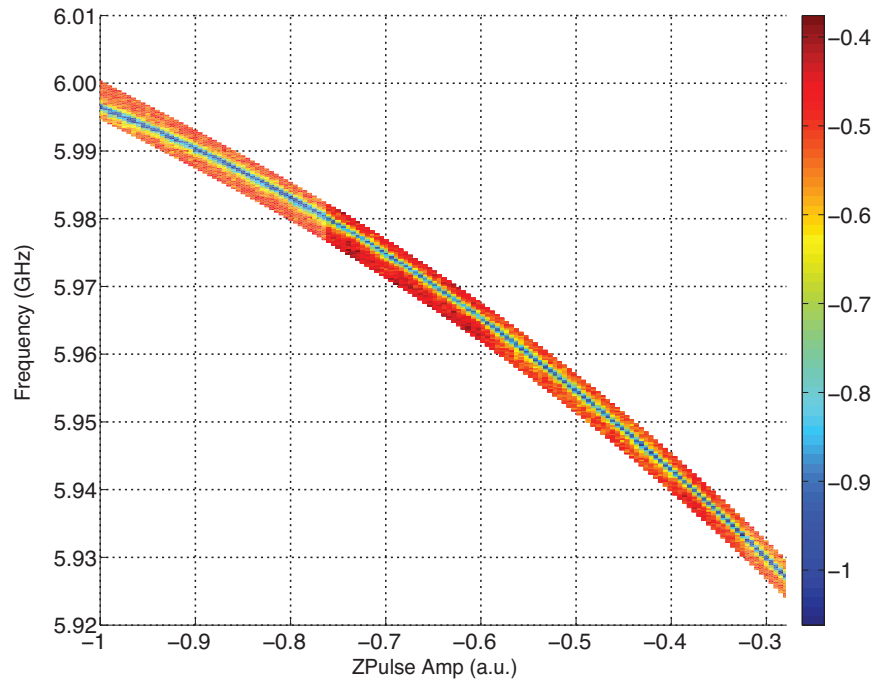


Figure 7.11: Fine spectroscopy scan of qubit. The averaged heterodyne signal as a function of qubit drive frequency and z-pulse amplitude is plotted.

second $\pi/2$ pulse places the state back on the z -axis of the Bloch sphere. We detune the qubit with a z -pulse, which allows the state of the qubit to precess about the z -axis at a frequency equal to the detuning of the qubit from the initial control pulse. The envelope of the resultant signal will decay with a time constant T_2^* , which is the parallel sum of two decay rates: $1/T_2^* = 1/T_2 + 1/T_2'$. We plot the results of a Ramsey experiment in Figure 7.12(b), with an extracted $T_2^* = 6.4 \mu\text{s}$. T_2 describes “homogenous broadening,” or the random rotations of the state vector present in every sequence of any gate operation. “Inhomogenous broadening,” described by T_2' , is a signature of low-frequency noise of the qubit bias over the course of acquiring the ensemble average. One can mitigate the effects of T_2' with a spin-echo measurement.

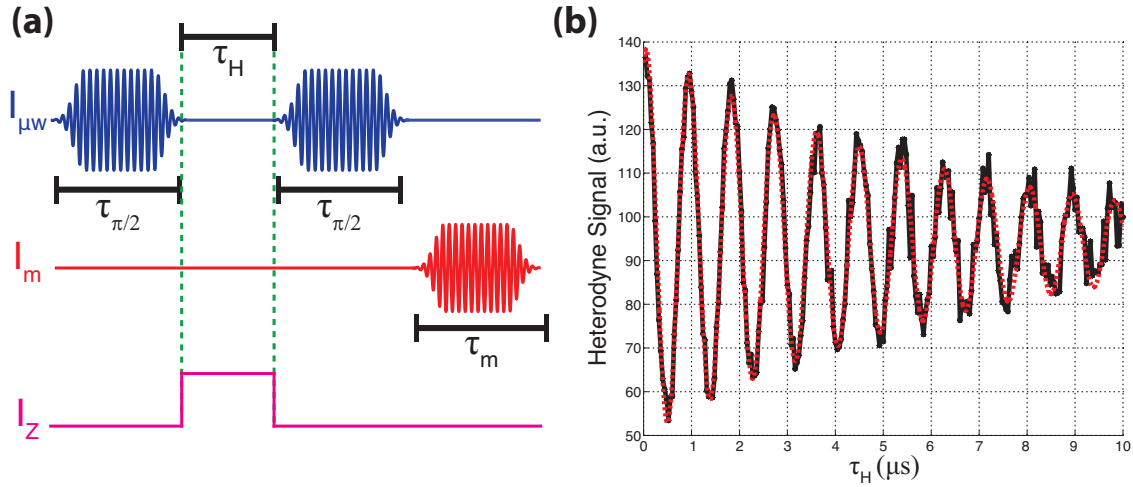


Figure 7.12: (a) The pulse sequence of the Ramsey experiment, where $\tau_{\pi/2}$ is the duration of a $\pi/2$ -pulse. (b) The measured Ramsey fringes with an extracted $T_2^* = 6.4 \mu s$.

7.7 Stark Shift Calibration

A calibration of the number of photons in the cavity as a function of drive power is necessary for benchmarking the readout of the qubit. As discussed in Appendix A, the qubit frequency ω_{10} will shift as a function of the average number of photons \bar{n} in the resonator. The pulse sequence for the Stark shift experiment, shown in Figure 7.13(a), drives the readout cavity for a duration longer than its ring-up time, ensuring that the cavity-qubit system is in the steady state. Once in the steady state, we perform qubit spectroscopy and measure the Stark shifted f_{10} . In Figure 7.13(b), we have stitched together the results of a number of Stark shift experiments for different drive voltages A_{Stark} . We fit each spectroscopic trace to a Lorentzian distribution and plot the change in f_{10} as a function of resonator drive, shown in Figure 7.14(a).

Using the measured g_{10} and the lowest three measured qubit energy splittings (f_{10} , f_{21} , and f_{32}), we calculate the Stark shift as a function of the average cavity photon population using Equation A.23. We fit the calculated Stark shift to the data in Figure 7.14(a), which

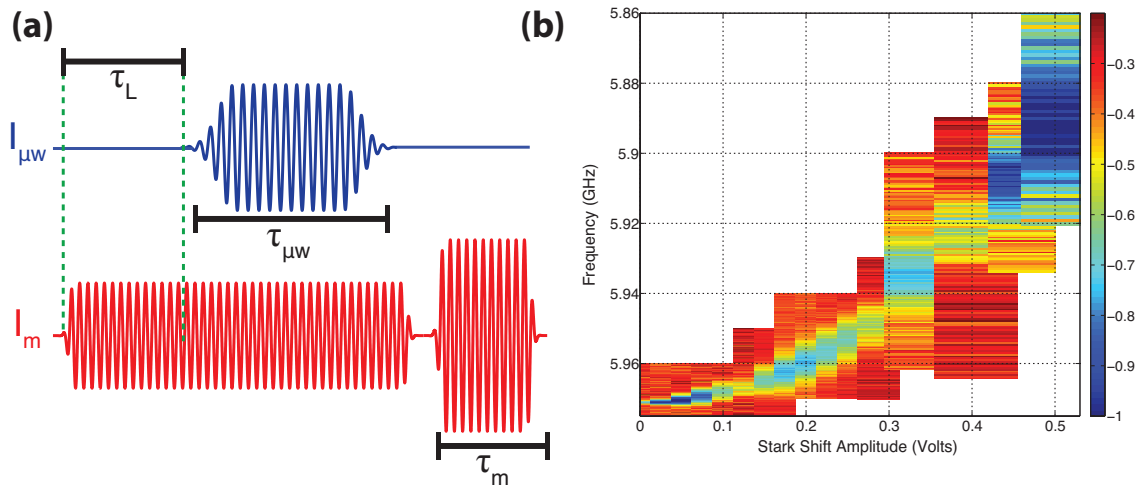


Figure 7.13: (a) The pulse sequence of the Stark shift experiment, where τ_L is the time the Stark shift pulse is on before qubit spectroscopy is performed. (b) The qubit spectroscopy data for a Stark shift pulse sequence with different amplitudes, where the Stark shift amplitude is the gate voltage generated by the DAC.

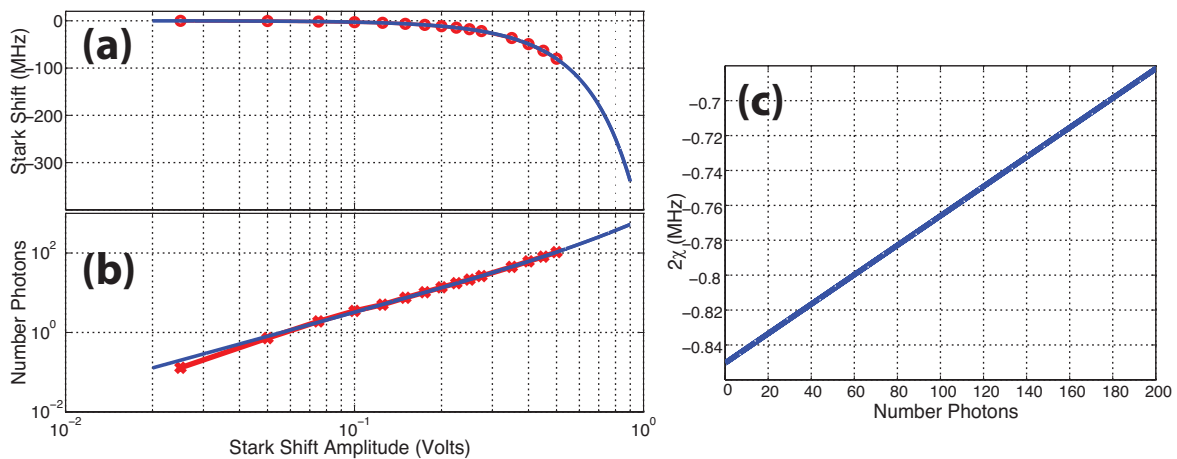


Figure 7.14: (a) The Stark shifted qubit frequency as a function of cavity drive amplitude, with the data plotted in red and the fit in blue. (b) The number of photons in the cavity as a function of cavity drive amplitude, with the data plotted in red and the fit in blue. (c) The calculated dispersive shift 2χ versus the average cavity photon population.

extracts the proportionality constant that relates \bar{n} to A_{Stark}^2 . This analysis incorrectly assumes that the dressed state of the cavity does not shift with readout drive power. In practice, the dressed state approaches the bare resonance of the cavity for large A_{Stark} , resulting in a non-quadratic relationship between A_{Stark} and \bar{n} [120]; however, the cavity photon population behaves quadratically for \bar{n} close to n_{crit} since the resonance of the cavity shifts much less than the linewidth κ of the cavity.

7.8 Cavity Response

As discussed in Section 6.3.5, we determine the measurement fidelity by comparing the response of the resonator when the qubit is prepared in either the $|0\rangle$ or the $|1\rangle$ state. In Figure 7.15, we plot the response of the readout cavity at a fixed readout drive amplitude for different qubit preparations. The quadrature components, plotted in Figure 7.15(a), of a quarter-wave resonator should follow a circular trajectory [Figure 6.5(c)], where the path in quadrature space is identical for two resonators of different resonances. In practice, the transmitted signal accumulates a phase with periodicity v_{ph}/L , where v_{ph} is the phase velocity of the signal and L is the total distance between the generator and the measured signal. This accumulation of phase explains the trajectory of the quadrature components away from the resonance in Figure 7.15(a). A model that accounts for complex in-line inductances [27] (*e.g.* wire bonds) and impedance mismatches explains the observed asymmetry of the resonator response.

In Figures 7.15(b) and (c), we plot the heterodyne amplitude and phase, respectively, of the recorded heterodyne signal as a function of probe frequency. Note that the photon occupation of the cavity changes with probe frequency since the amplitude of the readout signal is fixed; the number of photons in the resonator is $\bar{n} \approx 30$ at a probe frequency

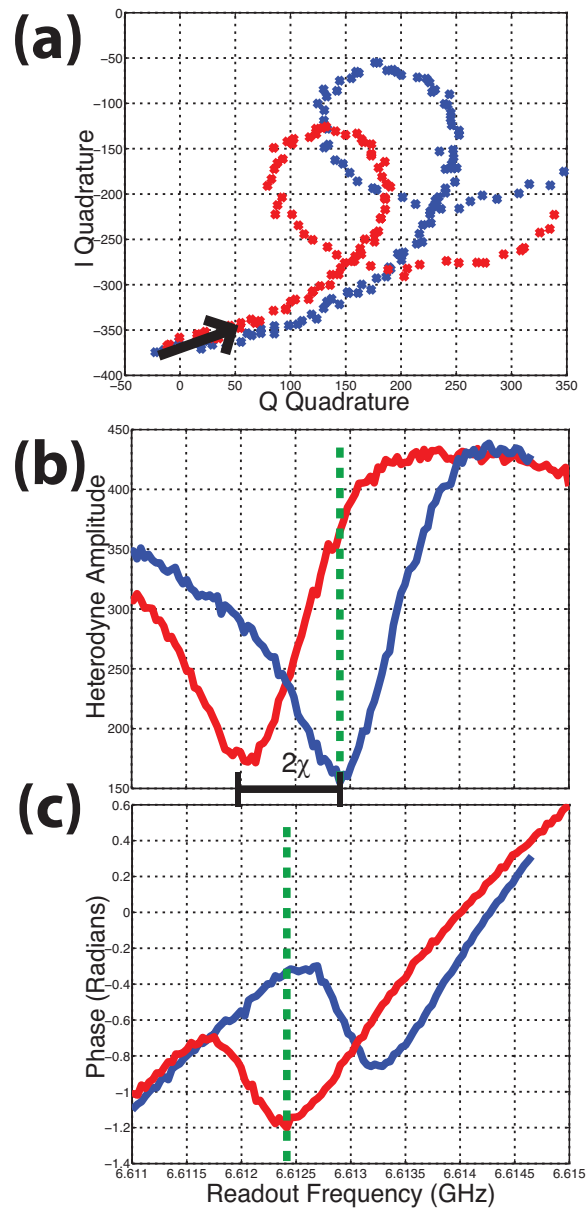


Figure 7.15: The average heterodyne signal as a function of readout drive frequency when the qubit is in the $|0\rangle$ state (blue) and the $|1\rangle$ state (red). **(a)** The average quadrature components of the readout signal is plotted for different frequencies, where the black arrow points in the direction of increasing frequency. The magnitude **(b)** and phase **(c)** of the average heterodyne signal. The dashed green line represents the frequency of maximum distinguishability between the two states.

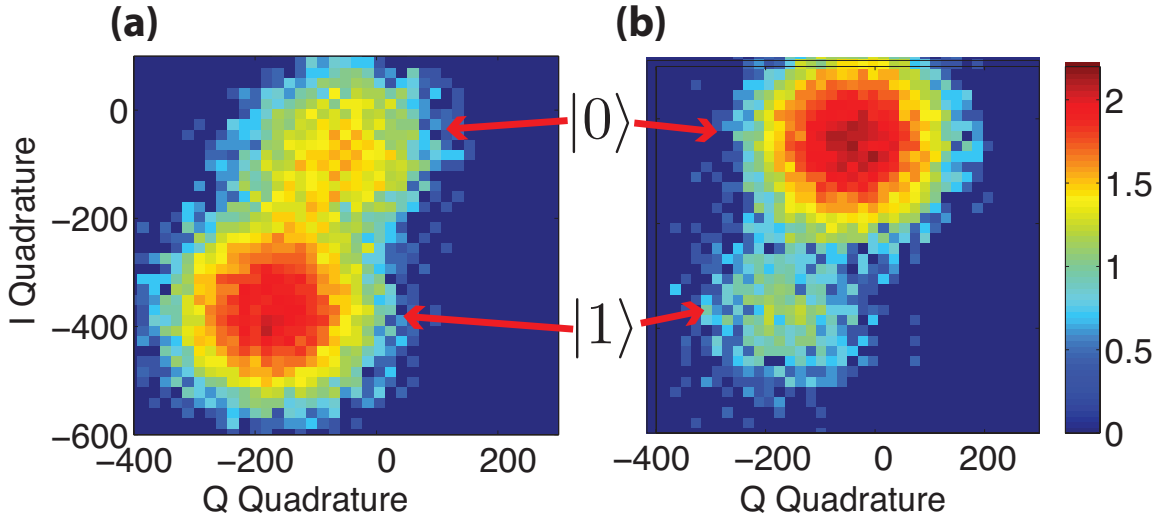


Figure 7.16: Two-dimensional histograms of the complex heterodyne signal when the qubit is prepared 15000 times in the $|1\rangle$ state **(a)** and the $|0\rangle$ state **(b)**. The measurement duration was $\tau_m = 2 \mu\text{s}$, with a calibrated $\bar{n} = 108$ photons. The color scale is the logarithm of the bin counts.

halfway between the two state dependent resonances. The observed dispersive shift $2\chi \approx -850$ kHz is consistent with the theoretical 2χ plotted in Figure 7.14(c).

7.9 Measurement Fidelity Without the SLUG

The qubit-cavity system has the following characteristics for the measurements reported in this section: $f_{10} = 6.0132$ GHz, $f_{21} = 5.7848$ GHz, $f_{23} = 5.5412$ GHz, the bare cavity resonance $f_r = 6.6129$ GHz, low-power resonator dressed state of $f^{(0)} = 6.6143$ GHz, $g_{10}/2\pi = 29.89$ MHz, internal quality factor $Q_i = 43.8 \times 10^3$, and a coupling quality factor of $Q_C = 5.8 \times 10^3$. We probe the response of the cavity at a frequency $f_p = f^{(0)}$. The measured energy relaxation time constant is $T_1 = 10.8 \mu\text{s}$. The average number of photons in the cavity \bar{n} assumes the driven resonator is in the steady state. The critical number of photons is $n_{crit} = \frac{\Delta_0^2}{4g_{10}^2} = 100.6$.

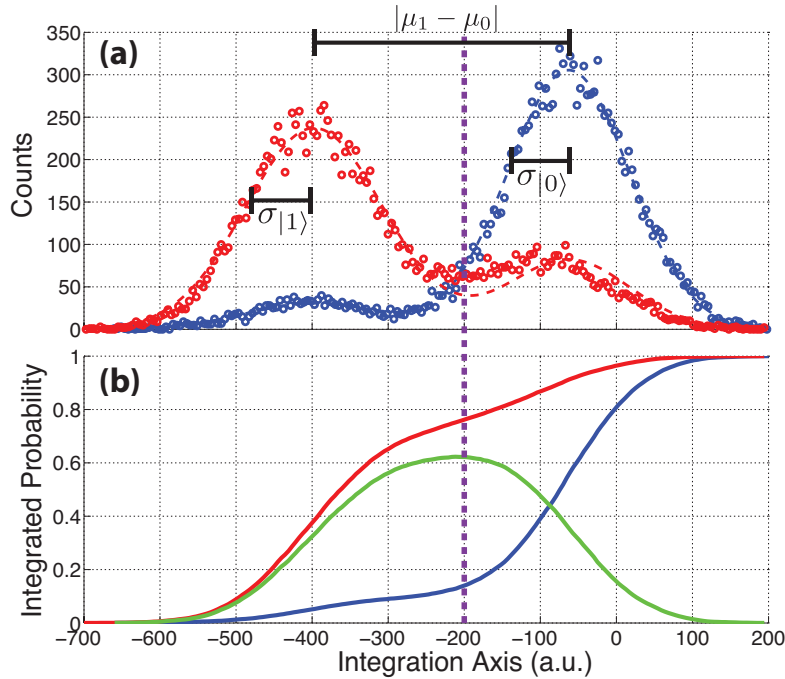


Figure 7.17: (a) The projected histograms and fits of the prepared $|0\rangle$ (blue) and $|1\rangle$ states (red). (b) The integrated probabilities of the prepared $|0\rangle$ (blue) and $|1\rangle$ states (red). The measurement fidelity (green) is just the difference between the two integrated probabilities. The dashed purple line is the threshold of the measurement.

Measurement fidelity is determined with repeated measurements of the qubit prepared in the $|1\rangle$ and $|0\rangle$ state. In Figures 7.16(a) and (b), we plot the two-dimensional histograms of the measured heterodyne signal for 15000 realizations of qubit prepared in the $|1\rangle$ and $|0\rangle$ state, respectively. The resonator was probed for a time $\tau_m = 2 \mu\text{s}$ and a drive power with $\bar{n} = 108$ photons. The $|0\rangle$ state of the qubit was prepared without a control pulse, while the $|1\rangle$ state was prepared with a π -pulse of duration $\tau_\pi = 64 \text{ ns}$. As expected, there are two distinct blobs in quadrature space that correspond to the $|1\rangle$ and $|0\rangle$ state of the qubit. Measurement fidelity depends on three factors: the distinguishability of the two states, quantified by the signal-to-noise ratio SNR of the measurement; the qubit relaxation rate; and our ability to repeatedly prepare the qubit in the expected

state. It is clear from Figure 7.16(b) that the qubit is not fully initialized into the $|0\rangle$ state.

We quantify the measurement fidelity of the qubit by projecting each two-dimensional heterodyne signal onto an integration line that maximizes the separation of the two states. We then fit the two histograms of the projected signal with a pair of double-Gaussian functions of the following form:

$$f_0 = \frac{\delta x N}{2 - P_0} \left[\frac{1}{\sigma_0 \sqrt{2\pi}} \exp\left(-\frac{(x - \mu_0)^2}{2\sigma_0^2}\right) + \frac{1 - P_0}{\sigma_1 \sqrt{2\pi}} \exp\left(-\frac{(x - \mu_1)^2}{2\sigma_1^2}\right) \right], \quad (7.3)$$

$$f_1 = \frac{\delta x N}{2 - P_1} \left[\frac{1 - P_1}{\sigma_0 \sqrt{2\pi}} \exp\left(-\frac{(x - \mu_0)^2}{2\sigma_0^2}\right) + \frac{1}{\sigma_1 \sqrt{2\pi}} \exp\left(-\frac{(x - \mu_1)^2}{2\sigma_1^2}\right) \right], \quad (7.4)$$

which depends on the following six fit parameters: P_0 (P_1) is the probability that the state is in the $|0\rangle$ state ($|1\rangle$ state) when preparing a $|0\rangle$ state ($|1\rangle$ state), μ_0 (μ_1) is the center of the $|0\rangle$ state ($|1\rangle$ state) along the axis of integration, and σ_0 (σ_1) is the standard deviation of the $|0\rangle$ state ($|1\rangle$ state) distribution. Additionally, δx is the bin size of the histogram, x is the location of the bin along the integration axis, and N is the total number of experiments in each distribution. The measured SNR is:

$$SNR_{meas} = \frac{|\mu_0 - \mu_1|}{\sigma_1 + \sigma_0}, \quad (7.5)$$

and the probability that the qubit is in the $|0\rangle$ state when preparing a $|1\rangle$ is:

$$P_{0|1} = 1 - P_1, \quad (7.6)$$

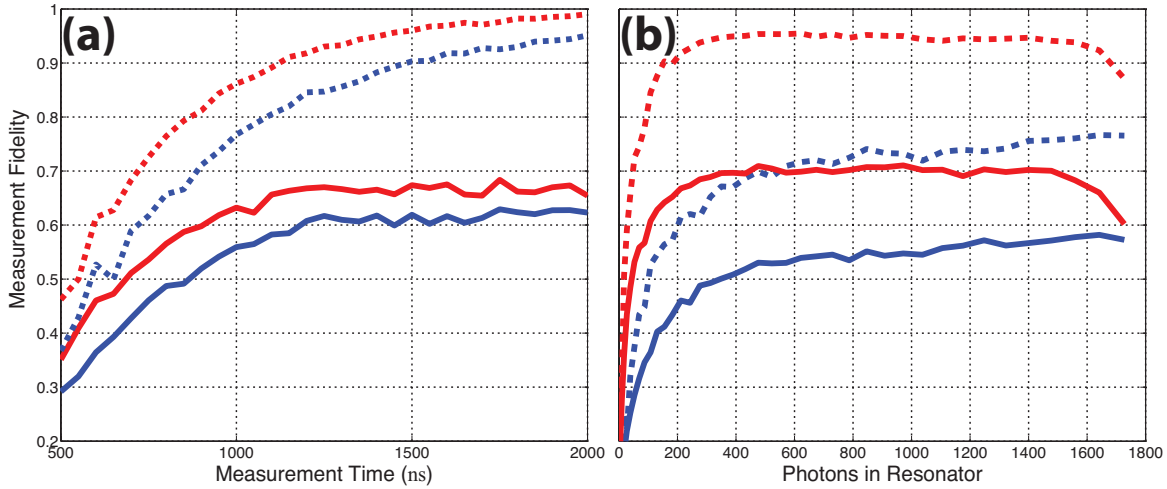


Figure 7.18: (a) The raw F_{raw} (solid lines) and corrected F_{cor} (dashed lines) measurement fidelities as a function of readout time τ_m for $\bar{n} = 108$ (blue) and $\bar{n} = 212$ photons (red). (b) The raw F_{raw} (solid lines) and corrected F_{cor} (dashed lines) measurement fidelities as a function of \bar{n} for $\tau_m = 600$ ns (blue) and $\tau_m = 1200$ ns (red).

and similarly, the probability that the qubit is in the $|1\rangle$ state when preparing a $|0\rangle$ is:

$$P_{1|0} = 1 - P_0. \quad (7.7)$$

A $P_{1|0} > 0$ can be blamed on poor initialization of the qubit or measurement induced excitation. The histogram fits of Figure 7.17(a) return a $P_{1|0} = 0.1014$, which remains constant as a function of measurement drive power and measurement time, suggesting that the qubit is not initialized in the $|0\rangle$ state properly. A $P_{0|1} > 0$ can be the result of measurement induced relaxation, poor state preparation, and the relaxation process described by the time constant T_1 . We extract a $P_{0|1} = .2350$ from the data in Figure 7.17(b). It is difficult to breakdown the contributions to $P_{0|1}$ without further analysis.

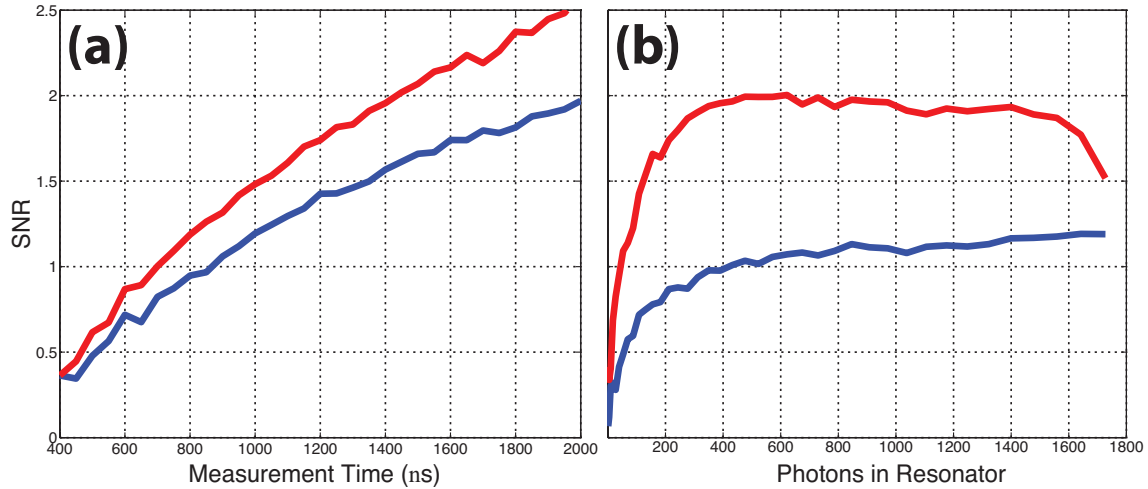


Figure 7.19: **(a)** The measurement SNR as a function of readout time τ_m for $\bar{n} = 108$ (blue) and $\bar{n} = 212$ photons (red). **(b)** The measurement SNR as a function of \bar{n} for $\tau_m = 600$ ns (blue) and $\tau_m = 1200$ ns (red).

We calculate the raw measurement fidelity from the data by integrating and then subtracting the histograms of the two states, plotted in Figure 7.17(b). The position along the integration axis with the maximum measurement fidelity is the threshold of the measurement, where a single measurement below the threshold is counted as the $|1\rangle$ state. The raw measurement fidelity for the data in Figure 7.17 is $F_{raw} = 0.6231$. We also calculate a corrected fidelity where $P_{0|1} = P_{1|0} = 0$ and $SNR_{meas} = 1.97$ is the limiting factor, with $F_{cor} = 0.9512$ for the data in Figure 7.17; this agrees perfectly with the expression for fidelity in Equation 6.64 in the limit that $T_1 \gg \tau_m$.

To draw parallels with earlier work by Gambetta *et al.* [114], we calculate the efficiency of the amplification chain η_{det} :

$$\eta_{det} = \frac{1}{1 + n_{sys}}, \quad (7.8)$$

where n_{sys} is the total number of noise quanta added by the amplification chain, we experimentally define as:

$$n_{sys} = \left(\frac{SNR_{ideal}}{SNR_{meas}} \right)^2 - \frac{1}{2}, \quad (7.9)$$

where SNR_{ideal} is the calculated SNR with $n_{sys} = 0.5$ [from Section 6.3.4³], where $SNR_{ideal} = 10.706$ for this particular measurement. We finally evaluate a $n_{sys} = 29.03$ quanta for a detector efficiency of $\eta_{det} = 0.033$. A $n_{sys} = 29.03$ is larger than the 20 quanta we estimated in Section 5.4; however, the signal leaving the qubit passes through almost 3 feet of copper cable, two isolators, two bias-T's, and two coax-relays before reaching the HEMT. The isolators alone have an insertion loss of approximately 0.5 dB each, while the copper cables are specced at room temperature to have about 0.8 dB of insertion loss per foot. A conservative estimate of 2 dB of attenuation between the qubit and the HEMT gives an adjusted n_{sys} of 18 quanta of added noise. The number that matters for measurement fidelity is the original $n_{sys} = 29.03$ but a trivial change in the wiring can significantly improve η_{det} in future measurements.

In Figures 7.18(a) and (b), we plot the raw and corrected measurement fidelities as a function of τ_m and \bar{n} . The raw measurement fidelity saturates at 0.62 for a $\bar{n} = 108 \approx n_{crit}$. Also note that the raw fidelity saturates and sharply bends down for large \bar{n} at $\tau_m = 1.2 \mu s$; the dispersive regime of the qubit-cavity system breaks down for large \bar{n} , which causes measurement induced relaxation and a reduced SNR as the dressed state of the cavity shifts towards ω_r . In Figure 7.19(a), we plot the measurement SNR as a function of τ_m for two different \bar{n} . As expected [see Figure 6.9], the SNR goes as $\tau_m^{3/2}$ for

³We calculate SNR_{ideal} by calculating $2\chi/2\pi = 0.726$ MHz from the qubit parameters specified at the beginning of this section. We also incorporate resonator loss into the model of Section 6.3.4.

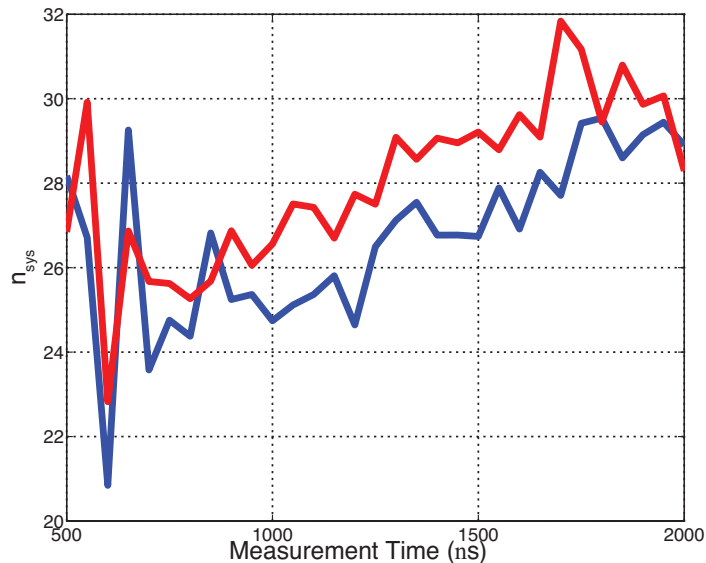


Figure 7.20: Added system noise quanta n_{sys} as a function of τ_m for $\bar{n} = 108$ photons (blue) and $\bar{n} = 212$ photons (red). We calculate n_{sys} using the SNR_{meas} of Figure 7.19(a).

$\tau_m \ll 2\pi/\kappa = 877$ ns and approaches $\tau_m^{1/2}$ for τ_m greater than the cavity ring-up time. In Figure 7.19(b), we plot SNR as a function of \bar{n} for two different τ_m ; the SNR rolls off at large \bar{n} for $\tau_m = 1.2 \mu\text{s}$, suggesting that a reduced SNR is responsible for the rolloff in fidelity plotted in Figure 7.18(b). In Figure 7.19, we plot n_{sys} as a function of τ_m for $\bar{n} = 108 \approx n_{crit}$ and $\bar{n} = 212 \approx 2n_{crit}$. An amplification chain with a large dynamic range has a n_{sys} that should not depend on τ_m or the number of photons in the resonator. The time dependence of n_{sys} suggests that the resonator rings-up slower than we calculated; a more complete model of SNR must include the τ_m dependence of the dispersive shift 2χ .

7.10 Improved Fidelity with SLUG Amplifier

A SLUG amplifier is switched into the amplification chain with the coax-relays. The SLUG used to measure the qubit in this section has similar noise and gain performance as

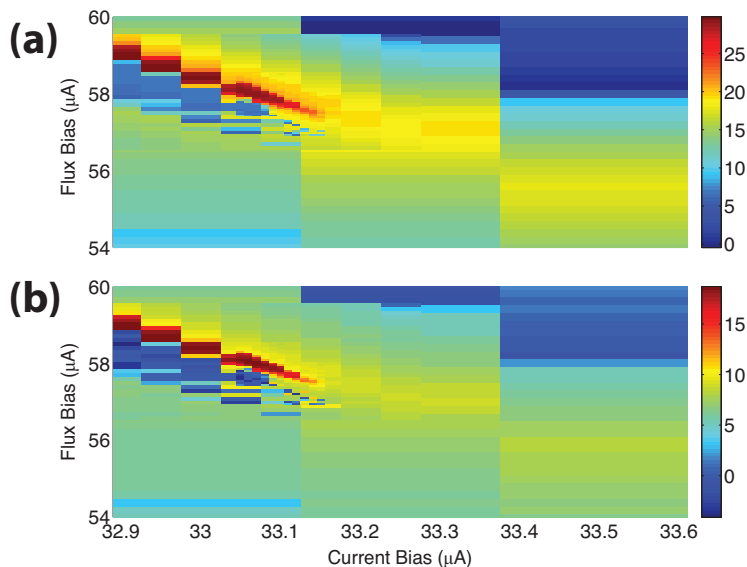


Figure 7.21: The measured gain **(a)** and SNR improvement **(b)** of the amplification chain with the SLUG amplifier. Both the gain and SNR are in units of dB.

SLUGA described in Chapter 5. We quickly estimate the SNR⁴ of the amplification chain by comparing the transmitted power when the cavity-qubit system is driven a few MHz off-resonance to the noise power with the microwave generator off. We measure the SNR of the amplification chain for different SLUG flux and current biases; the gain and SNR of the SLUG are plotted in Figures 7.19(a) and (b). There is a narrow range of SLUG bias points that appear to improve the SNR of the amplification chain by 17 dB with a gain of 29 dB. The sensitive dependence of SNR and gain on flux bias implies that the SLUG is being operated close to a resonant step edge in the $V - \Phi$ characteristics of the device. It has already been experimentally and theoretically verified that the non-linear performance of the SLUG when biased close to a step-edge performs with high-gain, low-bandwidth and low-dynamic range. It is likely that the measured SNR at these bias points will decrease with input power as the amplifier saturates. It is also likely that

⁴The SNR measured with the spectrum-analyzer is related to but different than the SNR that describes the ability of the amplification chain to distinguish the two states of the qubit.

these bias points are unstable in time and exhibit hysteretic behavior. There are bias points in Figure 7.21 that do not drastically vary with bias and show a respectable SNR improvement of 9 dB and a gain of 17 dB.

The cavity-qubit system is described by the same qubit and cavity resonances as the previous section; switching the SLUG into the amplification chain does not affect the measured relaxation time T_1 . In Figures 7.22 and 7.23, we plot the progression of the measured heterodyne signal for different average cavity photon occupations \bar{n} at measurement times $\tau_m = 600$ ns and $\tau_m = 2$ μ s. Notice the clear separation between the two states at $\bar{n} = 53$ photons and $\tau_m = 600$ ns – this level of distinguishability was not possible without the SLUG amplifier. We measure a $P_{1|0} = 0.0944$ and a $P_{0|1} = 0.2307$ for $\tau_m = 2$ μ s and $\bar{n} = 108$ photons – within the margin of error of the values measured without the SLUG.

As a reminder, \bar{n} was calibrated using the Stark shift with the probe tone set to the low-power resonance of the cavity dressed by the $|0\rangle$ state of the qubit. For $\bar{n} < n_{crit}$, there is a linear relationship between input power and \bar{n} ; however, as \bar{n} exceeds n_{crit} the $|0\rangle$ state resonance converges with ω_r , and in consequence the reported \bar{n} overestimates the actual average cavity photon population. The resonance shift is clearly seen in Figures 7.22 and 7.23 at high \bar{n} , where the position of the two states have rotated counterclockwise in the IQ plane. It also worth noting that \bar{n} was calibrated in the steady state, meaning \bar{n} at $\tau_m = 600$ ns is less than \bar{n} at $\tau_m = 2$ μ s for the same drive power.

A third blob in the IQ plane pulls away from the $|1\rangle$ state blob at large readout powers and long measurement times – this feature is quite clear in both columns of Figure 7.23. It isn't clear if the presence of the third blob is due to a strong measurement, or if a strong measurement is necessary to reveal the third blob – by squinting hard, one might be convinced that the extra blob starts to form at $\bar{n} = 53$, $\tau_m = 2$ μ s. We are still

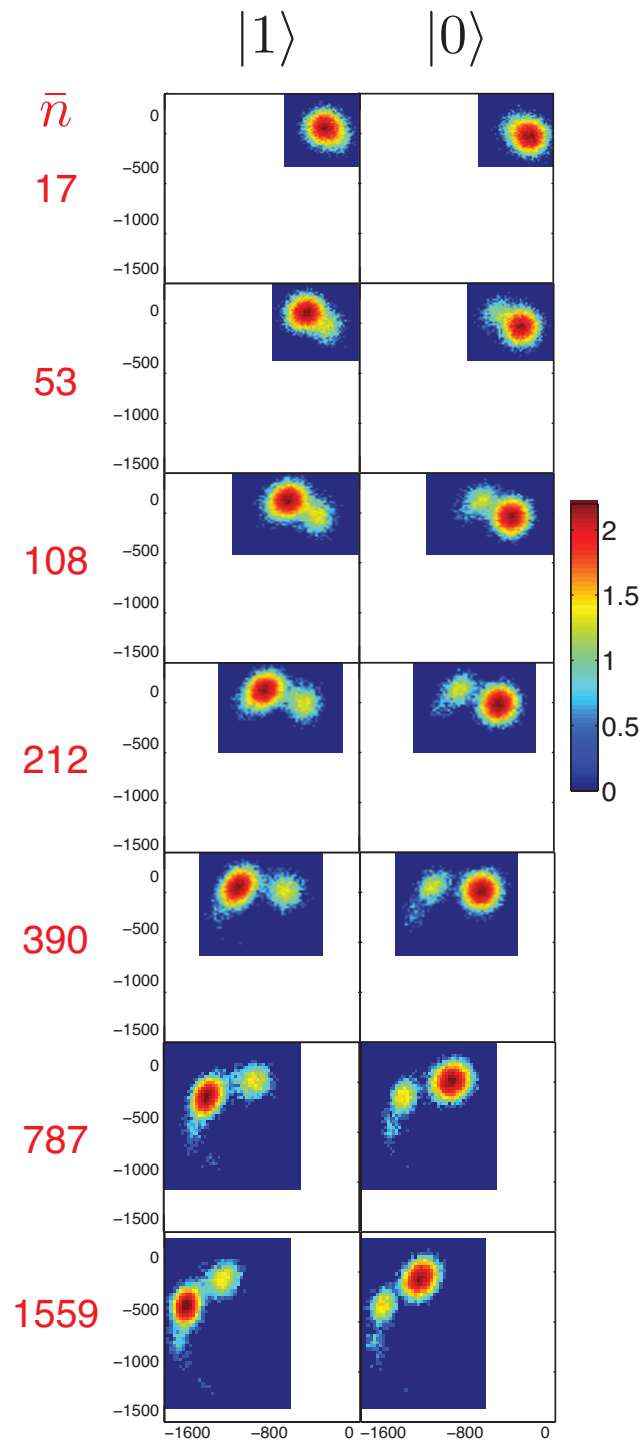


Figure 7.22: Histogrammed heterodyne signal for different average cavity photon populations \bar{n} when measured for a time $\tau_m = 600$ ns. Column one (two) is the signal when the qubit is prepared in the $|1\rangle$ ($|0\rangle$) state. The false color scale is the log of the bin counts.

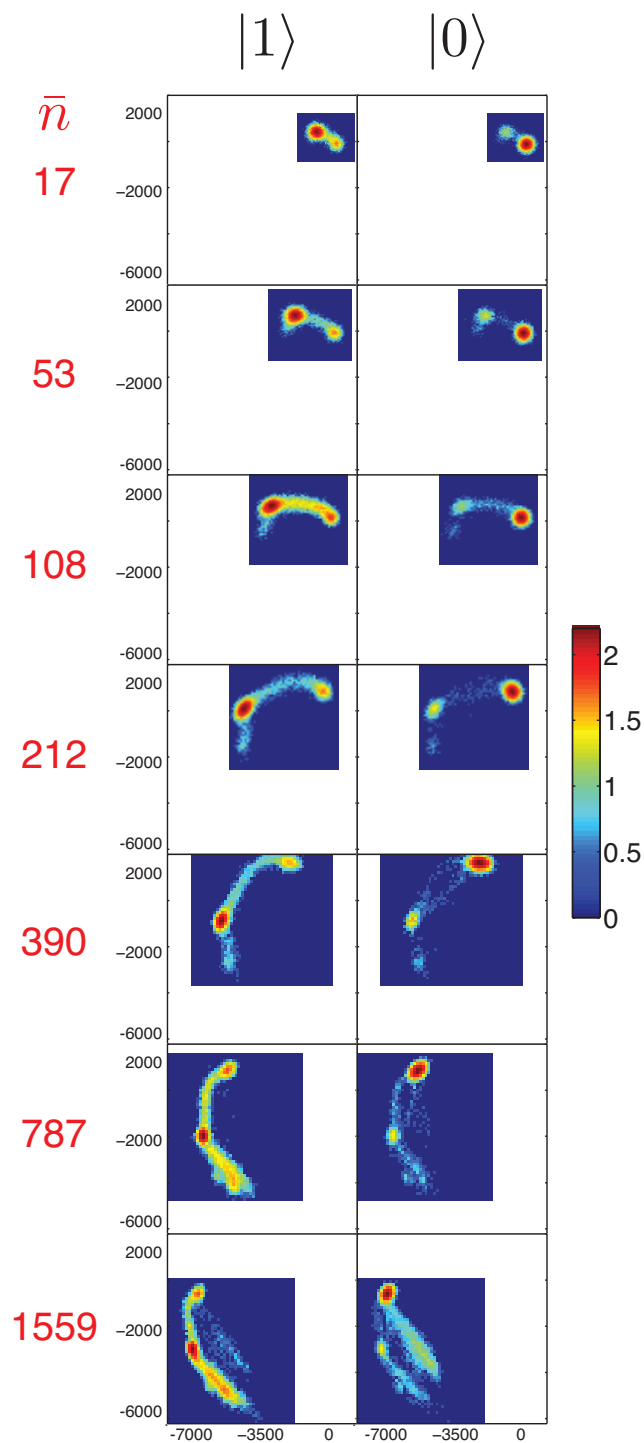


Figure 7.23: Histogrammed heterodyne signal for different average cavity photon populations \bar{n} when measured for a time $\tau_m = 2 \mu s$. Column one (two) is the signal when the qubit is prepared in the $|1\rangle$ ($|0\rangle$) state. The false color scale is the log of the bin counts.

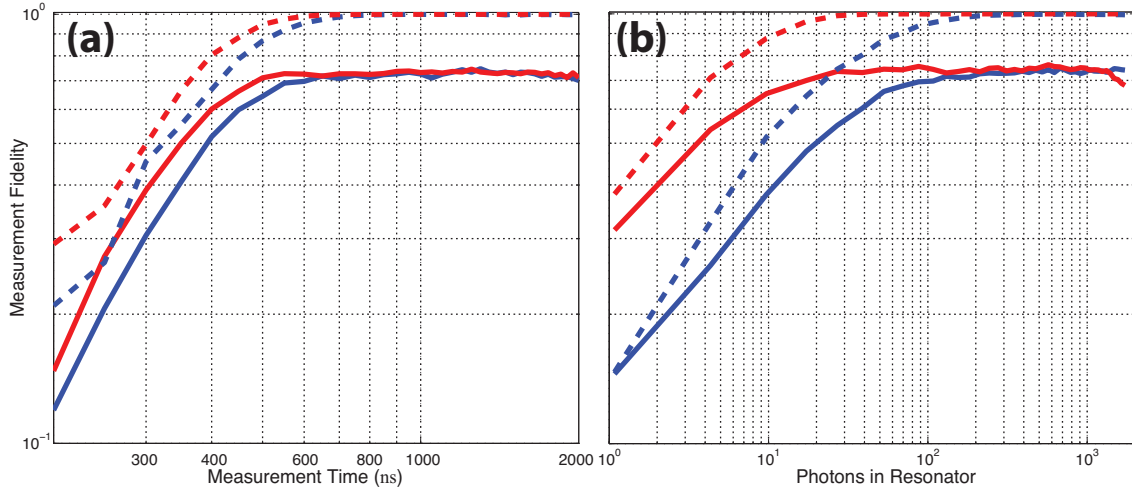


Figure 7.24: (a) The raw F_{raw} (solid lines) and corrected F_{cor} (dashed lines) measurement fidelities as a function of measurement time τ_m for $\bar{n} = 108$ (blue) and $\bar{n} = 212$ photons (red). (b), The raw F_{raw} (solid lines) and corrected F_{cor} (dashed lines) measurement fidelities as a function of \bar{n} for $\tau_m = 600$ ns (blue) and $\tau_m = 1200$ ns (red). These measurements were done with the SLUG in the amplification chain.

investigating the origin of the extraneous IQ blob, but we suspect the qubit levels outside the computational manifold play a role. It should also be noted that the presence of the extra IQ features invalidate our fidelity analysis described in the last section, where it is unclear how to define SNR and the integration axis for fitting the data.

We plot the raw and corrected measurement fidelities versus readout time for two different drive powers in Figure 7.24(a). The raw fidelity plateaus at 0.73 for a $\tau_m = 600$ ns when driving the resonator at a $\bar{n} = 212 \approx 2n_{crit}$; this is a substantial improvement when compared to the raw fidelity of 0.46 that was measured without the SLUG at the same τ_m and \bar{n} . A correction for relaxation and initialization errors give us a fidelity of 0.99 for $\bar{n} = 212$ and $\tau_m = 600$ ns. Note that the fidelity plateaus at a shorter τ_m when driving the cavity at a high power; this behavior is also captured in Figure 7.24(b).

The measurement SNR, determined with a fit of the heterodyne signal, is plotted versus τ_m and \bar{n} in Figures 7.25(a) and (b), respectively. The measurement SNR with

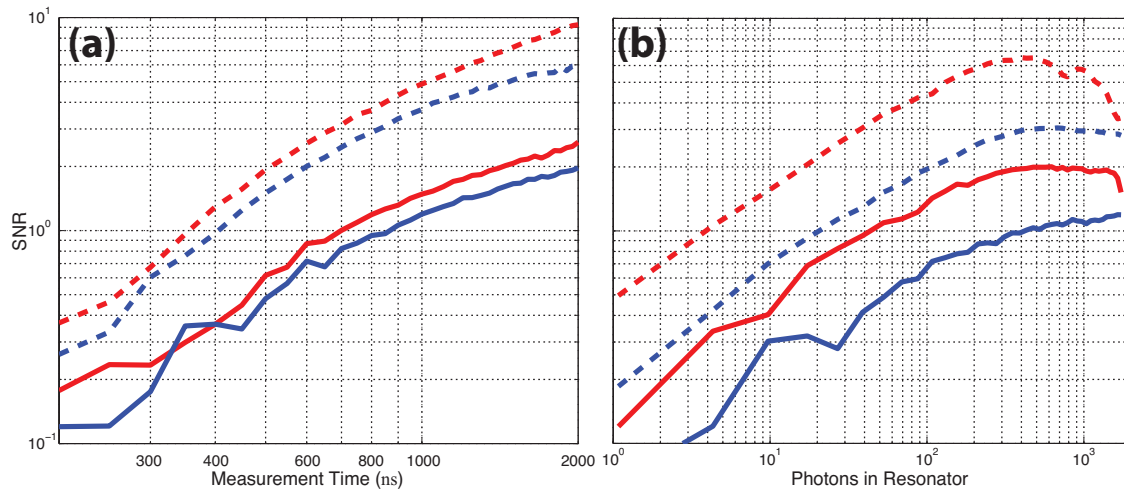


Figure 7.25: The measurement SNR with (dashed) and without (solid) the SLUGin the amplification chain. **(a)** The measurement SNR as a function of τ_m for $\bar{n} = 108$ (blue) and $\bar{n} = 212$ photons (red). **(b)** The measurement SNR as a function of \bar{n} for $\tau_m = 600$ ns (blue) and $\tau_m = 1200$ ns (red).

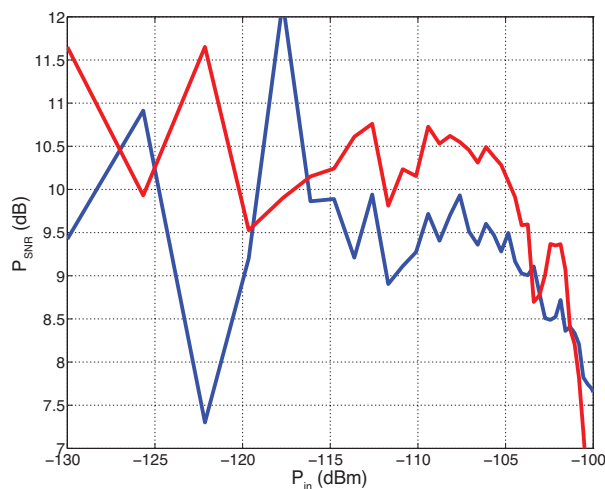


Figure 7.26: P_{SNR} versus P_{in} for $\tau_m = 600$ ns (blue) and $\tau_m = 1200$ ns (red). From Equation 7.11, a $\bar{n} = 1000$ corresponds to a $P_{in} = -102.0$ dBm.

the SLUG shows roughly the same dependence on τ_m and \bar{n} as the SNR without the SLUG in the amplification chain. The SLUG enhances the SNR of the measurement chain by roughly 10 dB in power, calculated as P_{SNR} :

$$P_{SNR} = \left(\frac{SNR_{meas}^{SLUG}}{SNR_{meas}^{ref}} \right)^2, \quad (7.10)$$

where SNR_{meas}^{SLUG} (SNR_{meas}^{ref}) is the measurement SNR with (without) the SLUG in the amplification chain; the 10 dB improvement in measurement SNR is consistent with the results reported in Figure 7.21(b). In Figure 7.27, we plot P_{SNR} as a function of input power for $\tau_m = 600$ ns and $\tau_m = 1200$ ns. The input power P_{in} is calculated using Equation 6.54 with $\Delta\omega^{(0)} = 0$:

$$P_{in} = \frac{\langle V_G^2 \rangle}{R_0} = \frac{|V_G|^2}{2R_0} = 2\hbar\omega\kappa\bar{n}, \quad (7.11)$$

where \bar{n} is the steady state number of photons in the resonator, meaning that the actual readout power at the input of the qubit for a $\tau_m = 600$ ns and $\tau_m = 1200$ is less (at most 3 dBm) than P_{in} . Also note that the SNR determined by the fit of the heterodyne signal becomes less accurate as P_{in} increases. With these caveats in mind, the data in Figure 7.27 suggests that the SLUG has a 1 dB compression point of roughly $P_{in} = -105$ dBm, or 505 photons in the resonator; this may be improved at a SLUG bias point further from the resonant step edge without noticeably sacrificing amplifier performance. A -105 dBm 1 dB compression point is over an order of magnitude better than the best JPA. In Figure 7.27, we plot n_{sys} calculated with Equation 7.9 as a function of τ_m for two different drive powers.

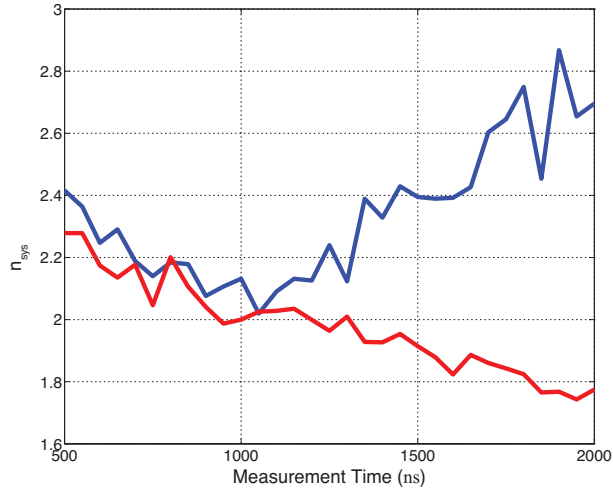


Figure 7.27: Added system noise quanta n_{sys} with the SLUG in the amplification chain as a function of τ_m for $\bar{n} = 108$ photons (blue) and $\bar{n} = 212$ photons (red). We calculate n_{sys} using the SNR_{meas} of Figure 7.25(a).

7.11 Conclusions and Outlook

7.11.1 Improving Measurement Fidelity

The measurement fidelity can be improved with a redesign of the qubit, as discussed in Section 6.3.4; additionally, a further reduction in the noise temperature of the SLUG will improve the readout. However, there are some simple adjustments that would immediately improve measurement fidelity with the same qubit and SLUG amplifier described above.

At a $\tau_m = 600$ ns and $\bar{n} = 211$ photons, we have an $SNR_{meas}^{SLUG} = 2.565$. Considering a $T_1 = 10$ μs , we use Equation 6.64 to calculate an estimated fidelity of $F = 0.96$; however, we observe a measurement fidelity of 0.725. We are throwing away roughly 20% of fidelity from the 10% initialization error. We suspect that the chip is at a higher effective temperature than the mixing plate of the DR, which would cause a non negligible population of the $|1\rangle$ state. While writing this thesis, we have added additional base

temperature attenuation to the input of each port of the Xmon for a reduced initialization error of roughly 4%. We believe that with the addition of inline infrared filters and with better heat sinking of the attenuators we can reduce the initialization error down to nothing.

According to Equation 6.64, even with an infinite SNR we are T_1 limited to a fidelity of $F = 0.970$ at a $\tau_m = 600$ ns. However, an overall improvement in the measurement SNR would allow us to measure the qubit in a shorter amount of time, slightly mitigating the effects of energy relaxation. There are two trivial changes in the measurement that we can make to improve the SNR. First, there is roughly 3 feet of copper coax, a circulator, a bias-T, and a two coax-relays between the qubit and the SLUG – all with an insertion loss that reduces the SNR before the signal reaches the SLUG amplifier. While we can't remove the circulator or the bias-T, we can replace the copper-cable with superconducting niobium, and we can remove the coax-relay at the price of modularity. For example, the removal of 2 dB of attenuation between the qubit and SLUG reduces a system noise of $n_{sys} = 2.5$ down to 1.4 quanta of added noise. Additionally, as shown in Figure 6.9, probing the readout resonator halfway between the two dressed states $\omega^{|0\rangle}$ and $\omega^{|1\rangle}$ will increase the SNR by roughly 20% when compared with probing at $\omega^{|0\rangle}$.

7.11.2 Future Qubit-SLUG Experiments

A near quantum limited SLUG amplifier paves the way for a number of exciting experiments involving qubits. The SLUG amplifier has a much larger dynamic range than the best JPA, and, with the demonstrated measurement fidelity and SNR of the SLUG, we should be able to resolve quantum jumps in the state of the qubit [39]. As discussed throughout this thesis, the dispersive limit of Jaynes-Cummings hamiltonian loses validity for $\bar{n} > n_{crit}$; however, no one has investigated the limits of QND detection.

For some critical readout power, the measurement will scramble the state of the qubit, leaving the qubit in a different state than the measured state. With a high fidelity measurement, we can resolve the state of the qubit as a function of time. By exploring the statistics of how the state of the qubit evolves as a function of measurement power and readout time, we can map out how a QND measurement transitions into the non-QND regime. An amplifier with a large dynamic range is needed to accurately explore this QND boundary.

We also want to explore how the backaction of the SLUG amplifier affects the performance of the qubit. While the SLUG is a non-reciprocal device, the elevated electron temperature of the shunt resistors along with high-frequency Josephson oscillations generated by the junctions in the voltage state may degrade the coherence of the qubit. For the experiments in this chapter we have placed an isolator between the SLUG and the qubit; however, isolators are bulky, costly, and have a non-negligible insertion loss. Removing the isolator will reduce the system noise of the measurement chain and free up space on the mixing plate. We plan on exploring how the relaxation rate of the qubit changes as a function of SLUG gain and noise temperature.

Appendix A

Jaynes Cummings Hamiltonian

A.1 Full Jaynes Cummings Hamiltonian

The Jaynes Cummings Hamiltonian describes a generalized two level system, or qubit, with an energy splitting $\hbar\omega_{10}$ interacting with photons in a cavity with resonance frequency ω_r . This system is described by the generalized Hamiltonian \hat{H}_{JC} :

$$\hat{H}_{JC} = \hat{H}_{TLS} + \hat{H}_{cav} + \hat{H}_{int}, \quad (\text{A.1})$$

where \hat{H}_{TLS} is the TLS Hamiltonian:

$$\hat{H}_{TLS} = \frac{1}{2}\hbar\omega_{10}\hat{\sigma}_z, \quad (\text{A.2})$$

with $\hat{\sigma}_z$ being:

$$\hat{\sigma}_z = |1\rangle\langle 1| - |0\rangle\langle 0| = \begin{pmatrix} 1 & 0 \\ 0 & -1 \end{pmatrix}, \quad (\text{A.3})$$

where the excited qubit state $|1\rangle = (1 \ 0)$ and $|0\rangle = (0 \ 1)$. \hat{H}_{cav} is the Hamiltonian of the field in the cavity:

$$\hat{H}_{cav} = \hbar\omega_r(\hat{a}^\dagger\hat{a} + \frac{1}{2}), \quad (\text{A.4})$$

where \hat{a}^\dagger and \hat{a} are the photonic raising and lowering operators, respectively. \hat{H}_{int} is the interaction Hamiltonian:

$$\hat{H}_{int} = \hbar g(\hat{a} + \hat{a}^\dagger)(\hat{\sigma}_+ + \hat{\sigma}_-), \quad (\text{A.5})$$

which is just the field operator $\hat{a} + \hat{a}^\dagger$ multiplied by the polarization operator $\hat{\sigma}^+ + \hat{\sigma}^-$, and scaled by the interaction strength g , or rate at which the cavity and qubit exchange

energy. $\hat{\sigma}^+$ and $\hat{\sigma}^-$ are the raising and lowering operators of the qubit respectively, defined as:

$$\hat{\sigma}^+ = |1\rangle\langle 0| = \begin{pmatrix} 0 & 1 \\ 0 & 0 \end{pmatrix}, \quad (\text{A.6a})$$

$$\hat{\sigma}^- = |0\rangle\langle 1| = \begin{pmatrix} 0 & 0 \\ 1 & 0 \end{pmatrix}. \quad (\text{A.6b})$$

In the Rotating Wave Approximation, we ignore the terms that do not conserve energy: $\hat{a}^\dagger\hat{\sigma}_+$ and $\hat{a}\hat{\sigma}^-$ ¹, giving us the following well know \hat{H}_{JC} :

$$\hat{H}_{JC} = \frac{1}{2}\hbar\omega_{10}\hat{\sigma}_z + \hbar\omega_r(\hat{a}^\dagger\hat{a} + \frac{1}{2}) + \hbar g(\hat{a}\hat{\sigma}^+ + \hat{a}^\dagger\hat{\sigma}^-). \quad (\text{A.7})$$

A.2 Dispersive Approximation for a Two Level System

A.2.1 First Order Approximation

In order to perform a QND measurement of the qubit state, \hat{H}_{JC} must take on a form that commutes with the projective measurement $\hat{\sigma}_z$. In the dispersive regime, the qubit and cavity do not exchange energy, such that the eigenstates of the system are

¹In the interaction picture $\hat{a}\hat{\sigma}^+$ and $\hat{a}^\dagger\hat{\sigma}^-$ oscillate at $|\omega_r - \omega_{10}|$, while the subsequently ignored terms rotate at $|\omega_r + \omega_{10}|$. On the relevant time scales the $|\omega_r + \omega_{10}|$ terms average to 0, as long as $|\omega_r + \omega_{10}| \gg |\omega_r - \omega_{10}|$.

well approximated by the product states of the qubit and cavity. Equation A.7 can be rewritten as:

$$\hat{H}_{JC} = \hat{H}_0 + \hbar g \hat{X}_+, \quad (\text{A.8})$$

where $\hat{H}_0 = \frac{1}{2}\hbar\omega_{10}\hat{\sigma}_z + \hbar\omega_r(\hat{a}^\dagger\hat{a} + \frac{1}{2})$ and $\hat{X}_\pm = \hat{\sigma}^- \hat{a}^\dagger \pm \hat{\sigma}^+ \hat{a}$. We apply a unitary transformation $\hat{D} = \exp(\lambda \hat{X}_-)$ to Equation A.8 and then expand about $\lambda = g/\Delta \ll 1$, where $\Delta = \omega_{10} - \omega_r$:

$$\begin{aligned} \hat{H}_{disp} &= \hat{D}^\dagger \hat{H}_{JC} \hat{D} \\ &= \hat{H}_{JC} + \lambda [\hat{H}_{JC}, \hat{X}_-] + \frac{\lambda^2}{2} [[\hat{H}_{JC}, \hat{X}_-], \hat{X}_-] + o(\lambda^3) \\ &\approx \frac{1}{2}\hbar\omega_{10}\hat{\sigma}_z + \hbar\omega_r(\hat{a}^\dagger\hat{a} + \frac{1}{2}) + \hbar\frac{g^2}{\Delta}(\hat{a}^\dagger\hat{a} + \frac{1}{2})\hat{\sigma}_z, \end{aligned} \quad (\text{A.9})$$

which is easy to show using the following commutation relations: $[\hat{\sigma}^+, \hat{\sigma}^-] = \hat{\sigma}_z$, $[\hat{\sigma}_z, \hat{X}_-] = -2\hat{X}_+$, $[\hat{a}^\dagger\hat{a}, \hat{X}_-] = \hat{X}_+$, and $[\hat{X}_+, \hat{X}_-] = 1 + 2\hat{\sigma}_z(\hat{a}^\dagger\hat{a} + 1/2)$. The final line of Equation A.9 has three terms corresponding to the qubit, the cavity, and their interaction. Note that the interaction term now commutes with our measurement σ_z . \hat{H}_{disp} can be rearranged as:

$$\hat{H}_{disp} = \frac{1}{2}\hbar(\omega_{10} + \frac{g^2}{\Delta} + \frac{g^2}{\Delta}\hat{a}^\dagger\hat{a})\hat{\sigma}_z + \hbar\omega_r(\hat{a}^\dagger\hat{a} + \frac{1}{2}), \quad (\text{A.10})$$

where the qubit's frequency is now shifted by g^2/Δ - the zero-point energy of the cavity field, known as the Lamb shift - plus the photon dependent Stark shift $\frac{g^2}{\Delta}\hat{a}^\dagger\hat{a}$, with $\hat{a}^\dagger\hat{a}$ being the number of photons in the cavity. To understand how the qubit influences the cavity resonance, we can finally recast \hat{H}_{dips} into the following form:

$$\hat{H}_{disp} = \frac{1}{2}\hbar\omega_{10}\hat{\sigma}_z + \hbar(\omega_r + \frac{g^2}{\Delta}\hat{\sigma}_z)(\hat{a}^\dagger\hat{a} + \frac{1}{2}), \quad (\text{A.11})$$

where the cavity frequency is shifted by the state dependent $\pm\chi = \pm g^2/\Delta$, known as the dispersive shift. In consequence, probing the resonance of the cavity measures the projective state of the qubit.

A.2.2 Higher Order Approximation

In the previous section, we derived the familiar form of the Jaynes Cummings Hamiltonian in the dispersive limit \hat{H}_{dips} , but the above perturbation is only correct to the first order in λ . Boissonneault et. al.[124] fully diagonalize \hat{H}_{JC} to give the following general dispersive Hamiltonian:

$$\hat{H}_{disp} = \frac{1}{2}\omega_{10}\hat{\sigma}_z + \hbar\omega_c\hat{a}^\dagger\hat{a} - \frac{1}{2}\hbar\Delta(1 - \sqrt{1 + 4\lambda^2N_q})\hat{\sigma}_z, \quad (\text{A.12})$$

where $N_q = \hat{a}^\dagger\hat{a} + |1\rangle\langle 1| = \hat{a}^\dagger\hat{a} + 1/2(\hat{\sigma}_z + 1)$. It follows that the Lamb shift δ_L is:

$$\begin{aligned}
\hbar\delta_L &= E_{disp}(\hat{a}^\dagger\hat{a} = 0, \hat{\sigma}_z = 1) - E_{disp}(\hat{a}^\dagger\hat{a} = 0, \hat{\sigma}_z = -1) - \hbar\omega_{10} \\
&= \frac{1}{2}\hbar\Delta(1 - \sqrt{1 + 4\lambda^2}) = \hbar\chi + o(\lambda^5),
\end{aligned} \tag{A.13}$$

where $\chi = g^2(1 - \lambda^2)/\Delta$. The Stark shift $\delta_S(\hat{a}^\dagger\hat{a})$ is:

$$\begin{aligned}
\hbar\delta_S(\hat{a}^\dagger\hat{a}) &= E_{disp}(\hat{a}^\dagger\hat{a}, \hat{\sigma}_z = 1) - E_{disp}(\hat{a}^\dagger\hat{a}, \hat{\sigma}_z = -1) - \delta_L - \hbar\omega_{10} \\
&= \frac{1}{2}\hbar\Delta(\sqrt{1 + 4\lambda^2(\hat{a}^\dagger\hat{a} + 1)} + \sqrt{1 + 4\lambda^2\hat{a}^\dagger\hat{a}} - 1 - \sqrt{1 + 4\lambda^2}) \\
&= \hbar\chi\hat{a}^\dagger\hat{a} + \hbar\zeta(\hat{a}^\dagger\hat{a})^2 + o(\lambda^5),
\end{aligned} \tag{A.14}$$

where $\zeta = -g^4/\Delta^3$. Expanding Equation A.12 to third order in λ leads to the following approximation:

$$\hat{H}_{disp} \approx \hbar(\omega_r + \zeta)\hat{a}^\dagger\hat{a} + \frac{1}{2}\hbar \left[\omega_{10} + 2\chi(\hat{a}^\dagger\hat{a} + \frac{1}{2}) + 2\zeta(\hat{a}^\dagger\hat{a})^2 \right] \hat{\sigma}_z, \tag{A.15}$$

The definition of the critical photon number n_{crit} comes from the above expansion about $4\lambda^2 N_q \ll 1$:

$$n_{crit} = \frac{\Delta^2}{4g^2}. \tag{A.16}$$

A.3 Dispersive Limit for Many-Level System

The above approximation breaks down for a weakly anharmonic system. For the superconducting qubits in this thesis, the anharmonicity is on the order of $\alpha = \omega_{10} - \omega_{21} \approx 250$ MHz. The presence of the higher order eigenstates modify the Jaynes-Cummings hamiltonian and in consequence the dispersive shift of the resonance frequency of the cavity. Boissonneault *et al.*[120] studied the MLS-resonator system, considering a truncated Hilbert space of M states labeled $|0\rangle, \dots, |M-1\rangle$, obtaining the following hamiltonian to fourth order in $\lambda_i = -g_{i+1,i}/\Delta_i$:

$$H_S^D \approx \tilde{H}_0 + \sum_{i=0}^{M-1} S_i \Pi_{i,i} \hat{a}^\dagger \hat{a} + \sum_{i=0}^{M-1} K_i \Pi_{i,i} (\hat{a}^\dagger \hat{a})^2, \quad (\text{A.17})$$

where $\Pi_{i,j} = |i\rangle\langle j|$ is the product state, \tilde{H}_0 is the Lamb shifted Hamiltonian of the bare qubit and cavity $H_0 = \omega_r \hat{a}^\dagger \hat{a} + \sum_{i=0}^{M-1} \omega_i \Pi_{i,i}$, S_i is the ac-Stark coefficient:

$$\begin{aligned} S_i = & [\chi_{i-1}(1 - \lambda_i^2) - \chi_i(1 - \lambda_{i-1}^2 - 2\chi_{i-1}\lambda_{i-1}^2)] \\ & + \frac{1}{4}[9\chi_{i-2}\lambda_{i-1}^2 - 3\chi_{i-1}\lambda_{i-2}^2 - \chi_i\lambda_{i+1}^2 + 3\chi_{i+1}\lambda_i^2] \\ & - g_i^{(2)}\lambda_i^{(2)} - 3g_{i-2}^{(2)}\lambda_{i-2}^{(2)}, \end{aligned} \quad (\text{A.18})$$

and K_i is the Kerr coefficient:

$$\begin{aligned}
K_i &= \frac{1}{4}[3\chi_{i-2}\lambda_{i-1}^2 - \chi_{i-1}\lambda_{i-2}^2 + \chi_i\lambda_{i+1}^2 - 3\chi_{i+1}\lambda_i^2] \\
&+ [\chi_i - \chi_{i-1}][\lambda_i^2 + \lambda_{i-1}^2] - g_i^{(2)}\lambda_i^{(2)} - 3g_{i-2}^{(2)}\lambda_{i-2}^{(2)}.
\end{aligned} \tag{A.19}$$

The above coefficient depend on the following definitions: $\chi_i = g_{i+1,i}^2/\Delta_i$, $\Delta_i = (\omega_{i+1} - \omega_i) - \omega_r$, $g_i^{(2)} = \lambda_i\lambda_{i+1}(\Delta_{i+1} - \Delta_i)$, and $\lambda_i^{(2)} = -g_i^{(2)}/(\Delta_{i+1} + \Delta_i)$, where $\chi_i = \lambda_i = 0$ for $i \notin [0, M-2]$. It follows that the cavity will have the following state dependent resonance frequency:

$$\omega_r^{(0),|1\rangle} = \omega_r + S_{0,1} + K_{0,1}\bar{n}, \tag{A.20}$$

where $\omega_r^{(0)}$ ($\omega_r^{(1)}$) is the resonance of the cavity when the qubit is in the $|0\rangle$ ($|1\rangle$) state, and $\bar{n} = \langle \hat{a}^\dagger \hat{a} \rangle$ is the average cavity photon population. Note that in the dispersive limit and for small \bar{n} , $\omega_r^{(0)}$ is well approximated by:

$$\omega_r^{(0)} \approx \chi_0 = \frac{g_{10}^2}{\Delta_0}, \tag{A.21}$$

which is a helpful identity when experimentally determining g_0 . The dressed cavity states are separated by 2χ :

$$2\chi = \omega_r^{(1)} - \omega_r^{(0)} = (S_1 - S_0) + (K_1 - K_0)\bar{n}, \tag{A.22}$$

while the qubit frequency is modified by the cavity pull, known as the ac-Stark shift, in the following way:

$$\zeta = 2\chi\bar{n} = (S_1 - S_0)\bar{n} + (K_1 - K_0)\bar{n}^2. \quad (\text{A.23})$$

The above discussion gives us the power to calculate the dispersive shift (2χ) and the ac-Stark shift (ζ) as a function of \bar{n} after experimentally determining ω_{10} , ω_{21} , ω_{32} , g_{10} , and ω_r . This is a useful tool for calibrating \bar{n} as a function of readout drive power.

Appendix B

Numerical Techniques

This appendix goes over the details of simulating both classical and quantized Josephson based electronics. For the classical numerics we follow the techniques discussed by Tesche et. al. [81].

B.1 Numerical Integration

All classical equations of motion in this thesis can be reduced to a set of coupled first order differential equations, with time as their independent variable. For example, the general second order differential equation:

$$\ddot{y}(t) = f[\dot{y}(t), y(t), t], \tag{B.1}$$

becomes two coupled single order differential equations:

$$\begin{aligned}\dot{g}(t) &= f[g(t), y(t), t], \\ \dot{y}(t) &= g(t),\end{aligned}\tag{B.2}$$

where the dot overhead is the time derivative. Once in this form, we use the common fourth order Runge-Kutta iterative method to numerically integrate the set of first order differential equations. Let's write down this method for the simple example of Equation B.2. We're interested in solving for time t between 0 and A , with time step h , where h is smaller than the relevant time scales of the solution— h can be iteratively chosen for a convergent solution that isn't unnecessarily computational intensive.

We first choose initial conditions $g^0 = g_0$, and $y^0 = y_0$, which for this thesis are arbitrarily set to 0 – the initial conditions are “forgotten” with enough time. In general, the superscripts k of the solution refer to k th time step. The solutions to g and y can be approximated as:

$$\begin{aligned}t^{n+1} &= t^n + h, \\ y^{n+1} &= y^n + \frac{1}{6}h(k_1 + 2k_2 + 2k_3 + k_4), \\ g^{n+1} &= g^n + \frac{1}{6}h(m_1 + 2m_2 + 2m_3 + m_4),\end{aligned}\tag{B.3}$$

where:

$$\begin{aligned}
k_1 &= g^n, \\
k_2 &= g^n + \frac{1}{2}m_1, \\
k_3 &= g^n + \frac{1}{2}m_2, \\
k_4 &= g^n + m_3,
\end{aligned} \tag{B.4}$$

and:

$$\begin{aligned}
m_1 &= f[g^n, y^n, t^n], \\
m_2 &= f[g^n + \frac{1}{2}m_1, y^n + \frac{1}{2}k_1, t^n + \frac{1}{2}h], \\
m_3 &= f[g^n + \frac{1}{2}m_2, y^n + \frac{1}{2}k_2, t^n + \frac{1}{2}h], \\
m_4 &= f[g^n + m_3, y^n + k_3, t^n + h].
\end{aligned} \tag{B.5}$$

The numerical techniques in this section are applied throughout this thesis when solving the classical equations of motion of any Josephson based device. It is straightforward to incorporate noise sources and voltage sources into the analysis.

B.2 Classical Thermal Noise

The classical voltage spectral density of a resistor R at temperature T is just:

$$S_V^N = 4k_B T R \tag{B.6}$$

In dimensionless units, Equation B.6 rescales as:

$$\tilde{S}_V^N = 4\Gamma \quad (\text{B.7})$$

where $\Gamma = \frac{2\pi k_B T}{I_0 \Phi_0}$ is the dimensionless temperature. The power spectral density is just the mean square of the voltage variance per hertz of bandwidth. With this definition, a discrete \tilde{V}_N series is generated from a normal distribution with a zero mean and a standard deviation $\sqrt{2\Gamma f_s} = \sqrt{2\Gamma/h}$, where h is once again the time step. \tilde{V}_N can then be plugged into the mechanics of our Runge-Kutta solver.

B.3 Quantum Thermal Noise

The quantum voltage spectral density of a resistor R at temperature T is just:

$$S_V^N = 2hfR \coth\left(\frac{hf}{2k_B T}\right), \quad (\text{B.8})$$

where h is Planck's constant and f is the frequency. In the quantum limit, where $hf \gg k_B T$, Equation B.8 reduces to:

$$S_V^N \approx 2hfR. \quad (\text{B.9})$$

In dimensionless units, Equation B.9 rescales as:

$$\tilde{S}_V^N = \chi \tilde{f}, \quad (\text{B.10})$$

where $\chi = 8h\pi^2 R / \Phi_0^2$, and \tilde{f} is the dimensionless frequency. Equation B.10 describes the voltage spectral density only for $f > 0$, where $\tilde{S}_V^N = 0$ for $\tilde{f} < 0$. We generate the noise in the frequency domain with an amplitude defined by Equation B.10 but with a random phase θ . The complex signal in the frequency domain has the following form:

$$S_q = f_s N \chi \tilde{f} [\cos \theta + i \sin \theta] \quad (\text{B.11})$$

which is true for $\tilde{f} > 0$, and where f_s is the sampling frequency and N is the total number of time steps. We then take the inverse Fourier transform of S_q to get the noise voltage as function time that we can plug into our Runge-Kutta solver, where we include the $\tilde{f} < 0$ side of the spectrum when $S_q = 0$.

B.4 SLUG Spectral Noise Components

The different SLUG noise components are numerically extracted from the equations of motion in the same way for both the thermal and quantum noise sources. For example, when calculating S_V , the output voltage is solved using the standard Runge-Kutta method described above. The power spectral density of the output voltage is computed using MATLAB's *pwelch*. S_V is computed in this way for many (~ 100) different realizations of the added Johnson noise, finally averaged together to give a smooth form for the spectral density, with an example plotted in Figure ???. The noise spectrum consists

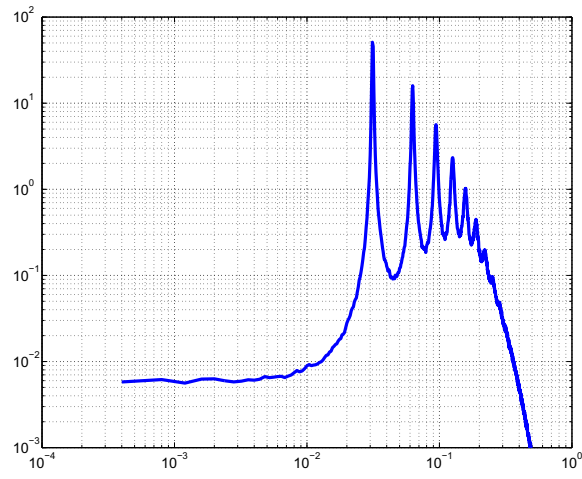


Figure B.1: S_V for the output voltage of a SLUG with $\beta_L = 1$, $\beta_C = 0.8$, $L = 10$ pH, $C = 50$ fF, $I_b = 1.9I_0$, $\Phi_b = 0.4\Phi_0$, $T = 100$ mK.

of a series of peaks at the Josephson frequency and its harmonics; the noises plotted in Sections 3.5 and 3.5 are evaluated at low frequency $f \ll f_j$ where the spectrum is white.

Bibliography

- [1] A. Wallraff et al., *Nature* **431**, 162 (2004).
- [2] D. Bozyigit et al., *Nature Physics* **7**, 154 (2010).
- [3] R. Koch, D. J. Van Harlingen, and J. Clarke, *Applied Physics Letters* **38**, 380 (1981).
- [4] R. Jaklevic, J. Lambe, A. Silver, and J. Mercereau, *Physical Review Letters* **12**, 159 (1964).
- [5] S. J. Asztalos et al., *Physical Review Letters* **104**, 041301 (2010).
- [6] J. Luomahaara et al., *Superconductor Science and Technology* **24**, 075020 (2011).
- [7] H. Tanaka, Y. Sekine, S. Saito, and H. Takayanagi, *Physica C: Superconductivity* **368**, 300 (2002).
- [8] J. R. Kirtley and J. P. Wikswo, Jr., *Annual Review of Materials Science* **29**, 117 (1999).
- [9] A. Zieba, *Review of Scientific Instruments* **64**, 3357 (1993).
- [10] J. P. Wikswo, *IEEE Transactions on Applied Superconductivity* **5**, 74 (1995).
- [11] M. Peters et al., *Journal of Perinatal Medicine* **29** (2001).
- [12] P. W. Shor, Algorithms for quantum computation: discrete logarithms and factoring, in *35th Annual Symposium on Foundations of Computer Science*, pages 124–134, IEEE Comput. Soc. Press, 1994.
- [13] R. L. Rivest, A. Shamir, and L. Adleman, *Communications of the ACM* **21**, 120 (1978).
- [14] R. P. Feynman, *International Journal of Theoretical Physics* **21**, 467 (1982).
- [15] M. A. Nielsen and I. L. Chuang, *Quantum Computation and Quantum Information*, 10th Anniversary Edition, Cambridge University Press, 2010.

- [16] J. M. Chow, Yale Thesis (2010).
- [17] D. H. Slichter, UC Berkeley Thesis (2011).
- [18] J. Lisenfeld, The Journal of Chemical Physics (2008).
- [19] I. Chuang, N. Gershenfeld, and M. Kubinec, Physical Review Letters **80**, 3408 (1998).
- [20] J. I. Cirac and P. Zoller, Physical Review Letters (1995).
- [21] D. Loss and D. P. DiVincenzo, Physical Review A **57**, 120 (1998).
- [22] C. B. Simmons et al., Applied Physics Letters **91**, 213103 (2007).
- [23] M. H. Devoret and R. J. Schoelkopf, Science **339**, 1169 (2013).
- [24] M. H. Devoret, A. Wallraff, and J. M. Martinis, arXiv.org (2004).
- [25] A. G. Fowler, M. Mariantoni, J. M. Martinis, and A. N. Cleland, Physical Review A **86**, 032324 (2012).
- [26] J. Martinis et al., Physical Review Letters **95** (2005).
- [27] A. Megrant et al., Applied Physics Letters **100**, 113510 (2012).
- [28] J. Chang et al., arXiv.org (2013).
- [29] V. Bouchiat, D. Vion, P. Joyez, D. Esteve, and M. H. Devoret, Physica Scripta **T76**, 165 (1998).
- [30] Y. Nakamura, Y. A. Pashkin, and J. S. Tsai, Nature **398**, 786 (1999).
- [31] J. Koch et al., Physical Review A **76**, 042319 (2007).
- [32] R. Barends et al., arXiv.org (2013).
- [33] D. Schuster, Yale Thesis (2007).
- [34] A. Blais, R.-S. Huang, A. Wallraff, S. M. Girvin, and R. J. Schoelkopf, Physical Review A **69** (2004).
- [35] E. T. Jaynes and F. W. Cummings, IEEE Xplore - Comparison of quantum and semiclassical radiation theories with application to the beam maser, in *Proceedings of the IEEE*, 1963.
- [36] T. Picot, R. Schouten, C. J. P. M. Harmans, and J. E. Mooij, Physical Review Letters **105**, 040506 (2010).

- [37] B. R. Johnson et al., *Nature Physics* **6**, 663 (2010).
- [38] N. Boulant, G. Ithier, and P. Meeson, *Physical Review B* **76**, 014525 (2007).
- [39] R. Vijay, D. H. Slichter, and I. Siddiqi, *Physical Review Letters* **106**, 110502 (2011).
- [40] H. Nyquist, *Physical Review* **32**, 110 (1928).
- [41] J. Johnson, *Physical Review* **32**, 97 (1928).
- [42] A. A. Clerk, M. H. Devoret, S. M. Girvin, F. Marquardt, and R. J. Schoelkopf, *Reviews of Modern Physics* **81**, 1155 (2010).
- [43] H. B. Callen and T. A. Welton, *Physical Review* (1951).
- [44] C. CAVES, *Physical Review D* **26**, 1817 (1982).
- [45] M. A. Castellanos-Beltran, K. D. Irwin, G. C. Hilton, L. R. Vale, and K. W. Lehnert, *Nature Physics* **4**, 929 (2008).
- [46] M. A. Castellanos-Beltran, K. D. Irwin, L. R. Vale, G. C. Hilton, and K. W. Lehnert, *IEEE Transactions on Applied Superconductivity* **19**, 944.
- [47] T. Yamamoto et al., *Applied Physics Letters* **93**, 042510 (2008).
- [48] M. Hatridge, R. Vijay, D. H. Slichter, J. Clarke, and I. Siddiqi, *Physical Review B* **83**, 134501 (2011).
- [49] R. Vijay, Yale Thesis (2008).
- [50] R. Vijay et al., *Nature* **490**, 77 (2012).
- [51] O. Yaakobi, L. Friedland, C. Macklin, and I. Siddiqi, *Physical Review B* **87**, 144301 (2013).
- [52] J. Bardeen, L. N. Cooper, and J. R. Schrieffer, *Physical Review* **108**, 1175 (1957).
- [53] H. K. Onnes, *KNAW* (1911).
- [54] W. Meissner and R. Ochsenfeld, *Die Naturwissenschaften* **21**, 787 (1933).
- [55] F. London, *Superfluids*, 1950.
- [56] M. Tinkham, *Introduction to Superconductivity: Second Edition*, 2004.
- [57] B. D. Josephson, *Physics Letters* **1**, 251 (1962).
- [58] D. E. McCumber, *Journal of Applied Physics* **39**, 3113 (1968).

- [59] D. MCCUMBER, *Journal of Applied Physics* **39**, 297 (1968).
- [60] W. C. Stewart, *Applied Physics Letters* **12**, 277 (1968).
- [61] W. J. Johnson, *Wisconsin Thesis* (1969).
- [62] V. Ambegaokar and A. Baratoff, *Physical Review Letters* **10**, 486 (1963).
- [63] M. Mück, C. Welzel, and J. Clarke, *Applied Physics Letters* **82**, 3266 (2003).
- [64] J. Clarke, *SQUID Sensors: Fundamentals, Fabrication and Applications* **329**, 1 (1996).
- [65] M. Ketchen and J. Jaycox, *Applied Physics Letters* **40**, 736 (1982).
- [66] C. Hilbert and J. Clarke, *Journal of Low Temperature Physics* **61**, 263 (1985).
- [67] M. Mück, M. Andre, J. Clarke, J. Gail, and C. Heiden, *Applied Physics Letters* **72**, 2885 (1998).
- [68] M. Mück and J. Clarke, *Applied Physics Letters* **78**, 3666 (2001).
- [69] D. Kinion and J. Clarke, *Applied Physics Letters* **98**, 202503 (2011).
- [70] M. P. DeFeo et al., *Applied Physics Letters* **97**, 092507 (2010).
- [71] M. P. DeFeo and B. L. T. Plourde, *Applied Physics Letters* **101**, 052603 (2012).
- [72] L. Spietz, K. Irwin, and J. Aumentado, *Applied Physics Letters* **93**, 082506 (2008).
- [73] L. Spietz, K. Irwin, and J. Aumentado, *Applied Physics Letters* (2009).
- [74] L. Spietz, K. Irwin, M. Lee, and J. Aumentado, *Applied Physics Letters* **97**, 142502 (2010).
- [75] J. Clarke, *Philosophical Magazine* **13**, 115 (1966).
- [76] G. J. Ribeill, D. Hover, Y. F. Chen, S. Zhu, and R. McDermott, *Journal of Applied Physics* **110**, 103901 (2011).
- [77] C. Tesche and J. Clarke, *Magnetics, IEEE Transactions on* **13**, 859 (1977).
- [78] C. D. Tesche, *Journal of Low Temperature Physics* **47**, 385 (1982).
- [79] C. TESCHE and J. Clarke, *Journal of Low Temperature Physics* **37**, 397 (1979).
- [80] O. Snigirev, *Magnetics, IEEE Transactions on* **19**, 584 (1983).

- [81] C. Tesche and J. Clarke, *Journal of Low Temperature Physics* **29**, 301 (1977).
- [82] C. Hilbert and J. Clarke, *Journal of Low Temperature Physics* **61**, 237 (1985).
- [83] D. J. Van Harlingen, *Applied Physics Letters* **41**, 197 (1982).
- [84] J. Rowell, M. Gurvitch, and J. Geerk, *Physical Review B* **24**, 2278 (1981).
- [85] M. Gurvitch, *Applied Physics Letters* **42**, 472 (1983).
- [86] J. Clarke, C. Tesche, and R. Giffard, *Journal of Low Temperature Physics* **37**, 405 (1979).
- [87] D. M. Pozar, *Microwave Engineering*, Wiley, 2011.
- [88] J. Clarke, W. M. Goubau, and M. B. Ketchen, *Journal of Low Temperature Physics* **25**, 99 (1976).
- [89] F. Wellstood, C. Urbina, and J. Clarke, *Physical Review B* **49**, 5942 (1994).
- [90] F. C. Wellstood, C. Urbina, and J. Clarke, *Applied Physics Letters* **54**, 2599 (1989).
- [91] A. J. Miller, S. W. Nam, J. M. Martinis, and A. V. Sergienko, *Applied Physics Letters* **83**, 791 (2003).
- [92] R. F. Miracky, J. Clarke, and R. H. Koch, *Physical Review Letters* **50**, 856 (1983).
- [93] Cawthorne, AB, C. B. Whan, and C. J. Lobb, *Journal of Applied Physics* **84**, 1126 (1998).
- [94] K. Wiesenfeld, E. Knobloch, R. Miracky, and J. Clarke, *Physical Review A* **29**, 2102 (1984).
- [95] M. B. Ketchen et al., *Applied Physics Letters* **59**, 2609 (1991).
- [96] D. Yohannes et al., *Applied Superconductivity*, *IEEE Transactions on* **15**, 90 (2005).
- [97] K. Hinode et al., *Physica C: Superconductivity* **412-414**, 1437 (2004).
- [98] S. Nagasawa, T. Satoh, K. Hinode, Y. Kitagawa, and M. Hidaka, *Applied Superconductivity*, *IEEE Transactions on* **17**, 177 (2007).
- [99] B. A. Mazin et al., *Applied Physics Letters* **96**, 102504 (2010).
- [100] M. Kamon, M. J. Tsuk, and J. K. White, *Microwave Theory and Techniques*, *IEEE Transactions on* **42**, 1750 (1994).

- [101] K. C. Gupta, *Microstrip Lines and Slotlines 2nd Ed.*, Artech House on Demand, 1996.
- [102] J. Wenner et al., *Superconductor Science and Technology* **24**, 065001 (2011).
- [103] J. Pleikies, O. Usenko, and J. Flokstra, *Journal of Physics: Conference ...* **97**, 012254 (2008).
- [104] V. F. Gantmakher, *Reports on Progress in Physics* **37**, 317 (2001).
- [105] S. X. Qu, A. Cleland, and M. Geller, *Physical Review B* **72**, 224301 (2005).
- [106] J. Pleikies et al., *Superconductor Science and Technology* **22**, 114007 (2009).
- [107] P. Falferi, R. Mezzena, and M. Mück, *Journal of Physics: ...* (2008).
- [108] A. Vinante, P. Falferi, R. Mezzena, and M. Mück, *Physical Review B* (2007).
- [109] S. Sendelbach, *Wisconsin Thesis* (2012).
- [110] L. Ranzani, L. Spietz, Z. Popovic, and J. Aumentado, *Review of Scientific Instruments* **84**, 034704 (2013).
- [111] M. H. Devoret, *Les Houches, Session LXIII* (1995).
- [112] G. Burkard, R. Koch, and D. DiVincenzo, *Physical Review B* **69**, 064503 (2004).
- [113] B. Mazin, *CalTech Thesis* (2005).
- [114] J. Gambetta et al., *Physical Review A* **77**, 012112 (2008).
- [115] J. M. Gambetta, A. A. Houck, and A. Blais, *Physical Review Letters* (2011).
- [116] J. Gambetta, W. Braff, A. Wallraff, S. Girvin, and R. Schoelkopf, *Physical Review A* **76**, 012325 (2007).
- [117] R. Barends et al., *Applied Physics Letters* **99**, 113507 (2011).
- [118] T. O. Klaassen et al., *Absorbing coatings and diffuse reflectors for the Herschel platform sub-millimeter spectrometers HIFI and PACS*, in *THz 2002. 2002 IEEE Tenth International Conference on Terahertz Electronics*, pages 32–35, IEEE, 2002.
- [119] M. Ansmann, *UCSB Thesis* (2009).
- [120] M. Boissonneault, J. M. Gambetta, and A. Blais, *Physical Review Letters* **105**, 100504 (2010).

- [121] L. S. Bishop, E. Ginossar, and S. M. Girvin, *Physical Review Letters* **105**, 100505 (2010).
- [122] M. D. Reed et al., *Physical Review Letters* **105**, 173601 (2010).
- [123] D. Sank et al., *Physical Review Letters* **109**, 067001 (2012).
- [124] M. Boissonneault, J. M. Gambetta, and A. Blais, *Physical Review A* **79**, 013819 (2009).